Instituto Tecnológico de Buenos Aires

DEPARTAMENTO DE INVESTIGACIÓN Y DOCTORADO

Estudio Teórico y Experimental del Proceso de Inversión de Fases en la Síntesis en Masa del Poliestireno de Alto Impacto

AUTOR: Juan M. Maffi

DIRECTOR: Dra. Diana Estenoz

CO-DIRECTOR: Dr. Emilio Berkenwald

TESIS PRESENTADA PARA OPTAR AL TÍTULO DE

DOCTOR EN INGENIERÍA

Jurado

Dra. Claudia Sarmoria | Dr. Luis Gugliotta | Dr. Marcelo Villar

CIUDAD AUTÓNOMA DE BUENOS AIRES

2021

Ing. Juan M. MAFFI: ESTUDIO TEÓRICO Y EXPERIMENTAL DEL PROCESO DE INVERSIÓN DE FASES EN LA SÍNTESIS EN MASA DEL POLIESTIRENO DE ALTO IMPACTO. *Tesis presentada como requisito parcial para acceder al grado de* ***DOCTOR EN INGENIERÍA*** *del Instituto Tecnológico de Buenos Aires.*

Instituto Tecnológico de Buenos Aires

DEPARTAMENTO DE INVESTIGACIÓN Y DOCTORADO

Theoretical and Experimental Study on the Phase Inversion Process during the Bulk Synthesis of High Impact Polystyrene

AUTHOR: Juan M. Maffi

ADVISOR: Dra. Diana Estenoz

CO-ADVISOR: Dr. Emilio Berkenwald

A THESIS SUBMITTED AS A REQUIREMENT FOR THE DEGREE OF

DOCTOR EN INGENIERÍA

Thesis committee

Claudia Sarmoria, PhD. Luis Gugliotta, PhD. Marcelo Villar, PhD.

CIUDAD AUTÓNOMA DE BUENOS AIRES

2021

Eng. Juan M. MAFFI: THEORETICAL AND EXPERIMENTAL STUDY ON THE PHASE INVERSION PROCESS DURING THE BULK SYNTHESIS OF HIGH IMPACT POLYSTYRENE.
A thesis submitted in partial fulfillment of the requirements for the degree of ***DOCTOR EN INGENIERÍA*** *of Instituto Tecnológico de Buenos Aires.*

A mi familia

"Men love to wonder, and that is the seed of science"

Ralph Waldo Emerson

Agradecimientos

Tomar la decisión de cambiar de rumbo profesional y abandonar la industria para dedicarme a la vida académica no fue algo fácil ni rápido. Fue el producto de muchas charlas, averiguaciones, planteos... Definitivamente no podría haber dado ese salto de fe sin la escucha y el apoyo de quienes constituyen el pilar básico de la vida: la familia. A mis padres, Hugo y Adriana, a mi hermana, Lucía, les agradezco por haber escuchado y aceptado mi deseo de dedicarme a la investigación y a la docencia - verdaderas pasiones - y por continuar haciéndolo todos los días. En particular, a quien comenzó esta tesis como mi novia, y la culminó como mi esposa y madre de mi hijo. Gracias Juli por haberme apoyado a pesar de la incertidumbre y de los miedos, por haber aceptado que este es el camino que quiero elegir día a día, por haber festejado cada paper publicado como si fueras la autora, por escucharme como si también fueses tesista. En fin, ¡por todo!

La piedra angular de este proyecto se la debo a mi co-director, Dr. Emilio Berkenwald, quien me abrió las puertas al grupo de investigación, con base en la Oficina A-2-6 del ITBA, dirigido por quien es un modelo en todo sentido: mi directora, Dra. Diana Estenoz. Gracias a ambos, por su apoyo, su ayuda, sus visiones y tantas discusiones compartidas. Solo su calidez humana y profesional ya justifican, sin lugar a dudas, la decisión de haber comenzado este proyecto.

Al ser este un trabajo en colaboración, debo extender mi gratitud hacia el grupo de Graciela Morales, del Centro de Investigación en Química Aplicada (CIQA), en Saltillo, México, por la oportunidad de trabajar en conjunto.

Pero ninguna tesis doctoral es posible sin el día a día de un grupo de becarios que, como uno, transita los altibajos de la investigación. Desde la euforía por un resultado esperado, hasta la indignación por un código que no compila o un reactivo que se agotó antes de tiempo. El apoyo mutuo es el sotén cotidiano que permite que la tesis llegue a buen puerto, muchos años después de comenzada. A ustedes, Lau, Echo, Mati, José, Lucio, gracias por la catarsis, por el soporte y por tantas risas.

En esta línea, no quisiera dejar de reconocer a los miembros del Departamento de Ingeniería Química del ITBA, con quienes compartir el día a día es una prueba de que un ambiente laboral ameno, positivo, cooperativo, cálido, amistoso, es posible. A Jorge, Guille, Lau, Marce, María Inés, mi agradecimiento por hacer esto posible. En especial, debo expresarle toda mi gratitud a Vergenie Aude Luppi y a Gonzalo Arufe por ser, además de excelentes personas, quienes les dan forma al modelo de docente al que uno le gustaría aspirar.

Al ITBA y al Departamento de Investigación y Doctorado, debo extenderles mi reconocimiento y agradecimiento por la posibilidad de otorgarme un lugar de trabajo y por el financiamiento provisto.

Finalmente, un agradecimiento especial a aquellos que, sin saberlo, me han formado en más de un sentido. Porque como la noche no es sin el día, ni la sombra sin la luz, un docente no es sin sus alumnos. Gracias a ustedes, por hacernos mejores todos los días.

"Educating the mind without educating the heart, is no education at all"

Aristotle

Resumen

Los polímeros del estireno son termoplásticos de ingeniería de altos volúmenes de producción y bajo costo, utilizados frecuentemente en diversas aplicaciones. Una ruta de producción comercial muy difundida es la de la polimerización radicalaria en masa. En particular, si la polimerización de estireno se lleva a cabo en presencia de una goma (polibutadieno o algún copolímero de butadieno), se obtiene un material con mejores propiedades mecánicas denominado Poliestireno de Alto Impacto (HIPS). Este material, compuesto por una matriz de poliestireno y partículas dispersas de caucho, es apto para ser utilizado en aplicaciones de frecuente exposición a golpes (juguetes, componentes electrónicos, embalajes, etc.)

Las propiedades mecánicas que le otorgan un elevado interés a este material guardan una estrecha relación con la morfología del mismo, que es consecuencia directa de un complejo fenómeno conocido como la *inversión de fases*. Este proceso tiene lugar durante la etapa inicial de la polimerización. El sistema estireno-poliestireno-polibutadieno se separa inicialmente en dos fases debido a la incompatibilidad de las dos especies poliméricas: la fase continua es una solución de estireno rica en caucho, mientras que la fase dispersa consta de una mezcla estireno-poliestireno. A medida que avanza la reacción, la fracción de fase vítrea (dispersa) aumenta hasta un punto crítico en el cual puede transformarse en la fase continua, dejando a la fase rica en caucho como dispersa. Durante este proceso, algunas partículas de fase vítrea quedan ocluidas dentro de las partículas disperas, generando distintos tipos de morfologías.

Debido a la crucial relación entre el tamaño (y forma) de las partículas dispersas y las propiedades finales del material, la posibilidad de predecir la morfología del mismo a partir de recetas y condiciones de reacción es de elevado interés industrial. Para ello, comprender los fenómenos que influencian la inversión de fases resulta de vital importancia, con vistas al desarrolo de una herramienta capaz de predecir el momento de ocurrencia a partir de las condiciones de la polimerización.

En esta tesis se estudia el fenómeno de la inversión de fases tanto desde un punto de vista cualitativo, teórico y experimental. El objetivo general es contribuir a la comprensión de este

fenómeno fluido- y termodinámico en su aplicación particular para el caso de HIPS. Se busca desarrollar un modelo físico-matemático capaz de predecir el punto de inversión de fases durante la reacción a partir de las condiciones del reactor. Dentro de las diferentes alternativas, se exploran enfoques basados en la evolución reológica de la mezcla reaccionante y otros basados en la fluidodinámica del sistema disperso. Los trabajos teóricos se complementan con mediciones experimentales, a fin de ajustar y validar los modelos desarrollados.

Se presenta una revisión general de la bibliografía sobre los fenómenos de inversión de fases, tanto en sistemas tradicionales (orgánicos-acuosos) como poliméricos. Se analiza críticamente lo observado experimentalmente por diferentes autores y se busca generalizar los aspectos físicos del fenómeno. Con la información obtenida del análisis bibliográfico se estudia la posibilidad de producir modelos de inteligencia artificial que sean capaces de comprender la estructura subyacente de los datos experimentales, y predecir puntos de inversión a partir de condiciones operativas. Al mismo tiempo, se busca entender las reglas físicas por las cuales se rige el fenómeno de inversión, para poder ayudar a comprender mejor lo observado para el caso de HIPS.

Finalmente se presenta un desarrollo teórico, basado en una técnica de balances poblacionales, para predecir el momento de ocurrencia de la inversión de fases para diferentes condiciones de reacción. Se combina este modelo con los resultados de modelos cinéticos ya validados, de manera que tanto los aspectos fisicoquímicos (composiciones, volúmenes de fase, viscosidades, pesos moleculares medios) como los fluidodinámicos (velocidades de coalescencia y de ruptura de partículas) puedan ser acoplados para seguir la evolución de las características de la fase dispersa a lo largo de la reacción.

Abstract

Styrene polymers are high-volume, low-cost engineering thermoplastics frequently used in a variety of applications. A widespread commercial production route is that of bulk radical polymerization. In particular, if the styrene polymerization is carried out in the presence of a rubber (polybutadiene or some butadiene copolymer), a material with better mechanical properties called High Impact Polystyrene (HIPS) is obtained. This material, made up of a polystyrene matrix and dispersed rubber particles, is suitable for use in applications with frequent exposure to collisions (toys, electronic components, packaging, etc.)

The mechanical properties that make this material highly interesting are closely related to its morphology, which is a direct consequence of a complex phenomenon known as *phase inversion*. This process takes place during the initial stages of the polymerization. The styrene-polystyrene-polybutadiene system initially separates into two phases due to the incompatibility between the two polymeric species: the continuous phase is a rubber-rich styrene solution, while the dispersed phase consists of a styrene-polystyrene mixture. As the reaction proceeds, the vitreous (dispersed) phase fraction increases to a critical point at which it can become the continuous phase, leaving the rubber-rich phase as dispersed. During this process, some glassy phase particles are trapped within the dispersed particles, generating different types of morphologies.

Due to the crucial relationship between the size (and shape) of the dispersed particles and the final properties of the material, predicting its morphology from recipes and reaction conditions is of high industrial interest. To this end, understanding the phenomena that influence phase inversion is of vital importance, if developing a tool capable of predicting this key moment is sought.

In this thesis, the phenomenon of phase inversion is studied from a qualitative, theoretical and experimental point of view. The general objective is to contribute to the understanding of this fluid- and thermodynamic phenomenon in its particular application in the case of HIPS. The aim is to develop a physical-mathematical model capable of predicting the point of phase inversion during the reaction from the reactor conditions. Among the different alternatives,

approaches based on the rheological evolution of the reaction mixture and others based on the fluid dynamics of the dispersed system are explored. Theoretical work is complemented with experimental measurements, in order to adjust and validate the developed models.

A general review of the bibliography on the phase inversion phenomenon is presented, both in traditional (organic-aqueous) and polymeric systems. Experimental observations informed by different authors are critically analyzed and the physical aspects of the phenomenon are generalized. With the information obtained from the literature analysis, the possibility of producing artificial intelligence models that are capable of understanding the underlying structure of the experimental data and predicting inversion points based on operating conditions is studied. At the same time, this seeks to understand the physical rules by which the inversion phenomenon is governed, in order to better understand what is observed in the case of HIPS.

Finally, a theoretical development is presented, based on a technique of population balances, aiming to predict the phase inversion point for different reaction conditions. This model is combined with the results of already validated kinetic models, so that both the physicochemical aspects (compositions, phase volumes, viscosities, average molecular weights) and the fluid dynamics (coalescence and particle rupture rates) can be coupled to follow the evolution of the characteristics of the dispersed phase throughout the reaction.

Contents

List of Figures xvii

List of Tables xxiii

Symbols and Abbreviations xxv

1 Introduction 1

1.1 Styrene and its derivatives 1

1.2 Polymers of styrene 3

1.2.1 General Purpose Polystyrene (GPPS) 5

1.2.2 Expanded Polystyrene (EPS) 5

1.2.3 Poly(styrene-*co*-acrylonitrile) (SAN) 5

1.2.4 Acrylonitrile-Butadiene-Styrene (ABS) 6

1.2.5 Styrene-Butadiene Rubbers (SBR) 7

1.3 High-Impact Polystyrene (HIPS) 8

1.3.1 Manufacturing process 8

1.3.2 Material morphology 9

1.3.3 The phase inversion phenomenon 11

1.3.3.1 Phase inversion prediction 13

1.4 Objectives 14

2 The Phase Inversion Process **17**

2.1 The Ambivalent Range 19

2.1.1 Viscosity ratio 20

2.1.2 Stirring speed 25

2.1.3 Phase density difference 25

2.1.4 Interfacial tension 26

2.1.5 Geometry and vessel material 28

2.2 Effect of surface-active components on phase inversion dynamics 28

2.3 Emulsion rheology and phase inversion 35

2.4 The PI mechanism 42

2.4.1 Coalescence vs break-up imbalance 42

2.4.2 Energy minimization 43

2.4.3 Interfacial zero shear 44

2.4.4 Drop breakage and coalescence processes in liquid-liquid dispersions . 44

2.4.4.1 Coalescence 45

2.4.4.2 Break-up 56

2.5 Multiple emulsions 68

2.5.1 Inclusion mechanisms 69

2.5.2 Manufacture methods 71

2.5.3 Effects on main variables in morphology and inversion point 73

2.5.3.1 Catastrophic vs transitional inversion and the role of multiple emulsions . . . 74

2.6 Summary and conclusions . . . 77

3 Phase Inversion Prediction in O/W Systems 81

3.1 Relevant operating variables . . . 82

3.2 Algorithms . . . 83

3.2.1 Decision trees . . . 83

3.2.2 Support-vector machines . . . 84

3.2.3 Neural networks . . . 86

3.3 Implementation and results . . . 88

3.3.1 Classification . . . 88

3.3.1.1 Decision tree . . . 89

3.3.1.2 Bootstrap aggregation (bagging) . . . 92

3.3.1.3 Support-vector machine and neural network . . . 93

3.3.2 Regression . . . 94

3.3.2.1 Decision (and bagged) trees . . . 94

3.3.2.2 Support vector regression . . . 95

3.3.2.3 Neural networks . . . 96

3.3.3 Theoretical predictions of the ambivalent range . . . 98

3.4 Summary and conclusions . . . 101

4 Phase Inversion Prediction in the HIPS Bulk Synthesis: A Rheological Perspective 103

4.1 Experimental work . . . 106

4.1.1 Materials . . . 106
4.1.2 Synthesis of HIPS . . . 106
4.1.3 Characterization . . . 107
4.2 Experimental results . . . 108
4.2.1 Polymerization kinetics . . . 108
4.2.2 Phase inversion points . . . 109
4.2.3 Morphology . . . 112
4.2.4 Rheology . . . 117
4.3 Empirical model for the evolution of apparent viscosity . . . 118
4.3.1 Polymerization module . . . 118
4.3.2 Viscosity correlation module . . . 121
4.3.2.1 Dispersed phase fraction . . . 121
4.3.2.2 Shear rate . . . 123
4.3.2.3 Apparent viscosity model . . . 123
4.4 Theoretical results during the PI process . . . 128
4.5 Summary and conclusions . . . 129

5 Phase Inversion Prediction in the HIPS Bulk Synthesis: A Fluid-Dynamic Approach 131

5.1 Model development . . . 133
5.1.1 Heterogeneous bulk polymerization . . . 134
5.1.2 Population balance . . . 137
5.2 Implementation . . . 139
5.2.1 Choice of kernel functions . . . 144

5.2.1.1 Break-up . . . 144

5.2.1.2 Coalescence . . . 145

5.2.2 Phase properties . . . 152

5.3 Results . . . 155

5.3.1 Model adjustment . . . 155

5.3.2 Phase inversion criterion . . . 158

5.4 Summary and conclusions . . . 165

6 Conclusions **167**

A Phase Inversion Data from Literature **171**

B Mathematical Model for the Homogeneous Polymerization of Styrene in Presence of Polybutadiene **187**

C Mathematical Model for the Heterogeneous Polymerization of Styrene in Presence of Polybutadiene **191**

Bibliography **195**

List of Figures

1.1 Dehydrogenation of ethylbenzene to produce styrene. 2

1.2 Distribution of St production capacity per region as in 2019. 2

1.3 Distribution of PS production capacity per region as in 2016. 4

1.4 Process flow diagram of a typical HIPS industry. 9

1.5 Typical morphologies of high-impact polystyrene. 11

1.6 Reaction path of the HIPS bulk polymerization. 12

1.7 Decrease in apparent viscosity at the inversion point. 12

1.8 Evolution of the energy consumption by the mechanical stirrer along the reaction. 13

2.1 Ambivalent ranges for toluene(O)-water(W), CCl4(O)-water(W) and heptane(O)-acetonitrile(W) 19

2.2 Ambivalence diagram as a function of phase viscosity ratio. 20

2.3 Comparison of predicted PI points with viscosity ratio. For simplification, the stress ratio was considered equal to the apparent viscosity ratio when necessary. 22

2.4 Interfacial tension of petroleum sulfonate aqueous solutions with different organic phases. 27

2.5 Water-cyclohexane-NPE inversion map for different HLB values. 30

2.6 Qualitative evolution of emulsion interfacial tension with temperature. 31

2.7 Phase inversion map as a function of temperature for water-cyclohexane-polyoxyethylene nonylphenylether. Surfactant load is 7%wt. 31

2.8 Effect of emulsifier concentration on surface tension. 32

2.9 Effect of Span concentration on PI of O/W to W/O systems. Values in parentheses represent the HLB of the emulsifie. 33

2.10 Effect of Tween concentration on PI of W/O to O/W systems. Values in parentheses indicate HLB of emulsifier. 33

2.11 Delayed PI with increasing surfactant concentration for a W/O emulsion. . . 34

2.12 Evolution of mixture viscosity with reaction time for HIPS bulk process. . . . 41

2.13 Storage modulus and loss factor of a PP-PS blend as a function of PS content. 41

2.14 Phase inversion detected with different emulsification methods. 43

2.15 Qualitative comparison of collision frequency of equal drops according to published models as a function of particle diameter. 47

2.16 Deformable drops with different interface mobility. 48

2.17 Difference in drop deformability. 48

2.18 Coalescence rate as a function of surfactant's HLB. 55

2.19 Coalescence suppression by copolymer steric repulsion. 56

2.20 Effect of dispersed phase viscosity on maximum stable drop size before break-up. 64

2.21 Deformation process of a polyamide 6 thread surrounded by a PS matrix. . . 65

2.22 Tipstreming breakup mechanism. 67

2.23 Two possible outcomes of drop-drop collisions. 68

2.24 Outcome after collision map for equal size drops. 68

2.25 Example of a drop-in-drop structure. 69

2.26 Inclusion of continuous phase by drop deformation. 70

2.27 Entrapment mechanism by multiple particle collision. 70

2.28 Two-step method to produce a multiple emulsion. 72

2.29 Catastrophic phase inversions at the vicinity of the transitional threshold for a cyclohexane/water emulsion with 2%wt NPE5/NPE12 at 22°C 75

2.30 Effect of initiator concentration on the drop-in-drop structure. 76

3.1 Optimal separating hyperplane in a 2D example. 85

3.2 Scheme of a feedforward multiple perceptron. 86

3.3 Decision tree to decide whether a given phase will be continuous. 90

3.4 Optimum tree, pruned with a CP of 0.007. 91

3.5 Prediction of PI points as per the decision tree models. Dashed lines represent a margin of ± 0.03, which is considered a suitable error gap. 95

3.6 Performance of different kernel functions used in SVR algorithms. Test set is the same for all kernels. Dashed lines represent a margin of ± 0.03, which is considered a suitable error gap. 96

3.7 Prediction of each neural network with one hidden layer and varying number of neurons. Test subset is the same for all and the same for the other models in this work. Dashed lines represent a margin of ± 0.03, which is considered a suitable error gap. 97

3.8 PI hypothetical map as predicted by the neural network model. 100

3.9 PI curves for systems having the same density difference and viscosity ratio. . 100

4.1 Effect of the BPO concentration on the main reactor variables. 109

4.2 Apparent viscosity of the prepolymerizing mixture as a function of monomer conversion. 110

4.3 Apparent viscosity of the prepolymerizing mixture for each pair of reactions at different stirring speeds. 112

4.4 TEM images for Run 3 at (a) 8.2% conversion and (b) 13%. 113

4.5 Particle size distribution for reaction 3 before and after PI. 113

4.6 Distribution of occluded fractions for each reaction at around the inversion point. . . . 115

4.7 Internal phase ratio (estimated by the ratio of the total area occupied by the occlusions to the area occupied by the entire particle) at the inversion point as a function of particle size. . . . 116

4.8 Final product morphology for a set of reactions. . . . 116

4.9 Rheological behavior of the prepolymerizing system in runs 1 and 4. . . . 117

4.10 Evolution of the power law model parameters for reactions 1 and 4. . . . 118

4.11 Relative viscosity of the polymerizing system before phase inversion, at the investigated stirring speeds. . . . 125

4.12 Predicted evolution of the apparent viscosity of each reaction mixture. . . . 127

4.13 Predicted system properties during the phase inversion process. . . . 128

5.1 Distribution of masses between each component of the system. . . . 137

5.2 A discretized moving grid. . . . 140

5.3 Predicted break-up frequency for variations of the most important parameters. 145

5.4 Coalescence efficiency model by Coulaloglou and Tavlarides. . . . 148

5.5 Coalescence efficiency model by Hasseine. . . . 149

5.6 Coalescence efficiency model by Hasseine 150

5.7 Coalescence efficiency model by Sovová. . . . 151

5.8 Comparison of coalescence efficiency models. . . . 152

5.9 Main reaction variables predicted by the heterogeneous model. . . . 156

5.10 Particle size distributions for the set of reactions for which available TEM images could be analyzed. . . . 157

5.11 Fractional coalescence frequency for each reaction. . . . 158

5.12 Coalescence-to-breakage velocity ratio for each reaction. . . . 159

5.13 Phase inversion through particle coalescence. 161

5.14 Visual representation of the volume cumulative frequency at the PI point. . . 163

5.15 Volume cumulative frequency and its derivative for each reaction. 164

List of Tables

1.1 Main properties of different styrenic polymers for injection molding. 3

1.2 Volume market of styrene polymers by product type 4

1.3 Properties of common ABS matrices. 7

1.4 Properties of the dispersed particles for different prepolymerization temperatures. 10

2.1 Models for the phase inversion point as a function of viscosity (or viscous stress) ratio. 24

2.2 Models for emulsion viscosity. 40

2.3 Models for collision frequency 50

2.4 Models for coalescence efficiency. 53

2.5 Models for break-up frequency. 62

2.6 Models for computing the daughter particle size distribution after break-up. . 63

2.7 Effect of main operating variables on the phase inversion mechanism as a general rule. $\cap$ and $\cup$ symbols indicate that the variable reaches a maximum or minimum value respectively 77

3.1 Variables chosen to buid the predictive models 82

3.2 Typical kernel functions used in SVM models. 85

3.3 Inferred rules from the ensemble of trees. 92

3.4 Confusion matrices for decision trees pruned at different complexity parameters and a bagging of 300 trees. Test subset is the same for all. 93

3.5 Confusion matrices for the support vector machine models with different kernels. 93

3.6 Confusion matrices for the neural networks with different hidden layer sizes. . 94

3.7 Performance of each decision tree model. 95

3.8 Parameters used in the SVR model. 95

3.9 Kernel functions tested, their scale parameters and the performance of each model as per the RMSE. 96

3.10 Performance of each neural network. 97

3.11 RMSE of the two-layered neural networks with the test set. 98

4.1 Recipies of the performed polymerizations. 107

4.2 Inversion periods (in % of styrene conversion) for each run. 110

4.3 Proposed kinetic mechanism of styrene polymerization in presence of rubber. 120

4.4 Model parameters implemented in the viscosity correlations. 126

5.1 Compound densities. 153

5.2 Phase viscosities (in cP). 153

5.3 Values of the adjusted parameters in the coalescence and breakage frequencies. 156

5.4 Average occluded fraction for each reaction at the PI point and the calculated inversion fraction. 163

A.1 Experimental data on different ambivalent ranges gathered from literature . . 186

Symbols and Abbreviations

Letters

Symbol	Description	Units
A	Hamaker constant	-
b	Average Kuhn length	Å
B	Breakage rate	1/s
C	Adjustable parameter, coalescence rate	-, $1/(m^6 s)$
d,d'	Drop diameter	m
D	Diameter	m
$\mathfrak{D}$	Diffusivity	m^2/s
f	Number density function	$1/m^6$
$\tilde{f}$	Probability density function	$1/m^3$
$\dot{F}$	Rate of transferred styrene	kg/s
k	Kinetic rate constant	-
m	Mass	kg
$\dot{m}$	Rate of change of a given mass	kg/s
M	Molecular weight	g/mol
n	Stirring speed	1/s
N	Number of particles	
$\hat{N}$	Number of particles per unit volume of physical space	$1/m^3$
P	Power	W
r	Viscosity or coalescence-to-breakage ratio	-
Rp	Polymerization rate	mol/s
t	Time	s
T	Temperature	°C
u	Particle volume (pivot)	m^3
v,v'	Particle volume	m^3
V	Volume	m^3

$\dot{V}$	Rate of change of a phase volume	m^3/s
w	Weight fraction	-
x	Monomer conversion	-
z	Degree of polymerization	-

Greek Letters

Symbol	Description	Units
α	Constant	m^2/mN^2
β	Daughter particle size distribution	-
γ	Interfacial tension	N/m
$\dot{\gamma}$	Shear rate	1/s
δ	Dirac's delta function	-
ε	Energy dissipation rate	m^2/s^3
ϵ	Relative permittivity	-
ζ	Grafting efficiency	-
η	Apparent viscosity	cP
λ	Coalescence efficiency	-
μ	Statistical parameter	-
ν	Allocation function	-
ρ	Density	kg/m^3
σ	Surface tension, statistical parameter	N/m, -
ϕ	Volume fraction	-
φ	Cumulative frequency	-
χ	Flory-Huggins parameter	-
ψ	Net birth rate of particles	1/s
τ	Shear stress	Pa
ω	Fractional frequency	1/s or m^3/s
Ω	Total frequency	1/s

Superscripts

Superscript	Description
$\cdot$	Radicals
$+$	Birth
$-$	Death

Subscripts

Subscript	Description
b	Breakage
c	Continuous phase, coalescence
cd	Colliding drops
d	Dispersed phase
$i0$	Thermal initiation
$i1$	Chemical initiation to monomer
$i2$	Chemical initiation to rubber
$i3$	Chemical initiation to monomer
fG	Transfer to the rubber
fM	Transfer to the monomer
I	Impeller
n	Repetitive units
o	Organic phase
p	Propagation, particles
pr	Propagation in the rubber-rich phase
pv	Propagation in the vitreous phase
PI	Phase inversion point
PS	Polystyrene
PB	Polybutadiene
r	Rubber-rich phase
St	Styrene
tc	Termination by combination
tcr	Termination by combination in the rubber-rich phase
tcv	Termination by combination in the vitreous phase
T	Total, tank
v	Vitreous phase
w	Aqueous phase, weight-average
η	Viscosity
Ω	Coalescence-to-breakage

Abbreviations

Abbreviation	Description
Ca	Capillary number
DoE	Design of Experiment
NI	Number of intervals (bins)
Np	Power number
PI	Phase inversion
PS	Polystyrene
PB	Polybutadiene
PBE	Population balance equation
PS-g-PB	Poly(styrene-g-butadiene)
Re	Reynold's number
RPM	Revolutions per minute
St	Styrene
Vi	Viscosity number
We	Weber number

Chapter 1

Introduction

"I never had to choose a subject - my subject rather chose me"

Ernest Hemingway

1.1 Styrene and its derivatives

Styrene (St, also known as phenylethene, vinylbenzene or cinnamene) is a colorless, gritty compound that is the simplest form of the unsaturated aromatic monomers. It is employed mainly in the polymerization processes of a variety of plastics, including Polystyrene (PS) in the form of General Purpose Polystyrene (GPPS), Expandable Polystyrene (EPS) and High-Impact Polystyrene (HIPS); Acrylonitrile-Butadiene-Styrene (ABS) copolymers; Styrene-Acrylonitrile (SAN) resins; Styrene-Butadiene Rubbers (SBR) and Styrene-Butadiene Latex (SBL); and Unsaturated Polyester Resins (UPR). In 2017, the worldwide consumption of styrene raised to 29.4 million tons [1]. Its total market value reached USD 44.3 billion in 2019, declining at an annual rate of 1.29% since 2015 [2] due to the increasing environmental concerns around the plastic industry.

Altough it may be found in a natural resin, it is obtained industrially by dehydrogenation of ethylbenzene (Figure 1.1), which is produced from benzene, or as a by-product in the production of propylene oxide. The manufacture route using ethylbenzene consumed about half of the commercial benzene in the world during the late 1990s [3]. The available manufacturing technologies are able to produce St with a purity of around 99.8-99.95%, but show some disadvantages, including high energy consumption in the form of superheated steam, low single-pass conversion (high recycling rate) and inefficient separation between styrene and ethylbenzene [4]. Improvement in reactor design and operating conditions showed that low conversion may be overcome without compromising styrene selectivity [5], especially with

selective membranes [6, 7].

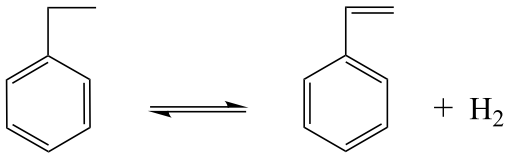

FIGURE 1.1: Dehydrogenation of ethylbenzene to produce styrene.

Most of the styrene produced worldwide occurs in facilities that use licensed technologies, since the available patents are held by a small group of companies. The volume market share in 2019 is shown in Figure 1.2 [8].

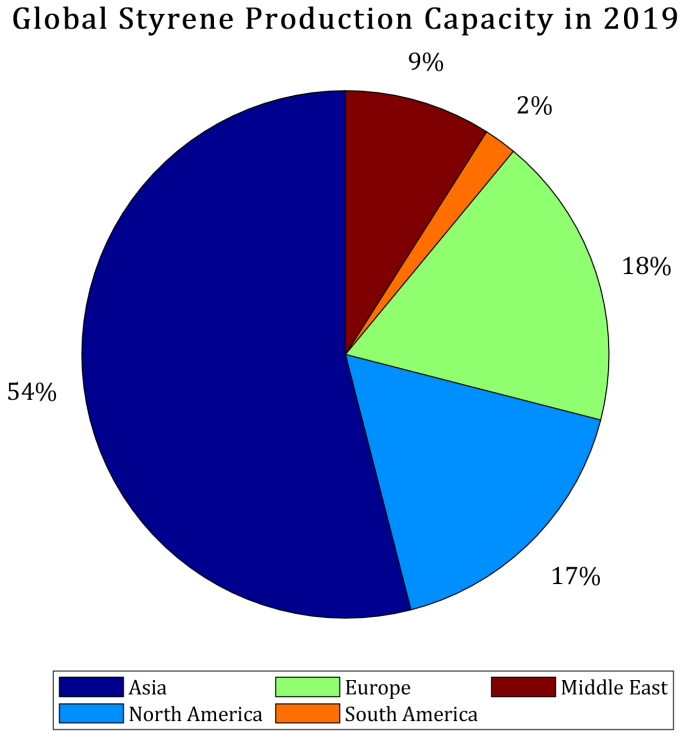

FIGURE 1.2: Distribution of St production capacity per region as in 2019. [8]

Several compounds related to St have been synthesized over the years, most of them referred to as *styrenic monomers* due to the presence of the vinyl group. These compounds are usually used in the production of special polymers, often too expensive to be large-scale. The most important among this family are vinitoluene, p-methylstyrene, α-methylstyrene, divinylbenzene and 4-*tert*-butylstyrene [3].

1.2 Polymers of styrene

The volume market of St polymers by product type is shown in Table 1.2, where the versatility of the polystyrenes family can be inferred. This polymer is easily extruded and molded, which makes it suitable for manufacturing a variety of products, from commodity plastics to engineering polymers. Polystyrene (in all its forms) is the most important product of this vinyl monomer, as it is used in a large number of applications. The global PS market was worth USD 42.7 billion in 2019 [9], with a total production capacity of 14.7 million tons in 2016, distributed per region as shown in Figure 1.3 [10].

Polystyrene plastics can be used for extrusion molding or injection molding, depending on the application. Combining PS with a suitable resin produces different specialized polymers. Table 1.1 offers a comparison of the quality variables of the main polymers of styrene for injection molding.

Property	**PS**	**SAN**	**Filled PS***	**HIPS**	**Standard ABS**	**Super ABS**
Specific gravity	1.05	1.08	1.20	1.05	1.04	1.04
Vicat softening point (°C)	96	107	103	95	103	108
Tensile yield (MPa)	42.0	68.9	131	29.6	41.4	34.5
Elongation at rupture (%)	1.8	3.5	1.5	58	20	60
Young's modulus (MPa)	3170	3790	7580	2140	2070	1790
Impact strength (notched Izod, J/m)	21	21	80	134	267	428
Relative ease of fabrication	Excellent	Excellent	Poor	Excellent	Good	Medium-Good

* Glass-filled PS

TABLE 1.1: Main properties of different styrenic polymers for injection molding. [3].

Product	Demand (%)
Polystyrene	64
Acrylonitrile-Butadiene-Styrene	9
Styrene-Butadiene Latex	7
Unsaturated Polyester Resins	5
Styrene-Butadiene Rubbers	4
Others	11

TABLE 1.2: Volume market of styrene polymers by product type [3].

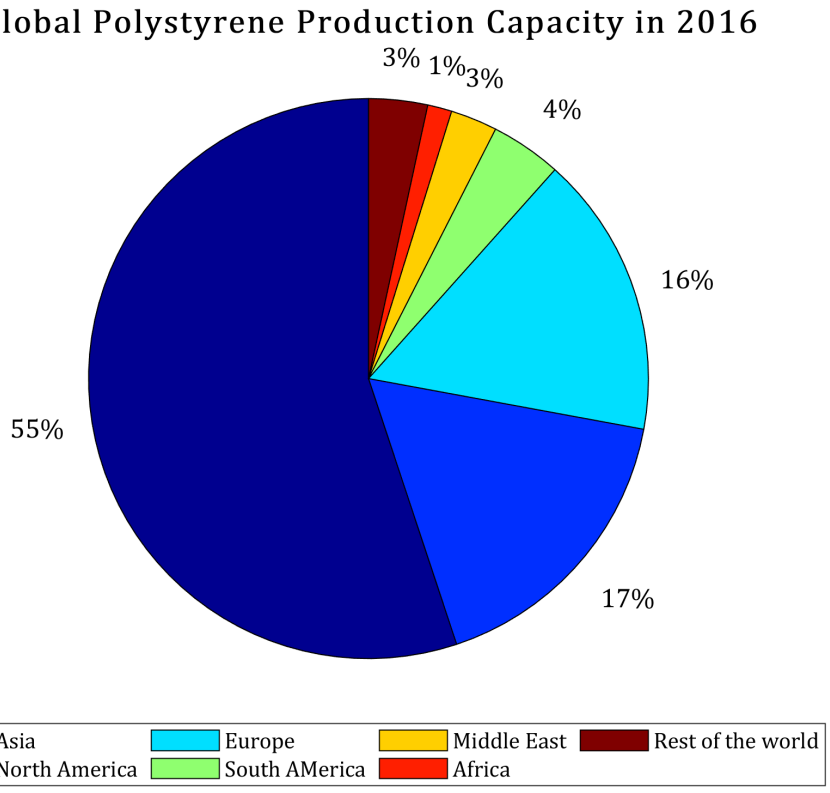

FIGURE 1.3: Distribution of PS production capacity per region as in 2016. [10]

1.2.1 General Purpose Polystyrene (GPPS)

General purpose polystyrene, also knwon as standard polystyrene, crystal polystyrene or styrene homopolymer, is the most common type of PS in the market. Its glass transition temperature is 100°C and, below this temperature, the material shows good dielectric properties, a high refractive index, and reasonable chemical resistance to a variety of compounds. This makes it a suitable material for a large number of applications [11].

Regarding its mechanical properties, GPPS shows a good tensile and flexural strength, but is a brittle material and is therefore not used in objects that are frequently exposed to collisions. Thus, the application fields include packaging (it is FDA compliant), optics, healthcare, consumer goods, etc. Quality product variables include stiffness, gloss and hardness [12].

1.2.2 Expanded Polystyrene (EPS)

Expanded polystyrene is obtained by addition of a blowing agent (originally, methyl chloride) during the polymerization process. The product is extruded into foams, which are then cut into different shapes depending on the application. Foamed polystyrenes are low-cost, good insulators (thermal conductivity is less than 0.05 W/mK) and suitable for certain packaging applications due to its low density (between 10-26 kg/m^3) [13].

In recent years, EPS waste has been tested as an additive in concrete (mixtures of cement and other compounds) with the goal of improving thermal insulation of the material, reducing the environmental impact of the circulating plastic waste [14, 15].

1.2.3 Poly(styrene-*co*-acrylonitrile) (SAN)

The acrylonitrile copolymer with styrene represents the second largest styrenic copolymer consumed (by volume) [16]. It is used in applications needing a better chemical resistance and mechanical strength compared to GPPS [3]. Applications include medical and dental light diffusers, autoclave devices, cosmetics, battery casings, and other consumer goods [17].

A typical composition is around 70-80% styrene and 20-30% acrylonitrile [18], which is suitable for most injection-molded articles. There is also a smaller, but growing, fraction of the market that uses 60-85% acrylonitrile to produce barrier plastics with low gas permeability [19]. Most of SAN copolymers (around 85%) are employed, however, in the production process of ABS, in which SAN is the matrix component [19].

The global market of SAN resins was worth USD 2 billion in 2015 and is forecasted to reach USD 2.84 billion in 2024, at an annual rate of 4% [18].

In the research and development field, SAN has ben recently tested as an adsorbant of copper ions, which opens the door for an application in water treatment [20].

1.2.4 Acrylonitrile-Butadiene-Styrene (ABS)

ABS is a thermoplastic heterogeneous material that consists of a poly(styrene-*co*-acrylonitrile) matrix with butadiene-based elastomer particles. ABS is frequently produced by adding an emulsion-made rubber into a SAN matrix, or by dissolving the rubber in a styrene-acrylonitrile mixture and polymerizing in bulk [21].

This material shows high toughness and high rigidity, and it is the result of a good adhesion between the polymer phases [22]. The dispersed rubbery phase lends its elasticity to the material [23]. Many of the good properties of this material are influenced by the composition of the matrix. Table 1.3 shows a summary of common ABS matrices and the properties that result in the final material [21].

The global ABS market was estimated at USD 23.09 billion in 2016, with a projected annual growth of 7.1%. Its main application is in the automobile industry, since it accounts for approximately 12.5 % of the total plastics used in a passenger car [24].

Matrix component	Chemical construction	T_g (°C)	Weight % in ABS blend	Softening point (°C)	Other properties
SAN random	S:AN 80-65:35-20	115	95-50	104	decrease in thermostability at high acrylonitrile contents
αMS-AN-S random	αMS:S:AN 45:35:20	-	95-50	108-110	
αMS-AN random	αMS:AN 70:30	128	95-50	117	depolymerization begins at 280 °C
αMS-AN sequence	αMS:AN 70:30	140	95-50	130	toughness is lower than with random copolymers
S-AN-NPMI	random terpolymer S:AN:NPMI 67:28:5	140	95-80	130	

S = styrene; AN = acrylonitrile; αMS = α-methylstyrene; NPMI = N-phenylmaleimide

TABLE 1.3: Properties of common ABS matrices [21].

1.2.5 Styrene-Butadiene Rubbers (SBR)

Styrene-butadiene rubber is the styrenic copolymer most produced in the world [16, 25]. It is manufacutred mainly by emulsion polymerization. A typical composition of SBR is 23-25% St and 75-77% butadiene [26]. The material has been replacing the use of natural rubber since World War II, and is currently the largest volume synthetic rubber [27].

If processed as a latex (in emulsion form), the copolymer presents a higher ramification degree, and is used in painting coatings, coated papers, adhesives, non-woven fabrics or backcoating of carpets and other textiles [25]. Otherwise, the copolymers are blended with PS to achieve a material with improved flexibility and optical properties. Some of the block copolymers are thermoplastic rubbers, showing a good flow at elevated temperatures [3].

The global market of SBR is valued at USD 8 billion and is expected to grow at an compound annual rate of 6% during the period 2019-2025. Of all the possible applications, the tire industry for automobiles gathers 68% of the market [28].

1.3 High-Impact Polystyrene (HIPS)

HIPS is a reinforced engineering plastic that is obtained by polymerizing St in presence of a rubber (polybutadiene, PB, or a copolymer of butadiene), typically at 6-8%wt. Its name refers to the improved mechanical properties compared to GPPS, as shown in Table 1.1. HIPS is commonly used in consumer goods that are often exposed to collisions, such as toys, cell phones and electronic devices, but also in medical equipment, packaging, etc. Its market is expected to grow at a 6.8% for the 2017-2023 period [29].

This material consists of a PS matrix that contains dispersed rubber particles which, in turn, may contain occluded PS droplets. It is the presence of these rubbery particles that lends its enhanced quality variables to the material [22, 30]. Such properties depend not only on the reaction recipe and the operating conditions, but also on the technology used [31].

1.3.1 Manufacturing process

The industrial manufacturing process of HIPS consists of four stages:

1. Dissolution
2. Prepolymerization
3. Finishing polymerization
4. Devolatilization

In the dissolution step, rubber and styrene are mixed in the desired proportion until a homogeneous mixture is obtained. This is usually achieved at a temperature between 50°C to 70°C [32] since, although spontaneous, it is a kinetically slow process. Solvents (mineral oil, toluene or ethylbenzene), antioxidants and other additives are also dissolved in the mixture [33].

The prepolymerization step is developed in one to three continually stirred tank reactors (CSTRs), which are usually equiped with anchor-type or other similar stirrers, suitable for viscous mixtures. If performed in solution, the apparent viscosity decreases and have a better control of the reaction temperature is achieved.

Since most commercial plants produce HIPS by radical polymerization [11], chemical initiators are also added in the prepolymerization stage. These may be either mono-, bi- or trifunctional depending on the desired combination of molecular weights and polymerization

rates [34]. Benzoyl peroxide (BPO), *tert*-butyl peroxide (TBPO), 1,1-di(*tert*-butylperoxy)-cyclohexane (L331) and 2,2'-azobisisobutyronitrile (AIBN) are some of the most common initiators used. In this stage, which is usually designed to operate at 90-120°C, monomer conversion reaches 30% approximately, which ensures that the dispersed phase is a solution of rubber in styrene that already contains the occluded vitreous phase [35]. The mixture emerges out of the reactor with the desired morphology.

The finishing polymerization stage proceeds at a higher temperature (140-170°C) and without agitation - to avoid modifying the developed morphology and because of the high viscosity of the mixture - until a typical conversion of 75% [32]. This step is usually conducted in plug flow or tower reactors, which do not require stirring.

The final devolatilization stage separates the remaining monomer and oligomers (and solvent, if present) from the polymeric melt, usually at 200-220°C and 14-18 mmHg [36]. Monomer is recycled back to the prepolymerization reactors and the final material is then cooled and pelletized.

A typical flow diagram of the entire process is shown in Figure 1.4.

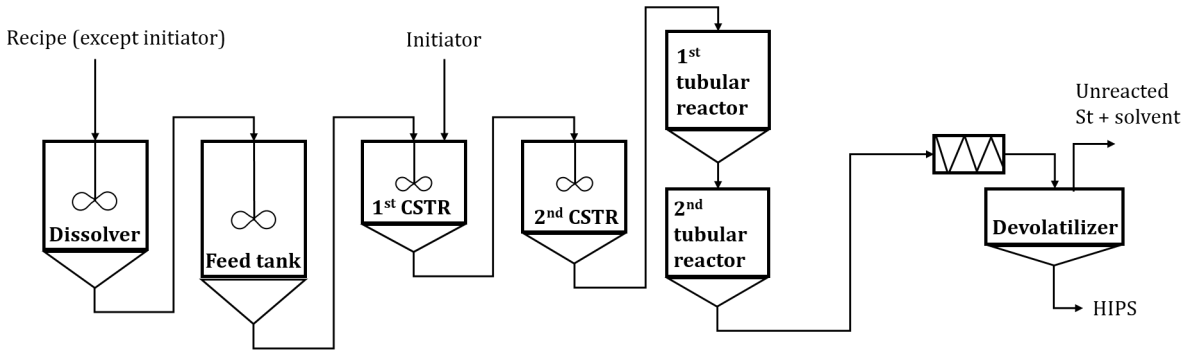

FIGURE 1.4: Process flow diagram of a typical HIPS industry (adapted from [32]).

1.3.2 Material morphology

The size, shape and number of occlusions in the dispersed particles are tightly related to the improvement in impact strength and Young's modulus [37], and a few works have put forward those interrelations [38–41]. Table 1.4 shows a summary of the characteristics of the dispersed rubber particles as a function of prepolymerization temperature, as found by Chang and Takahashi [42].

As observed, the relationship between prepolymerization temperature and particle morphology (number, size and properties of the occluded phase) is not straightforward. For the conditions studied by these authors, there appears to be an optimum temperature condition

Temperature (°C)	**Impact strength** (ft lb/in)	**Dispersed phase** (%wt)	**In-particle PB:PS**	**Particle size** (μm)	**Morphology**
80	1	36	1:2.6	3-15	circular to elliptical
85	2.6	24.3	1:1.43	1-2	spherical to elliptical
90	1	29.5	1:1.95	0.3-2	mostly elliptical
90-110	1	34	1:2.4	0.3-2	fairly irregular

TABLE 1.4: Properties of the dispersed particles for different prepolymerization temperatures [42].

for which the impact strength of the final material is maximum. In their discussion, the investigators observed no correlation between the polymerization temperature and the T_g of the occluded PS. However, they did postulate that fewer PS occlusions would favour craze initiation as the dispersed particles would appear more flexible.

Some authors have shown empirical evidence of the relationship between morphology and operating conditions [43, 44], but few have developed predictive models to forecast quality variables from reaction recipes. Depending on the size and number of occlusions, two types of morphologies are usually obtained [45]:

- "Salami" morphology: large rubber paticles with several PS occlusions
- Core-shell morphology: small rubber particles with only one large occlusion

An example of each is shown in the transmission electron microscopy (TEM) images of Figure 1.5. The core-shell particles are usually obtained when using a St-B diblock copolymer during the synthesis, and yield a transparent material [46].

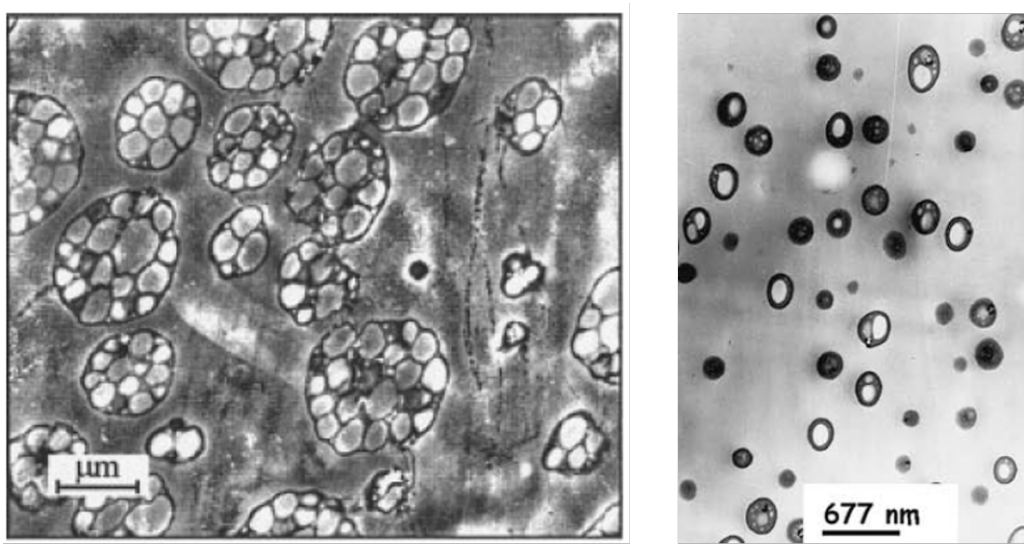

(a) (b)

FIGURE 1.5: Typical morphologies of high-impact polystyrene: (a) salami [47], (b) core-shell [44].

1.3.3 The phase inversion phenomenon

The typical morphologies of the material shown in Section 1.3.2 are the result of a phenomenon known as the *phase inversion* (PI) process, by which the continuous phase becomes the dispersed phase and *vice versa*. During the first stages of the polymerization, the mixture of St-PB-PS separates into two phases due to the incompatibilty between the two sets of polymers. At that point, the continuous phase consists of a solution of rubber in styrene, while the discrete phase is a mixture of PS and monomer. As the reaction proceeds (under strong agitation), the amount of PS produced reaches a point at which the vitreous phase engulfs the rubber-rich phase, making it the dispersed phase and developing the morphology. This process is not instantaneous, it usually proceeds through a co-continuous transition [44].

Figure 1.6, reproduced from Lee et al. [48], shows a scheme of the reaction path in a quasi-ternary phase diagram.

Given that the produced particles are responsible for the improvement in the material's quality variables, the PI phenomenon is a key moment in the manufacturing process. The ensemble of CSTRs is designed to reach a monomer conversion at which PI is sure to have occurred, since predicting the exact moment at which it happens is still an unfulfilled challenge.

Even detecting the instant at which inversion occurs is quite complex. At present, one of the most validated methods to observe such a moment is through the apparent viscosity of

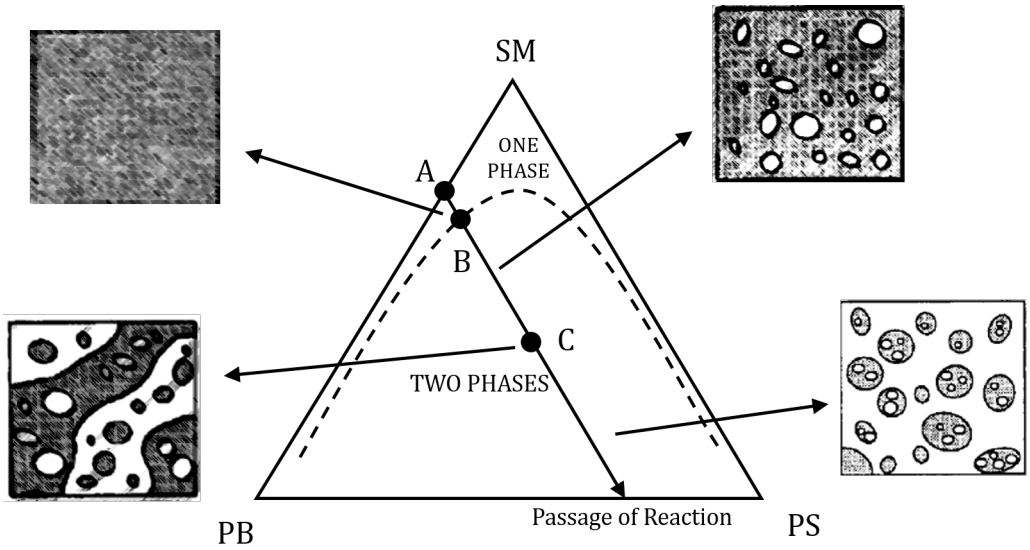

FIGURE 1.6: Reaction path of the HIPS bulk polymerization [48]. Point A is the original St-PB mixture; B is the phase separation point and C is the co-continuous sytem prior to the PI point. SM stands for styrene monomer.

the mixture: since the vitreous (PS-rich) phase is usually less viscous than the rubber-rich phase (at least within the industrial range of molecular weights [49]), the apparent viscosity of the entire mixture decreases during the inversion period. An example of such a behavior is observed in Figure 1.7, by Song et al. [50]. The curve reaches a local minimum at the PI point and then increases again as the production of PS continues.

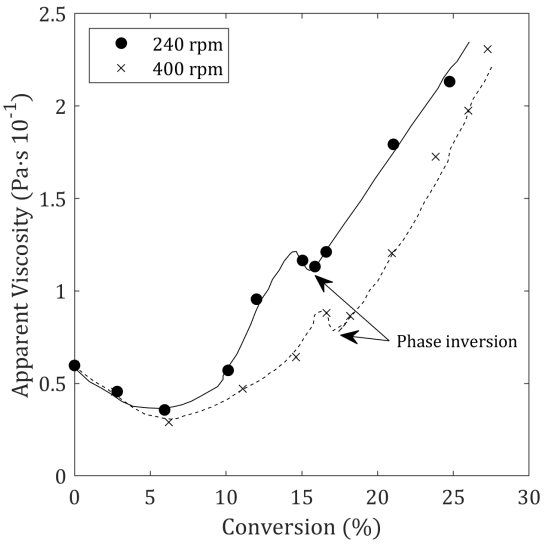

FIGURE 1.7: Decrease in apparent viscosity at the inversion point [50].

The main disadvantage of this method is that it is offline. Each of the measurements presented in Figure 1.7 were carried out on samples taken out of the polymerization reactor. In

consequence, in order to spot the inversion period accurately, samples need to be extracted at the exact time. A methodology that overcomes this obstacle consists in measuring the power consumed by the mechanical stirrer, which is tightly related to the viscosity of the mixture and thus follows its same evolution. Figure 1.8 reflects this effect for different reactions, as informed by Sardelis et al. [51]. Since the energy input may be measured continuously, the detection of the inversion point may be more readily achieved.

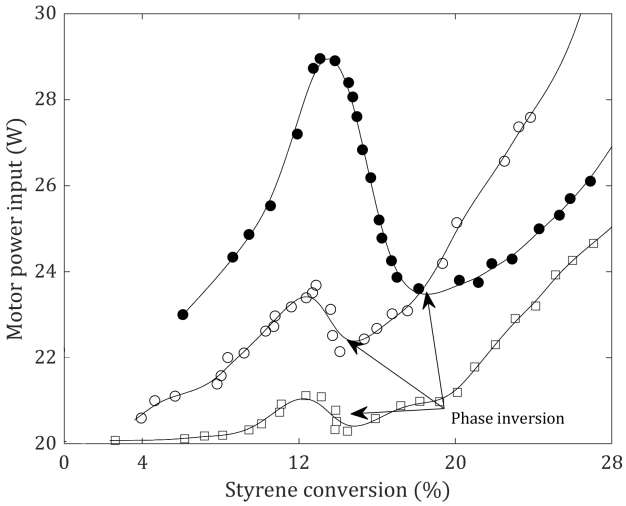

FIGURE 1.8: Evolution of the energy consumption by the mechanical stirrer along the reaction for different polymerization recipes [51].

The effective confirmation that phase inversion has occurred can be achieved by taking transmission electron micrographs along the reaction, like the ones shown in Figure 1.5.

1.3.3.1 Phase inversion prediction

The phenomenon of phase inversion has been reported and studied over the past 70 years and holds a significant industrial importance in several fields, not only in the HIPS manufacturing process, but also in liquid-liquid extraction, heat control operations, micro and nano-emulsification for controlled drug release and heavy oil transport in pipelines [52–54]. Yet, it is not a fully understood process and most of the published results are phenomenological and qualitative, especially in polymeric systems [55].

Few efforts have been conducted to develop comprehensive mathematical models to predict the PI point in the HIPS manufacturing process. Based on the origial work by Nauman and He [56], Vonka et al. [57] developed a theoretical model that combines a thermodynamic approach with diffusion-controlled mass transfer that simulates the growth of PS-rich droplets undergoing spinodal decomposition. They include the effect of agitation by forcing a shift of the concentration profiles along a random line of shear. Their work successfully

simulates the formation of the occlusion morphology during the inversion process. However, it lacks a predictive capability as it is not fully linked with the operating conditions of the prepolymerization reactor. Some of their model parameters can also be questioned.

In line with the previous investigators, Alfarraj and Nauman also presented a model to predict the formation of the occluded phase along the polymerization reaction [58], following some of the same hypotheses. Their work was used as benchmark by Vonka and Kosek [59], who developed a similar model but with some questionable parameter choices. Other authors just consider that the PI point occurs at equivolume conditions (that is, when the PS-rich phase has taken over 50% of the reaction volume) [60, 61].

Finally, some simple rheological expressions have also been developed to predict the PI point, but are mostly used in polymer blends and have not been derived for this reacting system [62]. A more detailed discussion on this matter is found in Chapter 2.

The lack of comprehensive mathematical models lies in the fact that this phenomenon is strongly nonlinear and largely multivariate. The PI point may be influenced by several aspects: phase viscosities, phase densities, stirring speed, vessel and agitator materials, interfacial tension (and the presence of surface-active components), and other geometric aspects. The relative weight and effect of each of these variables on the phase inversion point is discussed thoroughly in Chapter 2, with a special focus on traditional O/W non-polymeric systems, from which relevant phenomenological information may be gathered. Most of the empirical evidence regarding phase inversion points is found in batch experiments; the extension to continuously operated vessels or reactors is still an unresolved problem. Depending on the reactor technology (CSTR, plug flow, tower type), phase inversion may occur at different phase compositions. No models predicting this key moment in the continuous polymerization of HIPS are currently available.

There is an underlying optimization opportunity in the HIPS industry related to the PI point: since very few mathematical models can predict this key moment from polymerization recipes and reaction conditions, the product quality variables (which are a consequence of the morphology developed at the PI point) are difficult to correlate with the operating variables in an accurate way. The manufacturing of taylor-made materials and the global optimization of recipes remain therefore unfulfilled challenges.

1.4 Objectives

In view of the challenges described in the previous section, the main objective of this thesis is to study the phase inversion phenomenon during the bulk polymerization of HIPS, both from a theoretical and an experimental viewpoint. The development of a detailed mathematical

model, capable of accurately predicting the inversion point from reaction recipes is considered a central goal.

The specific objectives are:

1. To study the phase inversion phenomenon both in simple and polymeric systems, from which useful insight may be gathered.
2. To build a predictive model of such systems using the advantages of *machine learning* algorithms to validate the experimental evidence present in literature and put forward the most relevant aspects regarding the mechanisms that influence the phase inversion phenomenon.
3. To develop, adjust and validate a mathematical model to predict the rheological behavior of the HIPS polymerizing mixture and use it as a tool to study the phase inversion process.
4. To develop a theoretical model using a population balance technique to follow the evolution of the particle size distribution of the polymerizing vitreous phase and aim to predict the phase inversion point of the system.

The theoretical developments are supported with experimental work that is used to adjust the mathematical models and validate their predictions.

Chapter 2

The Phase Inversion Process

"Nothing endures but change"

Heraclitus

Any physical system consisting of two immiscible phases subject to constant stirring will form a dispersion. That is, one phase will be suspended in the continuous medium of the other. Dispersions and emulsions are frequently used interchangeably, but they do refer to slightly different systems. In general, an emulsion requires the presence of a surface-active component that is usually soluble in one of the phases, or locates itself at the interfaces so that it may interact with both simultaneously. If agitation is stopped, this agent will be able to stabilize the dispersed phase at a given particle size and a matrix/dispersed system will not be lost at a short time scale (it will eventually demix, as it is kinetically but not thermodynamically stable). A dispersion, on the other hand, is usually used to refer to systems that will separate into two continuous phases immediately after stirring is ceased [63].

Determining which phase will disperse in the other is not straightforward, since it is not always the one in smaller proportion. It depends on several interacting variables: physical properties (density, viscosity, interfacial tension), volume fraction, phase chemical composition, stirring speed, particle size and/or particle size distribution and, in some cases, the geometry of the vessel where the dispersion is produced. This implies that, for any emulsion or dispersion, changing one or more variables may result in a *phase inversion* process: the mechanism by which the continuous phase becomes the dispersed phase and *vice versa* [64].

The *phase inversion point* usually refers to the volume fraction of a given phase above which it can no longer be dispersed [65]. Since this phenomenon was studied, at first, mainly for oil-in-water systems (or rather organic-in-aqueous), a large number of results were presented using the organic phase volume fraction, even when the aqueous phase is the dispersed one.

Increasing the dispersed volume fraction (ϕ_d) at a constant stirring speed may result firstly in a co-continuous system and eventually in a phase inversion point, above which the reversed system is obtained. This is especially the case of polymer blends and mixtures [62]. Most O/W emulsions, conversely, do not present such a behavior and proceed to invert almost instantaneously when reaching a critical ϕ_d [66]. In both cases, PI is achieved by varying the phase volume ratios, which is known as a *catastrophic* inversion, owing to a suggestion by Dickinson [67]. It is important to note that there are two ways of varying such volume ratios: in a gradual, dynamic way (adding dispersed phase aliquots to an existing mixture) or in separate steady-state batches. Some of the experiments conducted in the former way try to keep total volume constant (by subtracting aliquots of the mixture) and others do not. Care should be taken when results among different authors, since they may refer to completely different scenarios. Comparing dynamic with steady-state experiments should also be done carefully, since the effects present in the former may significantly differ from the ones observed in the latter [68].

If surfactants are present in the system, there exists a different way to induce phase inversion that does not involve changing the volume fraction of the dispersed phase: it consists in modifying the affinity of the surface-active component for each phase. The idea behind this type of inversion is based on Bancroft's rule, which suggests that the continuous phase is the one in which the surface-active component is more soluble. Then, a given emulsified dispersion would *prefer* a certain morphology according to the affinity of its emulsifier; if changed, this affinity would induce a transition to a non-preferred morphology, which is why this type of PI is named *transitional* [69].

Phase inversion also occurs in systems other than O/W or W/O. Polymeric (oil-in-oil or water-in-oil) emulsions also present this phenomenon, and some work has been developed to address it [62, 70–72]. The physics that govern their dynamics are practically the same than those of traditional aqueous-organic systems, which justifies the study of the latter for simplicity. However, there are a few differences that are worth highlighting:

- Polymers are not pure compounds, but rather a collection of chains of varying lengths that may interact differently with their surroundings.
- Due to their average molecular weights (notoriously higher than that of pure compounds), their rheological behavior cannot be compared to simple liquids: they are ofter non-Newtonian, and their apparent viscosity is much higher than that of traditional O/W systems.
- The inversion point in polymer-polymer systems is often achieved after going through a co-continuous arrangement, in which it is not possible to distinguish which phase is continuous and which is dispersed.

In this Chapter, the phase inversion (PI) phenomenon is analyzed thoroughly from the information available in literature, with the aim of discussing the current understanding of the underlying mechanisms and the relative effect of each operating variable. This analysis (which is published and available [73]) is performed both in simple and polymeric systems.

2.1 The Ambivalent Range

In any emulsion there is a range of volume fractions for which either one of the two phases may be dispersed and stable [65], depending on how the mixture is prepared or initiated. This is known as the *ambivalent range*, and much work has been developed to predict its limits, *i.e.*, the highest ϕ_d for each phase that may be obtained before inversion. This hysteresis effect is characteristic of all emulsions reported in literature.

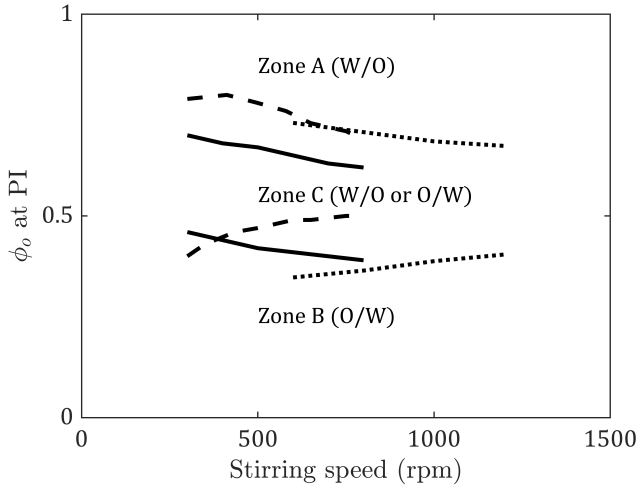

FIGURE 2.1: Ambivalent ranges for toluene(O)-water(W) (solid lines), CCl4(O)-water(W) (dashed lines) and heptane(O)-acetonitrile(W) (dotted lines). Lines were drawn from the data by Kumar [66] and Arashmid and Jeffreys [74]

Figure 2.1 shows typical ambivalence ranges, plotting the organic (or dispersed, depending on the author) volume fraction at the threshold of phase inversion as a function of stirring speed. **Zone A** is identified with oil-continuous systems, **Zone B** with water-continuous, while **Zone C** represents the operating conditions where either phase may be the dispersed one depending on how the process was started. While being the most widely spread range, authors like McClarey and Mansoori [75] have also found an intermediate inversion curve by preparing mixtures in a very specific manner. In general, the limits and span of this ambivalent range are influenced by the size, shape and material of the vessel, physical fluid properties (density and viscosity), stirring speed and interfacial tension [76]. These variables are discussed in the following sections.

2.1.1 Viscosity ratio

One of the most important variables that greatly influence the PI point is the viscosity of each phase. A general rule found by several workers [65, 77–80] states that the tendency to remain as the dispersed phase increases with viscosity. This is probably explained by the attenuation of coalescence probability with increasing viscosity [81]. Coalescence and break-up of dispersed particles are crucial aspects in determining the phase inversion hold-up and will be discussed in more detail in Section 2.4.4.

As an example, Figure 2.2 - which has been plotted with the data in Selker and Sleicher [65] - shows how more difficult (higher ϕ_d) it is for a given phase to become continuous as its viscosity increases. In some cases the phase viscosity is not as important as the ratio of dispersed-to-continuous phase viscosities $r_\eta = \frac{\eta_d}{\eta_c}$, since this addresses the difference in viscous stresses developed at the interface. This affects the interface mobility under a given shear condition and thus impacts the inversion process directly.

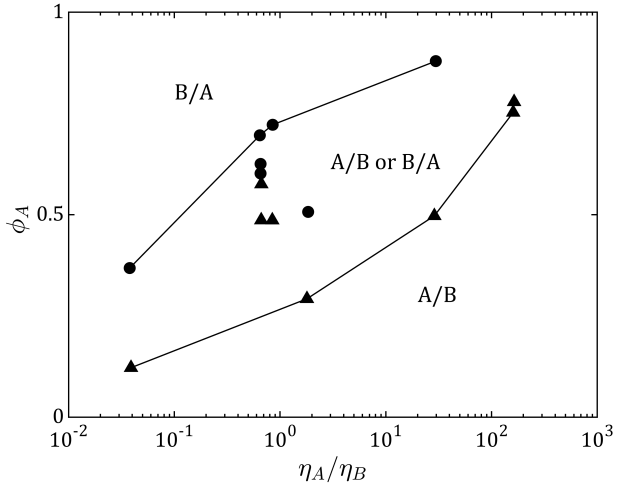

FIGURE 2.2: Ambivalence diagram as a function of phase viscosity ratio [65].

By applying momentum balances to a planar interphase of two immiscible liquids, Yeh et al. [77] suggested one of the very first phase fraction relationships at the PI point:

$$\frac{\phi_d}{1-\phi_d} = \sqrt{\frac{\eta_d}{\eta_c}} \tag{2.1}$$

where η_d and η_c are the dispersed and continuous phase viscosities respectively.

The authors, however, specified that a more accurate relationship would require finding the exact plane near the interface at which shear would occur. Given the difference in surface tensions between each phase, the shear plane would shift towards the interface and

a correction was suggested to replace the viscosity of the phase of higher surface tension by the viscosity at the *interface*. For example, if the continuous phase has a stronger surface tension than the dispersed one, then Eq. 2.1 would become:

$$\frac{\phi_d}{1-\phi_d} = \sqrt{\frac{\eta_d}{\eta_{int}}} \tag{2.2}$$

where η_{int} is the viscosity at the interface.

Note that the dependence of ϕ_d with r in Eq. 2.2 reproduces satisfactorily the *shape* of the upper limit of the ambivalent range in Figure 2.2, but predicts an equivolume inversion for phases with equal viscosity. This is not always the case, as observed from the data in the same figure, where the equivolume inversion occurs for a mixture with a viscosity ratio of 2 (although the experiments there reported do not keep total volume constant and are thus not directly comparable). On this same line, McClarey and Mansoori [75] prepared a mixture with equal phase viscosity and noted not the upper nor the lower but the intermediate inversion boundary was located at the equivolume conditions for all stirring speeds. This suggests that, in the absence of phase viscosity difference, other effects play a part in determining the maximum dispersed volume fraction of a given system. Early authors [65, 75] had ruled out interfacial tension, but later work proved that it may be of considerable importance, as it is discussed in Section 2.1.4.

In a theoretical investigation, Yeo et al. [78] found similar results with binary systems; yet, they suggested that surfactant-coated interfaces in systems with $r_\eta < 1$ may suppress the viscosity ratio effect on phase inversion due to Marangoni stresses. In the absence of viscous effects, all emulsions with low viscosity ratios and sufficiently laden interfaces would invert almost at equal phase volumes. For higher values of r_η, the authors predict similar trends to other workers' [65, 77].

In polymeric systems, in which viscosity depends on the molecular weight distribution of each species, several phase volume and viscosity ratio relations have been suggested at the inversion point, or at least at the beginning of co-continuity. In such systems it is common to observe a co-continuous transition before phase inversion takes place [82]. In polymer blends (*i.e.*, not in presence of monomer or solvent and in a non-reactive system) at low shear rate, the work by Jordhamo et al. [62] suggests the following relationship for predicting the onset of a co-continuous system:

$$\frac{\phi_d}{1-\phi_d} = \frac{\eta_d}{\eta_c} \tag{2.3}$$

This expression has been evaluated successfully in some polymeric two-phase systems

with minimum grafting extent (polyester-urethane/polystyrene, polyamide/polypropylene, polystyrene/polybutadiene) under low shear conditions, but has failed to produce accurate results in other blends, such as the propylene/ethylene-propylene rubber and other rubber blends prepared by Ho et al. at higher torques [83]. These authors suggested a modified version of Jordhamo's equation for a better fit of their results:

$$\frac{\phi_d}{1-\phi_d} = 1.22\left(\frac{\tau_d}{\tau_c}\right)^{0.29} \tag{2.4}$$

where τ_d and τ_c are the shear stresses at the dispersed and continuous phases respectively.

Even if the shear stress ratio is preferred to viscosity, but the physical meaning still holds. The 0.29-0.3 power of the viscosity ratio has also been suggested by Chen and Su [84], Kitayama et al. [85] and Everaert et al. [86].

Miles and Zurek [82] have found good results using Jordhamo's expression, but only when evaluated at the in-situ shear rate when preparing the blend. Other investigators, like Arirachakaran et al. [87], working on other systems (such as transport pipelines), have found logarithmic dependences on the viscosity ratio. A summary of the available models to calculate the PI point from the viscosity ratio is shown in Table 2.1 and compared in Figure 2.3. Some of them are empirical correlations and others are theoretical derivations or simplifications from emulsion rheological models.

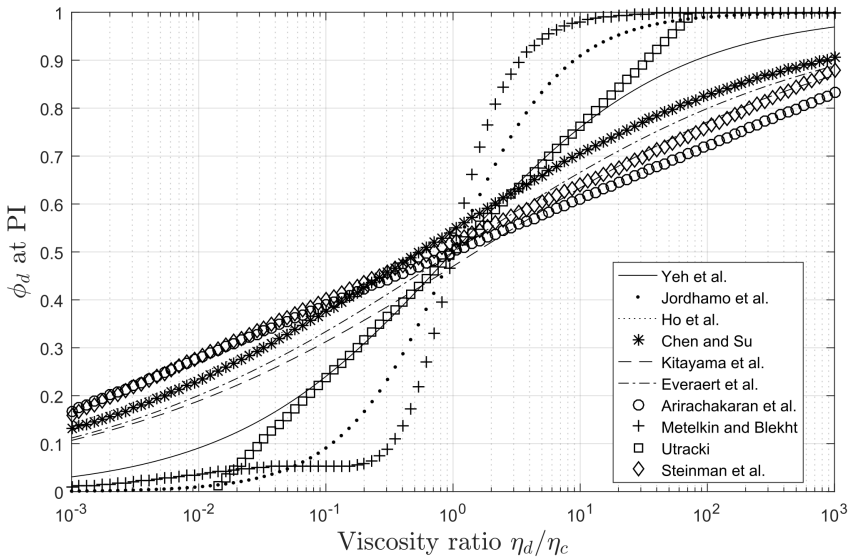

FIGURE 2.3: Comparison of predicted PI points with viscosity ratio. For simplification, the stress ratio was considered equal to the apparent viscosity ratio when necessary.

Whether in polymer blends or in O/W systems, the phases that were used in the validation of these expressions consisted essentially of pure, immiscible compounds. They have not been investigated under the presence of a third substance that is miscible with both phases simultaneously, as could be the case of a solvent or of a reacting monomer in a heterogenous polymerization.

There seems to be two distinct families of curves: a log-linear and a sigmoidal type. Near the isoviscous point, all curves predict inversion points near the equivolume scenario. However, it does not seem appropriate to plot the experimental points on top of this figure, since each point is usually produced varying not only the viscosity ratio, but also (inevitably) one or more other properties that might affect the inversion process. Moreover, the inversion point as per these equations is independent of *which* phase is dispersed and which continuous, a fact that would yield a symmetric ambivalence range, contrasting with the experimental findings have shown that this is not the case [65]. Thus, these models should be used carefully or coupled with extra terms that take into account the effect of other variables.

Model	Author	Physical system
$\frac{\phi_d}{1-\phi_d} = \frac{\eta_d}{\eta_c}$	Jordhamo et al. [62]	PS/PB. Castor oil +PS-U/PS
$\frac{\phi_d}{1-\phi_d} = \left(\frac{\eta_d}{\eta_c}\right)^{0.5}$	Yeh et al. [77]	O/W (Nitrobenzene, benzene, cyclohexanol, etc. in water)
$\frac{\phi_d}{1-\phi_d} = 1.22\left(\frac{\tau_d}{\tau_c}\right)^{0.29}$	Ho et al. [83]	PP/EPR. PS/SBR
$\frac{\phi_d}{1-\phi_d} = 1.2\left(\frac{\tau_d}{\tau_c}\right)^{0.3}$	Chen and Su [84]	PPS/PE
$\frac{\phi_d}{1-\phi_d} = 0.887\left(\frac{\tau_d}{\tau_c}\right)^{0.29}$	Kitayama et al. [85]	Nylon 6/SAN
$\frac{\phi_d}{1-\phi_d} = \left(\frac{\tau_d}{\tau_c}\right)^{0.3}$	Everaert et al. [86]	PP/(PS/PE)
$\phi_d = 0.5 + \log\left(\frac{\eta_d}{\eta_c}\right)^{0.1108}$	Arirachakaran et al. [87]	W/O systems for which $\eta_d = 1$ cP and $[\eta_c] =$ cP.
$\phi_d = 1 - \frac{1}{1+\frac{\eta_d}{\eta_d}F}$ $F = 1 + 2.25\log\left(\frac{\eta_d}{\eta_c}\right) + 1.81\left(\log\left(\frac{\eta_d}{\eta_c}\right)\right)^2$	Metelkin and Blekht [88]	Polymer blends in general
$\phi_d = 0.5 + \log\left(\frac{\eta_d}{\eta_d}\right)^{5/19}$	Utracki [89]	EPDM/PB. Polymer blends in general
$\phi_d = 0.52 + \log\left(\frac{\eta_d}{\eta_d}\right)^{3/25}$	Steinmann et al. [90]	PMMA/PS. PMMA/P(SA)

TABLE 2.1: Models for the phase inversion point as a function of viscosity (or viscous stress) ratio.

2.1.2 Stirring speed

For continually stirred batch vessels, agitation speed presents different effects depending on the mixture. A large number of systems are reported in literature and have been studied for several decades; yet, it is troublesome to compare results from different authors due to the difference between the operating variables. Increasing agitation favors phase inversion (meaning that it occurs at lower values of ϕ_d) in many dispersions inverting from O/W to W/O, while delays it in the opposite case; but there are several exceptions too [91]. Besides, not all organic phases present the same physical properties. In some cases, if the dispersed phase is less viscous than the continuous one, agitation helps phase inversion; but then again, this does not hold for all systems. Kumar [66] suggested an explanation for these discrepancies based on the electrostatic repulsion forces driven by a difference in dielectric constants.

A general trend that is satisfied by all dispersions is the asymptotic value of phase volume fraction at the inversion point with increasing stirring speed. This was first observed by Quinn and Sigloh [64] and further shown in other experiments [75, 92–96] in both batch and flow vessels. They suggest the following dependence with power input (W_P):

$$\phi_d = \phi_0 + \frac{k}{P} \tag{2.5}$$

where k is a constant that only depens on sytem properties. The power input may be related to the agitator speed, n, in a stirred baffle tank of diameter D_T through the *power number*, Np:

$$P = Np\rho_c n^3 D_T^5 \tag{2.6}$$

The power number is a function of the Reynolds number and is a chracacteristic of a given vessel. The assymptotic value of Eq. 2.5 suggests that, in extremely turbulent conditions there is a controlling mechanism that allows PI to take place only at a given composition.

2.1.3 Phase density difference

Very few studies aiming to determine the impact of the phase density difference have been developed. Some authors [65, 75, 76] argue that it plays a minor role on phase inversion and it is only important at low stirring speeds, when large density differences make dispersions more difficult to achieve (*i.e.* require higher energy inputs). Some other investigators [92, 97] suggest that a large density difference favor phase inversion because it increases local relative

velocity and therefore, the shear stress to which the system is subject to. This, in turn, promotes droplet breakage and interfacial area is substantially increased. However, enhanced breakage is not necessarily a promoter of phase inversion. Yeo et al. [78] observed that the tendency to invert was indeed increased at higher density differences if the dispersed phase was organic, but found the contrary in the opposite case.

Phase density may also affect the inversion characteristics of a system through wettability effects. For a dispersed phase to become in contact with an impeller blade, it must hold a larger density than the continuous phase [98]. Only then the droplets may reach the impeller by inertial impaction and form a thin film at its surface (rather than staying as a drop). This changes the breakage processes near the impeller region and can alter the critical ϕ_d for that phase.

2.1.4 Interfacial tension

At the interface of two immiscible liquids the difference in surface tension yields a stress known as interfacial tension (γ). Surface and interfacial tension are sometimes mistaken as equal, and many empirical correlations are expressed in terms of the former, while physical evidence suggests that it is the latter that exerts a greater effect on the inversion characteristics of a given dispersion.

Particularly in oil/water and oil/water/surfactant systems (the case of emulsions), there have been reports, since the original research by Cayias et al. [99], that there exists a given composition or formulation that yields markedly low interfacial tensions. As an example, Figure 2.4 - which was built with the data from Morgan et al. [100] - shows the case for a 0.2%wt aqueous solution of Witco 10-80 petroleum sulfonate (and 1%wt NaCl) with different organic phases. It is seen that interfacial tension reaches a minimum with n-heptane. In the emulsion world, this behavior gave rise to the so called "optimum formulations" [101], in which the surfactant or surfactant mixture is chosen in both structure and concentration to provide such ultra-low tension values (of utmost interest in the enhanced oil recovery processes).

A similar trend has been reported when varying salinity [102] or temperature [103–106]. In the latter case, probably the most renowned, there exists a critical temperature at which interfacial tension reaches a minimal value, usually sharply, and in a range of 0.1°C-2°C depending on the surfactant [104]. This aspect is further discussed in Section 2.2.

Effect on phase inversion

It is generally assumed that interfacial tension is a symmetric property, in the sense that an O/W dispersion bears the same interfacial tension than a W/O. This would lead to the

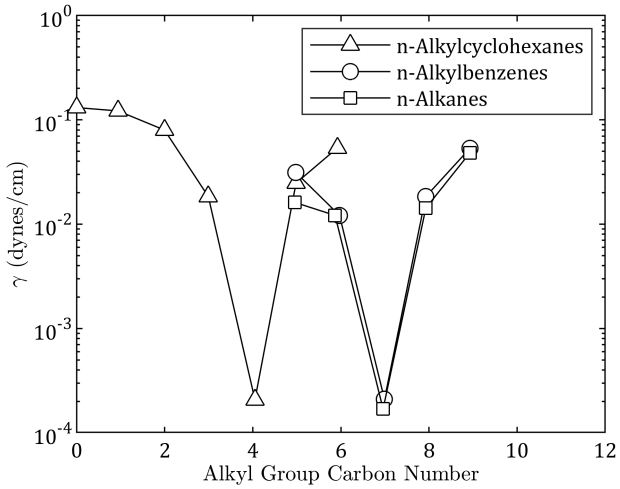

FIGURE 2.4: Interfacial tension of petroleum sulfonate aqueous solutions with different organic phases [100].

conclusion that for a system with phases of equal physical properties, PI occurs at the same volume fraction for both phases at a given stirring speed. This is not, unfortunately, the usual case as other factors must be considered, which are discussed in Section 2.5.1.

Few studies aiming to isolate the effect of interfacial tension on the phase inversion holdup have been published. According to Clarke and Sawistowski [107] and Kumar et al. [92], a system with lower interfacial tension should be less likely to invert. The span of the ambivalent region should be therefore wider. However, results by Reeve and Godfrey [94] challenge that idea. They prepared two O/W dispersions almost identical in viscosity ratio and density, but with a 50% difference in interfacial tension. Their results indicate that the system with lower γ finds it easier to invert from O/W to W/O but harder in the opposite direction. The work by Norato et al. [76] seems to support these findings but their systems presented a 25% disparity in phase density difference, and their batches were not performed under constant volume conditions. The theoretical model derived by Hu et al. [79], based on a population balance in a two-region vessel, agrees with those results.

If interfacial tension is associated with stress due to incompatibility, a minimization of free surface energy could be expected at the PI point. This would reflect the natural need of the system to invert. However, by measuring interfacial area, Clarke and Sawistowski [107] and Luhning and Sawistowski [108] found that a minimization of the interfacial energy happened only when inverting from W/O to O/W but not in the opposite case. Consequently, they postulate that phase energy minimization is not a criterion for phase inversion. Norato et al. [76] suggest that the lowering of γ would promote drop breakage, which would diminish coalescence rates and thus hinder phase inversion.

It would seem that the lowering of interfacial tension produces two opposing effects that

may either delay or promote PI, depending on the emulsion type. On the one hand, the compatibility enhancement would favor the transition to the inverted system; on the other hand, the increase in particle breakage rate may stabilize the configuration and delay the inversion.

2.1.5 Geometry and vessel material

It has long been reported that the way agitation is started may affect phase inversion [97]. Investigators have reported a wide variety of, sometimes opposing, results regarding impeller design, impeller height and position, stirring speed and vessel geometry [63–65, 76, 94, 96, 107, 109]. For example, if the impeller is equipped with baffles, the ambivalent range widens. A given impeller type may promote PI of O/W but delay it for W/O dispersions. The impeller-to-vessel diameter ratio also presents different results on either limit: increasing the ratio may promote or delay PI, or not have a consequential effect at all. For this reason, results from different authors are sometimes difficult to analyze quantitatively. A thorough research on this subject was conducted by Deshpande and Kumar [96] some years ago. Regarding the material of the vessel (and/or impeller), it has been found to have an effect on PI due to wettability effects [92].

In the case of the PI during the polymerization of styrene in presence of polybutadiene (HIPS manufacturing process), Freeguard and Karmarkar [110] have outlined several criteria that should be examined when designing the agitation system.

2.2 Effect of surface-active components on phase inversion dynamics

In emulsified dispersions, surface active species are commonly found at the interface between the dispersed and the continuous phases. This is usually because these species are somewhat miscible in both phases. In O/W (or W/O) emulsions, the emulsifiers usually present a hydrophilic head and a lipophilic tail, thus making the O/W interface a suitable place for the surfactant to accumulate. Traditionally, these molecules contain a carbon chain long enough to be the oil-soluble part. However, in recent years, the use of polymers as surface-active components has increased significantly [111–116], since their structure can be tailored to provide a target amphiphilicity.

How hydrophilic and how lipophilic an emulsifier is, comes represented in the hydrophilic-lipophilic balance or HLB, and its effect on phase inversion is well discussed by several investigators [78, 117, 117–119].

The role of emulsifiers in PI processes seems critical. Merely changing the affinity of an emulsifier for a given phase may lead to a phase inversion. Wade et al. [120] suggested that phase behavior could be a consequence of the differences in the chemical potentials between each phase, an idea later summarized in a parameter coined Surfactant Affinity Difference (SAD) [121]. The value of this parameter – which is a function of temperature, HLB, oil type and salt concentration – indicates the *structure* of the emulsion, usually related to the Winsor classification [122]. This categorization tabulates four possible O/W emulsions, namely:

- **Type I**. A water-soluble surfactant forms an O/W emulsion, which coexists with a pure oil phae (surfactant-poor).
- **Type II**. An oil-soluble surfactant forms a W/O emulsion, which coexists with the aqueous phase (surfactant-poor).
- **Type III**. A middle-phase with surfactant-oil-water emulsion that coexists with both an aqueous and an oil pure phases.
- **Type IV**. A single-phase micellar solution.

Consequently, modifying the SAD value for a given system may lead to an inversion process. By definition, the SAD is the difference between the standard chemical potential of the surfactant in the aqueous and organic phases. Thus, positive SAD values yield W/O emulsions and the opposite if negative, provided that there is enough volume so that the continuous phase is the expected one. The limiting case of SAD = 0 represents an unstable system that is on the verge of inverting and is associated with an ultralow interfacial tension value [123]. A similar parameter is the Hydrophilic-Lipophilic Deviation from the optimum formulation (HLD), and is qualitatively used as equivalent to the SAD, although Salager et al. [124] have pointed out that their relationship is actually given by Eq. 2.7 and depends on a reference state.

$$\frac{SAD}{RT} = HLD - \ln K_{ref} \tag{2.7}$$

The available calculation methods for HLD are only restricted to flexible interfacial films [125]. As an example, Figure 2.5 shows an inversion map for cyclohexane-water emulsions using nonylphenol ethoxylates (NPE) as surfactants, taken from Brooks and Richmond [117]. These emulsifiers, of the form of an aromatic head and a polyoxyethylene tail, may bare different HLB values depending on the length of their ethoxide chains.

In their work, these authors modified the SAD parameter by changing the HLB of the emulsifier at constant concentration (and temperature). The regions in the map show the

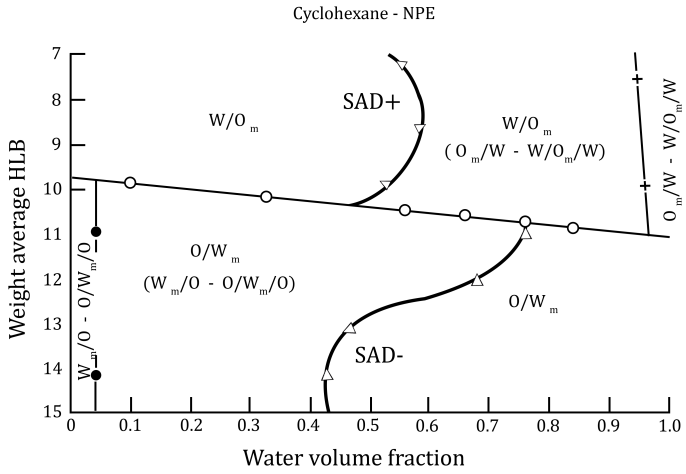

FIGURE 2.5: Water-cyclohexane-NPE inversion map for different HLB values [117].

emulsion structure (for example, W/Om denotes a Winsor II emulsion with surfactant-water micelles dispersed in an organic continuous phase) and their transition boundaries.

In a more recent work, developed by Acosta [126] and continued by others [127], the phase inversion map for O/W/surfactant systems can be predicted by an equation of state linking the HLD with the equivalent alkane carbon number (EACN) of the surfactant, and the net-average curvature (NAC) of the interphase. This physical model can describe quite accurately the structure of O/W or W/O emulsions as a function of surfactant concentration, surfactant type and salinity.

Transitional inversion may also be achieved by only changing temperature, or pH if the surfactant is ionic and may be hydrolyzed (for example following Maestro et al. [128]). This changes the surfactant solubility on either phase, modifies the interfacial curvature and may induce a spontaneous inversion at a critical temperature, known as the Phase Inversion Temperature (PIT). Some examples of this inversion type can be found in the works by Shinoda and Arai [129], Shinoda and Saito [130, 131], Shinoda and Takeda [132], Parkinson and Sherman [133], Dokic and Sherman [134] and Rao and McClements [135]. Figure 2.6 shows a qualitative evolution of interfacial tension as temperature varies. The structural changes at the interface induce a spontaneous inversion to the reverse emulsion type, a concept that was endorsed by Kabalnov and Wennerström [136]. Usually, at temperatures below the PIT, the aqueous phase is continuous since the effect of the hydrophilic heads is stronger. For example, for ethoxylated non-ionic surfactants, dehydration of the ethoxide chains is greater at higher temperatures, which results in an increase in the molecule's hydrophobicity [125].

Shinoda and Saito [130] assembled the PIT equivalent for the inversion map of Figure 2.5, and it is included here for illustration purposes in Figure 2.7.

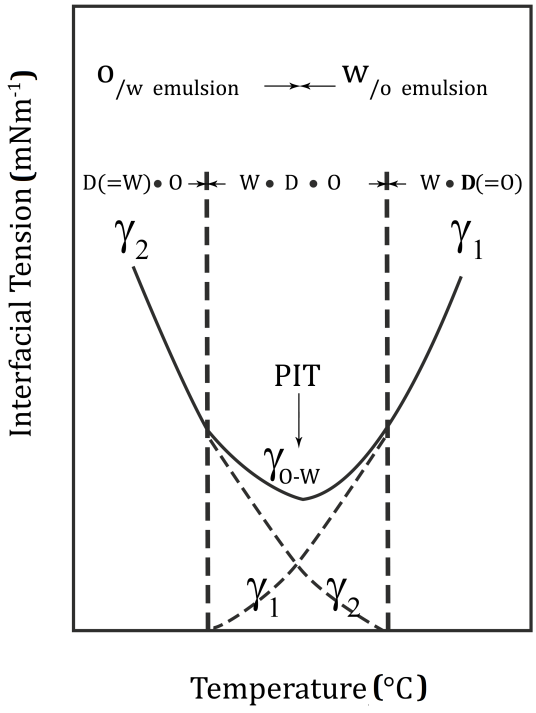

FIGURE 2.6: Qualitative evolution of emulsion interfacial tension with temperature. Here, "D" stands for the "dispersion phase" [137].

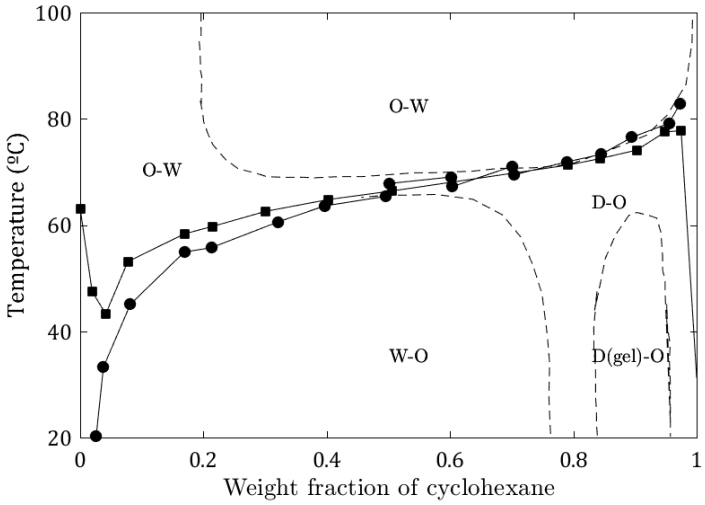

FIGURE 2.7: Phase inversion map as a function of temperature for water-cyclohexane-polyoxyethylene nonylphenylether. Surfactant load is 7%wt [130].

Emulsification by the PIT method has been largely used in traditional O/W systems, but can also be employed as a polymerization route to produce materials of the micro- and even the nano scale (see *e.g.* a recent work by Boscan et al. [138]).

The fact that inversion may occur by altering chemical affinity (through temperature, emulsifier structure or pH) sets the basis for a thermodynamic approach on phase inversion phenomena. It is of no surprise then that several models aiming to predict PI points have been proposed on phase equilibria and energy-minimization grounds, even for catastrophic inversions [77, 79, 139, 140]. However, dynamic effects should also be considered since the break-up and coalescence effects may change even with the emulsion preparation method [68].

The main physical action of an emulsifier is to stabilize the dispersion, reducing its interfacial tension: by adsorbing at the interfaces, the contact surface between polar and non-polar phases is reduced or avoided. Interfacial stresses are diminished because emulsifiers share structural properties with each separate phase, and thus alleviate incompatibility forces. This effect is well known to be asymptotical with surfactant's concentration [141–143], which is why they are only used in small amounts. Given that surfactants are usually found in the form of micelles, the highest concentration after which γ reduction is insignificant is known as the *critical micelle concentration* (CMC) [144].

Figure 2.8 shows, as an example, the interfacial tension reduction of the toluene-water system for different concentrations of sodium dodecyl sulfate (SDS) at several temperatures, as per Saien and Akbari [145].

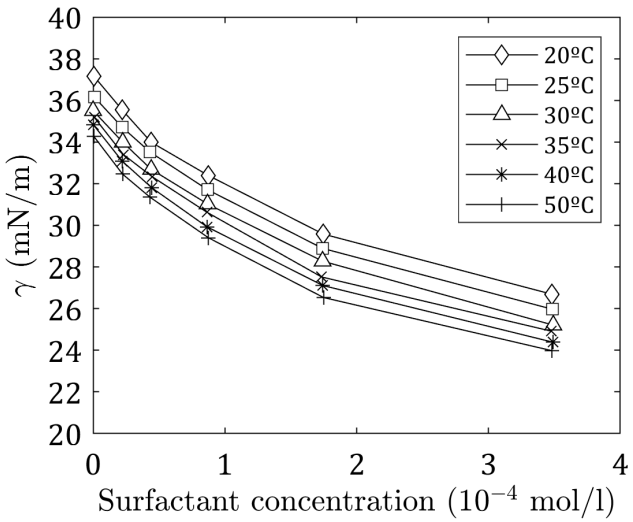

FIGURE 2.8: Effect of emulsifier concentration on surface tension [145].

Whether surfactants promote or delay phase inversion is still a matter of discussion, and experimental results show different tendencies depending on the emulsifier type. On the one hand, the interfacial tension reduction would produce a more stable system, which would imply higher dispersed phase fractions to force PI. On the other hand, if the emulsifier is more soluble in the dispersed phase, an increase in concentration may favor coalescence (in an effort to balance out the surfactant's presence) and thus promote PI.

Figure 2.9 and Figure 2.10, taken from Becher [119], show the effect of increasing emulsifier concentration on the PI point of mineral oil-water systems. For O/W systems inverting to W/O, the use of different Spans (sorbitan esters) favored the inversion as their concentration was raised. Since these emulsifiers are oil-soluble, they seem to favor a W/O structure. In the case of water-dispersed systems, the use of Tweens (ethoxylated sorbitan esters) also seem to favor inversion as concentration is increased (although tendency is not always monotonical).

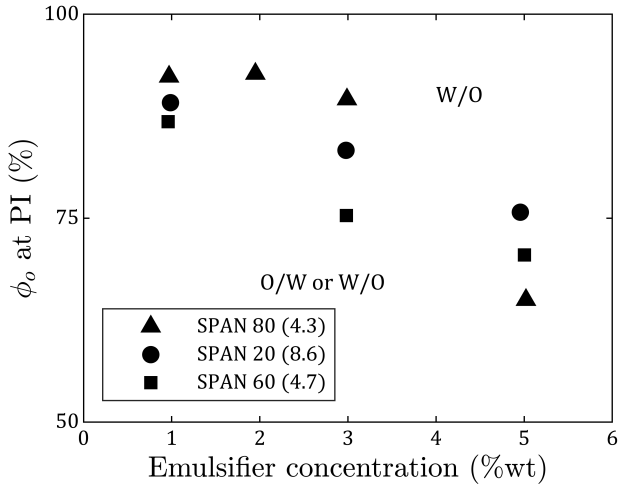

FIGURE 2.9: Effect of Span concentration on PI of O/W to W/O systems. Values in parentheses represent the HLB of the emulsifier [119].

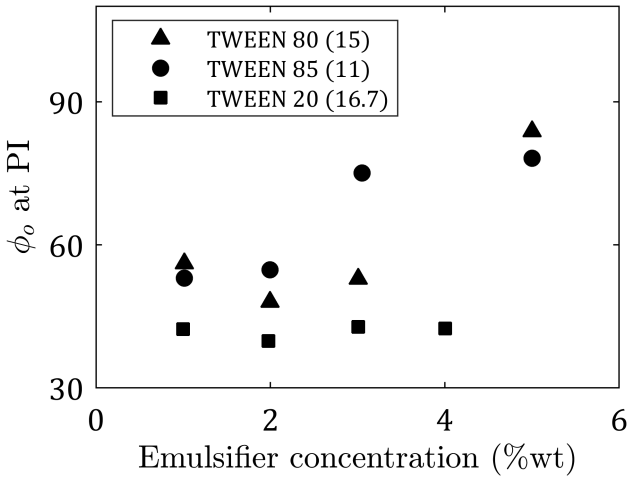

FIGURE 2.10: Effect of Tween concentration on PI of W/O to O/W systems. Values in parentheses indicate HLB of emulsifier [119].

These results would indicate that increasing surfactant concentration favors PI. However, if the "incorrect" emulsifier is used (for instance reversing Tween and Span in Becher's experiments), the opposite trend might be found. Groeneweg et al. [146] showed how increasing the concentration of an oil-soluble emulsifier (a monoglyceride) *delayed* PI of a water-in-

triglyceride oil system, as shown in Figure 2.11.

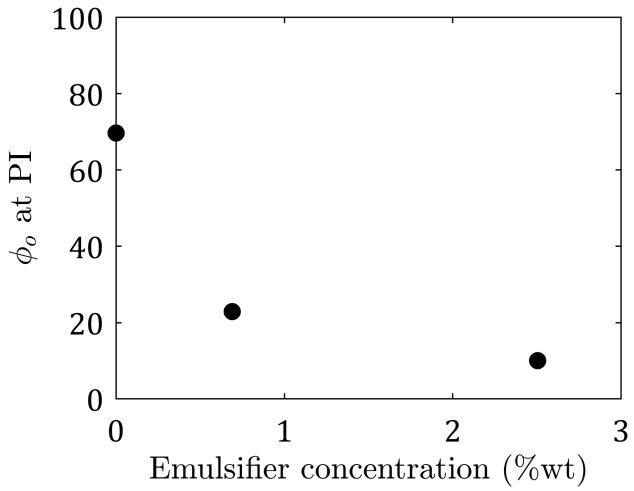

FIGURE 2.11: Delayed PI with increasing surfactant concentration for a W/O emulsion [146].

These two sets of results would seem, at first sight, opposing (emulsifier promotes vs emulsifier delays PI). However, they may actually refer to the same stabilization vs compatibilization effects: the chemical structure of each surfactant favors a given emulsion structure, which may serve to either stabilize the dispersed phase or to promote an inversion, depending on which phase is the dispersed one. Then, aiming to draw absolute conclusions about the effect of the surfactant concentration on the PI point seems worthless if not coupled with a view of its chemical structure. However, if the aim is to produce a target type of emulsion, optimization of the formulation recipe may be achieved and has already been reported for ionic [147] and non-ionic surfactants [148].

These previous considerations hold the following underlying assumption: surfactants adsorb at the interface in a homogeneous way. When analyzed from a dynamical point of view this is not always the case, since surfactants may gather irregularly around a dispersed drop, thus producing a concentration gradient throughout the interface. This, in turn, generates an interfacial tension gradient and a balancing force appears to counteract this difference: a dynamic known as the Marangoni effect [107, 149]. These forces may have a significant impact in the coalescence processes (which is discussed in Section 2.4.4.1) and may substantially affect PI. A summary of the current emulsification techniques through phase inversion mechanisms (catastrophic and transitional) can be found in Kumar et al. [150], who also included the effect of solid surfactant particles (Pickering emulsions) which have been left out of this thesis.

In polymer-polymer dispersions, copolymers are usually the surface-active species, since they show the same partial compatibility effect than the O/W emulsifiers. The similar-

ity between their respective interfacial roles can help to better understand the effect that copolymers exert on PI.

Not as many examples as in O/W systems may be found in literature, but a few experiments on polymer blends show evidence that the presence of copolymers modify (to a greater or lesser extent) the inversion holdup, which in most cases represents the onset of the co-continuous transition. Relevant examples are those by Deng and Thomas[151], Adedeji et al. [152], Charoensirisomboon et al., [153], Kitayama et al.[85], Zhang et al. [154], Dedecker and Groenickx [55], Epinat et al. [155] and Bourry and Favis [156] among others. In polymer-polymer solutions, there are articles by Díaz de Leon et al. [157], Soto et al. [47], and Fischer and Hellmann [61] on the PS-St-PB system.

If the copolymer's role is comparable to that of a traditional emulsifier/surfactant, then it would seem natural to study the effect of its structure and average molecular weight on the phase inversion dynamics, as it would appear to be the polymer equivalent of the HLB parameter in O/W emulsions. However, no advances have been reported on this matter so far, to the author's knowledge. The copolymers' role in the PI mechanism is further discussed in Section 2.5.

2.3 Emulsion rheology and phase inversion

Empirical phase inversion detection is usually achieved by monitoring a physical property that suffers a sudden change at the PI point. It is the widespread case of electrical conductivity in O/W systems. But it is not the only one: dispersion or emulsion viscosity may also change dramatically during the inversion process.

Unlike most emulsion properties, which are in fact the continuous phase properties, emulsion viscosity is always higher than the continuous phase viscosity. This is due to the drop-drop interactions that take place when the mixture is subject to shear. Van der Waal's attractive forces become significant when drops move past each other, which is the case in any conventional rheometer. These interactions generate extra stresses that reflect on an increase in the mixture viscosity. Then, the presence of a dispersed phase always makes the emulsion more viscous [158].

From Einstein's theory for dilute dispersions to Mooney's equation and fractal theory, a large number of models have been suggested to explain the rheological measurements in dispersed systems, and have been summarized in Table 2.2. There is common ground between all these equations:

- The higher the volume fraction of the dispersed phase, the higher the emulsion viscosity [159].
- For a given dispersed phase fraction, an increase in mean particle size results in a lower emulsion viscosity if drops are considered soft (deformable) [160]. There is no particle size effect on dispersion rheology if the dispersed phase consists of hard spheres [161].
- A widening of particle size distribution results in a reduction of the system's viscosity [162].
- In non-dilute dispersions, a higher phase viscosity ratio ($r = \frac{\eta_d}{\eta_c}$) may result in an increase of mixture viscosity [163].
- If either phase exhibits non-Newtonian behavior, the overall dispersion is non-Newtonian [164]. Yet, traditional Newtonian oil-water emulsions may exhibit non-Newtonian behavior at high dispersed phase fractions [160].
- Electrostatic forces, driven by surface charges or difference in dielectric constants, contribute to increase overall viscosity [165].

According to the available correlations, dispersion viscosity should change at the PI point since a system with a high concentration of dispersed phase is turned into one with low concentration. If inversion takes place without a co-continuous transition, then an abrupt change should be registered [158]. If a co-continuous system serves as transition from one dispersion type to the other, then the evolution of the mixture viscosity should follow a smooth transformation. This is the case of most polymeric systems, like the styrene-polystyrene-polybutadiene immiscible mixture in the manufacturing process of high-impact polystyrene [166]. An example is shown in Figure 2.12, taken from the work by Freeguard and Karmarkar [167] on the HIPS bulk synthesis.

Model	**Author**	**Comments**
$\eta = \eta_c (1 + a\phi_d)$	Einstein [168]	a is the 'intrinsic viscosity' and is 2.5 for dilute emulsions of rigid spheres.
$\eta = \eta_c \left(1 + a\phi_d + b\phi_d^2\right)$	Several authors	Usually, a is taken equal to 2.5 and b varies according to hypotheses undertaken by each author. Some correlations include a cubic term (e.g. Eirich et al.[169])
$\eta = \dfrac{\eta_c}{1 - c\phi_d}$	Oliver and Ward [170]	
$\eta = \eta_c \left(1 - \dfrac{\phi_d}{\phi_p}\right)^{-a\phi_p}$	Krieger and Dougherty [171]	ϕ_p is the maximum packing factor (0.74 for spheres). Usually, $a\phi_p \approx 2$, which makes it equivalent to the version of Quemada [172].
$\eta = \eta_c (1 - k\phi_d)^{-2.5}$	Roscoe [173]	For rigid spheres. The value of k is 1 for broad particle size distributions, and 1.35 for narrowly-distributed particles.

$\eta = \eta_c \left(1 - \frac{\phi_d}{\phi_p}\left(\frac{D}{d}\right)^{3-f}\right)^{-2}$	Lapasin et al. [174]	Correction for aggregated suspensions of monosized spheres of diamter d. D is the diameter of the aggregate. This is applicable for fractal systems of dimension f.
$\eta = \eta_c \frac{1-\phi_d}{\left(1 - \frac{\phi_d}{\phi_p}\left(1 + \frac{\eta}{\eta_c}\frac{\beta De^2}{(1+De^2)}\right)^{-1}\right)^2}$	Snabre and Mills [164]	De is the Deobrah number and β is a constant related to the flow type.
$\eta = \eta_c A \exp C\phi_d$	Broughton and Squires [175]	A and C are adjustable constants. The case of $A = 1$ simplifies to the model by Richardson [176]. This model is strictly valid for high ϕ_d values.
$\eta = \eta_c \exp \frac{a\phi_d}{1 - z\phi_d}$ $z = \exp 0.076 + \frac{0.01003}{d} + \frac{0.0029}{d^2}$ $a = \frac{br+1}{r+1}$	Mooney [177]	z is a correction factor for concentrated suspensions, named the *self-crowding factor*. The original work uses $a = 2.5$. The correlations for z and a were suggested afterwards [178]. d is the average particle diameter (in μm).

$\eta = \eta_c \left(\frac{1}{1 - \phi_d^{1/3}} \right)$	Hatschek [179]	For non-Newtonian behavior.
$\eta = \eta_c \left(\frac{1}{1 - (h\phi_d)^{1/3}} \right)$	Sibree [180]	Studied for paraffin-water emulsions. h is in the range 1.28-1.48 and depends on particle size (higher for finer emulsions) and possibly on surfactant concentration.
$\eta = \eta_c \left(1 + \frac{2.5\phi_d}{6(1 - \phi_d)} \right)^6$	Bredée and de Booys [181]	
$\eta = \eta_c \left(1 + \frac{2.5\phi_d}{c(1 - c\phi_d)} \right)^2$	Eilers [182]	c is in the range 1.28-1.35
$\eta = \eta_c 10^{\frac{C_1 C_2 \phi_d}{1 - C_2 \phi_d}}$	Maron and Madow [183]	For lattices, and $\phi_d < 0.6$.
$\eta = \eta_c \left[1 + \phi_d \left(\frac{2.5r + 1}{r + 1} \right) \right]$	Taylor [184]	$r = \frac{\eta_d}{\eta_c}$
$\eta = \eta_c \left[1 + \phi_d \left(\frac{2.5r + 1}{r + 1} \right) + 2.5 \left(\phi_d \left(\frac{2.5r + 1}{r + 1} \right) \right)^2 \right]$	Choi and Schowalter [185]	An expansion of the Taylor model.
$\ln \frac{\eta}{\eta_c} = \left(\frac{2.5r + 1}{r + 1} \right) \left(\phi_d + \phi_d^{5/3} + \phi_d^{11/3} \right)$	Leviton and Leighton [186]	Applied for milk fat emulsions.

$\eta = \eta_c A e^{B[C]\phi_d}$	Sherman [187]	A and B are adjustable constants. $[C]$ is the emulsifier concentration. This model is strictly valid for high ϕ_d.
$\eta = \frac{C_1}{d} + C_2$	Sherman [188]	At constant ϕ_d and η_c.
$\eta = \eta_c \left\{ 1 + 2.5\phi_d \left[1 + \frac{1}{\eta_c \kappa} \left(\frac{\epsilon \zeta}{\pi d} \right)^2 \right] \right\}$	von Smoluchowski [189]	ϵ is the dielectric constant of the continuous phase, ζ is the zeta potential, κ is the specific electric conductivity of the emulsion and d is the particle diameter.

TABLE 2.2: Models for emulsion viscosity.

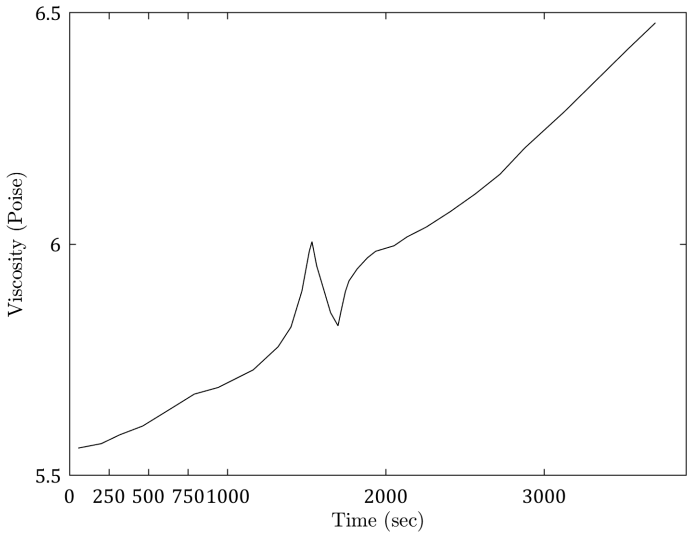

FIGURE 2.12: Evolution of mixture viscosity with reaction time for HIPS bulk process [167].

Other rheological properties also undergo similar changes at the phase inversion point. For example, Omonov et al. [190] measured the storage modulus (E') and the loss factor ($\tan(\delta)$) in immiscible polypropylene-polystyrene blends with equal phase viscosity, as shown in Figure 2.13.

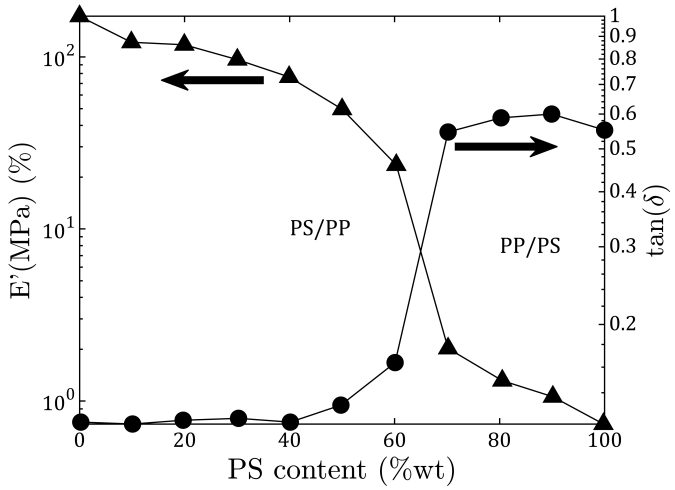

FIGURE 2.13: Storage modulus and loss factor of a PP-PS blend as a function of PS content [190].

In this sense, viscosity alone is not a factor contributing to cause phase inversion, but it serves to identify it. Then, modeling its evolution holds a significant interest as it may serve to predict this critical point.

2.4 The PI mechanism

The physical mechanisms by which a dispersed phase may become the continuous one are still under discussion. At least two big approaches are found in literature, as it is discussed in what follows.

2.4.1 Coalescence vs break-up imbalance

The idea behind this mechanism is that, under constant stirring, dispersed droplets may coalesce between each other but also be broken up by different external forces. If a given volume of dispersed phase is added to a continually stirred, stable dispersion, coalescence between the dispersed elements will readily occur, forming larger droplets. This, in turn, will enhance the breakage frequency, and this coalescence-break up processes will lead to a new steady state for the increased ϕ_d. However, there will be a critical dispersed volume fraction at which the coalescence of large drops will occur at a much faster rate than that needed for external forces to break up those larger particles. At that point, droplets will change shape from spherical to cylindrical, lamellar and ultimately other complex structures, trapping (in some cases) the continuous phase in the process. It is this imbalance between break-up and coalescence that makes PI possible. In non-stirred systems, the works by Bremond et al. [191], Kumar et al. [192] and Deblais et al. [193] have demonstrated, in different applications, that enhanced coalescence is also the mechanism that causes phase inversion.

Research on this line has been conducted by Arashmid and Jeffreys [74], Bouchama et al. [68], Groeneweg et al. [146], Hu et al. [52, 79], and Liu et al. [93], among others, all focusing in traditional O/W dispersions. In polymeric systems, especially in the case of polymer compounding and blending, this is also the usually suggested mechanisms as seen in the works by Shih [194], Mekhilef and Verhoogt [195], Sundararaj et al. [196], and Kitayama et al. [85]. An example of this mechanism in polymer-aqueous emulsions is presented in Zerfa et al. [197].

As explained previously, the PI point may strongly depend on the emulsification method (gradually adding dispersed phase to a mixture is essentially different from stirring a predefined volume of two separate phases). On this matter, Bouchama et al. [68] have compared a "direct" emulsification – in which organic and aqueous phases are mixed together at different phase ratios – with a "wash-out" method – by which dispersed phase is discretely added to the continuous phase until PI occurs. Their experiments, in which PI points were observed by conductivity measurements, are here reproduced in Figure 2.14 and show that the direct method produces a much earlier inversion than the "wash-out" route. Their explanation lies in a difference of the coalescence and break-up rates between each scenario, particularly

affected by the formation of multiple emulsions in the direct emulsification case (see Section 2.5 for further details). It is important to note that most of the empirical evidence found in literature deal with either one of the two methods, and this is one of the few works that have reported the difference between each method for the same physical system.

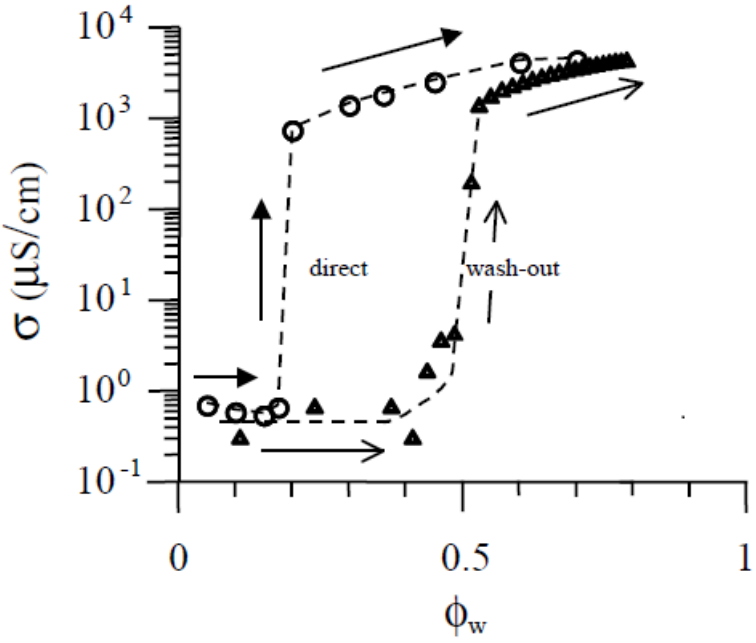

FIGURE 2.14: Phase inversion detected with different emulsification methods [68].

2.4.2 Energy minimization

This thermodynamic approach considers that the total system energy – that is, the sum of its internal, kinetic and surface energies – should find a minimum value at the inversion point. It originally finds its physical bases in the remarks by Luhning and Sawisotwski [108], who consider that PI is a spontaneous process and must consequently be accompanied by a total energy decrease. Counterintuitively, they have also observed partial inversions and re-inversions in the moments prior to the PI point, as if the system needed to attain a certain energy level in order to invert. This would indicate that there exist local energy minima prior to the PI point that should not be considered as a criterion for inversion; it would rather be the minimization after inversion.

These authors have also shown that interfacial area (and thus, interfacial energy) may either increase or decrease after inversion, in contrast with the findings of Fakhr-Din [198], who observed that it only decreases. This implies that surface energy minimization may not be a valid criterion for inversion.

In recent years, most models seeking to predict the PI point are based on a minimal total energy dissipation [140] rather than just interfacial energy. Nonetheless, Yeo et al., [199] on a theoretical model, suggested that minimization of interfacial energy could be used as PI criterion because kinetic energy variations would be negligible compared to that of the interface. In two-phase pipe flows, Brauner and Ullmann [200] suggested an equalization of the surface energy of each phase as a criterion for PI, an idea also used in static mixers by Tidhar et al. [95]. This mechanism has not been suggested, at least to the author's knowledge, for polymeric emulsions or blends undergoing PI.

In line with this energy minimization approach, some authors have suggested that it is the mechanical properties of the interphase that must play the key role in the PI process [136, 201] and suggested a "hole nucleation" model to represent the idea that continuous phase becomes entrapped at the moment of inversion.

2.4.3 Interfacial zero shear

The approach in this case is to study the interface and all the acting stresses. It was postulated by Yeh et al. [77], who suggested that, at the PI point, the shear stresses would balance out and the dispersed phase would overcome the continuous one. It is the dynamic forces that play a major role in this approach, which cannot unfortunately predict the hysteresis effect and, therefore, the ambivalent range.

2.4.4 Drop breakage and coalescence processes in liquid-liquid dispersions

While there are different approaches for identifying the PI point, a combination of the ones in 2.4.1 and 2.4.2 is possibly the closest to the real one. It is thus of interest to discuss the coalescence and break-up mechanisms (as described in literature), with the goal of presenting the most important concepts, variables and models that arise from their study.

In the past few years, several attempts have been made to deepen the understanding of break-up and coalescence phenomena by combining computational fluid-dynamics (CFD) and population balance models (PBM) [202–209]. In these works, the spatial dependencies of the break-up and coalescence rates are incorporated by simulating the geometry in question with a proper mesh and solving the equations with a finite elements method or similar. This methodology results in a greater physical accuracy but demands higher computational costs. An interesting trade-off has been recently developed by Castellano et al. [209], who have solved the space-dependent equations through a probability density function of the energy dissipation rate, thus avoiding the need of a CFD computation.

2.4.4.1 Coalescence

Coalescence kinetics were first described by von Smoluchowski [189] and later continued by Lawrence and Mills [210]. Their work was based on the trajectories of drops and neglected particle-particle hydrodynamic interactions. They distinguished two possible regions: a rapid coagulation and an ineffective coalescence region. In the former, all collisions between droplets result in coalescence. Then, if a dispersion begins with N_0 equally sized particles, then the number of particles made up of r units of the original droplets at time t, is given by:

$$N_{(r)} = N_0 \frac{(4\pi R_{eq} \mathfrak{D} N_0 t)^{r-1}}{(1 + 4\pi R_{eq} \mathfrak{D} N_0 t)^{r+1}} \tag{2.8}$$

where R_{eq} is the equivalent radius of the emulsion droplet and $\mathfrak{D}$ is the diffusion coefficients of the drops in the liquid.

If, on the other hand, collisions are not 100% effective, the authors suggest that a fraction λ_c of the form $\lambda_c = Ae^{-E/RT}$ can be used to account the portion of collisions that do result in coalesced drops. Then, Eq. 2.8 is modified to yield:

$$N_{(r)} = N_0 \frac{(\lambda_c 4\pi R_{eq} \mathfrak{D} N_0 t)^{r-1}}{(1 + \lambda_c 4\pi R_{eq} \mathfrak{D} N_0 t)^{r+1}} \tag{2.9}$$

Based on Harper's work, Howarth [211] derived the following simplified expression for calculating the frequency of colliding drops (of equal diameter d) in a turbulent flow field, ω_{cd}:

$$\omega_{cd} = \sqrt{\frac{24\phi_d \bar{u}^2}{d^3}} \approx \sqrt{\frac{24\phi_d n^2}{d^3}} \tag{2.10}$$

where $\bar{u}$ is the average Eulerian or Lagrangian turbulent velocity fluctuation and may be approximated to n, the agitation speed, according to Gillespie [212].

Considering the number of collisions that result in coalescence, the λ_c factor was found using gas kinetic theory:

$$\lambda_c = \exp\left[\frac{-3w^2}{4n^2}\right] \tag{2.11}$$

Thus, the overall coalescence frequency, ω_c, is given by:

$$\omega_c = \sqrt{\frac{24\phi_d N^2}{d^3}} \exp\left[\frac{-3w^2}{4n^2}\right] \tag{2.12}$$

where w represents the critical approach velocity above which the collision of two drops will result in coalescence. Howarth indicated that it should depend on the dispersed phase physical properties (surface tension, viscosity, density) and conducted a number of experiments to find the following correlation [211]:

$$\omega_c = C_1 \sqrt{\phi_d} n^{2.2} \exp\left[-\frac{C_2}{n^2}\right] \tag{2.13}$$

which is one of the earliest expressions for drop coalescence frequency in the form of the product between collision frequency and coalescence efficiency, *i.e.*, $\omega_c = \omega_{cd}\lambda_c$. However, this "critical approach velocity" criterion is not the most popular for drop coalescence.

Another approach, by Shinnar [213], is based on mechanical grounds, suggesting that coalescence could be prevented if the kinetic energy of the drops during a collision event is larger than the adhesion energy that drives drops together. Then, by performing the necessary balances, a minimum stable drop size above which coalescence is effectively prevented, can be found.

Yet, the most widely accepted theory (dating back to Allan and Mason [214] and MacKay and Mason [215]) explains that the fact that not all collisions result in coalescence is due to the continuous phase film that needs to drain between the two colliding drops before the drops interfaces collapse together. This mechanical process takes a given time, and drops may separate due to the constant energy fluctuations in the surrounding field; thus, there is a critical film thickness (hc) below which film rupture readily occurs. In this model, the efficiency of the coalescence process (λ_c) depends on whether the particles are considered rigid or deformable, and on the mobility of the interfaces [216]. Since the work by Ross [217], it is widely accepted that the efficiency is of the form $\lambda_c = \exp\left[-\tau_{dr}/\tau_a\right]$, where τ_{dr} is a film drainage time and τ_a a contact/adhesion time between the drops. Experimental evidence that supports film drainage theory can be found on the recent work by Liu et al. [218].

Inertial effects may also affect collision frequency depending on the phase density difference: if the drops hold a larger density than the continuous phase, collisions are favored compared to the opposite case [81]. It must be noted, though, that these effects only play an important role if $Re_d = \frac{\rho_c v d}{\eta_c} \gg 1$, where v represents particle velocity. In addition, the presence of electrolytes in the continuous phase also affects the collision rates, in particular by hindering coalescence and stabilizing particles, as recently detailed by Besagni and Inzoli [219].

Sovová [220] combined the film drainage theory with an energy-based model, in which the kinetic and interfacial energies of the drop are taken into consideration to compute the efficiency of turbulent collisions. This was adopted by other workers, such as Chatzi et al. [221] and Simon [222].

Several models to compute the collision frequency and the coalescence efficiency are available in literature [76, 81, 211, 223–233] and have been summarized here in Table 2.3 and Table 2.4. For the former, the dependency with particle volume is usually $\omega_{cd} \propto v^{7/9}$, although some others exist. Figure 2.15 shows a comparison for some of the available equations for ω_{cd} in a scenario with $\rho_c = 1000$ kg/m^3, $\eta_c = 1$ cP, $n = 100$ rpm, $D_I = 0.5$ m, $\phi_d = 0.1$ and $\gamma = 25$ mN/m. This comparison is only illustrative as all equations contain an adjustable parameter that is used to fit experimental data.

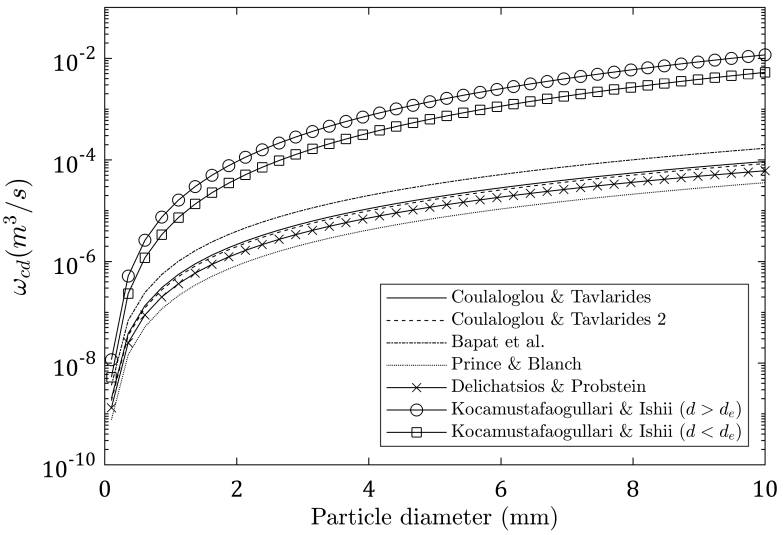

FIGURE 2.15: Qualitative comparison of collision frequency of equal drops according to published models as a function of particle diameter.

The differences between each curve shown lie on the set of hypotheses taken by each author. The common ground between them is described in what follows:

- Drop diameters (d) lie within the inertial subrange, which is defined by $L \gg d \gg \psi$, where L is the length scale of the energy-bearing eddies (usually identified with the length of the vessel or the impeller), and ψ is the Kolmogorov microscale (size of the smallest eddies), frequently calculated as $\psi = \left(\frac{{\eta_c}^3}{{\rho_c}^3 \varepsilon}\right)^{1/4}$, where ε is the energy dissipation rate per unit mass, and η_c and ρ_c are the viscosity and density of the continuous phase respectively.

- Droplets do not bear any particular electric charges that could modify coalescence rates due to electrostatic repulsion.

- Flow is isotropically turbulent.
- Energy is distributed uniformly throughout the vessel.
- Film drainage and contact times are random variables are only their average is computed in the equations.

Some models incorporate a correction factor to account for an observed increase in collision rates with an increase in dispersed phase fraction, usually explained by the loss of particle free space [234–236].

Interface mobility and particle deformation were later incorporated in the mathematical framework by several authors. Figure 2.16 shows a scheme of the concept behind interface mobility and Figure 2.17, the idea of particle deformation, both taken from Simon [222]. An immobile interface refers to the case where the liquid immediately around the interface moves with the velocity of the surface, where as a fully mobile interface cannot compensate any shear stress and thus is allowed to move independently of the liquid surrounding it. A partially mobile interface is naturally an intermediate case, frequently found in oil/water systems.

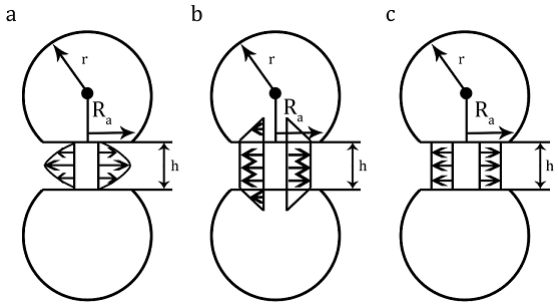

FIGURE 2.16: Deformable drops with different interface mobility: (a) Immobile interface, (b) partially mobile interface, (c) fully mobile interface [222].

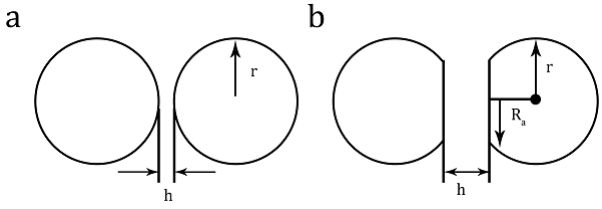

FIGURE 2.17: Difference in drop deformability: (a) Rigid drop. (b) Deformable drop [222].

A detailed review on coalescence processes considering these effects is offered by Chesters [81] and, more recently, by Vakarelski et al. [237] and Chan et al. [238], although their approach is fluid-mechanics based and the set of equations become more complex to solve.

The case for constant approach velocity (with both mobile and immobile interfaces) has been investigated by Klaseboer et al. [239]. For gas-liquid systems, a recent investigation by Guo et al. [240] showed that decreasing both liquid density and its surface tension lead to a hampering of the coalescence process.

According to Yiantsios and Davis [241], a particle interface will deform when the modified capillary number, $Ca^* = \frac{\eta_c a U}{\gamma h}$ is greater than unity. Here, U is a translational velocity, a is a characteristic length, and h is the film thickness. This means that the governing equations need to compute the value of the film thickness, which calls for a momentum balance at the interface and renders a more sophisticated mathematical model (although simplifications are possible, as shown by Chesters [81]).

For the immobile and partially mobile interfaces, some of the coalescence efficiency models depend on the critical film thickness h_c. This value depends on phase physical properties, but most authors have found that it lies around 500 $\mathring{A}$ for O/W dispersions [242] and 50 $\mathring{A}$ for some polymer mixtures [231]. A theoretical value was derived by Vrij [243] for drops of diameters d and d':

$$h_c = \left(\frac{A}{8\pi\gamma \left(\frac{1}{d} + \frac{1}{d'} \right)} \right)^{1/3} \tag{2.14}$$

where A is the Hamaker constant and γ is the interfacial tension.

Abid and Chesters [244] produced a model for a simplified case of partially-mobile films in the absence of van der Waal's forces. While hydrodynamic interactions due to particle deformation are included in the film drainage theory, no interactions induced by particle trajectories are considered. These hydrodynamic effects were first introduced by van de Ven and Mason [245] and Zeichner and Schowalter [246], and were later developed by several other authors in different configurations [247–251]. Further details on coalescence of liquid drops and bubbles may be found in a review by Liao and Lucas [252].

Model	Author	Comments
$\omega_{cd}(d,d') = \sqrt{\frac{C24 d_c \phi_d N^2}{d^3}}$	Howarth [211]	d_e is the collision diameter.
$\omega_{cd}(v,v') = C\left(v^{2/3}+v'^{2/3}\right)\left(v^{2/9}+v'^{2/9}\right)^{1/2}\left(\frac{9}{2}\pi\varepsilon\right)^{1/3}$ $\omega_{cd}(v,v') = \frac{C}{1+\phi_d}\left(v^{2/3}+v\prime^{2/3}\right)\left(v^{2/9}+v\prime^{2/9}\right)^{1/2}\left(\frac{9}{2}\pi\varepsilon\right)^{1/3}$	Coulaloglou and Tavlarides [228]	For liquid-liquid systems. The second expression is a correction that accounts for turbuelent damping.
$\omega_{cd}(v,v') = \frac{C}{1+\phi_d}\left(v^{1/3}+v\prime^{1/3}\right)^2\left(v^{2/9}+v\prime^{2/9}\right)^{1/2}\varepsilon^{1/3}$	Bapat et al. [223]	Probaby a correction to the model derived by Coulaloglou and Tavlarides.
$\omega_{cd}(d,d') = 0.089\pi\left(d+d\prime\right)^2\left(d^{2/3}+d\prime^{2/3}\right)^{1/2}\varepsilon^{1/3}$	Prince and Blanch [224]	For bubbles in liquids.
$\omega_{cd}(v,v') = 0.8906\left(v^{1/3}+v\prime^{1/3}\right)^{7/3}\varepsilon^{1/3}$	Delichatsios and Probstein [225]	For dilute dispersions ($\phi_d < 0.03$), non-charged dispersions.
$\omega_{cd}\left(d,d'\right) = 1.366\left(d+d\prime\right)^3\left(\frac{\varepsilon\rho_c}{\eta_c}\right)^{1/2} if d > d_e$ $\omega_{cd}\left(d,d'\right) = 0.618\left(d+d\prime\right)^3\left(\frac{\varepsilon\rho_c}{\eta_c}\right)^{1/2} if d < d_e and \rho_c \approx \rho_d$	Kocamustafaogullari and Ishii [226]	d_e is teh eddy diameter. Applied in shear-induced collisions under turbulent flow.
$\omega_{cd}\left(d,d'\right) = \frac{\pi}{4}\left(d+d\prime\right)^2\left(2.14\frac{\gamma}{\rho_c}+0.505g\right)^{1/2}\left\lvert\sqrt{d}-\sqrt{d\prime}\right\rvert$	Wang et al. [227]	For bubbles in liquids under buoyancy-driver flow.

TABLE 2.3: Models for collision frequency

Coalescence efficiency	Drop rigidity	Interface mobility	Author	Comments
$\lambda_c(d) = C_1 \left(\frac{3}{4}\right)^{-1/8} \left(\frac{3\pi\eta_c\dot{\gamma}d^3}{4A}\right)^{-C_2 1/8}$	Rigid	Immobile	Chesters [81]	A is the Hamaker constant. In viscous simple shear flow.
$\lambda_c(d) = \exp\left\{-\frac{C\eta_c}{\rho_c d^{4/3}\varepsilon^{1/3}}\right\}$	Rigid	Immobile	Nienow [229]	
$\lambda_c(d) = \exp\left\{-0.07668\frac{\eta_d}{\eta_c h_c}\left(\frac{\eta_c\dot{\gamma}}{\gamma}\right)^{3/2}\right\}$	Rigid	Immobile	Li et al. [253]	Used in polymer blends under the assumptions of the film drainage theory applicable to liquid-liquid systems.
$\lambda_c(d,d') = \xi \exp\left\{-\frac{C6\pi\eta_c}{\rho_c\varepsilon^{2/3}(d+d')^{2/3}}\frac{ND_I}{(D^2H)^{1/3}}\right\}$ $\xi = \left(\frac{{h_i}^{1/2}+1.378q}{{h_f}^{1/2}+1.378q}\right)^{1.872}\left(\frac{{h_i}^{1/2}+0.312q}{{h_f}^{1/2}+0.312q}\right)^{0.127}$ $q = \frac{\eta_c}{\eta_d}\sqrt{\frac{dd'}{2(d+d')}}$	Rigid	Immobile	Tsouris and Tavlarides [242]	h_i and h_f are the initial and final film thicknesses.
$\lambda_c(v,v') = \exp\left\{-\frac{C\eta_c\rho_c\varepsilon}{\gamma^2}\left(\frac{\sqrt[3]{vv'}}{\sqrt[3]{v}+\sqrt[3]{v'}}\right)^4\right\}$	Deformable	Immobile	Coulaloglou and Tavlarides [228]	The second equation is a correction that accounts for turbulent damping.

$\lambda_c(v,v') = \exp\left\{-\frac{C\eta_c\rho_c\varepsilon}{\gamma^2(1+\phi_d)^3}\left(\frac{\sqrt[3]{vv'}}{\sqrt[3]{v}+\sqrt[3]{v'}}\right)^4\right\}$				
$\lambda_c(v,v') = \lambda_1(v,v') + \lambda_2(v,v') - \lambda_1(v,v')\lambda_2(v,v')$ $\lambda_1(v,v') = \exp\left\{-\frac{C\eta_c\rho_c\varepsilon}{\gamma^2}\left(\frac{\sqrt[3]{vv'}}{\sqrt[3]{v}+\sqrt[3]{v'}}\right)^4\right\}$ $\lambda_2(v,v') = \exp\left\{-C\frac{\gamma}{\rho_d\varepsilon^{2/3}}\frac{(v+v')\left(v^{2/3}+v'^{2/3}\right)}{vv'\left(v^{2/9}+v'^{2/9}\right)}\right\}$	Deformable	Immobile	Sovová [220]	
$\lambda_c(d) = \exp\left\{-\frac{C\eta_c\rho_c d^4\varepsilon}{(\gamma h_c)^2}\right\}$	Deformable	Immobile	Nienow [229]	
$\lambda_c(d) = \exp\left\{-\left\{C\frac{\eta_d}{\eta_c}\left(\frac{\eta_c\dot{\gamma}d}{\gamma}\right)^{3/2}\left(\frac{2\pi\gamma d}{A}\right)^{1/3}\right\}\right\}$	Deformable	Partially mobile	Chesters [81]	A is the Hamaker constant. In viscous, simple shear flow.
$\lambda_c(d) = \exp\left\{-\left\{\frac{C\eta_c{\rho_c}^{1/2}d^{13/6}\varepsilon^{2/3}}{\gamma^{3/2}h_c}\right\}\right\}$	Deformable	Partially mobile	Nienow [229]	
$\lambda_c(d,d') = \left(1+0.26\frac{\eta_d}{\eta_c}\right)^{\alpha}$ $\alpha = -\frac{C\eta_c}{\rho_c{N_p}^{1/3}\varepsilon^{1/3}(d+d')^{2/3}{D_i}^{2/3}}$	Deformable	Partially mobile	Alopaeus et al. [254]	

$\lambda_c(d) = \exp\left\{-\frac{\sqrt{3}d}{8h_c}\frac{\eta_d}{\eta_c}\left(\frac{\eta_c d\dot{\gamma}}{\gamma}\right)^{3/2}\right\}$	Deformable	Partially mobile	Janssen and Meijer [231]	For liquid-liquid systems, also used in polymer blends by Lyu et al. [232].
$\lambda_c(d,d') = \exp\left\{-C_1\frac{\eta_d\rho_c^{1/2}\varepsilon^{2/3}d_{eq}^{11/6}(d+d')^{1/3}}{\gamma^{3/2}(1+C_2\phi_d)^2 h_c}\right\}$	Deformable	Partially mobile	Hasseine et al. [255]	$d_{eq} = 2\frac{dd'}{d+d'}$. h_c is a critical film thickness.
$\lambda_c(d,d') = \exp\left\{-C\frac{\eta_d}{\eta_c}\left[\frac{\eta_d\varepsilon^{1/2}d_{eq}}{\gamma}\left(\frac{\eta_c}{\rho_c}\right)^{-1/2}\right]^{3/2}\frac{d_{eq}}{h_c}\right\}$	Deformable	Partially mobile	Hasseine et al. [255]	$d_{eq} = 2\frac{dd'}{d+d'}$. h_c is a critical film thickness.
$\lambda_c(d,d') = \exp\left\{-2.3{\rho_c}^{1/2}\left[\frac{1}{4}\left(\frac{1}{d}+\frac{1}{d'}\right)^{-1}\right]^{5/6}\varepsilon^{1/3}\gamma^{-1/2}\right\}$	Deformable	Fully mobile	Prince and Blanch [224]	For bubbles in liquids.
$\lambda_c(d) = \exp\left\{-\frac{C\rho_c d^{5/3}\varepsilon^{2/3}}{\gamma}\right\}$	Deformable	Fully mobile	Chesters [81]	For bubbles in liquids. u_{rel} is the relative velocity of approaching bubbles.
$\lambda_c(d) = \exp\left\{-C\frac{\sqrt{3}}{\pi}\frac{{\rho_c}^{2/3}u_{rel}}{\gamma^{1/2}}\left(\frac{dd'}{d+d'}\right)\right\}$	Deformable	Fully mobile	Kamp et al. [256]	For bubbles in liquids in turbulent flow. C is in the range 1.12-1.41.

TABLE 2.4: Models for coalescence efficiency.

In polymeric systems, the coalescence process is modeled by the same governing equations used in traditional liquid-liquid drops. In fact, few differences arise when comparing both systems. An interesting example is the viscosity ratio effect on coalescence frequency found by Lyu et al. [232] in HDPE/PS blends, which is not always monotonically decreasing as theory suggests. Detailed reviews on coalescence in polymer blends are offered by Utracki and Shi [257] and Lyu et al. [258].

Chesters and Bazhlekov [259] incorporated the effect of insoluble surfactants (present at the drop surface) to the coalescence process. By computing the surface diffusion (which tends to reduce Marangoni effects) through the Péclet number and van der Waal's forces through the Hamaker constant, they developed the set of conclusions that are listed below.

- For sufficiently large particles ($d \gg 1$ μm), diffusion is negligible and van der Waal's forces are a function of the critical film thickness.
- Film drainage is unaffected by surfactant concentration up to a given film thickness, at which interface becomes immobile. At that point, film drainage is a function of surfactant concentration, which must be higher than a given critical value (a function of the Hamaker constant).
- Analytical expressions for calculating drainage times may be derived for both mobile and immobile interfaces.
- If the interface is immobile, no dispersed phase viscosity effects should be observable.
- For sufficiently small particles, diffusion of surfactants is considerable and surface tensions gradients become small. Then, film drainage rates are unaffected by Marangoni effects and the coalescence proceeds like the surfactant-free system, but with a lower interfacial tension.

For a given surfactant (or surfactant pair) concentration and temperature, the coalescence rate – at least in a non-stirred system – may vary with the emulsifier's HLB as shown by Boyd et al. [260] and exemplified in Figure 2.18 for various Span/Tween pairs in a dispersion of water and a commercial oil. Note that there is an HLB at which coalescence suppression is greatest, yielding a formulation that maximizes emulsion stability.

The effects reported for insoluble W/O surfactants were extended to copolymers in polymer-polymer mixtures by several authors [153, 167, 261–266]. Most authors consider that block or graft copolymers, which usually locate at the interface of immiscible polymer mixtures (blends or solutions), behave like surfactants and reduce the interfacial tension [267, 268]. This translates to smaller coalescence efficiencies as per film drainage theory. However, coalescence suppression is most likely due to steric hindrance of the copolymer chains.

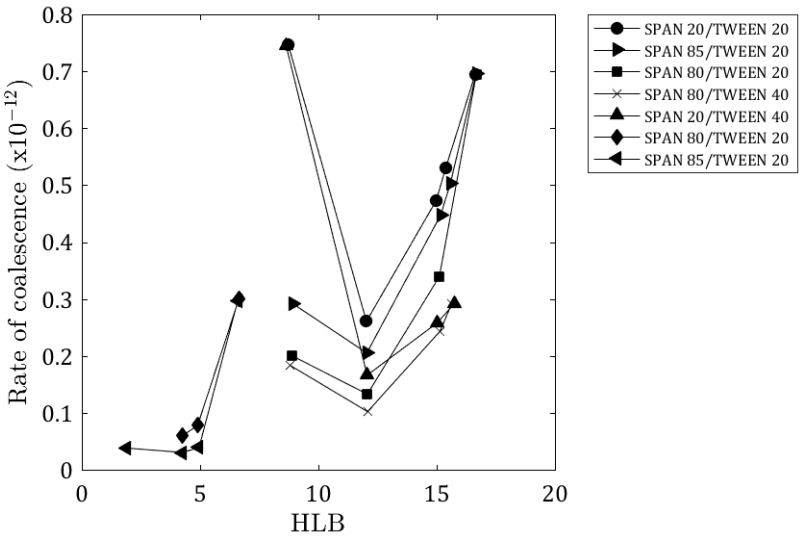

FIGURE 2.18: Coalescence rate as a function of surfactant's HLB [260].

These large molecules exert the following two effects on the coalescence process [269, 270]: 1) they provide extra stresses needed to collapse the particle interface and 2) they interact with the matrix chains and defer film drainage.

Beck et al. [271] ran a series of experiments with polystyrene and polyamide blends and showed that the presence of graft copolymers does reduce surface tension but not enough to explain the observed extent of coalescence suppression. It is rather the repulsive forces exerted by the copolymer chains that hamper coalescence rates. Milner and Xi [272] provided the theoretical and mathematical framework to support this evidence, also in line with Sundararaj and Macosko [273], Lyu et al. [258], Sundararaj et al. [196] and more recently with Luo et al. [274].

Figure 2.19 shows a schematic interpretation of this copolymer role taken from Sundararaj and Macosko [273]. It should be noted, however, that these conclusions were reached for polymer blends, while nothing on this line has been reported for solutions, to the author's knowledge.

Marangoni effects may also be considered a contributing cause of coalescence suppression, [258] just like in O/W emulsions.

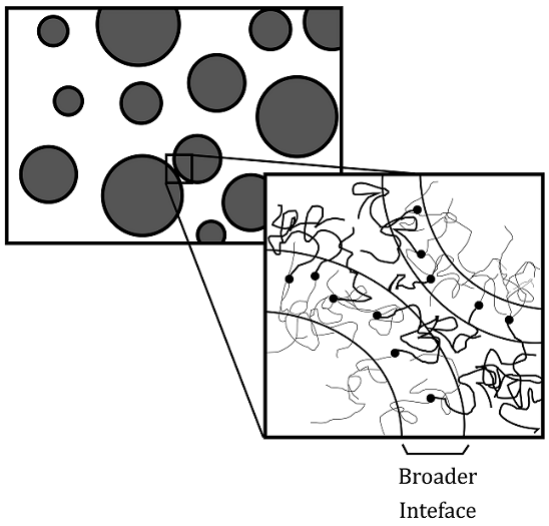

FIGURE 2.19: Coalescence suppression by copolymer steric repulsion [273].

2.4.4.2 Break-up

The breakage process of a liquid drop or a gas bubble involves complicated phenomena, which has led to define different criteria to decide when and how a particle breaks up [275]. In addition, most authors deal with simple binary break-up, and fail to recognize that daughter particles may continue to deform and undergo further splitting, as recently shown by Herø et al. [276]. The proposed mechanisms are presented in what follows.

a) Turbulent pressure fluctuation or particle-eddy collision

The idea behind this model is based on turbulent mixing, in which eddies constantly hit dispersed particles and cause them to deform. Pressure fluctuations caused by the same eddies can also modify particles' shape and eventually lead them to break into two or more smaller ones. Theory suggests that there is a balance between the dynamic pressure surrounding the particle, τ_c, and the surface stress, τ_s; breakage will occur depending on how different these forces are. Viscous stresses inside the particle are neglected. Different criteria were developed for deciding whether a particle may break up. At least five different cases can be found in literature; an extensive, critical analysis on the most relevant statistical models was presented by Kostoglou and Karabelas [277] and also reviewed by Lasheras et al. [278]. Perhaps one of the only models that considers the intermittent characteristic of turbulence is the multifractal approach originally developed by Baldyga and Podgorksa [279] and recently assessed by other workers [203, 204].

b) Viscous shear forces

The viscoelastic properties of the continuous phase may exert a deformation effect on the

dispersed particles as velocity gradients around the interface are generated. This mechanism then considers a balance between a viscous stress τ_v at the interface and the restituting surface stress τ_s, usually expressed in terms of a capillary number $Ca = \frac{\tau_v}{\tau_s}$. Early work by Shinnar [213] considers that break-up due to viscous shear is achieved only when applying a critical stress, given by $\tau_{cr} = \frac{C\gamma\phi_d}{d}\frac{\eta_d}{\eta_c}$, where C is a proportionality constant.

Wake effects are also considered as partly responsible for break-up in this model, since a difference in shape in contact with the continuous phase (head-tail instability) causes necking of the particle and surface shear stress may subsequently lead to splitting. Few authors incorporate this effect into their models; a recent example is the one by Yang et al. [206].

c) Shearing-off process

Also coined "erosive breakage", this mechanism is most commonly found in larger particles, whose surface instability is higher than smaller ones. A velocity gradient around the particle surface causes a number of smaller daughter particles to be sheared-off from its mother. On this mechanism, the works of Evans et al. [280], Bin [281] and Fu and Ishii [282] are especially pointed out, but a few other mathematical models are available.

d) Interfacial instability

Even in the absence of flow of the continuous phase (e.g., gases flowing up a liquid or drops falling into an immiscible liquid), breakage can still occur due to particle surface instability. This includes both Rayleigh-Taylor (density differences) and Kelvin-Helmholtz (velocity differences across an interface) instabilities. These effects are usually neglected without justification.

Models for break-up frequency

Exhaustive work has been conducted to develop models for computing the breakage frequency [221, 228, 235, 279, 283–288]. However, the vast majority only consider eddy-particle collisions as the most important cause for burst, neglecting the other present forces without much further validation. This is most likely due to the large availability of simple turbulent flow systems (*i.e.*, continually stirred liquid-liquid tanks, air-bubble columns, etc.). In other cases, for example polymer mixtures undergoing breakage due to shearing effects, particle-eddy turbulent models would rarely apply, and other models must be used or developed. Table 2.5 shows a summary of the available models for break-up frequency.

In addition, expressions for the breakage frequencies of bubbles and of drops are often used interchangeably; striking as it may seem, Andersson and Andersson [289] have shown that their breakage mechanism is very similar. The most important difference lays in the *daughter particle size distributions*: equal breakage is most likely for drops than for bubbles

(due mainly to pressure-driven internal fluid distribution after break-up), an obervation also found by Hesketh et al. [290]. It should be noted, however, that the viscosity of the dispersed phase plays a significant role in the break-up mechanism, as it is intrinsically involved in the force balances. Therefore, expressions should be used with caution when dealing with specially viscous materials (as it is the case with polymer systems [291]).

Regarding the mathematical models available to computing such distributions, Gao et al. [203] point out that their functionality, while bearing a considerable impact on the final particle size distribution, have a little effect on the Sauter mean diameter. Some of the available equations are presented in Table 2.6, where $\beta(f)$ is the probability density function of the generation of daugher particles that have a fraction f of their mother's volume. Further details may be found in Liao and Lucas [275] and more recently in Chu et al. [292] for bubble break-up.

Break-up frequency	**Author**	†	**Comments**
$\omega_b(d) = Cd^{-2/3}\varepsilon^{1/3}e^{-\left[\frac{\gamma}{\rho_d\varepsilon^{2/3}d^{5/3}}\right]}$	Coulaloglou and Tavlarides [228]	a	For liquid-liquid dispersions. The second equation accounts for turbulent damping.
$\omega_b(d) = \frac{Cd^{-2/3}\varepsilon^{1/3}}{1+\phi_d}e^{-\left[\frac{\gamma(1+\phi_d)^2}{\rho_d\varepsilon^{2/3}d^{5/3}}\right]}$			
$\omega_b(d) = C\frac{2}{\sqrt{\pi}}d^{-2/3}\varepsilon^{1/3}\Gamma_{\left(\frac{3}{2},\frac{C_2\gamma}{\rho_d\varepsilon^{2/3}d^{5/3}}\right)}$	Chatzi et al. [221]	a	$\Gamma_{\left(\frac{k}{2},\frac{x}{2}\right)}$ is the upper incomplete gamma function with k degrees of freedom.
$\omega_b(v) = N_e\frac{1}{2}\mathrm{erfc}\left(\frac{u_c}{\sqrt{2\gamma}}\right)$	Narsimhan et al. [283]	a	N_e is the average flow of eddies arriving atthe interface and u_c a critical velocity.
$u_c = \sqrt{\frac{\left(2^{1/3}-1\right)\gamma\sqrt[3]{36\pi v^2}}{\frac{1}{2}\rho_c v}}$			
$\omega_b(d) = C\varepsilon^{1/3}\mathrm{erfc}\left(\sqrt{C_2\frac{\gamma}{\rho_c\varepsilon^{2/3}d^{5/3}} + C_3\frac{\eta_d}{\sqrt{\rho_c\rho_d}\varepsilon^{1/3}d^{4/3}}}\right)$	Alopaeus et al. [293]	a	For liquid-liquid dispersions.
$\omega_b(d) = Cd^{-2/3}\varepsilon^{1/3}\left(1-\frac{1}{d}\int_0^d P_{\left(\frac{3}{2},\frac{C_2\gamma d^2}{\rho_c\varepsilon^{2/3}d_e{}^{11/3}}\right)}d(d_e)\right)$	Lee et al. [294]	a	Bubbles in liquids. $P_{\left(\frac{k}{2},\frac{x}{2}\right)}$ is the regularized gamma function with k degrees of freedom, and d_e is the eddy diameter.

$\omega_b(d) = \frac{C}{d}\sqrt{C_2(\varepsilon d)^{2/3} - \frac{12\gamma}{\rho_c d}}$	Martínez-Bazan et al. [295]	a	Bubbles in turbulent liquid flow.
$\omega_b(d) = \sum_{d_e} 1.4\frac{\pi}{16}(d+d_e)^2\sqrt{d^{2/3}+{d_e}^{2/3}}e^{-2.358\frac{\gamma}{d\varepsilon^{2/3}{d_e}^{2/3}}}$	Prince and Blanch [224]	a	Bubbles in liquids.
$\omega_b(d) = \frac{V_{ir}}{V}\left(\frac{\rho_c}{\rho}\frac{\eta}{\eta_c}\right)^2\varepsilon^{1/3}\frac{\pi}{20}\int_{\frac{d_c}{2}}^{\frac{d}{2}}(d_e+d)^2 F d(d_e)$ $F = \sqrt{8.2\left(\frac{2}{d_e}\right)^{-2/3} + 1.07 d^{2/3} e^{-\frac{E_c}{E_d}}\frac{4}{{d_e}^4}}$ $E_c = \frac{\pi\gamma}{2}\left[2\left(2^{-2/3}-1\right)d^2 + {d_{max}}^2 + \left(d^3 - {d_{max}}^3\right)^{2/3}\right]$ $E_d = C\rho_c\pi {d_e}^{11/3}\varepsilon^{2/3}$ $d_{max} = C\left(\frac{N^2 {D_i}^3\rho_c}{\gamma}\right)^{-0.6},\ D_i\left(\frac{\eta}{\eta_c}\right)^{1.2}$	Tsouris and Tavlarides [242]	a	Liquid-liquid dispersions. V_{ir} is the volume of the impeller region of the vessel, and V the total volume. Writing an energy balance and considering the mean energy dissipation rate calculated by Placek and Tavlarides [296] , $\frac{V_{ir}}{V} = 0.15$.
$\omega_b(d) = \int_0^{0.5} k(1-\phi_d)\left(\frac{\varepsilon}{d^2}\right)^{1/3}\int_{\xi_{min}}^1 \frac{(1+\xi)^2}{\xi^{11/3}} e^{-\left[g_{(f_b)}\right]} d\xi df_b$	Luo and Svendsen [297]	a	α is a universal constant [298], with a value of 1.5 in the original paper.

$k = \frac{(3\alpha)^{1/2}\pi^{1/3}}{\left(5\Gamma_{(1/3)}\right)^{1/2}2^{11/3}}$

$g_{(f_b)} = \frac{12\gamma\left[f_b{}^{\frac{2}{3}}+(1-f_b)^{\frac{2}{3}}-1\right]}{3/5\Gamma_{(1/3)}\alpha\rho_c d^{5/3}\xi^{11/3}}$

$\xi_{min} = \frac{d_{e,min}}{d} \approx 11.4 - 31.4$ in the intertial subrange

---

$\omega_b(v,w) = 1.5(1-\phi_d)\left(\frac{\rho_c}{\gamma}\right)^{11/5}\varepsilon^{9/5}\left(\frac{\bar{v}}{\bar{w}^4}\right)^{1/3}\left(\min\left(\bar{w}^{7/6},\bar{w}^{-7/9}\right)-\bar{v}^{-7/9}\right)$ $\bar{v} = \frac{v}{\frac{\pi}{6}\left[\left(\frac{\gamma}{\rho_c}\right)^3\varepsilon^2\right]^{3/5}}$	Lehr and Mewes [285]	a	Break-up frequency of bubbles of volume v breaking into two daughters of sizes w and v-w.
$\omega_b(d) = 0.5\left(\frac{\rho_c}{\gamma}\right)^{7/5}\varepsilon^{19/15}d^{5/3}\exp-\left[\frac{\sqrt{2}}{d^3\varepsilon^{6/5}}\left(\frac{\rho_c}{\gamma}\right)^{-9/5}\right]$	Lehr et al. [235]	a	Bubbles in liquids.
$\omega_b(d) = \int_0^{0.5} k(1-\phi_d)\varepsilon^{1/3}\int_{d_{e,min}}^{d}\frac{(d+d_e)^2}{{d_e}^{11/3}}Fd(d_e)df_b$ $F = \int_0^{\infty}\frac{1}{f_{b,max}-f_{b,min}}\frac{6}{\pi {d_e}^3\rho_c(\varepsilon d_e)^{2/3}}\exp-\left[\frac{6E_{(d_e)}}{\pi {d_e}^3\rho_c(\varepsilon d_e)^{2/3}}\right]d(E_{(d_e)})$ $f_{b,min} = \left(\frac{\pi {d_e}^3\gamma}{6E_{(d_e)}d}\right)^3$	Wang et al. [287]	a	$E(d_e)$ is the kinetic energy of an eddy of size d_e. $f_{b,max}$ and $f_{b,min}$ are chosen such that: $f_{b,min} < f_b < f_{b,max}$

$f_{b,max}$ is the solution of: $f_b^{\frac{2}{3}} + (1-f_b)^{\frac{2}{3}} - 1 = \min\left(2^{1/3}-1, \frac{E_{(d_e)}}{\pi d^2 \gamma}\right)$ $d_{e,min} \approx (11.4 - 31.4)\, d$			$f_{b,max} - f_{b,min} \leq \delta$ f_b is the break-up volume fraction and δ is an arbitrarily chosen constant to avoid a singularity when $f_{b,min} \to f_{b,max}$.
$\omega_b(d) = C \dfrac{\gamma g_{(r)}}{\eta_c d \ln\left(\dfrac{\sqrt{2/3}d}{\alpha_0}\right)}$	Elemans et al. [299]	b	For viscous liquid threads (similar to elongated, slender drops) surrounded by continuous viscous fluid. α_0 is the initial distortion amplitude. The function $g(r)$ may be calculated with the equations 38-40 by Tomotika [300], with r being the viscosity ratio.
$\omega_b(d) = C \dfrac{(d-d_c)^{C_2}}{(d-d_c)^{C_2} + {d_c}^{C_2}}$	Wang et al. [227, 236]	d	Bubbles in liquids. dc is the critical bubble diameter considering interfacial instability. For air in water in gravity-driven flow, $d_c =$ 27 mm [301].

TABLE 2.5: Models for break-up frequency. † represents the breakage mechanism described at the beginning of this section.

Model	Author	Comments
$\beta(f) = \frac{cm}{\sqrt{2\pi}} e^{-\frac{(f-0.5)^2}{2}}$	Valentas et al. [302]	m is the number of daugher particles and c is the model tolerance.
$\beta(f) = 30 f^2 (1-f)^2$	Hsia and Tavlarides [303]	A beta distribution suggested for O/W dispersions, like the ones in Ross et al. [304]
$\beta(f) = \frac{\Gamma(c_1+c_2)}{\Gamma(c_1)\Gamma(c_2)} f^{c_1-1} (1-f)^{c_2-1}$	Lee et al. [294, 305]	c_1 and c_2 are model parameters.
$\beta(f) = \frac{\Gamma(12)}{\Gamma(3)\Gamma(9)} f^8 (1-f)^2$	Konno et al. [306]	
$\beta(f) = 3\frac{\left[f^{2/9)} - \alpha^{5/3}\right]\left[(1-f)^{2/9} - \alpha^{5/3}\right]}{\int_{f_{min}}^{f_{max}} f^{-2/3}\left[f^{2/9} - \alpha^{5/3}\right]\left[(1-f)^{2/9} - \alpha^{5/3}\right] df}$	Martínez-Bazán et al. [295]	For bubbles in liquids. $\alpha = \frac{\left(\frac{12\gamma}{c\rho_c}\right)^{3/5} \varepsilon^{-2/5}}{\left(\frac{6}{\pi} v_0\right)^{1/3}}$. v_0 is the mother bubble volume and $c \approx 8.2$. $f_{min} = \left(\frac{12\gamma}{c\rho_c}\right)^{9/2} \left(\frac{6v_0}{\pi}\right)^{-3/2} \epsilon^{-3}$, $f_{max} = \frac{6}{\pi} v_0^3 \left(1 - f_{min}^{1/3}\right)$.
$\beta(f) = \frac{2\int_{u_{min}}^{1} (1+u)^2 u^{-11/3} e^{-\chi u^{-11/3}} du}{v_0 \int_0^1 \int_{u_{min}}^{1} (1+u)^2 u^{-11/3} e^{-\chi u^{-11/3}} du df}$	Luo and Svendsen [297]	For bubbles in liquids. v_0 is the mother bubble volume, $\chi = \frac{12c\gamma\pi^{5/9}}{\rho_c \varepsilon^{2/3} (6 f v_0)^{5/9}}$, $u_{min} = \psi_{min}\left(\frac{6 f v_0}{\pi}\right)^{-1/3}$, $\psi_{min} \approx (11.4 - 31.4)\psi$, with ψ being the Kolmogorov microscale length.
$\beta(f) = \frac{1}{\sqrt{\pi} f} \frac{\exp\left\{-\frac{9}{4}\left[\ln\left(\left(2\varepsilon^{2/5}\right)(6v)^{1/3} \rho_c^{3/5} \pi^{-1/3} \gamma^{-3/5}\right)\right]^2\right\}}{1 + erf\left[\frac{3}{2}\ln\left(\left(2\varepsilon^{2/5}\right)(6 f v_0)^{1/3} \rho_c^{3/5} \pi^{-1/3} \gamma^{-3/5}\right)\right]}$	Lehr et al. [235]	

TABLE 2.6: Models for computing the daughter particle size distribution after break-up.

Break-up mechanisms that do not consider particle-eddy collision

Exhaustive studies on drop deformation in simple and rotational shear flows were conducted by Grace [307] and by Bentley and Leal [308]. These last authors showed that, the lower the viscosity ratio the greater the extent to which the particle is stable (yielding larger critical Ca values). In rotational flows, deformation depends on the orientation angle of shear and particle viscosity may help dissipate shear-induced vorticity through internal circulation. This means that, in slightly rotational flows, the more viscous the particle, the more "solid-like" behavior it presents, needing greater shear rates to induce break-up. In stronger rotational flows, the authors showed that there exists a critical viscosity ratio above which break-up cannot occur (the orientation of the drop is such that the effective strain rate is very low), which was first predicted by Taylor in dilute, Newtonian dispersions [184]. Their results are also in agreement with Arai et al. [309], who particularly studied this effect (both theoretically and experimentally) in fully turbulent conditions. Figure 2.20 illustrates an example taken from their work, in which the dispersed phase is a solution of PS in a polystyrene-o-xylene and the continuous phase is an aqueous solution of polyvinylalcohol.

Depending on the phase properties and on the local shear conditions, the critical viscosity ratio above which break-up does not occur may widely vary. Taylor's limit for small deformation is a known value of 2.5 and some polymeric systems in simple shear exhibit a value of 4 [307], but this is by far not the case for extensional flow as shown by Wu [310] or Sundararaj and Macosko [273].

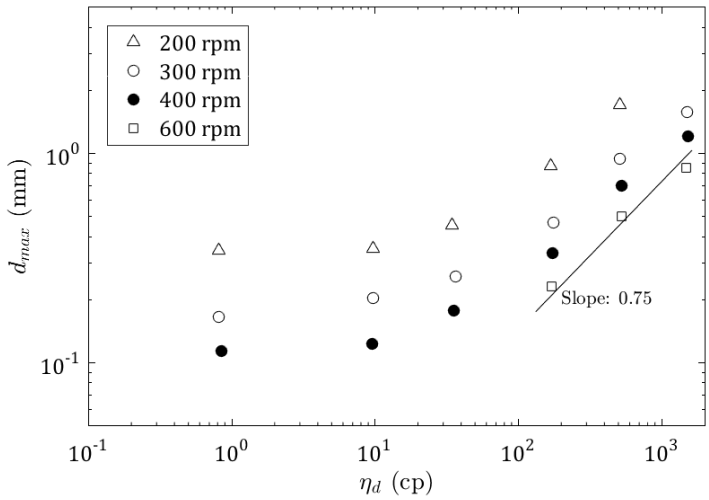

FIGURE 2.20: Effect of dispersed phase viscosity on maximum stable drop size before break-up [309].

The works by Grace [307], Elemans et al. [299], Elmendorp [311], de Bruijn [312], Tomotika [300] and Hinze [313] consider the effects of different mechanisms other than eddy-particle collision for splitting. Hinze highlights that there are different types of drop de-

formation and that the condition at which a drop deforms may be described in terms of a general Weber number $\left(We = \frac{\tau d}{\gamma}\right)$ and a Viscosity number $\left(Vi = \frac{\eta_d}{\sqrt{\rho_d \gamma d}}\right)$ and suggests a simple model to predict drop deformation, as a function of a critical Weber number:

$$We_c = C\left(1 + C_2 Vi\right) \tag{2.15}$$

The critical value would depend on the deformation type (namely lenticular, elongated or bulgy). Even if the simplicity of this model casts further validation questions, both theory and practice (in rotational shear flow) yield an interesting result: for very low and very high viscosity ratios the critical We rises to an infinitely large value, meaning that no break-up occurs, which is in line with previously stated authors.

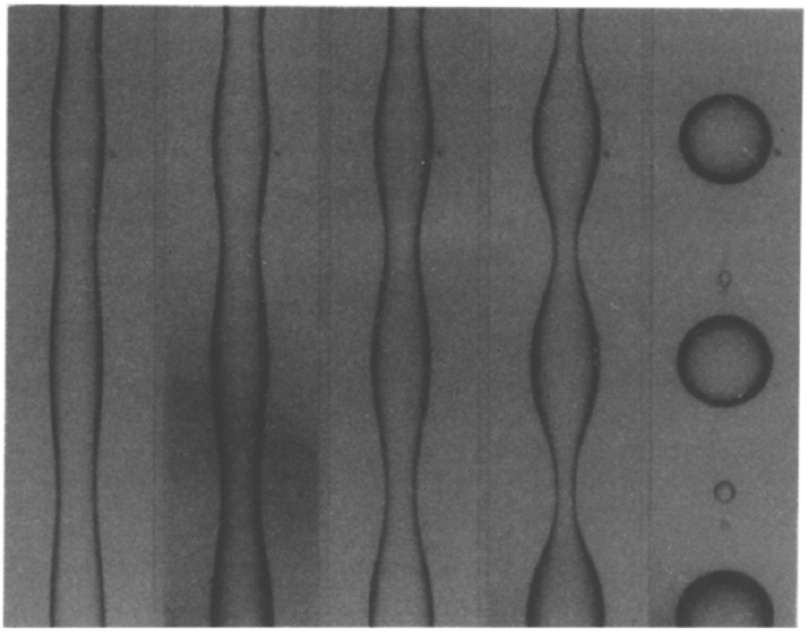

FIGURE 2.21: Deformation process of a polyamide 6 thread surrounded by a polystyrene matrix [299].

Liquid thread break-up, as shown in Figure 2.21 (reproduced from Elemans et al. [299]), was firstly discussed by Tomotika [300], and later continued by Elmendorp [311] and Janssen and Meijer [231]. Polymer liquid-liquid systems, especially under extruding conditions, are examples that may be modeled following their work, which includes both Newtonian and non-Newtonian behavior. This particular process accounts for the sinusoidal reshaping of slender threads caused by shear, up to a point after which break up occurs, splitting the thread into several daughter drops. A recent investigation by Epinat et al. [155] on polyamide/HDPE blends is also in line with their work, and has further shown the effect of the viscosity ratio on the break-up mechanism and the yielded particle morphology. Particularly for extruded polymer blends, Wu [310] suggested a correlation between Ca and the viscosity ratio that

can predict final particle mean size considering only thread break-up:

$$d = 4\frac{\gamma}{\dot{\gamma}\eta_c}\left(\frac{\eta_d}{\eta_c}\right)^{\pm 0.84} \tag{2.16}$$

where the power is +0.84 when $\frac{\eta_d}{\eta_c} > 1$ and -0.84 otherwise.

In stirred dispersions, the breakage process of non-Newtonian drops was incorporated by Lagisetty et al. [314], who presented a model to predict the maximum stable size at a given shear rate. Their work was based on the theory and models developed by Hinze [313], Coulaloglou and Tavlarides [315] and Arai et al. [309]. Considering viscoelastic drops modeled by a power law equation, the maximum stable drop diameter may be calculated by computing the following non-dimensional breakage time:

$$t^* = \int_0^1 \left[\left(\theta - \frac{1}{2}\right)^2 + CWe\left(\frac{d}{D_i}\right)^{5/3} - \tau_0\frac{d}{\gamma} - \frac{1}{4}\right]^{-1/n} d\theta \tag{2.17}$$

and then solving:

$$t^* = \left(\frac{K\gamma}{d_{max}}\right)^{1/n}\frac{(d_{max}D_i)^{2/3}}{N} \tag{2.18}$$

where θ is the dimensionless strain, τ_0 a yield stress (nonzero for Bingham plastics), and K and n are the power law model parameters. The authors have provided solutions of the integral for several values of n, and noted that break-up can only occur if the term $CWe\left(\frac{d}{D_i}\right)^{5/3} - \tau_0\frac{d}{\gamma} - \frac{1}{4}$ is positive.

Koshy et al. [316] studied the effects of including drag-reducing agents in the continuous phase and incorporated this feature into the model by Lagisetty et al. [314]. They indicated that these species contribute to change the magnitude of the turbulent stresses (probably due to turbulent damping) and showed that the maximum stable drop size before break-up increases with the presence of such agents, as experiments confirm.

The effect of insoluble surfactants on droplet breakup was studied by Stone and Leal [317] and recently simulated by Li et al. [204]. The former showed that the presence of these agents translates into a lower Ca needed for break-up since the interfacial tension reduction allows for increased drop deformation. However, they demonstrated (at least numerically) that the predictions on such critical Ca depend on the dominant flow regime at the interface (convection or diffusion) since two opposing effects appear, as described in what follows.

If surfactant diffusion is fast, concentration profiles along the interface are almost constant, and shear-induced drop deformation will only serve to 'dilute' the surfactant's effect, lowering its surface concentration and thus increasing the interfacial tension compared to the saturated case. If convection is dominant, drop deformation causes the surfactant to accumulate at the end of the drop (where surface curvature is greatest), leading to extra tangential stresses (Marangoni effect) but lower interfacial tension compared to the fully coated interface. Depending on the dominating regime, the critical shear rate needed for break-up may differ substantially compared to the ideal case in which interfacial tension is held constant at an equilibrium value. Yet, compared to a clean, surfactant-free interface, the addition of surface-active species will lower interfacial tension and promote break-up.

The convection-dominant case described by Stone and Leal [317] may result in a particular break-up mode named tip-streaming, in which drops deform into a sigmoidal shape and small daughter droplets break off at the tips, as it is shown schematically in Figure 2.22, reproduced from de Bruijn [312]. This case was also subject of different studies [318] and show that this mode of breakage may occur at much lower shear rates than traditional binary splitting.

FIGURE 2.22: Tipstreming breakup mechanism [312].

All the above described mechanisms are only concerned with shear-induced deformation, most often based on a single particle. In concentrated dispersions under mixing conditions it is likely that particle-particle collisions become of importance, and most available works on this matter focus mainly on the coalescence process that results (as described in Section 2.4.4.1). However, a thorough analysis of water drop-drop collisions in air was presented by Ashgriz and Poo [319], who have empirically and theoretically shown that particle break-up also occurs as a result of collisions. As explained by the authors, there are four possible outcomes to drop-drop collision: bouncing, coalescence, separation and shattering. Figure 2.23 shows examples of coalescence (above) and separation (below).

The mechanics of drop-drop collisions are affected by both dispersed and continuous fluid properties, the relative velocity between drops, and the contact angle before collision. Even though their work was not carried out in stirring conditions (drops were generated from jets), the conceptual conclusions that arise are of interest, since they provide a thorough explanation of some of the mechanisms that are frequently cited in literature. In the case of air drops in water, the authors found that a Weber number (here defined $We = \frac{\rho_c d {u_r}^2}{\gamma}$, with u_r being a relative velocity), was a governing parameter together with the particle size ratio and an arbitrary dimensionless relative position. They thus produced maps like the one in Figure 2.24, which show clearly that: a) not all drop-drop collisions result in coalescence

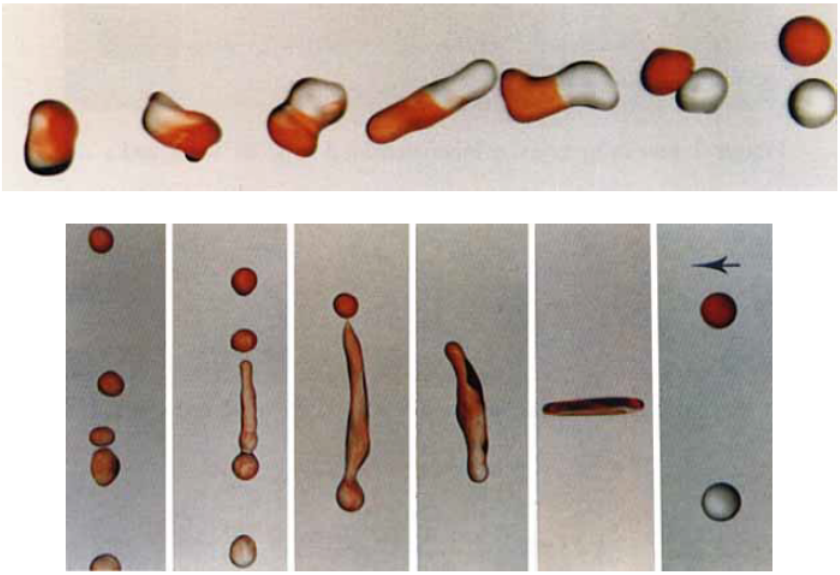

FIGURE 2.23: Two possible outcomes of drop-drop collisions: coalescence (above) and separation (below). Evolution of the process is from right to left [319].

nor in bouncing and b) break-up can occur as a result of particle-particle impact, even if *We* increases.

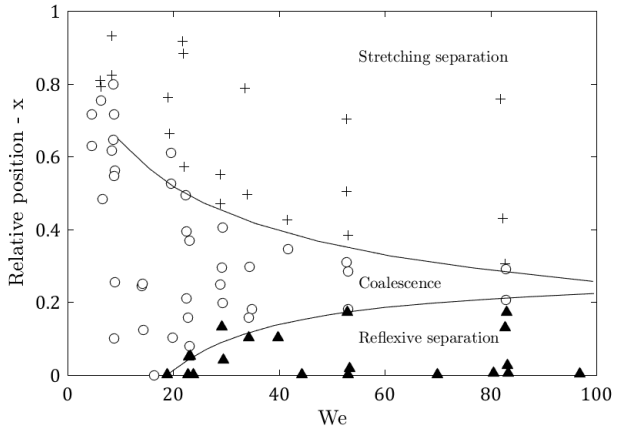

FIGURE 2.24: Outcome after collision map for equal size drops [319].

2.5 Multiple emulsions

Very often, the structure of an O/W or W/O emulsion is not made up of simple drops dispersed in a continuous matrix: it is also possible for some volume of the continuous phase to become entrapped in the dispersed one, giving rise to an *emulsion within an emulsion*, as illustrated in Figure 2.25, from Jahanzad et al. [320]. These kind of structures have

been observed for almost a century (perhaps since the work by Seifriz [321]) and may be either intentionally prepared or a consequence of a phase inversion process. In several cases, these structures were also observed for surfactant-free systems (dispersions), especially in the vicinity of the phase inversion threshold [64, 66, 91, 108, 322, 323].

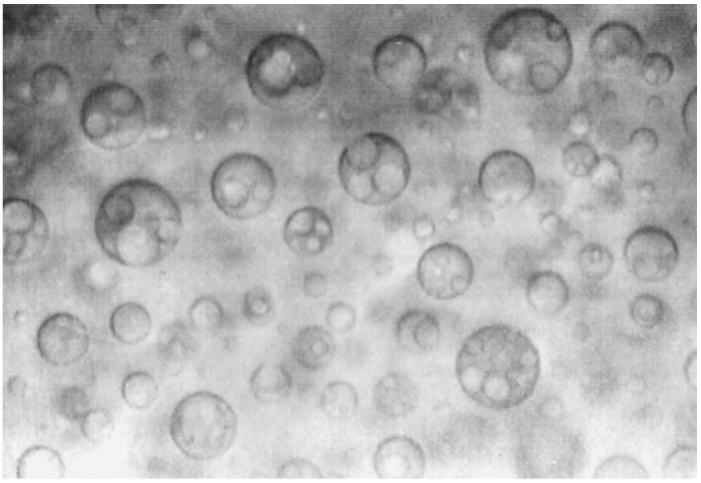

FIGURE 2.25: Example of a drop-in-drop structure [320].

Extensive work [158, 324–332] has been conducted since the earlier 1970's to describe the properties of these emulsions and their potential applications (they are of interest in the pharmaceutical, food, waste water treatment and even upstream oil production industries, though nowadays have limited applicability due to their inherent instability [333]). These fractal-like systems are not necessarily drop-within-a-drop structures; there have been reports of triple, quadruple and even quintuple emulsions [158, 321]. Some authors refer to this type of emulsions as abnormal, as opposed to the normal emulsions that satisfy Bancroft's rule [106, 123, 334].

2.5.1 Inclusion mechanisms

The process of continuous phase entrapment inside dispersed drops has been observed to occur both with and without emulsifiers. Examples of the former include those of Brooks and Richmond [123], Jahanzad et al., [320], Groeneweg et al. [146], and Pal [335], while cases of the latter are seen in Pacek et al. [91, 323, 336] and Gilchrist et al. [322]. Whichever the case, two main mechanisms have been suggested and described hereafter.

1. *Deformation* of dispersed drops under high shear rate. This is mostly observed with large drops [337] and particularly enhanced in the presence of surfactants [338].
2. *Simultaneous coalescence* of two or more drops, by which continuous phase is engulfed following film rupture [66, 339].

These mechanisms are illustrated respectively in Figure 2.26 - reproduced from Yan and Pal [338] - and Figure 2.27 - from Kumar [66]. The former is based on the pressure fluctuations that occur in turbulent stirred systems, which promote particle break-up. The restoring force in this case is the interfacial tension, which increases locally when deformation occurs, as interfacial area is created. If surfactants are present at the interface, the Marangoni effect tends to counteract such local increase. Thus, if interfacial forces are higher than pressure fluctuations, then no inclusion occurs. Conversely, if the interfacial tension is not as high and/or surfactant diffusion is rapid (so that any attempt to locally increase the interfacial tension is counteracted), then continuous phase protrusions take place and further drop sealing (inter-particle coalescence) ensures the occlusion [338].

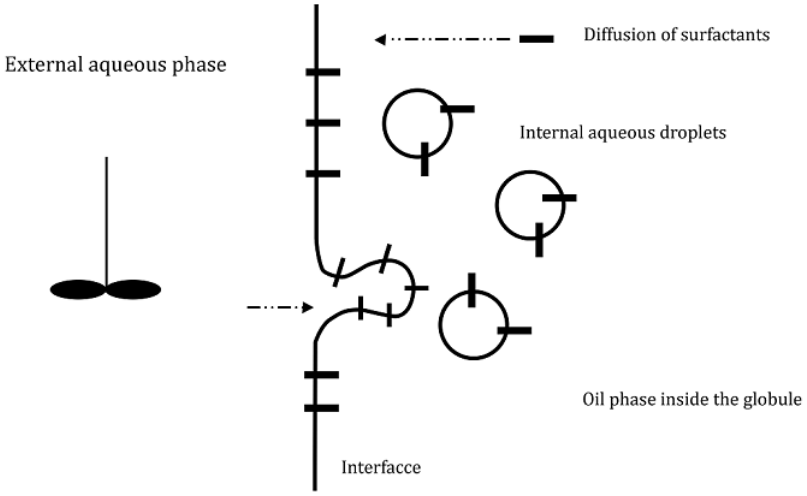

FIGURE 2.26: Inclusion of continuous phase by drop deformation [338].

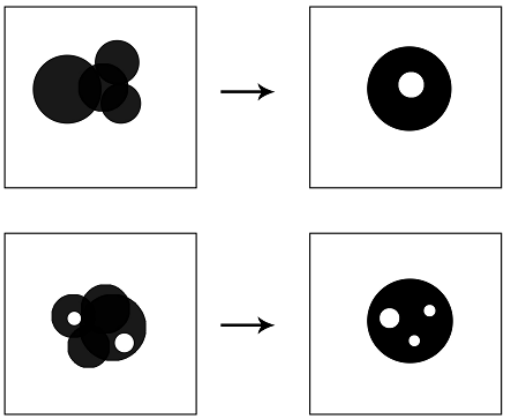

FIGURE 2.27: Entrapment mechanism by multiple particle collision [66].

The latter case is believed to occur as a result of a multiple coalescence processes (two-body collision may also produce continuous phase entrapment but is highly dependent on

the intensity of the collision and the interfacial properties [339, 340]. In this context, film drainage occurs simultaneously between more than two drops and most of the liquid from each film is forced out to a common bulk inside the drop.

According to Sajjadi et al. [106], mechanism 1 is usually dominant at low dispersed fractions, since multi-drop coalescence occurs preferably at more densely packed systems. Thus, a gradual change between mechanisms is expected when increasing the dispersed phase fraction: larger and/or more numerous drops promote coalescence, which favors continuous-phase inclusion, and finally increases the effective dispersed volume fraction. It is of no surprise, then, that the drop-in-drop structure has been observed prior to catastrophic phase inversion processes.

At intermediate values of ϕ_d (*i.e.*, not low enough for inclusions to be deformation-induced and not high enough for PI to occur), two conditions should be satisfied for entrapment to be possible (as explained by Pacek et al. [336]):

1. *Enhanced coalescence frequency*, so that multiple drops may coalesce and engulf part of the continuous phase.
2. *Stability* of the entrapped droplet inside the drop, without which the drop-in-drop structure would only be temporary.

When surfactants are present, post-inclusion stability is naturally a function the emulsifier's structure and concentration. In the absence of any surface-active species, experimental evidence shows that occlusions are more frequently seen in O/W/O rather than the reverse dispersions [91, 341]. This would seem to indicate that water-in-oil droplets are much less stable (*i.e.* their escape processes are enhanced) than oil-in-water ones. Kumar [66] suggests that this asymmetry lies in the difference of dielectric constants (*e.g.*: 78.3 for water and 1.88 for n-hexane at 25°C), which explains the disparity in coalescence rates between water-water and oil-oil drops, the latter being much lower due to the overlapping of the electrical double layers. In fact, this is the argument that explains the asymmetry observed in many ambivalent ranges (in the absence of emulsifiers) even with systems that hold similar physical properties.

2.5.2 Manufacture methods

An early procedure for the preparation of multiple emulsions (for example W/O/W) consisted in a two-step process: a first emulsification of an aqueous phase in a continuous organic matrix (with a lipophilic surfactant), followed by the emulsification of the organic phase by the addition of water and a hydrophilic emulsifier. This is illustrated in Figure 2.28, from

Florence and Whitehill [342]. The final structure and properties of the multiple emulsion depend on surfactants concentration, their weighted HLB [329], phase volume fractions and electrolyte concentration [342].

The stability of the multi-emulsions produced this way has been the subject of several papers, for there are numerous mechanisms by which occluded continuous phase may escape the dispersed particle and rejoin the matrix. This is usually known as the breakdown of the multiple emulsion, and a review on the mentioned mechanisms was produced by Florence and Whitehill [332].

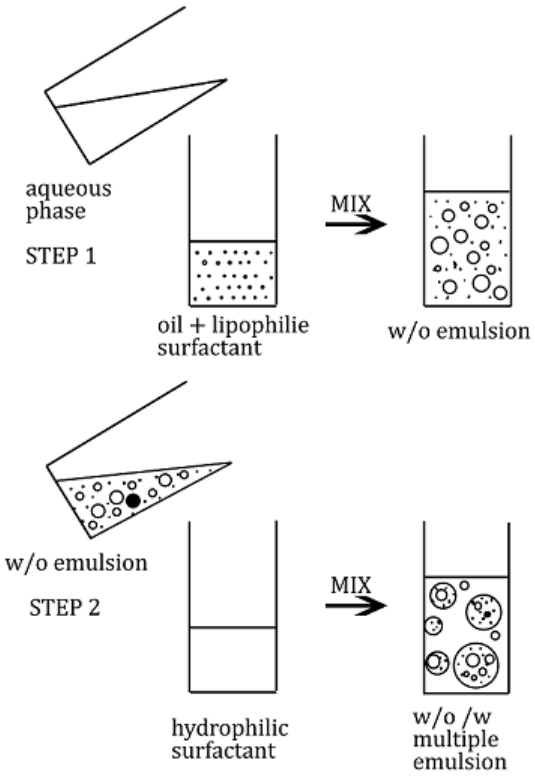

FIGURE 2.28: Two-step method to produce a multiple emulsion [332].

Multiple emulsions may also be obtained via a one-step process, prior to or as a result of a phase inversion [106, 333, 334]. In this case, the procedure begins with a continuous phase in which a pair of surfactants is solubilized; then, the dispersed phase is gradually added with sustained agitation. Depending on the average HLB of the surfactant pair and its concentration, a drop-in-drop structure may be readily obtained at low dispersed phase fraction [106]. This type of morphology is sometimes considered "unstable" and the addition of further dispersed phase gives rise to a catastrophic phase inversion to the normal reverse emulsion. For this structure to be possible, the weighed HLB should favor the stability of the continuous phase inside the dispersed one, of which there is not enough volume to become continuous and satisfy Bancroft's rule. Remarkably, Jahanzad et al. [320] have shown

that, for an O/W emulsion produced after the inversion of an O/W/O system, the average particle size is always lower than when produced by a direct emulsification method (and the size difference is greater as surfactant loading increases). This gives abnormal emulsions an interesting application if fine dispersions are targeted.

According to Morais et al. [334], stable multiple emulsions may be produced in one step by adding dispersed phase to a normal emulsion (continuous phase plus dissolved surfactant mixture) and subsequently crossing the PIT threshold. The combination of both catastrophic and transitional phase inversion (at a suitable HLB) may produce a stable multi-emulsion as a result continuous phase being transferred across the interface, which is deemed possible due to the very low interfacial tension at the PIT.

The relationship between operating conditions and the final emulsion structure obtained with the methods of Sajjadi et al. [106] and Morais et al. [333, 334] is discussed in the next section. It should be noted, nevertheless, that the experimental procedures reported by these authors were conducted without keeping a constant total volume, which is at least questionable in stirred systems. Moreover, their manufacture procedure requires a precise mixture of two types of surfactants. In this line, the work by Hong et al. [343] shows that stabilized multi-emulsions are obtained just as easily with one single surface-active species, if an amphiphilic block copolymer is used (although they reported the preparation of samples of only 4 ml).

In a more targeted procedure, originally developed by Utada et al. [344] and later continued by others [331, 345, 346], double or multiple emulsions may also be obtained with specific inner structures, using microfluidic capillary devices. This approach generates the emulsion structure by "forcing" part of the continuous phase (or sometimes a third phase) directly inside the dispersed drop. Unlike the previous methods, this one enables a much precise control of inside-drop dispersity. However, it is much more goal-specific and requires expertise in microfluidic device managing.

2.5.3 Effects on main variables in morphology and inversion point

Sajjadi and coworkers studied the influence of surfactant concentration [347] and its HLB [337] on the structure of the O/W/O emulsions (prior to the catastrophic inversion to O/W). The main conclusions of their work are summarized in what follows:

1. Larger drops usually accommodate a higher number of internal droplets (at a given system composition). More but smaller occlusions are observed with increasing ϕ_d and increasing surfactant concentration.

2. For a constant drop size, the number of internal droplets increases as the surfactant

concentration increases.

3. At low surfactant concentrations, the internal phase volume ratio (volume of entrapped droplet/volume of dispersed drop) does not change considerably with ϕ_d. Conversely, at higher surfactant loadings, more occluded droplets are found when increasing ϕ_d.

4. There is a minimal drop size below which little continuous phase is entrapped. This critical size decreases when increasing surfactant concentration.

5. High surfactant loading yields a bimodal size distribution of internal droplets. The work by Liu et al. [348] also added that it may lead to a radical change in the emulsion structure, going from micellar to hexagonal liquid crystal.

6. Phase inversion occurs at lower values of dispersed phase fraction as surfactant loading increases (a natural consequence of conclusion 1).

7. At a high surfactant concentration, most occluded droplets remain unchanged in size after PI has occurred.

8. The number of occluded droplets increases with decreasing HLB values (at constant loading). As a natural consequence, PI occurs at lower HLB values at constant ϕ_d (note that the system under study is an O/W/O with HLB values always higher than the transitional threshold, where O/W is the preferred structure). This conclusion has also been reached for W/O/W emulsions by Tyrode et al. [349] by clever conductimetric measurements.

9. Larger internal droplets are found with increasing HLB.

10. PI points are modified by the surfactant's chain length distribution. Their results show that a broader distribution caused a delayed PI, because of the preferential solubility in the oil phase by the short-chain homologues. Yet, only two systems were compared, thus limiting the conclusion on the direction of change in the PI point.

In turn, Jahanzad et al. [320] have partially proven that the inner droplet size distribution is mainly the result of a surfactant concentration gradient between oil and water phases, at least in batch systems. In continuous operation, Tyrode et al. showed that it also depends on the rate at which dispersed phase is added to the emulsification vessel [349]. Regarding the viscosity ratio, Liu et al. [348] concluded that an increase in the dispersed-phase viscosity leads to fewer occlusions, which is in line with the mechanism outlined by Kumar [66].

2.5.3.1 Catastrophic vs transitional inversion and the role of multiple emulsions

Sajjadi et al. [350] have revealed an interesting behavior of multiple emulsions when subject to a decrease of the average HLB at constant ϕ_d. In most inversion maps, varying the HLB

parameter yields a transitional PI; however, the authors managed to track the evolution of the emulsion structure at a close range of the transitional inversion threshold, and noticed that the emulsion goes through a catastrophic inversion before undergoing the expected transitional process. Path B in Figure 2.29, reproduced from the original paper, depicts this scenario.

The explanation is as follows: a multiple emulsion (for example O/W/O) with constant dispersed water fraction will present a number of occlusions that depend on the average HLB, being higher at lower values of this parameter [337]. This means that a decrease of HLB will produce higher effective dispersed fractions (water + occluded oil phase), which is comparable to an increase in water phase fraction at constant HLB. Hence, coalescence is expected to be stimulated and PI may occur, not as a result of affinity changes of the emulsifier, but rather as an imbalance between break-up and coalescence, enhanced by the occlusion process that is a consequence of interfacial fluctuations. Yet, the W/O emulsion formed this way will present a near-ultralow interfacial tension and is prone to go through a transitional inversion at a slightly lower HLB. These studies have shown that, in fact, catastrophic phase inversion should be associated with the coalescence vs break-up rates rather than only with an increase in dispersed phase fraction.

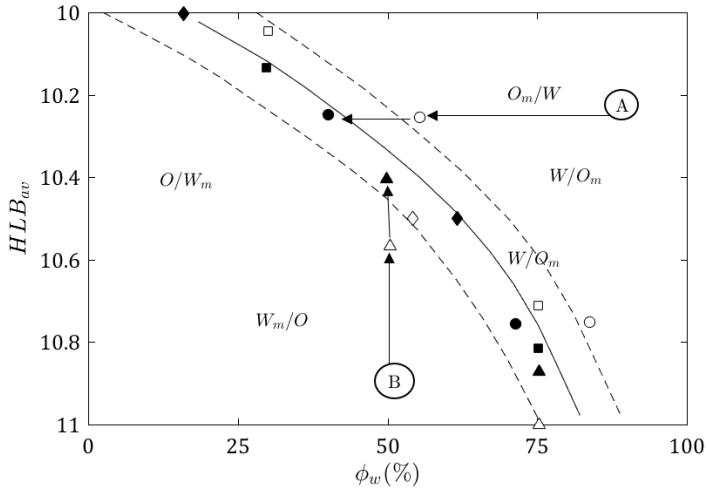

FIGURE 2.29: Catastrophic phase inversions at the vicinity of the transitional threshold for a cyclohexane/water emulsion with 2%wt NPE5/NPE12 at 22°C [350]. Solid curve shows the threshold of transitional inversion and the dotted lines are the boundary of the catastrophic inversion from abnormal to normal morphology. In each case, white symbols represent a catastrophic inversion and black ones, a transitional one. The approach direction is given always from white to black, as represented by the A and B examples.

In turn, numerous examples of a drop-in-drop structure have been reported in polymer-polymer or polymer-solvent-polymer systems. Most often, they are reported for extruded blends, such as the SAN-PS-(PMMA-b-PS) by Adedeji et al. [152], a PSU-PA by Charoensirisonboon et al. [153], a PP-PA by Hietaoja et al. [70], and the PA-SAN by Kitayama et al. [85]. There are also reports of a water-PU emulsion by Saw et al. [351] and the well-known

case of the in-situ formed occlusions in the HIPS manufacture process, which is the study system of this thesis.

In all these cases, the particle-particle morphology holds a significant interest, since many mechanical properties strongly depend on their characteristics [352]. Here, the block or graft copolymers play the role of traditional O/W emulsifiers, as described in sections 2.2 and 2.4.4.1. These copolymers are either added intentionally or produced in-situ as part of the polymerization mechanism. Consequently, the concentration of such polymer species and its molecular-weight distribution affects the number of occluded particles inside the dispersed phase. For example, Leal and Asua [44] reported that the number of entrapped droplets increases when the concentration of chemical initiator increases (reproduced in Figure 2.30). This is because the chemical initiator used for the free-radical polymerization may induce the formation of graft copolymers, as is the case of the polymerization of styrene in presence of polybutadiene studied by the authors.

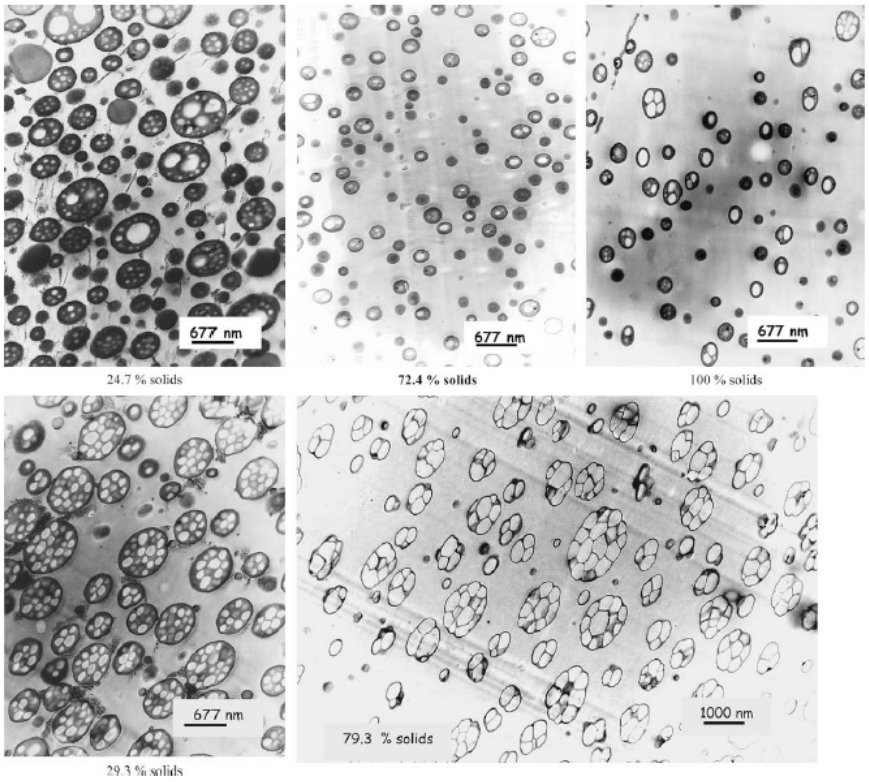

FIGURE 2.30: Effect of initiator concentration on the drop-in-drop structure. Upper figures: low concentration; lower figures: higher concentration [44].

2.6 Summary and conclusions

After having analyzed both the physical evidence and the mathematical models presented in the previous sections, the effects of phase viscosity, phase density, interfacial tension and surfactant properties on the phase inversion mechanism are summarized in Table 2.7. Since some of the models suggest different dependencies on some of these properties, this table should serve as a *general guide* while the real interdependence should be assessed on a case-by-case basis.

		Effect on				
		Break-up frequency ω_b	**Coalescence frequency** ω_c	**Average particle diameter**	**Number of (stable) occlusions**	ϕ_d **at PI**
An increase in	Stirring speed (N)	$\uparrow$	$\uparrow$	$\downarrow$ if $\omega_b \uparrow > \omega_c$ $\uparrow$ if $\omega_b \uparrow < \omega_c$	$\downarrow$ $\uparrow$	$\uparrow$ $\downarrow$
	Continuous phase density (ρ_c)	$\uparrow$ if turbulent break-up	$\downarrow$	$\downarrow$	$\downarrow$	$\uparrow$
	Dispersed phase density (ρ_d)	$\uparrow$	$\uparrow$	$\downarrow$ if $\omega_b \uparrow > \omega_c$ $\uparrow$ if $\omega_b \uparrow < \omega_c$	$\downarrow$ $\uparrow$	$\uparrow$ $\downarrow$
	Continuous phase viscosity(η_c)	$\downarrow$ if turbulent break-up	$\downarrow$	$\downarrow$ if $\omega_b \uparrow < \omega_c$ $\uparrow$ if $\omega_b \uparrow > \omega_c$	$\downarrow$ $\uparrow$	$\uparrow$ $\downarrow$
		$\uparrow$ if viscous break-up	$\downarrow$	$\downarrow$	$\downarrow$	$\uparrow$
	Dispersed phase viscosity (η_d)	$\downarrow$	$\downarrow$	$\downarrow$ if $\omega_b \uparrow < \omega_c$ $\uparrow$ if $\omega_b \uparrow > \omega_c$	$\downarrow$ $\uparrow$	$\uparrow$ $\downarrow$
	Interfacial tension (γ)	$\downarrow$	$\uparrow$	$\uparrow$	$\uparrow$	$\downarrow$
	Surfactant concentration	$\uparrow$	$\downarrow$	$\downarrow$	$\downarrow$	$\uparrow$
	Surfactant's HLB	$\cap$	$\cup$	$\cup$	$\cup$	$\cap$
	Relative permitivity (ϵ)	$\downarrow$	$\uparrow$	$\uparrow$	$\uparrow$	$\downarrow$

TABLE 2.7: Effect of main operating variables on the phase inversion mechanism as a general rule. $\cap$ and $\cup$ symbols indicate that the variable reaches a maximum or minimum value respectively

It is clear that the phase inversion phenomenon (both in O/W and polymer-polymer systems) is a very complex, multivariable, nonlinear process. Even though it has been studied in depth by many researchers, it has been mostly treated in a qualitative, descriptive way: the effect of the main operating variables on the PI point is rarely analyzed under a *ceteris paribus* condition, and is therefore troublesome to understand the real output and relative weight of each parameter. Moreover, when comparing results from different authors, care must be taken to ensure that all the operating variables in question are considered, since otherwise the resulting conclusions could be (at least partially) erroneous or misleading.

The analysis of each variable in isolation is a challenge, since it is empirically troublesome (or impossible) to generate liquid mixtures with all but one similar properties. The viscosity ratio is probably the best example: changing the viscosity of one phase is usually achieved by changing its composition (or choosing an entirely new fluid), which often yields a different density, interfacial tension or electrostatic behavior. Since the most widespread mechanism that explains PI is strongly based on the interfacial interactions (particle break-up vs coalescence), an unforeseen change in one operating variable may readily introduce an effect on the dynamics of the agitated system and completely alter the inversion point. Vessel geometry is also a good example: even the position of the impeller at the beginning of the experiment has proven to exert an effect on the PI point.

Regarding its mechanism, PI is most commonly explained through an imbalance between particle break-up and coalescence rates, the latter being much greater than the former at the onset of inversion. This approach has not been entirely validated since accurate measurements of these frequencies are an experimental challenge. Yet, this mechanism better explains the empirical evidence found when changing the emulsification route: the thermodynamic, energy minimization-based model does not account for dynamic nor initial-condition effects that could change the inversion point dramatically. Moreover, the conclusions of the energy-minimization model arise from theoretical considerations that lie on systems under thermodynamic equilibrium, which is not always the case – especially in polymer-polymer mixtures and in systems where PI occurs during a chemical reaction.

Interestingly, regardless of its mechanism, the PI process seems to strongly depend on one common feature: interfacial activity. The role of interfacial tension, and all the operating variables that modify it, is essential in determining which phase will invert at a given stirring speed. The presence of surface-active agents, in the form of emulsifiers, impurities, block or graft copolymers, can change the inversion point substantially, depending on their concentration and chemical structures. The affinity of these species towards a given phase usually determines that it will be preferred as the continuous one (provided that there is enough volume of it), which can be regarded both as a thermodynamic argument but also as being the result of interfacial curvature that favors one structure over the other. Moreover, the potential formation of drop-in-drop arrangements, for which interfacial tension (and electro-

static behavior) is a key variable, may favor the occurrence of phase inversion by increasing the effective dispersed volume fraction.

The formation of a preferred structure in O/W or polymer/polymer emulsions is essential in a number of industrial applications. Therefore, a better understanding of the phase inversion process seems vital, and developing representative mathematical models to predict it, a useful tool and a great challenge.

Chapter 3

Phase Inversion Prediction in O/W Systems

"To expect the unexpected shows a thoroughly modern intellect"

Oscar Wilde

Oil-water dispersions are present in a wide variety of industrial fields, from energy generation to food production. In most applications, the structure of the dispersion (*i.e.* which phase is continuous and which is dispersed) constitutes a strong constraint: the reversed dispersion (or emulsion) is undesired, for reasons related to each specific process. For example, in the transport of heavy oils, which usually flow with water present in the well, the W/O structure is considerably more viscous than the O/W counterpart, which impacts negatively in the energy requirements. Thus, the O/W is the sought dispersion. Therefore, predicting the phase inversion point for a given operational condition is of great interest, both in design and rating stages.

However, few mathematical models have been developed to predict such a point, perhaps the most interesting being those by Hu et al. [52, 79] for stirred tanks, and by Brauner and Ullmann [200] for transport pipe flow. While the work of these authors show that it is possible to fit their models to experimental data, they need to make simplifications to reduce the physical complexity of this phenomenon, which is multivariate and greatly non-linear, as discussed in Chapter 2.

The main obstacle that arises when trying to understand the effect of each variable on the PI point is that the experimental conditions vary significantly from author to author, so that isolating the weight of each variable is quite complex. However, this may be exactly the kind of problem that *machine learning* algorithms are suited for: generalizing implicit behavior difficult to understand at first hand [353, 354].

In this Chapter, the experimental results of phase inversion measurements present in literature are summarized and fed to four different models – from heuristic to black-box – in an effort to better understand the inversion phenomenon. To this end, two types of problems are treated: a **classification** and a **regression** one. The goal of the former is to predict which phase would be continuous at a given composition and operating condition; while that of the latter is to predict the dispersed phase volume fraction (ϕ_d) at which PI would occur for a given condition. The results of this work are published and available [355].

3.1 Relevant operating variables

As described in Section 2.1 several physical properties have an influence on the PI point: namely phase density, phase viscosity, and interfacial tension. Furthermore, the geometry used (vessel size, agitation speed, impeller type and size, number of baffles, their materials) can also contribute significantly on the inversion point. Even the initial conditions and the experimental procedure may exhert an effect [68]. In consequence, in order to prepare a predictive model it is necessary to analyze the available data and choose the input variables that may be considered the most relevant (both judging from availability and relative weight).

Table A.1, shown in the Appendix, gathers the experimental results of both the upper and lower bounds of the ambivalent ranges found in literature for stirred O/W systems. After analyzing the physical and geometrical conditions used in each investigation, the following set of variables was chosen to be used in the models that will be developed in this Chapter:

Physical properties	**Geometrical parameters**
Phase densities (ρ_o and ρ_w)	Number of baffles
Phase viscosities (η_o and η_w)	Impeller-to-vessel size ratio
and their ratio ($r_\eta = \frac{\eta_o}{\eta_w}$)	Type of impeller
Interfacial tension (γ)	Vessel material

TABLE 3.1: Variables chosen to buid the predictive models

The choice of viscosity ratio may seem unnecessary since it may be built from each phase viscosity. However, in the implementation of the regression algorithms, if the ratio is deemed an important variable, then it must be fed as such. This viscosity ratio has been extensively studied and considered an important variable on PI [65], but the viscosities of each phase (separately) play a major role on the break-up and coalescence rates, as was described in Section 2.4.4; then, the ratio alone does not suffice. Regarding interfacial tension, the values shown in Table A.1 correspond to either the ones informed in the authors' work or – in their absence – to the ones predicted by the Girifalco and Good [356] equation:

$$\gamma_{12} = \sigma_1 + \sigma_2 - 2\frac{4\sqrt[3]{V_1 V_2}}{\sqrt{\sqrt[3]{V_1} + \sqrt[3]{V_2}}}\sqrt{\sigma_1 \sigma_2} \tag{3.1}$$

where γ_{12} is the interfacial tension between phases 1 and 2, V is the molar volume and σ is the surface tension. This equation has the advantage of being simple enough to be implemented with the available information and has been found to provide good results with traditional O/W systems [69].

The ratio D_I/D_T is chosen as one of the most important geometrical variables because its effect on the energy dissipation rate has long been reported [357], and because other parameters are usually not informed by the authors. Moreover, gathered data refer only to stainless-steel impellers, ruling out impeller material as a variable.

3.2 Algorithms

Four techniques were selected to predict the experimental data presented in Table A.1, namely: a) decision tree, b) bagged decision trees, c) support-vector machine and d) feed-forward neural network. These techniques may be classified as *supervised learning* models, since they feed on a given dataset in order to "learn" the underlying structure of the data and provide a predictive output. The learning or *training set* is usually a subset of all the available data and is used by the models to fit their own predictions; the *testing* or *test set* is the remaining subset, and is used to measure the model performance with "new" data (information not seen by the model in the training stages). A brief overview of each algorithm is presented in what follows.

3.2.1 Decision trees

A decision tree is a classic heuristic model that may be used for both regression and classification problems. It is a simple model that may yield good performances with little training effort while providing the set of *if-then* rules inferred from the dataset. The complexity of the tree may be adjusted (usually through a "complexity parameter"): long trees with a large number of branches may improve the classification or regression accuracy, but almost certainly result in a loss of generalization capability, since each branch turns into a *particular case* rather than a *general rule* (which is known as "data overfitting"). There exists an optimum tree size that provides a good balance between accuracy and generalization.

The main drawback of a decision tree is its high sensitivity to the training set (what is known as high *variance*) [358]. To deal with this issue, bootstrap aggregating (*bagging*) trees

were developed. Essentially, this algorithm consists of a number of decision trees created in a way that each one has its own train/test subset of the formal training set [359]. Then, each tree is trained independently of the rest and, when presented with the formal test set, the outcome is the average of the prediction of each tree (for regression problems) or the majority vote (for classification goals). This compensates the variance problem but complicates the heuristic nature of the decision tree, by which interesting, useful rules may be inferred. However, some rule-extraction algorithms exist [360, 361] that may explain the general rules found by the ensemble of trees.

3.2.2 Support-vector machines

The support-vector machine (SVM) is a supervised learning algorithm that may be implemented for both regression and classification goals. In the first case, it is designed to find the smoothest function $f(x)$ whose images lie within a user-defined margin (ϵ) around the data points of the training set, x_i:

$$f(x) = \boldsymbol{w}^T \langle \boldsymbol{\psi}_{(x_i)}, \boldsymbol{\psi}_{(x)} \rangle + b \tag{3.2}$$

where $\boldsymbol{w}^T$ is a vector of weights, $\boldsymbol{\psi}_{(\boldsymbol{x})}$ is the non-linear mapping of the input space to a higher dimensional space ($\boldsymbol{\psi}_{(x_i)}$ refers to the map applied to the elements in the training set), b is the bias, and $\langle \cdot, \cdot \rangle$ stands for the dot product.

To this end, a certain number of training samples that lie *outside* the desired image region are used as pivot points (named *support vectors*) to determine the function that may accommodate the majority of the predicted values inside the ϵ margin region. This results in a constrained optimization problem usually expressed as in Eqs. 3.3 and solved using Lagrange multipliers.

$$\max \begin{cases} -\frac{1}{2} \sum_{i,j=1}^{n} (\alpha_i - \alpha_i^*) (\alpha_j - \alpha_j^*) \langle \psi_{(x_i)}, \psi_{(x)} \rangle \\ -\epsilon \sum_{i=1}^{n} (\alpha_i + \alpha_i^*) + \sum_{i=1}^{n} y_i (\alpha_i + \alpha_i^*) \end{cases} \tag{3.3}$$

where α_i, α_i^* are the Lagrange multipliers and y_i is the i-th element of the target vector. α_i, $\alpha_i^* \in [0, \mathcal{C}]$, with $\mathcal{C}$ being a regularization parameter that determines the trade-off between the flatness of the function $f(x)$ and error deviation (which is why this model is usually referred to as *ϵ-insensitive support-vector regression*).

The non-linear map $\boldsymbol{\psi}_{(x)}$ need not be known, since only the dot product $\langle \boldsymbol{\psi}_{(x_i)}, \boldsymbol{\psi}_{(x)} \rangle$ is actually computed. Then, kernel functions $k_{x,x_i} = \langle \boldsymbol{\psi}_{(xi)}, \boldsymbol{\psi}_{(x)} \rangle$ are used instead, the most frequent being quadratic, cubic or Gaussian. These are shown in Table 3.2, where λ is a scaling parameter.

Kernel type	**Kernel function**
Linear	$k_{(x_i,x_j)} = \frac{\langle x_i,x_j \rangle}{\lambda^2}$
Quadratic	$k_{(x_i,x_j)} = \left(1 + \frac{\langle x_i,x_j \rangle}{\lambda^2}\right)^2$
Cubic	$k_{(x_i,x_j)} = \left(1 + \frac{\langle x_i,x_j \rangle}{\lambda^2}\right)^3$
Gaussian	$k_{(x_i,x_j)} = e^{-\frac{\|x_i - x_j\|^2}{2\lambda^2}}$

TABLE 3.2: Typical kernel functions used in SVM models.

In classification problems, the SVM is designed to find a hyperplane that divides the dataset in two or more groups, each containing "only" the set of points belonging to a given class. The distance between the plane and the nearest sample points of each set is a margin that may be adjusted, and those points lying on the margin are the *support-vectors*. A schematic example is shown in Figure 3.1. The algorithm is also implemented as a constrained optimization problem, similar to the one described previously for the regression case, where a classification score is defined to represent the distance between an input and the hyperplane defined.

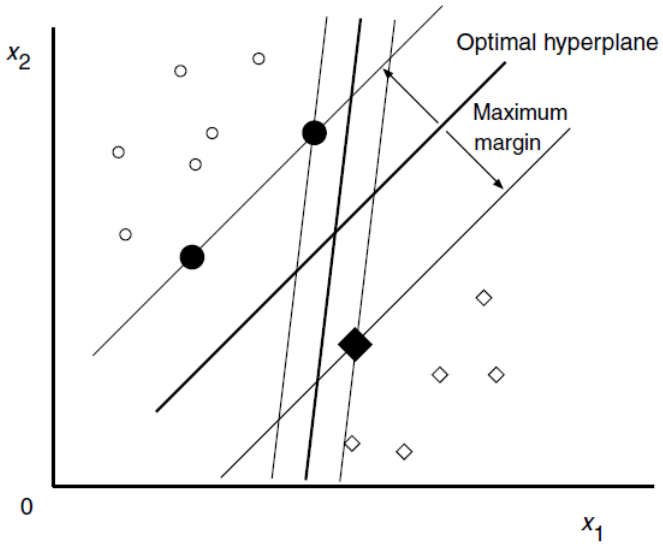

FIGURE 3.1: Optimal separating hyperplane in a 2D example [362].

3.2.3 Neural networks

Several types of neural networks have been developed over the years, from the simple perceptron to complex deep convolutional inverse graphics networks [363, 364]. For the purpose of this work, the standard feed-forward multilayer perceptron, with one or more hidden layers, is a suitable model. The idea behind this algorithm is to either classify or predict function values by using a matrix of weights (which are tuned to minimize prediction errors) and an activation function, which is any form of a sigmoid function that may mimic an "on-off" response in a continuous way. This enables the model to behave like the brain neurons, in the sense that each input variable (stimulus) produces a different effect (response) on each neuron, ultimately resulting in a combined response that produces the output.

Figure 3.2 shows a scheme of a traditional perceptron with three layers: the input layer, receiving the input variables, a hidden layer, where the effect of each input is combined and treated with the chosen activation function, and the output layer, which combines the effect of every neuron. In regression problems, in order to shift the output from the (0,0) coordinate, *bias* neurons are also introduced, usually before and after the hidden layer.

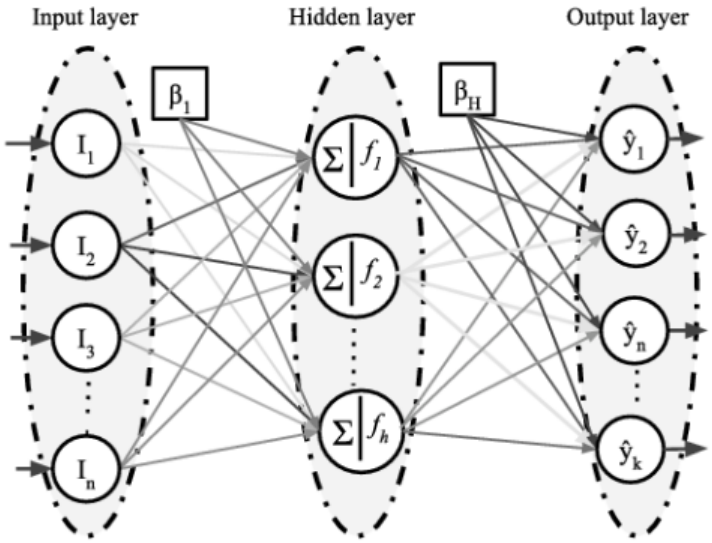

FIGURE 3.2: Scheme of a feedforward multiple perceptron.

The neural weights may be initialized randomly and then tuned with different training algorithms, trying to minimize the prediction errors. Among others, the most frequently used are [365]:

1. Gradient descent (GD)
2. Gradient descent with adaptive rate (GDA)
3. Scaled conjugate gradient (SCG)

4. Levenberg-Marquardt (LM)

5. Bayesian regularization (BR)

The GD method is perhaps the simplest of all. It may be applied as long as the derivative of the activation function exists. Essentially, this algorithm modifies the network weights by differentiating a cost function with respect to the neural weights in an efficient way known as *backpropagation*. Then, given a cost function to minimize, C, the rate at which this function changes with respect to a weight in a given layer is:

$$\frac{\partial C}{\partial w_{jk}^{l}} = a_{k}^{l-1}\delta_{j}^{l} \tag{3.4}$$

where l is the layer at which the neuron j is located, k is the neuron at the layer $l-1$ that is connected to neuron j, a_k^{l-1} is the result of the activation function applied to the k-th neuron, and δ_j^l is the error of layer l, defined as:

$$\delta_{j}^{l} = \frac{\partial C}{\partial \left(\sum_j w_{jk}^{l} a_{k}^{l-1} + b_{j}^{l}\right)} \tag{3.5}$$

This algorithm evolves in the direction of the gradient and updates each weight according to a constant training rate, η:

$$\Delta w_{jk} = -\eta \frac{\partial C}{\partial w_{jk}} \tag{3.6}$$

Once it reaches the maximum number of iterations, it stops.

The GDA method is a version of the GD algorithm that modifies the learning rate η at each step, according to the performance of the training, usually "slowing down" as the algorithm progresses. Several rate functions exsist, from step to exponential decays [366, 367].

The SCG method is a variant of the traditional conjugate gradient method, which is an algorithm suited for iteratively solving large systems of linear equations or unconstrained optimization problems. This method converges to the solution by following a gradient in a given search direction. The scaled variant introduces a scaling parameter that improves the search direction by means of a spectral formula [368]. For this method to be implemented, the matrix defining the search direction must be positive definite; if it is not, workarounds using a quasi-Newton BFGS approach are available [369].

The Levenberg-Marquardt algorithm can be viewed as a version of the traditional Gauss-Newon method, the difference being that it introduces the use of a damping parameter, λ, in the calculation. It computes the Jacobian matrix ($\boldsymbol{J}$) between the errors ($\boldsymbol{e}$) and the neural weights and updates the value of the latter using:

$$\Delta w = -\left(\boldsymbol{J}_k^T \boldsymbol{J}_k\right) + \lambda \boldsymbol{I})^{-1} \boldsymbol{J}_k \boldsymbol{e} \tag{3.7}$$

where $\boldsymbol{I}$ is the identity matrix.

When using the LM algorithm it is customary to separate a subset of the training data for a *validation* stage. The data in this subgroup is used to stop the training early if the performance is not improving after a given number of repetitions. This makes it a fast algorithm.

Finally, the BR method is implemented similarly to LM but also minimizing the value of the neural weights. The cost function to minimize is then:

$$C = \alpha E_w + \beta E_y \tag{3.8}$$

where E_w is the errors with respect to the weights and E_y is the sum of the square errors between the predicted and measured outputs. α and β are updated after each LM step according to the error of each step.

3.3 Implementation and results

In the implementation of the previously discussed algorithms, the dataset was divided randomly as follows: 70% for training, 10% for validation and 20% for testing. These subsets were kept the same throughout the procedure, so that comparing the results between each algorithm is done with the same testing set. The decision trees were coded in R while the SVM and neural networks were programed in Matlab R2019a ©.

3.3.1 Classification

In order to build the classification problem, the table of experimental data found in Table A.1 had to be filtered, since only a fraction of the entries share exactly the same operating conditions for both O/W→W/O and W/O →O/W inversions (for example, some authors only studied the lower bound of the ambivalent range, or used different stirring speeds between

the upper and the lower curves). For those data points where both inversions have been studied at the same conditions, a clear identification of three classes is possible for any phase composition: "oil continuous", "water continuous" and "not determined". Then, for this subset, which only contains the upper and lower bounds of the ambivalent range, any number of extra points may be added artificially (above, below, and between each curve), to create a new database that includes the phase behavior for each case, thus yielding the classification problem. Upon inspection, this filtered subset shared the same impeller type, number of baffles and equipment material; therefore, they were left out as input variables.

With this subset, 30 extra entries were added (10 for each class), by creating random artificial points above, inside and below the ambivalent range for each operating condition. The algorithms presented before were then implemented with this newly formed database.

3.3.1.1 Decision tree

A decision tree was trained to predict the phase behavior at a given condition, with a default *complexity parameter* (CP) of 0.01 using the *rpart* library in R [370]. This parameter reflects the extent of the tree branches and may be adjusted to optimize the trade-off between accuracy and generalization.

An overall accuracy of 81.% was obtained with the testing subset, with the confusion matrix shown in Table 3.4. A schematic figure of the tree, with its if-then rules is depicted in Figure 3.3. The classes were named **O** (for oil-continuous), **W** (for water continuous) an **ND** (for non-determined). The percentages shown in each box represent the fraction of data points from the test set that ended in each branch. Interestingly, with this complexity parameter, only three variables were used in the construction of the tree: ϕ_o, μ_o and D_I/D_T.

Upon optimization of the complexity parameter, a trade-off between accuracy and complexity (and strong overfitting) must be obtained. The goal is to arrive to a decision tree that may explain the problem as accurately as possible but with simple rules inferred by the most relevant variables. After analyzing trees with different complexity levels, the one shown in Figure 3.4 was found to be the optimum case, with a CP value of 0.007. The overall accuracy of 85.7%. An increase in both sensitivity and sensibility of the class "water continuous (W)" is observed.

The interesting feature of this second tree is that one may infer the following rules to determine whether the aqueous or the organic phase would be continuous. The intuitive rule (the phase whose volume fraction is above 0.5) almost never holds directly.

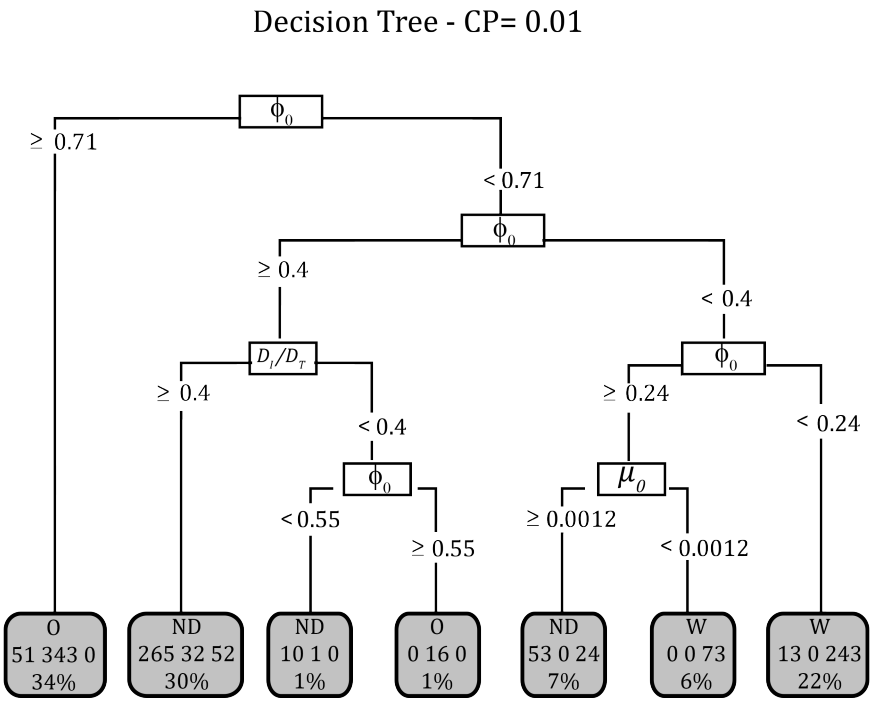

FIGURE 3.3: Decision tree to decide whether a given phase will be continuous.

1. If the organic phase volume fraction is above 70%, it is very likely (87% of cases studied) to be the continuous phase regardless of the operating conditions.

2. The organic phase shall be continuous following the intuitive rule ($\phi_o > 0.5$) only if the size of the impeller is at most 40% the size of the vessel. This may imply that a rather inefficient mixing (small impeller) is related to the inability of the dispersed phase to become continuous, perhaps due to lack of turbulence which produces few occluded droplets and deters phase inversion at low holdups.

3. In contrast, if the organic phase is the one in higher proportion but larger impellers are used ($D_I/D_T > 0.4$), then it is almost never the continuous phase. The only case possible for it to be continuous is to have a very large density difference with the aqueous phase (notice the $\rho_o > 1398$ kg/m^3 condition). This again may reflect the same effect described in the previous rule: the increase in turbulence provided by a bigger impeller – which would promote breakage, coalescence and occlusion formation – may be countered by a very high momentum of the continuous phase, thus disabling the aqueous phase to become continuous. In all other cases, either the aqueous phase is continuous, or the result is undetermined.

4. If the aqueous phase volume fraction is above 76% then it will be the continuous phase almost without question. There is only one exception that yielded a "not determined"

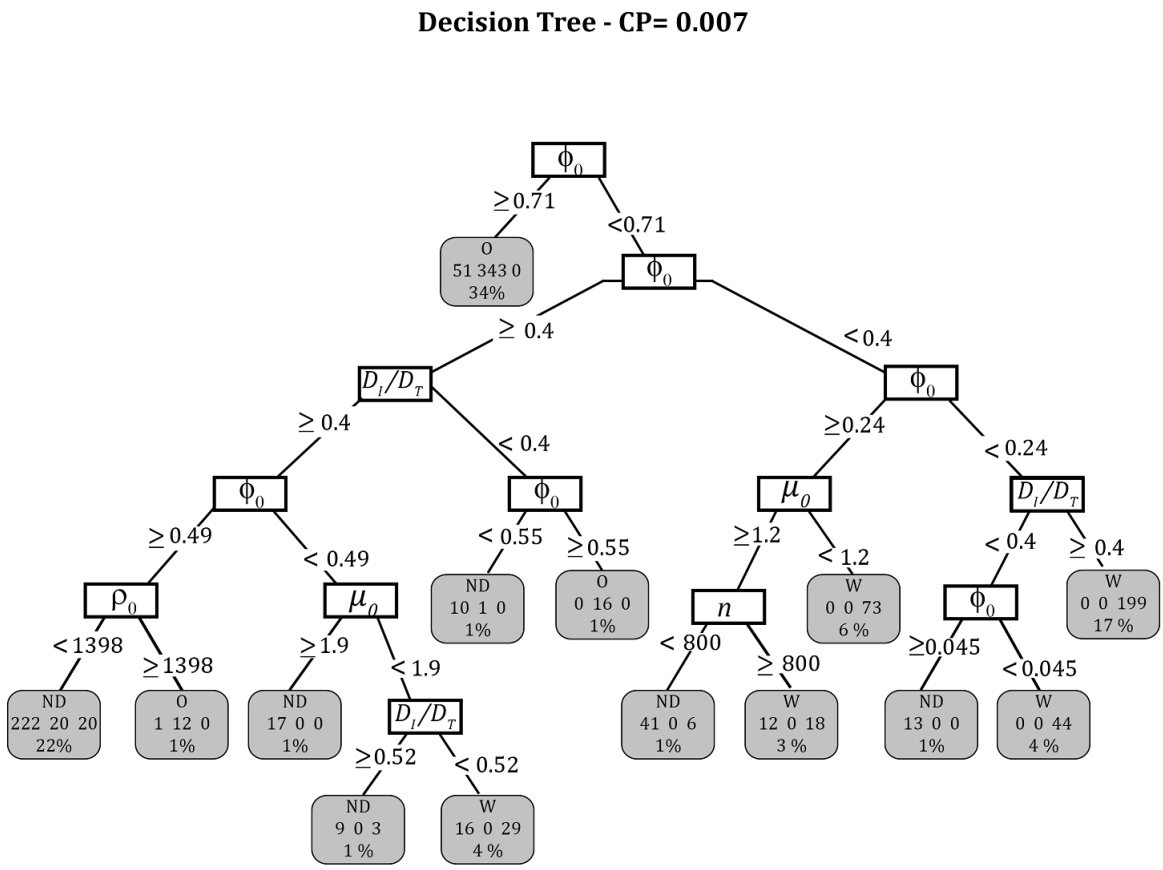

FIGURE 3.4: Optimum tree, pruned with a CP of 0.007.

case (notice the $0.4 > \phi_o \geq 0.045$ branch) which, upon verification of the dataset, refers to a very particular mixture of kerosene/water with a very low interfacial tension (≈10 mN/m) by Arashmid and Jeffreys [74] and a small impeller ($D_I/D_T < 0.4$). This means that the effect of poor mixing was countered with a very low interfacial tension, which enhanced particle break-up and coalescence to a point that the only way to ensure an aqueous continuous phase is to have an extremely high fraction of it. Leaving this exception aside, then all dispersions with at least 76% aqueous phase will be O/W.

5. Finally, at an intermediate range of aqueous phase composition ($0.76 > \phi_w \geq 0.6$) the organic phase will almost surely be dispersed. If its viscosity is high enough, the probability of getting a "not determined" result somewhat increases, but an oil-continuous phase is never assured. More so, at high stirring speeds the aqueous phase is very likely to be the continuous one, since the attenuation of coalescence of viscous oil drops will deter the formation of W/O dispersions.

3.3.1.2 Bootstrap aggregation (bagging)

The former inferred set of rules may not be the only one, since different decision trees may be obtained varying the train/test subsets. For this reason, a bagging technique was implemented with 300 trees (after running with different number of trees, this number was found to be optimum). All variables were included in the analysis and a rule-extraction technique following Deng [361] was applied. Table 3.3 summarizes some of the rules found by this algorithm across the ensemble of trees. A total of 37 rules were extracted, but only the ones with no prediction error and simple enough not to be considered "special cases" are shown here.

	Condition	**Predicted continuous phase**	**Frequency (%)**
1	$\phi_w > 0.75$ & $D_I/D_T > 0.4$	W	17.5
2	$\phi_o > 0.74$, $\gamma < 50$ mN/m & $N > 700$ rpm	O	11.1
3	$\phi_w > 0.6$ & $\mu_o < 1.17$ cP	W	6.1
4	$\phi_o > 0.55$ & $D_I/D_T < 0.4$	O	3.1
5	$\phi_o > 0.5$ & $\rho_o > 1398$ kg/m^3	O	1.5
6	$\phi_o > 0.63$ & $D_I/D_T > 0.5$	O	1.5
7	$\phi_w > 0.5$, $r > 1.2$ & $N > 1274$ rpm	W	1

TABLE 3.3: Inferred rules from the ensemble of trees.

In general, the same pattern is observed in this set of rules compared to the ones obtained with one tree (some are even repeated, which is a good sign for the tree presented in the previous section): being in a greater proportion is not a sufficient condition to be the continuous phase. For instance, the first rule cited in the previous section has been extended to 100% accuracy by adding two constraints: low interfacial tension and high stirring speed (2nd condition in Table 3.3). As a general rule, with a volume fraction between 50% and 75%, there is a "turbulence constraint" needed to ensure that a given phase will be surely continuous. Otherwise, it would depend on how the dispersion was prepared and thus end up inside the ambivalent range.

A clear advantage of the ensemble model is that it outperforms one single decision tree in its classification goal (overall accuracy of 93.5%), as observed from the confusion matrix shown in Table 3.4.

		Reference								
		One tree CP = 0.01			**One tree CP = 0.007**			**300 bagged trees**		
Prediction		N/D	O	W	N/D	O	W	N/D	O	W
	N/D	74	7	25	73	5	12	88	3	6
	O	19	91	0	19	93	0	8	95	0
	W	5	0	73	6	0	86	2	0	92

TABLE 3.4: Confusion matrices for decision trees pruned at different complexity parameters and a bagging of 300 trees. Test subset is the same for all.

3.3.1.3 Support-vector machine and neural network

The last two techniques considered in this Chapter are not heuristic. Then, the analysis here offered is only related to their performance in their classification goal. For the SVM models, three kernels (apart from the simple linear one) were tested, since the problem is suspected to be strongly nonlinear and thus a transformation is required to generate a hyperplane such that the three classes become *separable*. The functions in question were quadratic, cubic and a radial basis (Gaussian). Their confusion matrices are reproduced in Table 3.5.

		Reference											
		Linear SVM			**Quadratic SVM**			**Cubic SVM**			**Gaussian SVM**		
Prediction		N/D	O	W	N/D	O	W	N/D	O	W	N/D	O	W
	N/D	81	10	12	88	6	12	85	5	5	88	9	8
	O	10	88	1	7	92	0	10	93	0	7	89	0
	W	7	0	85	3	0	86	3	0	93	3	0	90

TABLE 3.5: Confusion matrices for the support vector machine models with different kernels.

The best performance is offered by the cubic kernel, with an overall classification accuracy of 92.18%, which is still slightly below the performance of the bagging model.

Regarding the artificial neural network, the scaled conjugate gradient was implemented as training algorithm. Each training procedure was performed 20 times to account for the randomness in the initialization of weights. The activation function chosen was:

$$f(x) = \frac{2}{1 + e^{-2x}} - 1 \tag{3.9}$$

A total of four cases were compared, changing the number of neurons of the hidden layer. The general rule of thumb states that this number should be between the number of predictors and the size of the output vector; *i.e.*, in this case between 3 and 9. Thus, networks with 3 to 10 neurons were tested to assess the quality of this rule. Confusion matrices are shown in Table 3.6: the net with 7 neurons performed slightly better than the rest, but almost no difference is observed with the 5 or 10-neuron net.

		Reference											
		3 neurons			**5 neurons**			**7 neurons**			**10 neurons**		
Prediction		N/D	O	W	N/D	O	W	N/D	O	W	N/D	O	W
	N/D	75	16	11	86	5	13	83	9	14	81	7	6
	O	13	82	0	8	93	0	8	89	0	11	91	0
	W	10	0	87	4	0	85	7	0	84	6	0	92

TABLE 3.6: Confusion matrices for the neural networks with different hidden layer sizes.

Comparing the classification performances of all four implemented techniques, it would seem that the bagging model resulted in the most accurate one, followed closely by the cubic SVM, with the extra advantage of being able to put forward a set of physical rules behind the data. This is an interesting result since, in the past few years, this technique has left ground for the more sophisticated models, like artificial neural nets.

3.3.2 Regression

All four techniques compared for the classification case can be modified to behave as regression models, in this case aiming to predict the dispersed phase volume fraction at which phase inversion would occur. Since, as explained at the beginning of Section 3.3.1, some of the entries of Table A.1 correspond only to one of the two possible inversions, two different models had to be developed for each technique: one to predict the organic phase volume fraction at which the dispersion becomes oil-continuous (ϕ_o), and another one for the opposite inversion case (ϕ_w). The following paragraphs describe the results obtained with each model. In all cases, the performance is measured with the root mean squared error (RMSE).

3.3.2.1 Decision (and bagged) trees

The number of trees in the bagging models was set to 300, as in the classification problem. Results are show in Figure 3.5 and Table 3.7, where a comparison with the predictions by only one decision tree is offered. As observed, a slightly better performance is obtained with

the ensemble model for the O/W →W/O inversion but no improvement was gained for the opposite case.

RMSE	One decision tree	300 bagged trees
ϕ_w	0.0657	0.0712
ϕ_o	0.0637	0.0564

TABLE 3.7: Performance of each decision tree model.

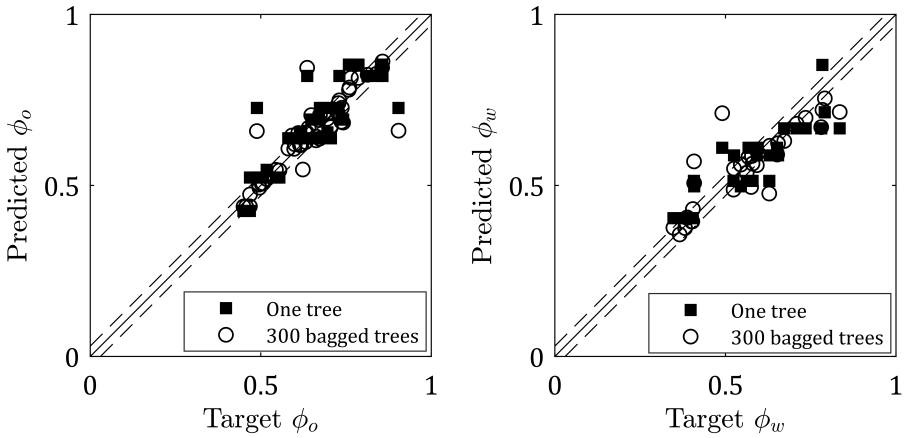

FIGURE 3.5: Prediction of PI points as per the decision tree models. Dashed lines represent a margin of ± 0.03, which is considered a suitable error gap.

3.3.2.2 Support vector regression

The ε-insensitive SVR model was implemented setting the cost factors ($\mathcal{C}$) and the margin of errors (ε) as shown in Table 3.8. Kernel functions and their scale parameters used are shown in Table 3.9, as well as their performance measured by the RMSE. Predicted phase volume fractions are shown in Figure 3.6. The quadratic kernel showed very good fit with both prediction sets (ϕ_o and ϕ_w), outperforming even the classic radial basis function. The fact that the kernel that gave better results is different from the classification problem is not surprising since the implementation algorithm and the dataset are different.

Prediction of	$\mathcal{C}$	ε
ϕ_w	0.1490	0.01490
ϕ_o	0.1291	0.01291

TABLE 3.8: Parameters used in the SVR model.

Kernel type	**Kernel function**	**Scale parameter**	**RMSE**	
			ϕ_o	ϕ_w
Linear	$k_{(x_i,x_j)} = \frac{\langle x_i,x_j\rangle}{\lambda^2}$	$\lambda = 0.4135$	0.0713	0.0858
Quadratic	$k_{(x_i,x_j)} = \left(1 + \frac{\langle x_i,x_j\rangle}{\lambda^2}\right)^2$	$\lambda = 0.3495$	0.0678	0.0570
Cubic	$k_{(x_i,x_j)} = \left(1 + \frac{\langle x_i,x_j\rangle}{\lambda^2}\right)^3$	$\lambda = 0.4703$	0.0821	0.0695
Gaussian	$k_{(x_i,x_j)} = e^{-\frac{\|x_i-x_j\|^2}{2\lambda^2}}$	$\lambda = 0.9$	0.0630	0.0717

TABLE 3.9: Kernel functions tested, their scale parameters and the performance of each model as per the RMSE.

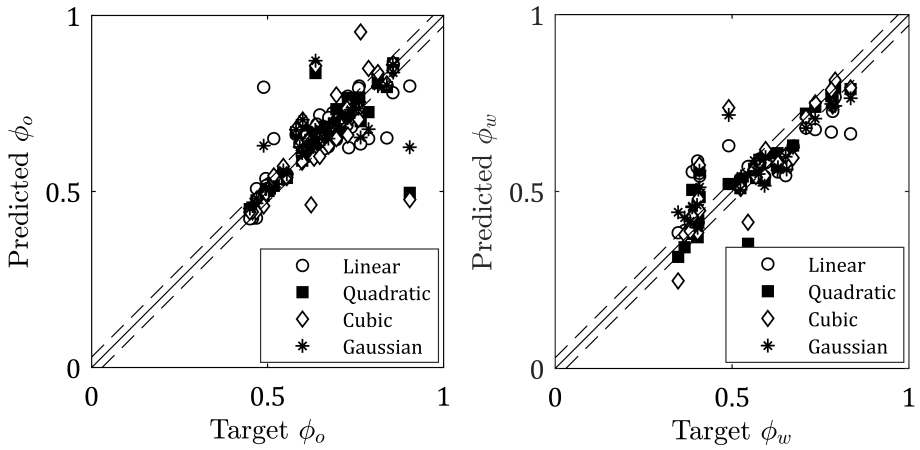

FIGURE 3.6: Performance of different kernel functions used in SVR algorithms. Test set is the same for all kernels. Dashed lines represent a margin of ± 0.03, which is considered a suitable error gap.

As in the classification problem, the bagging model slightly outperforms the SVM technique for both inversion curves.

3.3.2.3 Neural networks

A multiple perceptron with the traditional Levenberg-Marquardt training algorithm was implemented, using one or two hidden layers, as it shows good performance both interms of stability and calculation speed [371]. The effect on the number of neurons on each layer was analyzed to find an optimum network size, which may differ from the classification case. Due to the random initialization of synaptic weights, each net was trained and assessed 20 times and the best network (based on its performance with the test subset) was chosen for each

case. The activation function was kept as the one in Eq. 3.9.

The performance of each net is summarized in Table 3.10 and Figure 3.7, where an improvement is observed compared to the SVR and bagging models. Prediction of the PI point does not vary substantially with the number of neurons. Standard deviation of errors lie around 0.009 for the O/W→W/O inversion point and around 0.004 for the opposite case.

Number of neurons	**RMSE**	
	ϕ_o	ϕ_w
5	0.0556	0.0591
10	0.0537	0.0595
15	0.0532	0.0577
20	0.0533	0.0590

TABLE 3.10: Performance of each neural network.

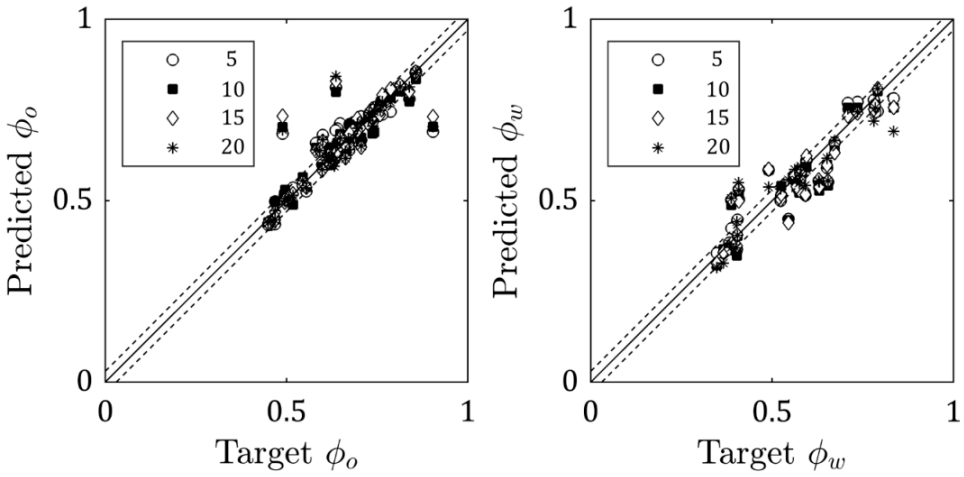

FIGURE 3.7: Prediction of each neural network with one hidden layer and varying number of neurons. Test subset is the same for all and the same for the other models in this work. Dashed lines represent a margin of ± 0.03, which is considered a suitable error gap.

A second hidden layer was added to test for any performance improvement, which is usual among nonlinear problems [372]. However, no significant change in the RMSE was observed compared to the one-layer case, as observed in Table 3.11. Therefore, adopting a 15-neuron, one-layered neural network seems reasonable for the prediction of each PI point.

	Neurons in 1st layer	Neurons in 2nd layer			
		2	4	6	8
ϕ_o	5	0.0554	0.0542	0.0537	0.0543
	10	0.0542	0.0551	0.0539	0.0539
	15	0.0569	0.0537	0.0531	0.0534
	20	0.0541	0.0537	0.0533	0.0539
ϕ_w	5	0.0585	0.0573	0.0586	0.0601
	10	0.0610	0.0536	0.0596	0.0569
	15	0.0590	0.0591	0.0590	0.0587
	20	0.0581	0.0610	0.0583	0.0592

TABLE 3.11: RMSE of the two-layered neural networks with the test set.

3.3.3 Theoretical predictions of the ambivalent range

Considering the good results offered by the neural net with 15 neurons in the hidden layer, this model was used to analyze the results of several hypothetical scenarios. The goal is to build a phase inversion map with the most relevant operating and geometrical variables. A base case was chosen fixing: $\rho_o = 800$ kg/m^3, $\rho_w = 1000$ kg/m^3, $\mu_o = 0.8$ cP, $\mu_w = 1$ cP ($r_\eta = 0.8$), $\gamma = 30$ mN/m, $D_I/D_T = 0.5$, Rushton turbine, 4 baffles, stainless-steel vessel.

Figure 3.8 shows the evolution of the ambivalent range when subject to variations in phase viscosity ratio (r_η), interfacial tension, phase density difference ($\rho_o - \rho_w$) and D_I/D_T, as predicted by the model. Some interesting remarks arise from these theoretical predictions by the net:

1. Increasing the phase viscosity ratio – $\frac{\mu_o}{\mu_w}$ as previously defined – widens significantly the ambivalent range, especially in the lower section of stirring speeds, which is in line with the empirical rule find by several workers [65, 79, 80] that states that "the tendency to remain dispersed increases with viscosity". Moreover, the curvature of both bounds changes significantly: for higher viscosity ratios, it appears to be easier for the W/O dispersions to invert to O/W (lower bound) when increasing the agitation rate, which is the opposite tendency at low viscosity ratios. But this is not surprising since the ambivalent ranges are plotted as a function of the organic phase volume fraction, ϕ_o,

and not a generic "dispersed phase". Then, if the dispersed phase is more viscous than the continuous phase, it will need higher agitation rates to be able to invert.

2. At very low interfacial tensions, the span of the ambivalent range is quite wide, especially at high stirring speeds. This is possibly explained by the fact that low interfacial tensions yield almost plane curvatures and so favor the formation of co-continuous systems [373] (with continuous phase entrapment), so that the dynamics of drop break-up and coalescence may favor either type of dispersion. This effect is particularly enhanced at high energy dissipation rates, where the occlusion formation is frequent (thus increasing the effective phase volume fraction), especially if the dispersed phase is the aqueous one [66]. At low rates, the W/O structure is apparently preferred.

3. Increasing the interfacial tension hampers the previous effect and thus O/W structures become more likely (oil drops are far less likely to entrap water droplets [91]), especially if the energy input is not high enough to compensate this effect.

4. A surprising effect is observed regarding the phase density difference: it is not a symmetric property, in the sense that two systems owning the same absolute difference do not invert at the same composition. Phase viscosity difference could be responsible for this behavior, but simulated results show otherwise, as observed in Figure 3.9, where the lower bound of the ambivalent range has been reploted as a function of the aqueous phase volume fraction. Increasing ρ_o shortens the span of the ambivalent range, implying that both structures are favored. The fact that this does not happen when increasing ρ_w may be due to the difference in the dynamics of the break-up and coalescence processes (and perhaps to the ability to form multiple dispersions).

5. The impeller-to-vessel size ratio is strongly nonlinear and, as it appears, not monotone. This parameter has a formidable effect on the mixing efficiency, through the energy dissipation rate. The break-up vs coalescence imbalance is greatly affected by the flow patterns throughout the vessel, thus producing different dispersion structures.

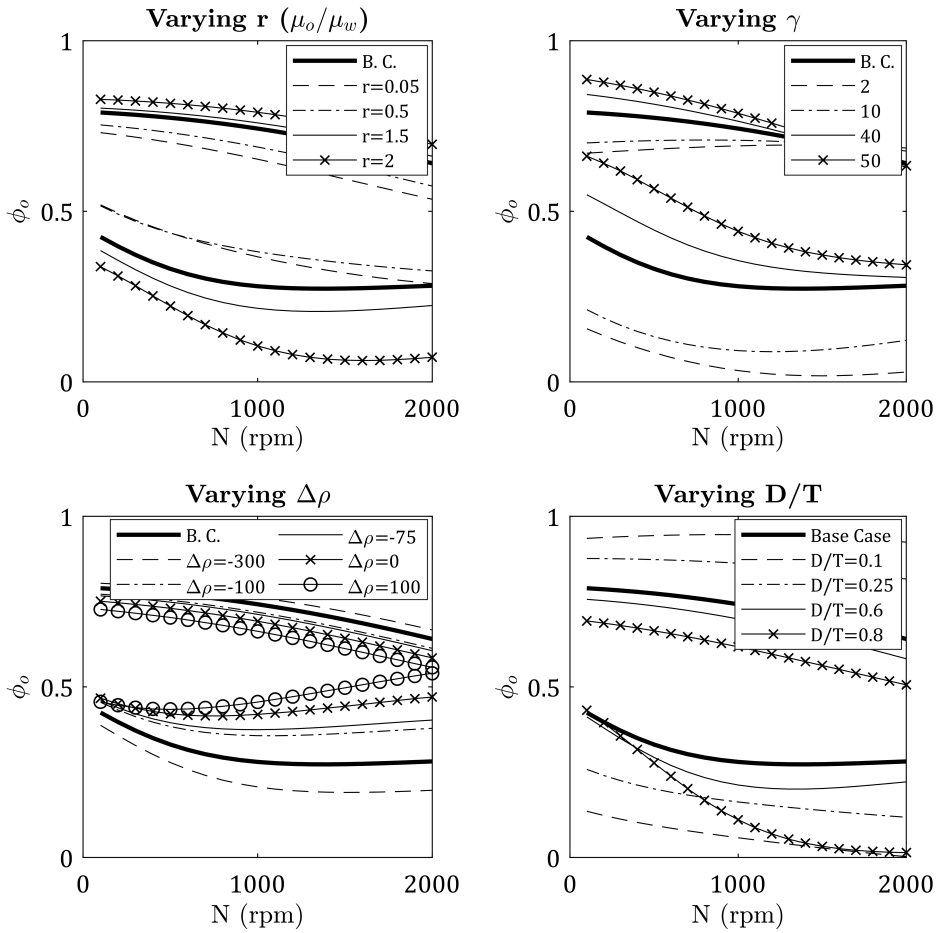

FIGURE 3.8: PI hypothetical map as predicted by the neural network model.

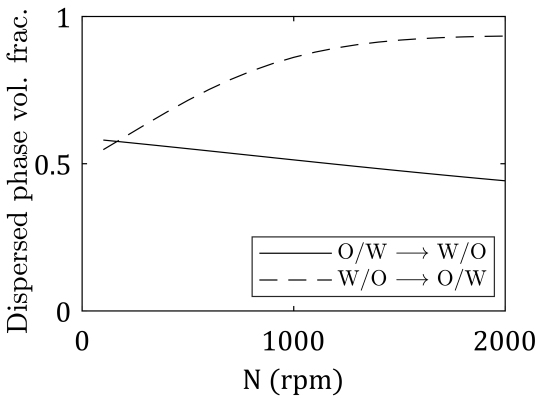

FIGURE 3.9: PI curves for systems having the same density difference and viscosity ratio.

3.4 Summary and conclusions

The phase inversion ambivalent curves presented in literature were simulated with different approaches, from heuristic to *machine learning* models. A decision tree with a manageable complexity level was presented, allowing to decide whether the aqueous or the organic phase will be the continuous phase under a given condition (only valid for stainless-steel, four-baffled vessels equipped with a Rushton turbine). The *if-then* rules inferred by the model were analyzed thoroughly and a physical explanation for the PI phenomenon was offered. More sophisticated classification techniques, like the support vector classifier and the multiple perceptron, which provide no heuristic rules, did not offer a differential improvement in the classification goal.

Among the regression techniques, the neural network multiple perceptron with 10 to 20 neurons in its hidden layer showed the best results in terms of its fit to the experimental data. The number of hidden layers was found not to be an important parameter of the model. Theoretical predictions were then made using theoretical values within the experimental range used to fit the network. This allowed to further understand the hidden mechanisms that lie in the phase inversion phenomenon with a tool capable of generalizing unseen behavior.

This model may continue to be perfected as new experimental findings are fed. It would be of interest to use it under particularly different conditions where phase inversion takes place, like polymer-polymer blends or polymer-solvent mixtures (for example, in the HIPS manufacture process), where phase viscosities are out of range compared to traditional O/W dispersions. Furthermore, it could be extended to O/W/surfactant systems, but it would require to fully characterize the structure of the surface-active components, as both its concentration and its hydrophilic-lipophilic balance (HLB) – or surface affinity difference (SAD) – have a major role in the PI point [337]. If enough information is gathered and used to train the neural network model, then a much complete, comprehensive idea of the phase inversion phenomenon could be achieved.

Chapter 4

Phase Inversion Prediction in the HIPS Bulk Synthesis: A Rheological Perspective

"You can cut all the flowers, but you cannot keep Spring from coming"

Pablo Neruda

High impact polystyrene (HIPS) is a heterogeneous thermoplastic that consists of a polystyrene (PS) matrix with dispersed polybutadiene (PB) particles which often contain occluded PS. Depending on the rubber particle size and the number of occlusions, two typical morphologies are usually identified: a "salami morphology" (large rubber particle with several occlusions) or a "core-shell morphology" (relatively small rubber particle with only one large occlusion) [374]. These structures provide the material with improved mechanical properties in comparison with general purpose PS, as discussed in Chapter 1.

The bulk HIPS polymerization process involves three main stages: a pre-polymerization of styrene (St), a finishing polymerization, and a devolatilization. The reacting system is homogeneous only up to 1-5% of monomer conversion [375, 376] (although these values were determined using blends, not actually measured during the polymerization), after which PS and PB are no longer miscible, and two phases are separated: a continuous PB-rich phase, and a dispersed PS-St phase [377]. Some authors refer to this system as a *polymeric oil-in-oil emulsion* [378]. Experimental studies – using mixtures of St, PS and PB – have shown that St is almost evenly partitioned between both phases [374] and that each polymer separates almost completely from the other [375], despite the high viscosity of the macromolecular species. This incompatibility between the PS and PB chains, which is predicted in the Flory-Huggins theory, can be improved with the presence of poly(styrene-*g*-butadiene) copolymers as shown by the measurements of St-PS-PB mixtures prepared by White and Patel [379].

The mechanism and conditions that dictate the phase separation of this system have not

been demonstrated yet. This reaction-induced phase separation (RIPS) may either follow a binodal or a spinodal decomposition [380] and, although some authors argue that it can only follow the spinodal line, [57–59] they report no actual measurements to support their views, which are often based on the curing reaction of epoxy resins. These reactions are performed without agitation and thus fail to provide the necessary energy input to favor nuclei formation (which is the accepted mechanism of binodal decomposition [380]), and so proceed following the spinodal. The pre-polymerization of HIPS is performed with intense agitation, which makes it essentially different from curing reactions. As stated by Ludwico and Rosen [377], standard agitators could easily supply the energy needed to cross the phase boundary.

As the polymerization continues to produce free PS and a graft copolymer (PS-g-PB), a critical point is reached where the PS content is such that the mixture undergoes a phase inversion process. Thereafter, the PS-rich phase becomes the continuous phase, and the morphology is essentially developed, making the PI point a key moment in the polymerization reaction. The finishing stage is carried out with gentle agitation – to preserve particle size and morphology – and at a higher temperature.

The PI process is affected by many parameters, such as phase viscosity ratio, phase volume fractions, rubber cis/trans content, stirring speed, reaction temperature, grafting efficiency (*i.e.*, the fraction of grafted St with respect to the total polymerized St), monomer conversion, PS and PB molar weights, etc., all of which have been described empirically by different authors [44, 50, 62, 157, 167, 378, 381, 382]. For instance, and as discussed in Chapter 2, in simple O/W systems it was found that the higher the viscosity of a given phase, the greater its tendency to remain as the dispersed phase [65]. In the polymerization of HIPS, this would imply that, for two St-PS-PB reacting mixtures with identical composition (same monomer conversion and same grafting efficiency), the one producing a PS with higher molecular weight would invert later, as its phase viscosity would be higher (note that an increase in the molecular weight of PS in the usual industrial range (120-300 kg/mol) [383] would not have any effect on the interfacial tension with PB [384]).

In turn, the role of copolymers on PI is not straightforward: on the one hand, an increase in copolymer concentration would stabilize the mixture by reducing the interfacial tension (as observed by Gaillard et al. [385]), thus producing a finer emulsion [386] and reducing its ability to invert. On the other hand, the compatibilizing effect would lower surface energies, reduce interface concavity, help to form a co-continuous mixture and thus favor phase inversion. These two opposing effects (increase in compatibility vs decrease in particle size) are not always considered, but have already been observed by Willemse et al. [387].

Regarding particle morphology, several authors have suggested global relationships between particle size and variables such as stirring speed [51, 388], initiator concentration [44, 389], rubber molecular weight (or rubber-phase viscosity) [51, 390], grafting efficiency

[44, 47] and apparent viscosity [47]. Some efforts have been conducted to model the evolution of particle morphology during the polymerization [57, 59], but are quite constrained to several theoretical simplifications. The influence of particle morphology in the final material properties is well-known [391, 392] and this highlights the importance of understanding and predicting the PI point. It is of industrial interest to optimize current synthesis recipes, improve production performances, and reduce unnecessary costs while keeping high product standards: a full chemical engineering challenge.

The experimental detection of the PI period remains a challenging and unresolved problem. Direct observation by electron microscopy is not possible because the monomer present in the sample evaporates during its preparation, meaning that adequate samples are impossible to produce with the present cryogenic microtome technology. Thus, only monomer-free (or "unswollen") particle morphologies have been observed by TEM [44, 47, 61]; and the preferred method for detecting the PI point is based on the apparent viscosity reduction [381]. After phase separation and before the PI point, the continuous rubber-rich phase is usually more viscous than the dispersed PS-rich phase (since normally the rubber molecular weight is higher than that of the free PS). During the inversion transition, while the vitreous (less viscous) phase is becoming the continuous one, the global apparent viscosity first drops, and then increases again after the inversion is completed. As described in Section 2.3 the viscosity of an emulsion depends on several variables, such as phase volume fractions, interfacial tension, and particle size, all of which are difficult to measure along the reaction. Published mathematical models (see Section 4.3) are incapable of accurately estimating the evolution of the apparent viscosity of the HIPS reacting mixture along the prepolymerization.

Regarding the theoretical prediction of the inversion point, some mathematical models have been developed, as discussed in Chapter 2, but are almost exclusively for traditional oil/water, non-reacting systems. For polymer mixtures, most of them refer to polymer-polymer blends in molten state (usually during extrusion operations), which is not the case of the HIPS pre-polymerization. In those models, the PI point is unequivocally determined by the phase viscosity ratio, which is – at least – an oversimplification of this multivariate phenomenon. Few models of the PI process *during* the HIPS polymerization are available. For example, that of Fisher and Hellmann [61] is a coupled kinetic-rheological model with simplified polymerization kinetics that assumes that PI occurs at equal phase volumes and is fitted with experimental data unusual for industrial conditions (PS molecular weight ($M_{w,PS}$) of 27 000 g/mol). The one developed by Vonka et al. [57] is thermodynamically-based (which neglects the fluid-dynamic effects) and lacks the ability to predict PI under different conditions (retuning of parameters is needed even with small changes in the reaction recipe).

In this Chapter, a new insight on the physics that govern the occurrence and duration of the inversion process during the HIPS pre-polymerization is offered. This is achieved by studying the effects of the main reaction variables on the evolutions of the apparent viscosity

and the particle morphology. Several experiments are conducted involving different reactor conditions, such as temperature, initiator concentration, and stirring speed. The following variables are measured along the reaction: conversion, grafting efficiency, PS molecular weights, morphology, and apparent viscosity. Based on theoretical and empirical aspects regarding the rheology of emulsions, a new empirical model is developed for predicting the evolution of the apparent viscosity of the reacting mixture as a function of phase viscosities, before and after the PI point. The results of this work are published and available [166].

4.1 Experimental work

4.1.1 Materials

Styrene monomer was purchased from Plastiformas (Monterrey, Mexico), polybutadiene UBEPOL was provided by Mitsubishi (M_w = 610 000 g/mol, M_n = 210 000 g/mol, high cis) and both of them were used as received. The chemical initiator, benzoyl peroxide (BPO) with a purity > 98% was purchased from Fluka and recrystallized from a methanol/chloroform mixture. Solvents N,N-dimethylformamide (DMF, anhydrous grade), methylethylketone (MEK, ACS reagent) and tetrahydrofuran (THF, HPLC grade) were purchased from Sigma-Aldrich and used as received.

A 3.8-liter stirred stainless-steel Parr reactor (Series N° 4550, model 4843) with an external heating jacket, and an anchor-turbine stirrer was used in all the pre-polymerization experiments, while glass ampoules were preferred for the finishing stage.

4.1.2 Synthesis of HIPS

Eight polymerizations reactions of St in the presence of PB were carried out varying the pre-polymerization conditions (temperature, agitation rate and initiator concentration) as shown in Table 4.1. All pre-polymerization reactions were carried out at 6%-wt of PB and performed up to a 30% conversion, using BPO for chemical initiation. First, the PB was dissolved in styrene monomer at room temperature for 12 h. Then, the initiator was incorporated into the reactor. The reactor was sealed and pressurized to 100 psi, stirred at the desired speed (using an anchor-turbine configuration) and heated from room temperature to 80 or 90°C at 2°C/min. Once the desired temperature was reached, the reaction continued under isothermal conditions (no significant heat generation was observed). The finishing stage was carried out in glass ampoules which were placed into a stainless-steel reactor under 100 lb inert atmosphere, at 150°C and lasted at least 12 hours to ensure full monomer conversion. All stages, including rubber dissolution; were performed under a nitrogen atmosphere to

prevent photo-oxidation.

Run	[BPO] (%wt)	T (°C)	Stirring speed (rpm)
1	0.05	80	30
2	0.1	80	30
3	0.05	90	30
4	0.1	90	30
5	0.05	80	60
6	0.1	80	60
7	0.05	90	60
8	0.1	90	60

TABLE 4.1: Recipies of the performed polymerizations.

4.1.3 Characterization

Samples were taken along each reaction to determine monomer conversion, St grafting efficiency, molecular weight distributions, apparent viscosity and, in some cases, to analyze their morphology. A small amount of hydroquinone was added to every sample immediately after being taken to deactivate the propagating chains while they were introduced in dry ice to lower their temperature. Samples taken for calculating monomer conversions were dissolved in toluene and stirred during 12 h. Then, St was isolated from the polymeric sample by precipitation in methanol. Solids were filtered and vacuum-dried at 50°C until constant weight.

Free PS was isolated from the rest of the polymeric species by solvent extraction, using a MEK/DMF 50:50 (volume ratio) mixture. After a 12 h agitation, the mixture was centrifuged at -20°C for 4 h at 10000 rpm. The insoluble precipitate obtained (namely PB and PB-g-PS) was vacuum-dried at 50°C until constant weight. The soluble free PS was precipitated in methanol, filtered and vacuum-dried at 50°C until constant weight. The grafted PS mass was obtained from the difference between the insoluble mass and initial PB mass and the St grafting efficiency was obtained from the ratio between the grafted and total bound St masses.

The molecular weight distributions and average molecular weights of each polymeric components were determined by size-exclusion chromatography (SEC) at room temperature using a Waters 1515 chromatograph fit with a set of μ-Styragel columns and a differential refrac-

tometer detector Waters 2487 employing THF as carrier solvent. A "universal" calibration was obtained from a set of PS standards.

Apparent viscosity was measured with a Brookfield LVTDV-II viscometer, using a LV N°4 spindle at four different shear rates: 0.063, 0.126, 0.316 and 0.632 s-1 at 25°C. Viscosity of PB-St solutions of varying concentrations were also measured with this device at the same shear rates, but using the LV N°1 spindle, suited for lower viscosities.

Finally, the morphology of selected samples was examined by a scanning transmission electron microscopy (STEM) on a JEOL JSM-7401F at 30 kV. Samples were prepared by an ultramicrotomy technique and stained with osmium tetra-oxide (OsO_4) vapors.

4.2 Experimental results

4.2.1 Polymerization kinetics

Figure 4.1 shows the effects of BPO concentration, reaction temperature, and stirring speed on: (a) the monomer conversion (x), (b) the weight-average molecular weight of the free PS ($M_{w,PS}$), and (c) the grafting efficiency (ζ). The evolution of all three variables resulted as expected from this type of polymerization [389, 393] (ignoring the isolated outliers of subfigure (b)): regardless of stirring speed, the reactions with the lower initiator concentration produced polymers of higher molecular weights and lower grafting efficiencies.

It appears that temperature has a greater effect on grafting efficiency than on molecular weight, while the opposite is observed with the initiator concentration. This is due to the fact that the reactions involving an attack on the rubber are more thermally activated than the initiator decomposition [393]. Stirring speed showed no appreciable effect on either variable. Grafting efficiency measurements are somewhat scattered around a mean, which is usual given the empirical uncertainties that arise from the extraction technique (before PI, the amount of graft copolymer is not substantial and after PI, it is difficult to extract the occluded PS from the PB-rich droplets, thus producing an error by excess [32]).

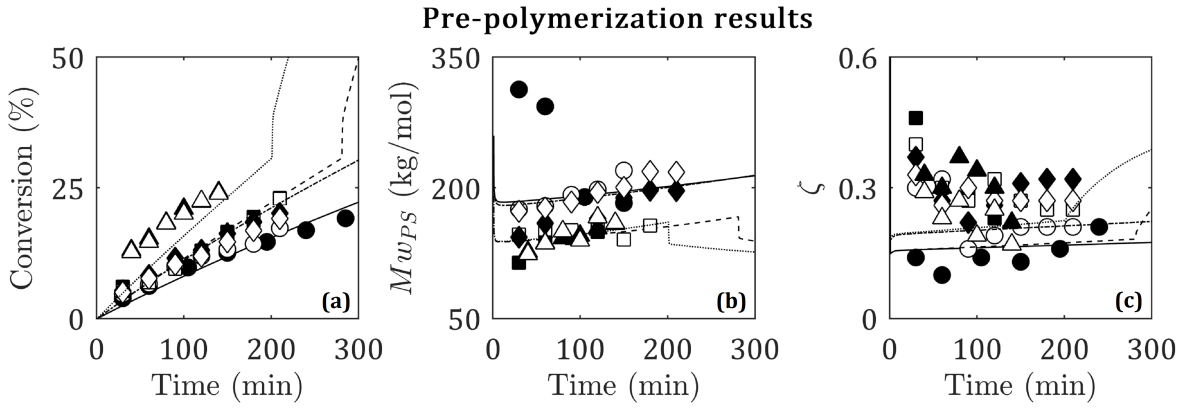

FIGURE 4.1: Effect of the BPO concentration, reaction temperature and stirring speed on the time evolution of conversion (a), PS Mw (b), and grafting efficiency (c) in pre-polymerizations carried at 80°C and 90°C, at 30 rpm. Markers refer to each reaction as follows: circles, 0.05wt% and 80°C; squares, 0.1wt% and 80°C; diamonds, 0.05wt% and 90°C; triangles, 0.1wt% and 90°C. Black markers: 30 rpm and white markers: 60 rpm. Lines correspond to the predicted evolution according to the polymerization model.

4.2.2 Phase inversion points

Figure 4.2 compares the evolution of the apparent viscosity of the polymerizing mixture for the investigated stirring speeds. For all other conditions held constant, the increase in agitation produced mixtures with lower viscosity, except for reactions 3 and 7 (90 °C, 0.05%wt BPO), which showed almost no change. Moreover, all reactions at 30 rpm followed an almost identical evolution before PI, and separated in two groups after PI: a high-viscosity one (associated with the higher $M_{w,PS}$ of reactions 1 and 3, both with 0.05%wt BPO) and a low-viscosity one (in line with the low molecular weights of reactions 2 and 4, which were run with 0.1%wt BPO). At 60 rpm, all curves seem to differ, both before and after PI. Sorted in descending order, the viscosity curves would correspond to the following reacting conditions: low temperature, low [BPO] > low temperature, high [BPO] ≈ high temperature, low [BPO] > high temperature, high [BPO].

This behavior should be explained by a change in the average droplet diameter: an increase in agitation may favor both coalescence and particle break-up, depending on the dispersed-phase fraction, stabilizer/emulsifier concentration and global physical properties [394, 395]. In this case, it is likely that, given the low values of stirring speeds and the high volume fraction of dispersed particles (both before and after the PI), the increase in stirring speed has favored coalescence over break-up, producing larger particles and, in consequence, a lower apparent viscosity [161]. The only reaction that showed little variation in viscosity with stirring speed is the one carried out at 90°C and 0.1%wt BPO; in this case, the increase in the coalescence rate may have been counteracted by a reduction in the interfacial tension caused by an increased grafting efficiency and molecular weight. The role of copolymers on interfacial

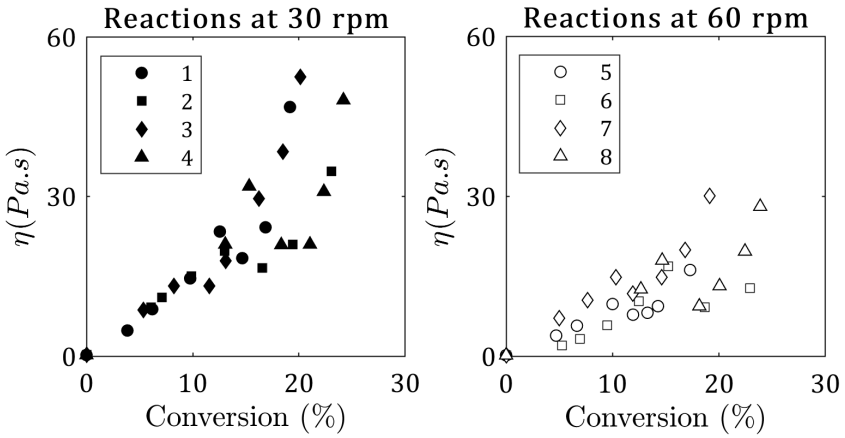

FIGURE 4.2: Apparent viscosity of the prepolymerizing mixture as a function of monomer conversion. Markers refer to reaction number as defined in Table 4.1.

properties and mean particle diameter has been previously reported [396], and the present results seem to indirectly support the following: an increase in either the concentration or the molecular weight of the grafted PS reduces interfacial tension (up to a limit) and produces smaller particles.

Regarding the PI point, no major effect is observed between the two stirring speeds, except perhaps in the 80°C and 0.05%wt BPO reactions. Molau and Keskkula [378] reported that agitation speed is vital to ensure phase inversion, but does not necessarily affect its dynamics (a higher stirring speed will not automatically promote an earlier inversion and vice versa). The PI periods for each run were estimated from the apparent viscosity local maximum and minimum for each case, and summarized in Table 4.2.

T	**[BPO]**	**Stirring speed (RPM)**	
(°C)	**(%wt)**	30	60
80	0.05	12 - 15 %	10 - 14 %
	0.1	13 - 17 %	15 - 18 %
90	0.05	10 - 12 %	10 - 12 %
	0.05	15 - 18 %	15 - 18 %

TABLE 4.2: Inversion periods (in % of styrene conversion) for each run.

Figure 4.3 shows a closer view of the phase inversion paths for each reaction. For the investigated temperature range, the BPO concentration considerably affects the molecular weights of the synthesized PS and, consequently, the mixture viscosity. The beginning of the PI process seems to depend strongly on the coupled effects of initiator concentration and reaction temperature: a simultaneous increase of both delayed the PI the furthest. The PI

point (viscosity local minimum) is greatly shifted towards higher conversions when increasing initiator concentration.

The observed effect on PI is possibly due to the presence of graft copolymer in the mixture, which is somewhat higher in the reactions at 90°C, as expected. Given that the copolymer chains are preferably located at the interface of the rubber/PS particles [61, 389], their effect on the polymer mixture is comparable to that of a surfactant: they are expected to increase phase "compatibility" [47, 385, 396, 397] by reducing the surface tension of the mixture. Under such conditions, one would expect two opposing effects. On the one hand, by accumulating at the interfaces, the graft copolymer stabilizes the PS droplets before the inversion, so that coalescence is thermodynamically and sterically hindered, as previously reported with copolymers and surfactants [146, 153, 261, 273, 398]. This effect causes a delayed inversion point due to the coagulating difficulty of the PS nuclei. On the other hand, by providing a certain compatibility between the PS-rich and the PB-rich phases [399], the graft copolymer favors the beginning of the inversion period: even though phase immiscibility still holds, the influence of the dispersed phase on the mixture properties becomes increasingly important, as surface energies are reduced and particle deformability is enhanced.

Moreover, since surface-active components tend to increase interfacial viscosity [187], grafted PS may contribute to increase the viscosity of the PB-rich phase. In addition, if enhanced grafting is coupled with a decrease in $M_{w,PS}$ (*e.g.* by increasing initiator concentration), then a lower PS-rich phase viscosity is to be expected. These effects may favor the inversion process since, as discussed in Section 2.3 , the lower the phase viscosity ratio $\left(\frac{\eta_d}{\eta_c}\right)$, the easier for the low viscosity phase (*i.e.*, the PS-rich phase) to become the continuous phase. Besides, a decrease in the PS molecular weight, also implies shorter graft copolymer chains. This lowers its effect on surface tension, thus favoring PI.

Both effects are probably present and competing in the reacting system, and the prevailing effect will eventually have an impact on the phase inversion period in one way or the other. On a general scale, the effect of an emulsifier on the PI of a two-phase system is not straightforward. As decribed in Section 2.2, the experimental work available in literautre shows different results according to the emulsion type and the emulsifier characteristics, including the average molecular weight of copolymers [400, 401]. There is no general trend as to whether the increase of an emulsifier concentration promotes or delays the PI point, mainly because it is not the only variable related to surface-active components that should be considered: its affinity towards a given phase and how it changes with operating conditions also play substantial roles [106, 350].

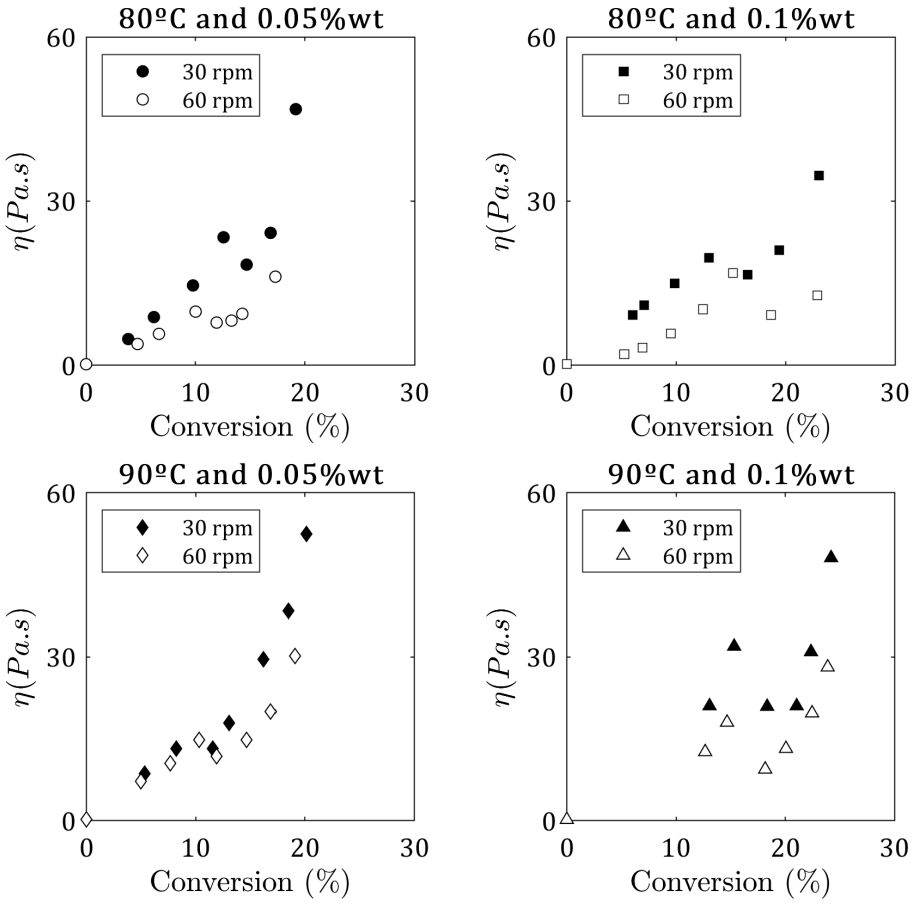

FIGURE 4.3: Apparent viscosity of the prepolymerizing mixture for each pair of reactions at different stirring speeds. Markers refer to reaction number as defined in Table 4.1.

4.2.3 Morphology

For each reaction, samples before and after the apparent viscosity minima were observed by TEM, to verify the occurrence of the inversion phenomenon. As an example, Figure 4.4 presents the micrographs taken for run 3 (90°C, 0.05%wt, 30 rpm) at (a) 8.2% conversion and (b) 13% conversion. The light-gray areas represent the PS-rich phase and the dark gray, the PB-rich phase. As observed, after PI (subfigure (b)) the particle "salami morphology" is developed. Particle size distributions for this reaction, estimated with an image-analysis technique, are shown in Figure 4.5.

All the images corresponding to post-PI systems were also processed with an image-analysis technique, to estimate the fraction of occluded vitreous phase in each reaction immediately after the inversion point. This was achieved by computing the areas of the image that correspond to occluded vitreous phase and assuming a spherical geometry to convert such areas to volumes. However, since the monomer evaporates during the sample preparation, a

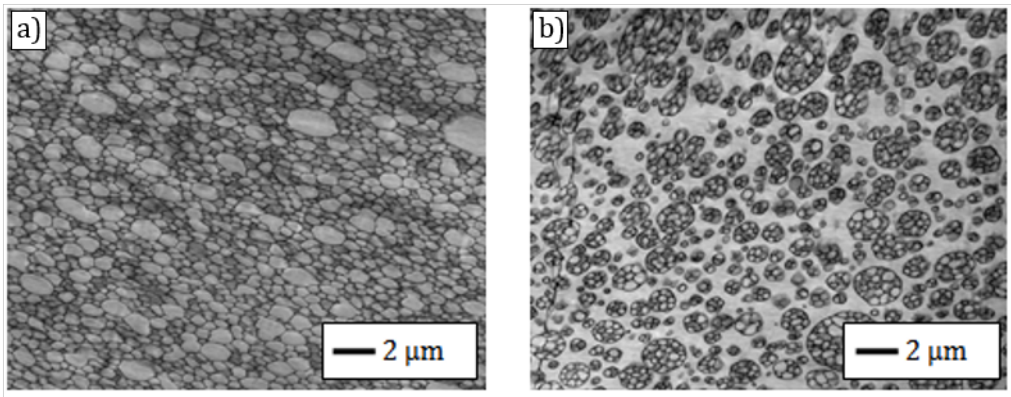

FIGURE 4.4: TEM images for Run 3 at (a) 8.2% conversion and (b) 13%.

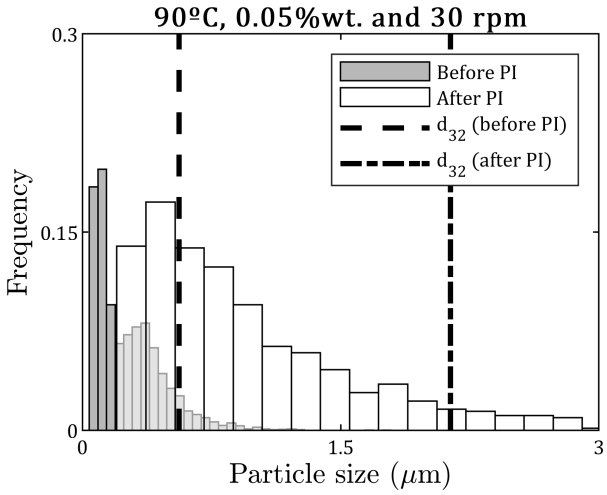

FIGURE 4.5: Particle size distribution for reaction 3 before and after PI.

correction is needed to determine the *actual* phase volumes.

Considering that the styrene is distributed between both phases with a partition coefficient of 1 [374], the mass of monomer present in each phase can be calculated as:

$$m_{St,v} = \frac{m_{St}}{1 + \frac{m_{PB}}{\rho_{PB}} \frac{\rho_{PS}}{m_{PS}}} \tag{4.1}$$

$$m_{St,r} = \frac{m_{St}}{1 + \frac{m_{PS}}{\rho_{PS}} \frac{\rho_{PB}}{m_{PB}}} \tag{4.2}$$

where subscripts v and r represent the vitreous and rubbery phases respectively. ρ_{PS} and ρ_{PB} are the densities of polystyrene and polybutadiene respectively.

This means that the weight fractions, in terms of total monomer conversion (x), are:

$$w_{St,v} = \frac{1-x}{1+\frac{\rho_{PS}}{\rho_{PB}}\frac{w_{PB}}{1-w_{PB}}} \tag{4.3}$$

$$w_{St,r} = \frac{1-x}{1-x\left(1-\frac{\rho_{PB}}{\rho_{PS}}\right)+\frac{w_{PB}}{1-w_{PB}}} \tag{4.4}$$

Therefore, the phase volumes in the presence of styrene can be calculated from the monomer-free phase volumes:

$$V_r = V_{PB}\left[\frac{\rho_{PB}}{\rho_{St}}\frac{w_{St,r}}{(1-w_{St,r})}+1\right] \tag{4.5}$$

$$V_{v,oc} = V_{PS,oc}\left[\frac{\rho_{PS}}{\rho_{St}}\frac{w_{St,v}}{(1-w_{St,v})}+1\right] \tag{4.6}$$

With this technique and correction factors, the internal phase ratio *at the PI point* may be computed for each particle:

$$\phi_{oc,0} = \frac{V_{v,oc}}{V_r + V_{v,oc}} \tag{4.7}$$

thus producing a number distribution for each image. The result is shown in the histograms of Figure 4.6 for samples taken around the inversion point. This distribution could not be determined for reaction 4, due to the poor quality of the TEM image at that point.

From examination of this figure, it would seem that both an increase in BPO concentration and in temperature yield particles with a higher internal phase ratio. Since both these conditions favor the generation of graft copolymer, which acts as a surfactant, this behavior is interestingly similar to what has been observed for O/W/O systems [347]. This means that the mechanisms frequently studied for simple systems may also apply for this complex monomer-polymer-polymer-copolymer mixture. This could be especially true for the role of interfacial tension (which is seen here through the concentration of graft copolymer).

Moreover, as shown in Figure 4.7, the approximate internal phase ratio of each particle varies according to its size. The dependence also seems in agreement with previously published results in O/W/O emulsions [347], which show that the increase in the occluded fraction with particle size is much steeper for small particles than for large ones. This means

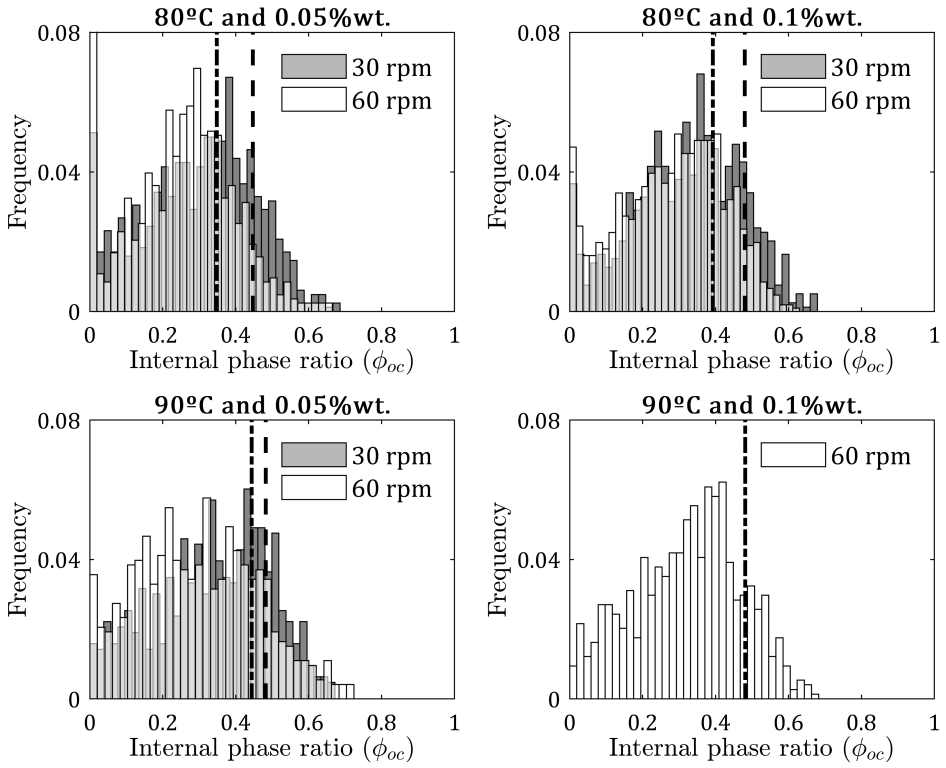

FIGURE 4.6: Distribution of occluded fractions for each reaction at around the inversion point. Vertical lines represent the mean values: dashed line for reactions at 30 rpm and dash-dot line for 60 rpm cases.

that bigger particles may accommodate a larger number of occlusions, but as particle size increases, this ability is less efficient. Interestingly, this behavior is observed regardless of the reaction recipe.

All reactions show a mean internal phase fraction at the inversion point, $\overline{\phi_{oc,0}}$, of around 0.35-0.5, with the experiments at 60 rpm being slightly lower than those at 30 rpm.

To complete the analysis, samples were observed by TEM at complete conversion. The effect of reaction conditions on final particle morphology is presented in Figure 4.8. The increase in BPO concentration showed a minor effect on particle size, while an increase in temperature produced, on average, smaller dispersed particles. This is possibly due to the effect of temperature on grafting efficiency, which, for the investigated conditions, appears to be more pronounced than that of the initiator concentration.

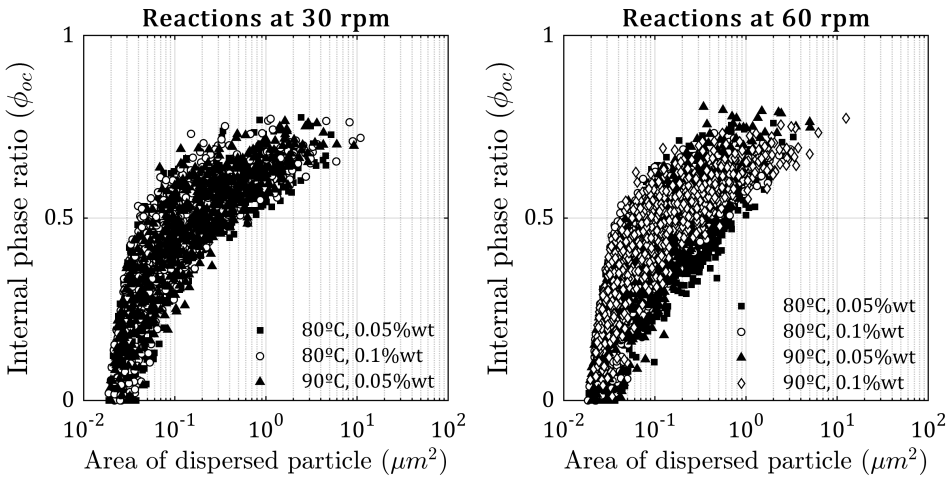

FIGURE 4.7: Internal phase ratio (estimated by the ratio of the total area occupied by the occlusions to the area occupied by the entire particle) at the inversion point as a function of particle size.

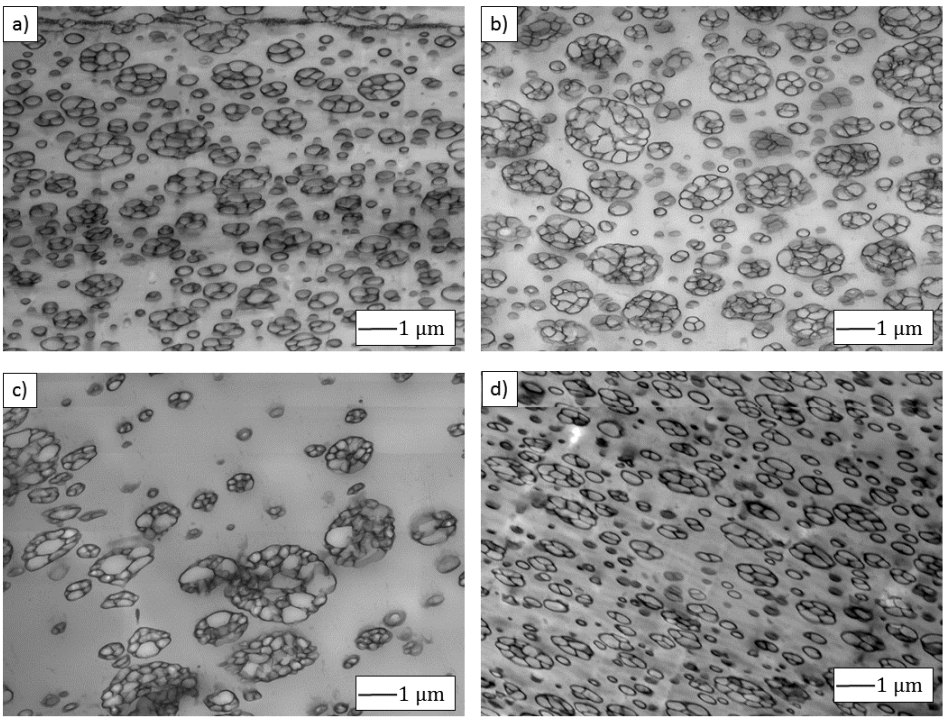

FIGURE 4.8: Final product morphology for reactions at (a) 80°C, 30 rpm and 0.05%wt, (b) 80°C, 30 rpm and 0.1%wt, (c) 80°C, 60 rpm and 0.05%wt and (d) 90°C, 30 rpm and 0.05%wt.

4.2.4 Rheology

The apparent viscosity measurements showed that the reaction mixture is pseudoplastic, which is most probably due to the presence of rubber [402], since the amount of PS present in each sample would not justify the difference in viscosity with shear rate (as per the data gathered by Kim and Nauman [403]). As an example, Figure 4.9 shows the results of the measurements taken with the Brookfield viscometer for reactions 1 and 4. It is worth noting that, in the measured range of shear rate, the location of the PI point remains almost unchanged.

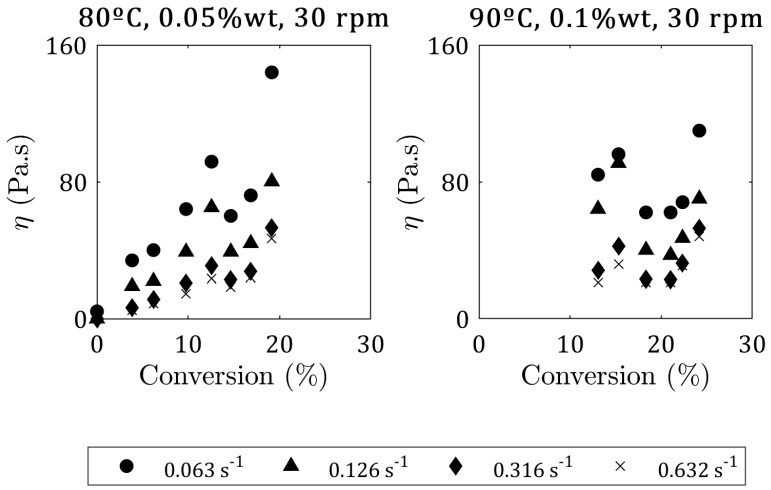

FIGURE 4.9: Rheological behavior of the prepolymerizing system in runs 1 (80°C, 0.05%wt BPO, 30 rpm) and 4 (90°C, 0.1%wt BPO, 30 rpm).

This pseudoplasticity may be modeled following a power law expression:

$$\eta = K\dot{\gamma}^{n-1} \tag{4.8}$$

Since the phase compositions change along the reaction, it becomes natural to adjust the model parameters (K and n) with conversion, instead of trying to fit the evolution of the whole viscosity curve with only two global constants. This methodology has already been reported by Song et al. [50]. Figure 4.10 depicts the result of this procedure for the same reactions shown in Figure 4.9. The pattern shown in the rest of the reactions is very similar and it is not shown here to avoid redundancy.

The consistency coefficient K shows the same shape than the apparent viscosity, with a local minimum at the inversion point. The flow index, in turn, increases almost monotonically until the PI point is reached but, from that point, its value seems to depend on each

reaction. Interestingly, it stays between 0.5 and 1. This shows that the pseudoplasticity of the overall mixture tends to decrease as the reaction proceeds (at least until the inversion point), probably because the effect of the rubber present in the system is being gradually overcome by the produced PS. After the PI point, where the vitreous phase becomes the continuous phase, the rheological behavior of the system is more strongly affected by the characteristics of the St-PS solutions.

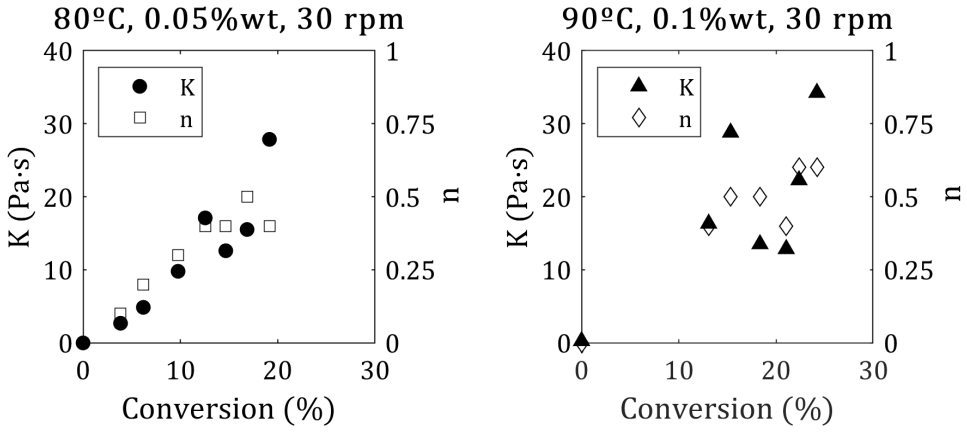

FIGURE 4.10: Evolution of the power law model parameters for reactions 1 (80°C, 0.05%wt BPO, 30 rpm) and 4 (90°C, 0.1%wt BPO, 30 rpm).

4.3 Empirical model for the evolution of apparent viscosity

For given reaction conditions (*i.e.*, polymerization temperature, initiator concentration, stirring speed, etc.), phase inversion will occur at a defined conversion range and, if the vitreous phase is less viscous than the rubber-rich one, the apparent viscosity of the mixture will go through minimax points, as the ones shown in Figure 4.2, Figure 4.3 and Figure 4.8. The evolution of such curves (before and after the PI) was predicted by the following methodology, which is divided in two modules: one concerning the prepolymerization kinetics and another involving the viscosity evolution.

4.3.1 Polymerization module

The batch and bulk polymerization of HIPS was mathematically modelled following Estenoz et al. [389]. The model is based on a kinetic mechanism that assumes homogeneous polymerization and involves chemical and thermal initiation, monomer propagation, transfer to monomer and to the rubber, and combination termination. This mechanism is described in Table 4.3. The autoacceleration or "gel" effect is taken into account by following Hui and Hamielec [404], that is, by making the rate constant of the combination termination to de-

pend on conversion. The set of equations are presented in Appendix B, and were solved with a standard Rosenbrock formula, suited for stiff and nonlinear ordinary differential equations. To integrate the expressions for the $M_{w,PS}$, an Euler method was employed.

The model was adjusted to fit the measurements of St conversion, $M_{w,PS}$, and grafting efficiency; and was used to provide the viscosity equations with smooth evolutions of $M_{w,PS}$ and ζ, thus obtaining continuous theoretical curves.

Proposed kinetic mechanism	**Nomenclature**	
Inititation	St	Monomer
$3\,St \xrightarrow{k_{io}} 2\,S_1^{\bullet}$	$S_1^{\bullet}$	Monomer radical
$I_2 \xrightarrow{fk_d} 2\,I^{\bullet}$	I_2	Initiator
$I^{\bullet} + St \xrightarrow{k_{i1}} S_1^{\bullet}$	$I^{\bullet}$	Initiator radical
$I^{\bullet} + B \xrightarrow{k_{i2}} P_0^{\bullet}$	B	Unreacted butadiene unit
$P_0^{\bullet} + St \xrightarrow{k_{i3}} P_1^{\bullet}$	$P_0^{\bullet}$	Primary radical produced by attack to a butadiene unit
Propagation	$P_1^{\bullet}$	Copolymer radical with one styrene unit
$S_n^{\bullet} + St \xrightarrow{k_p} S_{n+1}^{\bullet}$	$P_n^{\bullet}$	Copolymer radical with n repetitive units of St in active branch
$P_n^{\bullet} + St \xrightarrow{k_p} P_{n+1}^{\bullet}$	$S_n^{\bullet}$	Free PS radical with n repetitive units
Transfer	S_n	PS with n repetitive units
$S_n^{\bullet} + St \xrightarrow{k_{fM}} S_n + S_1^{\bullet}$	P_n	Copolymer with n repetitive units
$P_n^{\bullet} + St \xrightarrow{k_{fM}} P_n + S_1^{\bullet}$		
$P_0^{\bullet} + St \xrightarrow{k_{fM}} B + S_1^{\bullet}$		
$S_n^{\bullet} + B \xrightarrow{k_{fG}} S_n + P_0^{\bullet}$		
$S_n^{\bullet} + P_n \xrightarrow{k_{fG}} S_n + P_n^{\bullet}$		
Termination		
$S_n^{\bullet} + S_m^{\bullet} \xrightarrow{k_{tc}} S_{n+m}$		
$S_n^{\bullet} + P_m^{\bullet} \xrightarrow{k_{tc}} P_{n+m}$		
$P_n^{\bullet} + P_m^{\bullet} \xrightarrow{k_{tc}} P_{n+m}$		
$P_n^{\bullet} + P_0^{\bullet} \xrightarrow{k_{tc}} P_n$		
$S_n^{\bullet} + P_0^{\bullet} \xrightarrow{k_{tc}} P_n$		
$P_0^{\bullet} + P_0^{\bullet} \xrightarrow{k_{tc}} B$		

TABLE 4.3: Proposed kinetic mechanism of styrene polymerization in presence of rubber.

4.3.2 Viscosity correlation module

In emulsion theory, the emulsion viscosity is higher than the continuous phase viscosity, due to the contribution of the dispersed phase viscosity, the average dispersed particle size, and the dispersed phase volume fraction, as described in Section 2.3. On these grounds, it is suggested that the viscosity curves of the reacting system should follow that of a PB-rich continuous/PS-rich dispersed emulsion before PI, and then that of a PS-rich continuous/PB-rich dispersed emulsion after PI. More precisely, by considering the PS droplets occluded in the PB-rich particles after the PI point, this mixture actually consists of a PS-rich/PB-rich/PS-rich double-emulsion.

Therefore, in order to compute the apparent viscosity using the results of the Polymerization module, the following three aspects have to be considered.

4.3.2.1 Dispersed phase fraction

For the system after the inversion point (PS-rich continuous), the dispersed phase fraction, ϕ_d, may be calculated from both the rubber-rich phase fraction ϕ_r and the initial internal phase fraction $\phi_{oc,0}$, as follows:

$$\phi_d = \frac{V_p}{V_v + V_r} \tag{4.9}$$

where V_p is the total volume of dispersed particles, V_v is the volume of the vitreous (PS-rich) phase and V_r is the volume of the rubber-rich phase. The former may be computed considering additive volumes, as:

$$V_p = \frac{m_{PB}}{\rho_{PB}} + \frac{m_{St,r}}{\rho_{St}} + \frac{m^{oc}_{St,v}}{\rho_{St}} + \frac{m^{oc}_{PS}}{\rho_{PS}} \tag{4.10}$$

where the superscript *oc* refers to the occluded phase, which can be computed from the initially engulfed vitreous phase (that is, *at the inversion point*) and introducing a *shifted conversion*, x', to compute the PS mass produced inside the droplet from that point onwards.

$$x' = \frac{m_{St(x=x_{PI})} - m_{St(x)}}{m_{St(x=x_{PI})}} = 1 - \frac{1-x}{1-x_{PI}} \tag{4.11}$$

Using this definition and assuming that the propagation rates are similar in each phase,

Eq. 4.10 turns into:

$$V_p = \frac{m_{St0}}{\rho_{PB}}\left(\frac{w_{PB}}{1-w_{PB}}\right) + \frac{\left(m^{oc}_{St,v0} + m_{St,r0}\right)(1-x')}{\rho_{St}} + \frac{m^{oc}_{PS0} + \left(m^{oc}_{St,v0} + m_{St,r0}\right)x'}{\rho_{PS}} \quad (4.12)$$

$$V_p = \frac{m_{St0}}{\rho_{PB}}\left(\frac{w_{PB}}{1-w_{PB}}\right) + \left(m^{oc}_{St,v0} + m_{St,r0}\right)\left[\frac{(1-x')}{\rho_{St}} + \frac{x'}{\rho_{PS}}\right] + \frac{m^{oc}_{PS0}}{\rho_{PS}} \quad (4.13)$$

where subscript 0 refers to the PI point (which is time zero for the occlusions).

Combinig Eqs. 4.4-4.13 and introducing the initially occluded phase fraction $\left(\phi_{oc,0} = \frac{V_{v,oc0}}{V_p}\right)$ yields:

$$V_p = \frac{m_{St0}}{\rho_{PB}}\left(\frac{w_{PB}}{1-w_{PB}}\right) + \left[\frac{V_r|_{x=x_{PI}}\frac{\phi_{oc,0}}{1-\phi_{oc,0}}}{\frac{1}{\rho_{St}} + \frac{1-w_{St,v}}{\rho_{PS}w_{St,v}}\Big|_{x=x_{PI}}} + m_{St0}(1-x_{PI})\left(1 - \frac{x_{PI}}{x_{PI} + \frac{\rho_{PS}}{\rho_{PB}}\left(\frac{w_{PB}}{1-w_{PB}}\right)}\right)\right]\left(\frac{1-x'}{\rho_{St}} + \frac{x'}{\rho_{PS}}\right) + \frac{m^{oc}_{PS0}}{\rho_{PS}} \quad (4.14)$$

where $V_r|_{x=x_{PI}}$ is the volume of the rubber-rich phase at the inversion point, x_{PI}, and is calculated as:

$$V_r|_{x=x_{PI}} = \frac{m_{St0}(1-x_{PI})\left(1 - \frac{x_{PI}}{x_{PI} + \frac{\rho_{PS}}{\rho_{PB}}\left(\frac{w_{PB}}{1-w_{PB}}\right)}\right)}{\rho_{St}} + \frac{m_{St0}}{\rho_{PB}}\left(\frac{w_{PB}}{1-w_{PB}}\right) \quad (4.15)$$

Similarly, the occluded PS at the inversion point is:

$$m^{oc}_{PS0} = \left[\frac{V_r|_{x=x_{PI}}\frac{\phi_{oc,0}}{1-\phi_{oc,0}}}{\frac{1}{\rho_{St}} + \frac{1-w_{St,v}}{\rho_{PS}w_{St,v}}\Big|_{x=x_{PI}}}\right]\left(\frac{1 - w_{St,v}|_{x=x_{PI}}}{w_{St,v}|_{x=x_{PI}}}\right) \quad (4.16)$$

Finally, the total volume of each phase is easily computed from the weight fractions in Eqs. 4.3 and 4.4:

$$V_v = m_{St0} x \left[\frac{1}{\rho_{PS}} + \frac{\rho_{PB}}{\rho_{St}} \left(\frac{1-x}{\rho_{PB}(1-x) + \frac{w_{PB}}{1-w_{PB}} \rho_{PS}} \right) \right] \tag{4.17}$$

$$V_r = m_{St0} \frac{w_{PB}}{1-w_{PB}} \left[\frac{1}{\rho_{PB}} + \frac{\rho_{PS}}{\rho_{St}} \left(\frac{1-x}{\rho_{PB} x + \frac{w_{PB}}{1-w_{PB}} \rho_{PS}} \right) \right] \tag{4.18}$$

The dispersed phase fraction after the PI point is thus computed between Eqs. 4.14, 4.17 and 4.18. Using these equations implies knowing the location of the PI points *beforehand*, which means, unfortunately, that predicting this key moment from the evolution of these viscosity curves is strictly not possible.

Before the PI point, the calculation is straightforward since no occlusions are observed and the dispersed phase is the vitreous phase: $\phi_d = \phi_v = \dfrac{V_v}{V_v + V_r}$.

4.3.2.2 Shear rate

Given that this mixture is non-Newtonian (as described in Figure 4.9), the next aspect to consider before calculating the viscosity of each phase (and that of the entire mixture) is the shear rate, $\dot{\gamma}$. However, since the PI point was seen to be little affected by it, the viscosity prediction may be performed choosing any rate and keeping it constant throughout the calculation. In this case, based on the quality and availability of the experimental points, the set of curves at 3 rpm (0.632 s^{-1}) was chosen for this fitting procedure. In any case, if the available information is at a different rate, only the model parameters need to be changed.

4.3.2.3 Apparent viscosity model

Several equations have been developed over the past 60 years to model the viscosity of emulsions. The most relevant for the system under study (summarized in Table 2.2), were tested against the experimental data at 0.632 s^{-1}. When possible, the adjustable parameters were modified to fit the measured values. However, none of the equations showed good fitting results, mainly for the following two reasons:

1. All these models were fitted with systems whose continuous phase viscosity, η_c, is constant (*i.e.*, the continuous phase is always the same liquid), which is not the case in this reacting system ($\eta_c = \eta_{c(x,M_{w,PB})}$) as styrene is transferred from the continuous to the dispersed phase as the reaction proceeds

2. None of the equations include a particle size effect, which is key to understand the

differences between the observed viscosities at the studied stirring speeds. In this work, this effect is contemplated through the concentration of graft copolymer, which is the responsible for altering the particle diameter during the reaction (at a given stirring speed) as, behaving like a surfactant, it modifies the interfacial energy of the polymerizing system.

Analyzing the equations in Table 2.2, the relative viscosity ($\frac{\eta}{\eta_c}$) is seen to be an increasing function of the dispersed phase volume fraction. In the reacting system analyzed in this work, this is not necessarily the case, since the viscosity of the mixture increases during the polymerization both because the continuous phase becomes increasingly viscous and because new dispersed phase is formed. Since the continuous phase changes at the PI point, the fitting of the experimental data is done separately before and after PI.

a) Before PI

Figure 4.11 shows the evolution of the relative viscosity for each reaction before the PI point, as measured by the Brookfield viscometer at 0.632 s^{-1}. As observed, none of them is strictly increasing. Based on the non-monotonic evolution of this curve, the following empirical correlation for the apparent viscosity of the system before PI (η_{rc}) was derived and adjusted to fit the experimental data:

$$\eta_{rc} = \eta_r \left(1 + c_1 {Mw_{PS}}^{c_2} {w_{PS-g}}^{c_3} \phi_v \exp\left\{c_4 {\phi_v}^{c_5}\right\}\right) \tag{4.19}$$

where ϕ_v is the vitreous phase volume fraction, w_{PS-g} the weight fraction of grafted PS, $M_{w,PS}$ the PS molecular weight in kg/mol, and η_r the rubber-rich phase viscosity in cP. The latter was found to fit the following expression, where $w_{St,r}$ is the weight fraction of styrene, $\dot{\gamma}$ is the shear rate in s^{-1} and η_r is the viscosity in cP:

$$\ln\left(\eta_r\right) = \alpha\left(1 - w_{St,r}\right) + \beta \tag{4.20}$$

where

$$\alpha = 38.7\left[1 - \exp\left(-1.6974\dot{\gamma}\right)\right] \tag{4.21}$$

$$\beta = \frac{2.4589}{\dot{\gamma} + 0.3472} + 2.3387 \tag{4.22}$$

A very good fit is observed between the predicted evolution of Eq. 4.19 and the experimental data in Figure 4.11. The derived correlation accounts for the changes in interfacial properties (and consequently, particle size) through the weight average molecular weight of the grafted PS branches and the copolymer concentration (here behaving as a surfactant). Accounting for the stirring speed effect is more troublesome and the adjustable parameters (c_1, c_2, c_3 and c_4) are here reported for each agitation rate studied. With a sufficiently high number of stirring speed values, this correlation could be certainly improved.

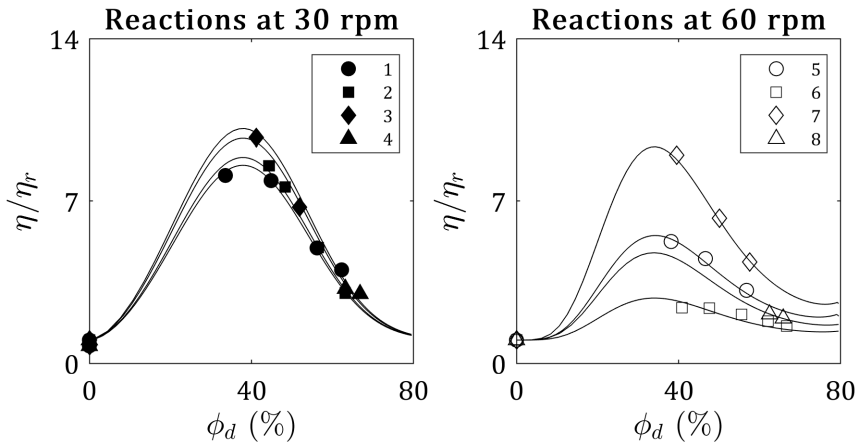

FIGURE 4.11: Relative viscosity of the polymerizing system before phase inversion, at the investigated stirring speeds. Markers refer to each reaction number, as in Table 4.1.

b) After PI

For the already inverted systems, the volume fraction of the discrete phase, ϕ_d, must contemplate the occluded continuous phase. Following the set of equations shown in Section 4.3.2.1, this volume fraction is readily computed, and is further related to the rubber-phase fraction through $\phi_d = \frac{\phi_r}{1-\phi_{oc}}$.

The empirical correlation for the mixtures after PI resulted in:

$$\eta_{vc} = \eta_v \left(1 + c_6 {Mw_{PS}}^{c7} {w_{PS-g}}^{c8} \phi_d\right) \tag{4.23}$$

where $M_{w,PS}$ is the weight-average free PS molecular weight (in kg/mol), w_{PS-g} is the grafted PS weight fraction and ϕ_d the dispersed phase volume fraction. η_v (in cP) is the viscosity of the vitreous phase, computed using the correlation by Kim and Nauman [403]:

$$\eta_v = \frac{\eta_{0v}}{\left(1 + \frac{\eta_{0v}\dot{\gamma}^{1.2}}{35000}\right)^{0.6}} \tag{4.24}$$

where η_{0v} (in cP) is the viscosity at very low shear rates and is calculated with the following equation, by the same authors (T in °K):

$$\eta_{0v} = 1000 \exp\left\{-11.091 + \frac{1109}{T} + M_{w,PS}^{0.1413}\left[12.032 w_{PS,v} - 19.501 w_{PS,v}^2 + 2.923 w_{PS,v}^3 + \frac{1}{T}\left(-1327 w_{PS,v} + 1359 w_{PS,v}^2 + 3597 w_{PS,v}^3\right)\right]\right\} \quad (4.25)$$

c) Model adjustment

The model parameters were adjusted to fit the viscosity curves for each reaction. Predicted evolutions are represented in Figure 4.12, where a general good agreement with the experimental data is observed.

The values of the adjusted parameters are listed in Table 4.4 (parameters for the polymerization module were taken from literature [389, 405, 406]).

Parameter	**30 rpm**	**60 rpm**
C_1	2733.4	1193.6
C_2	-0.1912	3.0425
C_3	0.6514	3.1961
C_4	12.3988	19.5266
C_5	2.9554	1.4520
C_6	0.0764	0.0016
C_7	1.3954	2.5234
C_8	0.0128	0.7786

TABLE 4.4: Model parameters implemented in the viscosity correlations.

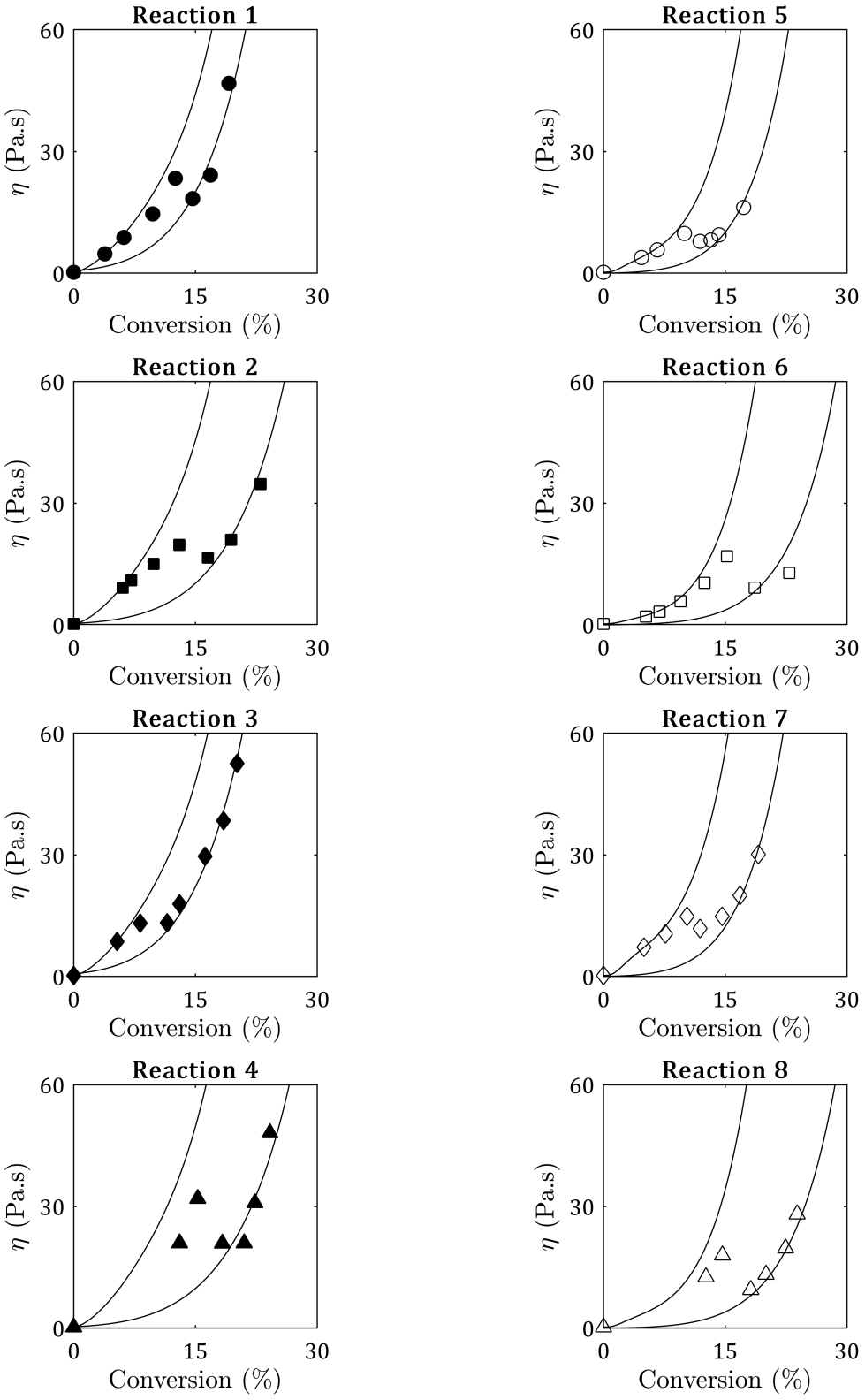

FIGURE 4.12: Predicted evolution of the apparent viscosity of each reaction mixture.

4.4 Theoretical results during the PI process

Combining the results of the polymerization module and the viscosity correlations developed in the previous section, some interesting properties may be compared between each reaction at the onset of the inversion process. Some of the physical parameters associated with this phenomenon are the dispersed phase volume fraction, ϕ_v, the phase viscosity ratio, r, and the grafting efficiency, ζ. Figure 4.12 shows the predicted values of such parameters during the polymerization. The experimental apparent viscosities and the PI region have been added as a visual aid.

As observed, none of the inversion periods begin at equivolume conditions, a criterion that is commonly adopted on theoretical grounds [61, 376] but is evidently far from being correct. Furthermore, the system that inverts the latest (reactions 4 and 8) show the lowest phase viscosity ratios and the highest grafting efficiencies.

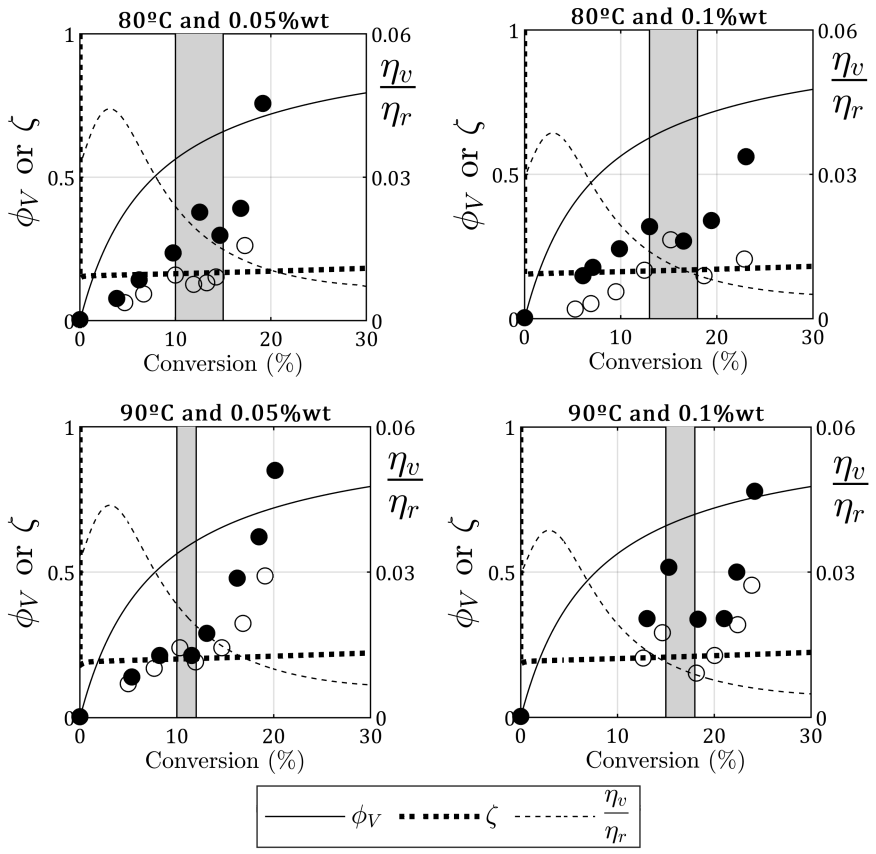

FIGURE 4.13: Predicted system properties during the phase inversion process. White markers correspond to viscosity measurements at 60 rpm, while black markers at 30 rpm. They are included in the figure as a visual aid.

4.5 Summary and conclusions

The polymerization of styrene in the presence of PB was studied under different reaction conditions, focusing on the phase inversion phenomenon through the evolution of the apparent viscosity of the reacting mixture along the prepolymerization. The results show that it is possible to predict the evolution of such viscosity before and after the PI process. The description of the co-continuous transition remains a challenge, but it is likely that, if enough experimental evidence were gathered, a comprehensive model could be developed to accurately predict the evolution of the entire curve.

Empirical correlations were developed for predicting the viscosity evolution of the St-PS-PB mixture during the polymerization of St under the investigated conditions. The proposed equations accurately describe the apparent viscosity before and after the PI period, as the system behaves like a polymeric oil-in-oil emulsion. Naturally, the adjusted parameters are valid under the reaction conditions investigated; should these change considerably, the fitting procedure would have to be performed again to obtain a different set of values. These correlation themselves are not the prime goal of this work, but rather the methodology followed to obtain phase behavior predictions.

According to the available measurements, the most important parameters that affect viscosity curves were phase composition (a function of conversion), the occluded phase fraction (after PI) and overall particle size, whose effect was deemed to be the result of stirring speed, $M_{w,PS}$, $M_{w,PB}$, and the copolymer weight fraction. Since the mixture presents non-Newtonian behavior, the analysis was performed at a (chosen) constant shear rate. For different shear rate values, the adjustable parameters and continuous phase viscosities should be recalculated.

The challenge of predicting the mixture viscosity **after** the PI point lies on the fact that the dispersed phase fraction depends both on the initially occluded continuous phase and on the amount of rubber-rich phase present at that moment, which is itself a function of the St conversion at the inversion point, x_{PI}. Thus, estimating the PI period for a given polymerization only using viscosity models was proven unviable. However, validating such models with real quantifiable data could set the basis for a better understanding of the complex physicalchemistry that govern the PI process.

According to the presented experimental results, the produced graft copolymer plays a major role on the dynamics of the phase inversion process of this system. A reduction in interfacial tension causes dispersed particles to be prone to interfacial deformation, which may lead both to larger or smaller particles depending on the relative effect on coalescence and break-up frequencies. It is then conceivable that there is an optimum recipe where phase inversion occurs readily at low conversions, produces a desired particle size distribution, and

minimizes the use of rubber by increasing the amount of PS occlusions. Further experimental results are required to validate this conjecture.

Chapter 5

Phase Inversion Prediction in the HIPS Bulk Synthesis: A Fluid-Dynamic Approach

"Nature's standard operating procedure, pairing a population explosion with a population crash"

Alfred W. Crosby

One of the most accepted mechanisms that explains the phase inversion process in a dispersed system is the imbalance between the coalescence and break-up of the discrete particles. Although other approaches have been studied (as reviewed in Chapter 2), the intuitive physics behind this mechanism makes it perhaps the most popular. After showing that it is not possible to predict the PI point during the HIPS bulk polymerization by forecasting the evolution of its apparent viscosity, a different technique is essayed in this Chapter.

The idea is based on the coalescence *vs* break-up imbalance, which is the result of the coalescence *frequency* rapidly overcoming the breakage one at the onset of the inversion point. Both frequencies depend on the physical properties of each phase and, most importantly, on the particle sizes. This means that, for a given initial particle size distribution (PSD), if the particle-particle interactions are computed as a function of time, the number of particles of a given size may be calculated. That is, the evolution of the particle size distribution may be simulated along the reaction. This shall be achieved by performing a *population balance*.

The population balance equation (PBE) has been used for years to predict the evolution of a characteristic feature held by any discrete set, ranging from particle size in an oil-water emulsion [207] to cellular age in a biological mitosis process [407]. Based on the Reynolds transport theorem, the population balance equation describes the rate of change of

a continuous density function $f_{(\boldsymbol{x},\boldsymbol{r},t)}$ for a given particle *state* ($\boldsymbol{x}$), both in time (t) and in a spatial coordinate ($\boldsymbol{r}$). The state of a particle is given by the characteristic property upon which the balance is performed.

Let $\boldsymbol{\Omega_x}$ and $\boldsymbol{\Omega_r}$ be the domain of internal states and the domain of external coordinates respectively. Consider any extensive property p of a single particle with state $\boldsymbol{x}$, located at $\boldsymbol{r}$, and an aribitrary domain $\boldsymbol{S_{(t)}}$ in the particle space continuum at time t. This domain comprises a subdomain $\boldsymbol{S_{x(t)}}$, which is in $\boldsymbol{\Omega_x}$ and a subdomain $\boldsymbol{S_{r(t)}}$ which is in $\boldsymbol{\Omega_r}$. The total amount of the considered property p in the domain $\boldsymbol{S}$, denoted $\mathcal{P}$, evolves with time as:

$$\mathcal{P}(t) = \int_{S_x(t)} \int_{S_r(t)} f_{(\boldsymbol{x},\boldsymbol{r},t)} p_{(\boldsymbol{x},\boldsymbol{r})} dV_r dV_x \tag{5.1}$$

Making use of the Reynolds transport theorem [408], the rate of change of Eq. 5.1 is:

$$\frac{\partial \mathcal{P}}{\partial t} = \int_{S_x(t)} \int_{S_r(t)} \left[\frac{\partial (pf)}{\partial t} + \nabla_x \cdot \dot{\boldsymbol{X}} pf + \nabla_r \cdot \dot{\boldsymbol{R}} pf \right] dV_r dV_x \tag{5.2}$$

where $\nabla_x \cdot$ and $\nabla_r \cdot$ are the divergences of the internal and the external states respectively. $\dot{\boldsymbol{X}}$ is the rate of change of the particle state in its internal coordinates, and $\dot{\boldsymbol{R}}$, the rate of change in the spatial coordinates. This means that the term $f(\boldsymbol{x}, \boldsymbol{r}, t)\dot{\boldsymbol{X}}$ represents the *flux* of particles deforming through the internal coordinate space, where $\dot{\boldsymbol{X}}$ is the velocity at which particle state is changing in the continuous particle state vector. Usually, this is associated with particle growth (or shrinkage).

The total number of particles in the domain $\boldsymbol{S}$ can change either because new particles are "born", or existing particles disappear. These phenomena are usually referred to as *birth* and *death* processes. For example, in the context of an agitated liquid-liquid dispersion with inter-phase mass transfer, one may choose particle *volume* as the desired particle state; then, the birth and death processes could be the reult of:

- **Particle coalescence**: if two particles of volumes v and v' coalesce, those two "die" and a new particle of volume $v + v'$ is "born".
- **Particle break-up**: if a particle of volume v breaks-up into two smaller particles of volumes v' and $v - v'$, then the former diseappears and the latter are born.
- **Nucleation**: new particles can appear as the result of a nucleation process, and are usually of minimal size. If it is the case, this is a process that occurs only at the boundary of the internal state space.
- **Dissolution**: if mass transfer is occurring from the dispersed to the continuous phase,

then particles may be considered to disappear at zero size due to a dissolution process.

Let $f_{(\boldsymbol{x},\boldsymbol{r},t)}$ be the number density function of particles of state $\boldsymbol{x}$ per unit volume of physical space at time t. Assuming that there is a **net** birth rate of particles, denoted $\psi_{(\boldsymbol{x},\boldsymbol{r},t)}$, per unit volume of particle state space, the conservation of particle number is:

$$\frac{\partial}{\partial t}\int_{S_{x(t)}}\int_{S_{r(t)}} f_{(\boldsymbol{x},\boldsymbol{r},t)}dV_r dV_x = \int_{S_{x(t)}}\int_{S_{r(t)}} \psi_{(\boldsymbol{x},\boldsymbol{r},t)}dV_r dV_x \tag{5.3}$$

The left hand side of Eq. 5.3 is the right hand side of Eq. 5.1 with $p = 1$. Therefore, using Eq. 5.2:

$$\int_{S_x(t)}\int_{S_r(t)}\left[\frac{\partial f}{\partial t} + \nabla_x \cdot \dot{\boldsymbol{X}} f + \nabla_r \cdot \dot{\boldsymbol{R}} f - \psi\right] dV_r dV_x = 0 \tag{5.4}$$

Given that the domain $\boldsymbol{S}$ has been chosen arbitrarily, Eq. 5.4 implies that the integrand should be zero, thus yielding the population balance equation:

$$\frac{\partial f}{\partial t} + \nabla_x \cdot \dot{\boldsymbol{X}} f + \nabla_r \cdot \dot{\boldsymbol{R}} f = \psi \tag{5.5}$$

This equation is naturally a general case and must be supplied with initial and boundary conditions to be solved. Its application in the particular case of the bulk polymerization of HIPS is developed in the next sections of this Chapter.

5.1 Model development

Prior to applying Eq. 5.5 to the particular case of the polymeric system of this thesis, the following is considered:

- The dispersed phase that is object of this study is the vitreous phase (PS in St) of the polymerizing mixture up until the phase inversion point.
- Particle state is chosen to be the particle's volume, v.
- The rate of continuous change in particle state space, $\dot{\boldsymbol{X}}_{(t)}$ shall be noted $\dot{V}_{v(v,t)}$ and will consider the shrinkage of particles due to volume contraction during the reaction, and the growth of particles due to the flux of styrene from the continuous to the dispersed phase.

- The polymerization reactor will be considered to be perfectly mixed, thus eliminating the need to compute $\dot{\boldsymbol{R}}$.
- Even if they polymerizing system is homogeneous in the initial stages of the reaction, the model computation shall consider an heterogeneous system all along. The short period in which the system is homogeneous is considered not to have an effect on the location of the PI point.
- An initial particle size distribution shall be supplied as initial condition, but no further sources of new particles shall be considered (*i.e.* nucleation rates shall be considered negligible).

5.1.1 Heterogeneous bulk polymerization

The total volume of the vitreous phase changes along the polymerization for two main reasons:

1. Volume contraction, since the PS density is higher than the St density, causes the disperesed phase to shrink along the polymerization.
2. Thermodynamic incompatibility between the PB and PS chains forces St to migrate from the PB-rich phase to the PS-rich phase so as to keep a partition coefficient approximately constant. This effect causes the dispersed phase to grow during the reaction.

Since both these effects change along the reaction, a heterogeneous bulk kinetic model is required. This model will also serve the PBE with the evolution of the physical properties needed to compute the birth and death processes, since they depend on monomer conversion, PS molecular weights and grafting efficiency. The main hypotheses considered before developing the model are the following:

1. The flux of styrene from the continuous to the dispersed phase serves to transfer the PS propagating radicals in the rubbery phase to the vitreous phase. However, copolymer molecules or copolymer propagating radicals are left in the rubber-rich phase.
2. The flux of styrene is envisaged to keep the partition coefficient as close to 1 as possible.
3. Each phase follows the same kinetic mechanism that the one shown in Table 4.3, but rate constants are allowed to differ between each phase. This is especially considered for the termination rate constants, since the *gel effect* may vary, according to the polymer concentration in each phase.

Considering these hypotheses and assuming additive volumes, $\dot{V}_v$ is derived from its definition:

$$\dot{V}_v = \frac{\dot{m}_{St_v}}{\rho_{St}} + \frac{\dot{m}_{PS}}{\rho_{PS}} \tag{5.6}$$

where $\dot{m}_{St_v}$ and $\dot{m}_{PS}$ represent the rate of change of the styrene and polystyrene masses respectively.

Accepting the "long chain approximation", by which St is mainly consumed in the propagation reactions, these rates of chage are calculated as:

$$\frac{d}{dt}(m_{St_v}) = -k_{pv}[St_v][S_v^{\bullet}]V_v M_{St} + \dot{F} \tag{5.7}$$

$$\frac{d}{dt}(m_{PS}) = k_{pv}[St_v][S_v^{\bullet}]V_v M_{St} + k_{pr}[St_r]\left([S_r^{\bullet}] + [P^{\bullet}]\right) V_r M_{St} \tag{5.8}$$

where subscripts v and r represent the vitreous and rubbery phase respectively. The term $\dot{F}$ is the mass flux of monomer transferring from the continuous phase to the dispersed phase. $[St]$ and $[St^{\bullet}]$ stand for styrene and styrenic radicals concentrations respectively. $[P^{\bullet}]$ is the concentration of propagating copolymer radicals.

The St consumption in the rubber-rich phase is:

$$\frac{d}{dt}(m_{St_r}) = -k_{pr}[St_r]([S_r^{\bullet}] + [P^{\bullet}])V_r M_{St} - \dot{F} \tag{5.9}$$

The flux of transferred styrene, $\dot{F}$, is calculated so that the equilibrium partition coefficient is satisfied at all a times:

$$[St_v] = [St_r] \tag{5.10}$$

$$m_{St_v}\left(\frac{m_{PB}}{\rho_{PB}} + \frac{m_{St_r}}{\rho_{St}}\right) = m_{St_r}\left(\frac{m_{PS}}{\rho_{PS}} + \frac{m_{St_v}}{\rho_{St}}\right) \tag{5.11}$$

Expanding and differentiating both sides:

$$\dot{m}_{St_v}\frac{m_{PB}}{\rho_{PB}} = \dot{m}_{St_r}\frac{m_{PS}}{\rho_{PS}} + m_{St_r}\frac{\dot{m}_{PS}}{\rho_{PS}} \tag{5.12}$$

Using Eqs. 5.7, 5.8 and 5.9:

$$\left(\dot{F} - Rp_v M_{St} V_v\right) m_{PB}\frac{\rho_{PS}}{\rho_{PB}} = -\left(\dot{F} + Rp_r M_{St} V_r\right) m_{PS} + m_{St_r}\left[\left(Rp_v V_v + Rp_r V_r\right) M_{St}\right] \tag{5.13}$$

from which:

$$\dot{F} = \frac{\left[\left(m_{St_r} + m_{PB}\frac{\rho_{PS}}{\rho_{PB}}\right) Rp_v V_v + \left(m_{St_r} - m_{PS}\right) Rp_r V_r\right]}{m_{PB}\frac{\rho_{PS}}{\rho_{PB}} + m_{PS}} M_{St} \tag{5.14}$$

Where Rp_v and Rp_r are the polymerization rates of the vitreous and rubber-rich phase respectively. Using the volume phase fractions (which only depend on monomer conversion):

$$\dot{F} = \frac{\left[\left(m_{St_r} + m_{PB}\frac{\rho_{PS}}{\rho_{PB}}\right) Rp_v + \left(m_{St_r} - m_{PS}\right) Rp_r \frac{(1-\phi_v)}{\phi_v}\right]}{m_{PB}\frac{\rho_{PS}}{\rho_{PB}} + m_{PS}} M_{St} V_v \tag{5.15}$$

Finally, the flux of monomer that is received by one droplet of volume v, $\dot{F}_{(v)}$, is simply Eq. 5.15 evaluated at $V_v = v$. This way:

$$\dot{F}_{(v)} = \dot{F}\frac{v}{V_v} \tag{5.16}$$

Therefore, the rate at which the volume of a given particle changes is:

$$\dot{V}_{(v)} = \left[k_{pv}[St_v][S_v^{\bullet}]\left(\frac{1}{\rho_{PS}} - \frac{1}{\rho_{St}}\right) M_{St} + \frac{\dot{F}}{\rho_{St} V_v}\right] v \tag{5.17}$$

The fact that this rate of change is proportional to the particle's volume (note that the term in square brackets of Eq. 5.17 is solely a function of time) is advantageous for the implementation of the population balance equations, as will be shown in section 5.2. The rest of the heterogeneous model follows a similar mechanism than the one discussed in Chapter 4. The remainder of the equations are described in Appendix C, where a more detailed balance for each radical species can be found. In the implementation of the model, for simplicity, the

propagation and transfer reactions rates in each phase were assumed equal.

A qualitative representation of the mass partition between each component of the system, as well as the theoretical evolution of the vitreous phase volume (Eqs. 4.1, 4.2 and 5.9), is shown in Figure 5.1:

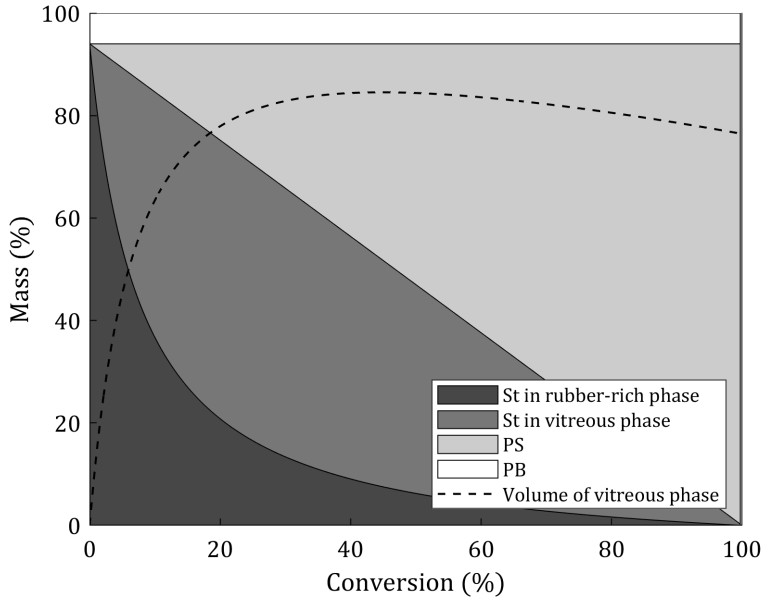

FIGURE 5.1: Distribution of masses between each component of the system.

5.1.2 Population balance

Considering Eq. 5.5 with the hypotheses stated at the beginning of Section 5.1, the population balance equation for the bulk polymerization of HIPS is:

$$\frac{\partial f_{(v,t)}}{\partial t} + \frac{\partial}{\partial v}\left(\dot{V}_{(v,t)} f_{(v,t)}\right) = \psi_{(v,t)} \tag{5.18}$$

Here, $f_{(v,t)}$ is the number density function of vitreous droplets of volume v per unit of physical volume at time t. With this definition, the total number of particles at a given time is:

$$N_{(t)} = V_{T(t)} \int_0^\infty f_{(v,t)} dv \tag{5.19}$$

where V_T is the total volume of the polymerization reactor ($V_r + V_v$).

The net birth of particles, $\psi_{(v,t)}$, shall be broken down into the sources and sinks that represent the break-up and coalescence of particles:

$$\frac{\partial f_{(v,t)}}{\partial t} + \frac{\partial}{\partial v}\left(\dot{V}_{(v,t)} f_{(v,t)}\right) = B^{+}_{(v,t)} - B^{-}_{(v,t)} + C^{+}_{(v,t)} - C^{-}_{(v,t)} \tag{5.20}$$

where superscripts + and − represent the source and sink terms respectively.

Regarding the breakage process, these terms are defined as follows:

$$B^{+}_{(v,t)} = \int_{v}^{\infty} \theta_{b(v')} \omega_{b(v')} f_{(v',t)} \beta_{(v|v')} dv' \tag{5.21}$$

$$B^{-}_{(v,t)} = \omega_{b(v)} f_{(v,t)} \tag{5.22}$$

where $\theta_{b(v')}$ represents the number drop distribution of daughter drops after break-up of a particle of volume v'. In this case, only binary break-up shall be considered. Thus, $\theta_{b(v')} = 2$. The term $\omega_{b(v)}$ is the *break-up frequency* and represents the *fraction* of particles of volume v that are breaking per unit time. Some of the available models are found in Table 2.5. $\beta_{(v|v')}$ stands for the probability density function of droplets of volume v generated by break-up of a particle of volume v'. A summary of the available models to compute such functions are shown in Table 2.6.

The total number of particles breaking per unit time is then:

$$\Omega_{b(t)} = V_{T(t)} \int_{0}^{\infty} \omega_{b(v)} f_{(v,t)} dv \tag{5.23}$$

In turn, the source and sink terms for the coalescence process are:

$$C^{+}_{(v,t)} = \frac{1}{\theta_c} \int_{0}^{v} \omega_{c(v-v',v')} f_{(v-v',t)} f_{(v',t)} dv' \tag{5.24}$$

$$C^{-}_{(v,t)} = f_{(v,t)} \int_{0}^{\infty} \omega_{c(v,v')} f_{(v',t)} dv' \tag{5.25}$$

where θ_c is the number of times identical particle pairs undergoing coalescence have been considered. In this case, the collision of only two particles at a time will be studied. Therefore, $\theta_c = 2$. The term $\omega_{c(v,v')}$ is the *average coalescence frequency* per unit volume between particles of volumes v and $v - v'$, and is usually the product of a collision frequency (ω_{cd})

and a coalescence efficiency (λ_c). A summary of the available models to compute these are presented in Tables 2.3 and 2.4.

In Eq. 5.24, the product $f_{(v-v',t)}f_{(v',t)}$ is a "closure approximation" that represents the *number density of pairs* of particles of volumes v and v'. The actual density function is usually unkwnown and this approximation is frequently used, which considers that there is no statistical correlation bewteen particles of volumes v and $v-v'$ at any time t [409].

The total number of *pairs of particles* coalescing per unit time is then:

$$\Omega_{c(t)} = V_{T(t)} \int_0^\infty f_{(v,t)} \int_0^\infty \omega_{c(v,v')} f_{(v',t)} dv' dv \tag{5.26}$$

Eq. 5.18 then reads:

$$\begin{aligned} \frac{\partial f_{(v,t)}}{\partial t} + \frac{\partial}{\partial v}\left(\dot{V}_{(v,t)} f_{(v,t)}\right) = 2\int_v^\infty \omega_{b(v')} f_{(v,t)} \beta_{(v|v')} dv' - \omega_{b(v)} f_{(v,t)} \\ + \frac{1}{2}\int_0^v \omega_{c(v-v',v')} f_{(v-v',t)} f_{(v',t)} dv' - f_{(v,t)} \int_0^\infty \omega_{c(v,v')} f_{(v',t)} dv' \end{aligned} \tag{5.27}$$

5.2 Implementation

The population balance of equation 5.27 is a hyperbolic partial differential equation. Several methods are available to solve such equations [410–413]. In this case, a moving pivot technique that is a combination of two methods proposed by Kumar and Ramkrishna [414, 415] is selected. The time variable is discretized in the same intervals used during the computation of the kinetic model. This way, all the information provided by that module is used in a consistent way in the solution of the PBE.

The state variable (v) is discretized into adjoining size ranges, as shown in Figure 5.2. The ith bin is associated with its smallest size, of volume v_i. The continuous interval $[v_i, v_{i+1})$ is then represented by a characteristic particle volume u_i, called the ith pivot. Any volume belonging to the interval can be chosen. In this case, since particle diameters are expected to cover a wide range of sizes (from nm to cm), a logarithmically spaced grid is used, and the pivots are placed at the midpoint of each interval (in log scale).

Eq. 5.27 follows the evolution of the number density for an observer moving at a velocity equal to the particle growth rate; then, the grid boundaries and the pivot also move with such a velocity:

$$\frac{dv_i}{dt} = \dot{V}_{(v_i)} \tag{5.28}$$

$$\frac{dv_{i+1}}{dt} = \dot{V}_{(v_{i+1})} \tag{5.29}$$

$$\frac{du_i}{dt} = \dot{V}_{(u_i)} \tag{5.30}$$

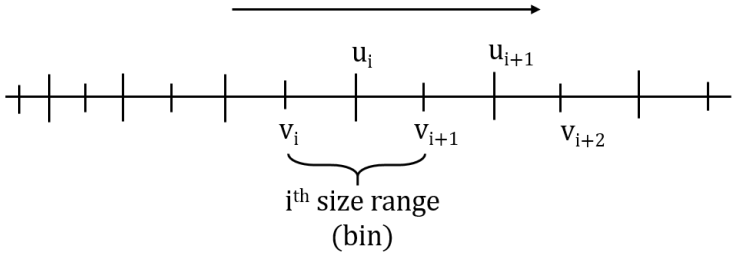

FIGURE 5.2: A discretized moving grid.

The discretization of the size variable into a grid with pivots means that the number density function can be expressed as a collection of Dirac's delta functions:

$$f_{(v,t)} \approx \sum_{i=1}^{\mathrm{NI}} \hat{N}_{i(t)} \delta_{(v-u_i)} \tag{5.31}$$

where $\hat{N}_{i(t)}$ is the average number of particles in the ith interval at time t, and NI is the total number of intervals in the grid.

The source of particles due to either breakage of larger particles, or to coalescence of smaller ones, must contemplate the fact that these processes may generate particles of sizes different from the chosen pivots. In that case, an assignment criterion must be defined to correctly compute the birth of particles due to this processes. In other words, if a droplet of volume $u_i < v < u_{i+1}$ is to be born, it is necessary to define a way to distribute the newborn particle between the pivots such that both number and mass of particles are preserved. Kumar and Ramkrishna [416] have suggested a procedure that guarantees such a preservation, thus making the computation physically consistent.

The source term due to breakage is then computed as:

$$2\int_{v}^{\infty}\omega_{b(v')}f_{(v,t)}\beta_{(v|v')}dv' \approx 2\sum_{j=i}^{\mathrm{NI}}\omega_{b(u_j)}\hat{N}_{j(t)}\left[\int_{u_{i-1}}^{u_i}\frac{v-u_{i-1}}{u_i-u_{i-1}}\beta_{(v,u_j)}dv+\int_{u_i}^{u_{i+1}}\frac{u_{i+1}-v}{u_{i+1}-u_i}\beta_{(v,u_j)}dv\right] \tag{5.32}$$

where the first term inside the square brackets represents the contribution to the ith pivot of the particle births in the interval (u_{i-1}, u_i), where as the second accounts for the births in (u_i, u_{i+1}).

The sink term is more readily computed:

$$\omega_{b(v)}f_{(v,t)} \approx \omega_{b(u_i)}\hat{N}_{i(t)} \tag{5.33}$$

In turn, the source term due to coalescence of smaller droplets is discretized as:

$$\frac{1}{2}\int_{0}^{v}\omega_{c(v-v',v')}f_{(v-v',t)}f_{(v',t)}dv' \approx \sum_{u_{i-1}\leq u_j+u_k\leq u_{i+1}}^{i\geq j\geq k}\left(1-\frac{1}{2}\delta_{(u_j-u_k)}\right)\nu\omega_{c(u_j,u_k)}\hat{N}_{j(t)}\hat{N}_{k(t)} \tag{5.34}$$

where $\delta_{(x)}$ is Dirac's delta function (here used to avoid computing repeated pairs of particles that undergo coalescence) and ν is the allocation function defined as:

$$\nu = \begin{cases} \dfrac{u_j+u_k-u_{i-1}}{u_i-u_{i-1}} & u_{i-1}\leq u_j+u_k\leq u_i \\ \\ \dfrac{u_{i+1}-(u_j+u_k)}{u_{i+1}-u_i} & u_i\leq u_j+u_k\leq u_{i+1} \end{cases} \tag{5.35}$$

In the implementation of Eq. 5.34, the domain upon which the sum is performed would have to be calculated at each time step. However, since the pivots change with time as per Eq. 5.30, which in this case is computed with Eq. 5.18, the inequalities do not change with time at all given that $\dot{V}_v$ is proportional to v [414]. Thus, it will be necessary to compute such domain only once during the numerical solution.

Finally, the sink term due to coalescence is computed as:

$$f_{(v,t)}\int_{0}^{\infty}\omega_{c(v,v')}f_{(v',t)}dv' \approx \hat{N}_{i(t)}\sum_{j=1}^{\mathrm{NI}}\omega_{c(u_i,u_j)}\hat{N}_{j(t)} \tag{5.36}$$

Turning to the solution of Eq. 5.27, the change in the total number of particles in the ith bin is obtained by integration between v_i and v_{i+1} after performing the product derivative rule on the growth term [415]:

$$\int_{v_i}^{v_{i+1}} \frac{df_{(v,t)}}{dt} dv + \int_{v_i}^{v_{i+1}} f_{(v,t)} \frac{d\dot{V}_{(v)}}{dv} dv = \int_{v_i}^{v_{i+1}} 2 \int_{v}^{\infty} \omega_{b(v')} f_{(v,t)} \beta_{(v|v')} dv' dv - \int_{v_i}^{v_{i+1}} \omega_{b(v)} f_{(v,t)} dv + \int_{v_i}^{v_{i+1}} \frac{1}{2} \int_{0}^{v} \omega_{c(v-v',v')} f_{(v-v',t)} f_{(v',t)} dv' dv - \int_{v_i}^{v_{i+1}} f_{(v,t)} \int_{0}^{\infty} \omega_{c(v,v')} f_{(v',t)} dv' dv \quad (5.37)$$

where

$$\frac{df_{(v,t)}}{dt} \equiv \frac{\partial f_{(v,t)}}{\partial t} + \frac{\partial f_{(v,t)}}{\partial v} \dot{V}_{(v)} \quad (5.38)$$

Solving the second term of the left hand side of Eq. 5.37 by parts yields:

$$\int_{v_i}^{v_{i+1}} \frac{df_{(v,t)}}{dt} dv + f_{(v,t)} \dot{V}_{(v)} \Big|_{v_i}^{v_{i+1}} - \int_{v_i}^{v_{i+1}} \dot{V}_{(v)} \frac{\partial f_{(v,t)}}{\partial v} dv = \int_{v_i}^{v_{i+1}} 2 \int_{v}^{\infty} \omega_{b(v')} f_{(v,t)} \beta_{(v|v')} dv' dv - \int_{v_i}^{v_{i+1}} \omega_{b(v)} f_{(v,t)} dv + \int_{v_i}^{v_{i+1}} \frac{1}{2} \int_{0}^{v} \omega_{c(v-v',v')} f_{(v-v',t)} f_{(v',t)} dv' dv - \int_{v_i}^{v_{i+1}} f_{(v,t)} \int_{0}^{\infty} \omega_{c(v,v')} f_{(v',t)} dv' dv \quad (5.39)$$

Combining the first and third terms of Eq. 5.39 and using Leibnitz rule, the final population balance equation for the ith bin is obtained:

$$\frac{d}{dt} \left[\int_{v_i}^{v_{i+1}} f_{(v,t)} dv \right] = \int_{v_i}^{v_{i+1}} 2 \int_{v}^{\infty} \omega_{b(v')} f_{(v,t)} \beta_{(v|v')} dv' dv - \int_{v_i}^{v_{i+1}} \omega_{b(v)} f_{(v,t)} dv + \int_{v_i}^{v_{i+1}} \frac{1}{2} \int_{0}^{v} \omega_{c(v-v',v')} f_{(v-v',t)} f_{(v',t)} dv' dv - \int_{v_i}^{v_{i+1}} f_{(v,t)} \int_{0}^{\infty} \omega_{c(v,v')} f_{(v',t)} dv' dv \quad (5.40)$$

which, using the discretizations suggested in Eqs. 5.31-5.36, results in:

$$\frac{d\hat{N}_{i(t)}}{dt} = 2\sum_{j=i}^{\mathrm{NI}} \omega_{b(u_j)}\hat{N}_{j(t)} \left[\int_{u_{i-1}}^{u_i} \frac{v-u_{i-1}}{u_i-u_{i-1}}\beta_{(v,u_j)}dv + \int_{u_i}^{u_{i+1}} \frac{u_{i+1}-v}{u_{i+1}-u_i}\beta_{(v,u_j)}dv \right] - \omega_{b(u_i)}\hat{N}_{i(t)} + \sum_{u_{i-1}\leq u_j+u_k\leq u_{i+1}}^{i\geq j\geq k} \left(1-\frac{1}{2}\delta_{(u_j-u_k)}\right)\nu\omega_{c(u_j,u_k)}\hat{N}_{j(t)}\hat{N}_{k(t)} - \hat{N}_{i(t)}\sum_{j=1}^{\mathrm{NI}}\omega_{c(u_i,u_j)}\hat{N}_{j(t)} \quad (5.41)$$

The pivots positions change with time due to growth as per Eq. 5.30. Eq. 5.41 is ready to be solved when coupled with the corresponding boundary and initial conditions. In this case, since nucleation is taken to be negligible and there are no particles of infinite mass, the boundary conditions are stated as:

$$\begin{cases} \dot{V}_{(v_{min},t)} f_{(v_{min},t)} = 0 \\ f_{(v_{max})} = 0 \end{cases} \quad (5.42)$$

The initial number density functions for each reaction are considered to follow a lognormal distribution with parameters μ and σ, with respect to particle diameter, as many dispersed systems (both polymeric and O/W) have shown such a behaviour [417–419]:

$$f_{(0,d)} = \hat{N}_0 \tilde{f}_{(0,d)} \quad (5.43)$$

where

$$\tilde{f}_{(0,d)} = \frac{1}{d\sigma\sqrt{2\pi}} \exp\left\{ -\frac{(\ln(d)-\mu)^2}{2\sigma^2} \right\} \quad (5.44)$$

In terms of particle volume, if spherical geometry is considered, the number density is:

$$f_{(0,v)} = \hat{N}_0 \frac{1}{3v\sigma\sqrt{2\pi}} \exp\left\{ -\frac{\left(\ln(6v/\pi)^{1/3}-\mu\right)^2}{2\sigma^2} \right\} \quad (5.45)$$

which means that it is a lognormal distribution with parameters $\ln\left(\frac{6}{\pi}\right) - 3\mu$ and 3σ. $\hat{N}_0$ is the number of particles at time $t = t_0$ (the time at which the system is considered to phase separate) per unit volume of reacting mixture, which is calculated as:

$$\hat{N}_0 = \frac{V_{v(t=t_0)}}{V_{T(t=t_0)} \sum_{i=1}^{\mathrm{NI}} \left[\int_{v_i}^{v_{i+1}} \tilde{f}_{(v)} dv \right] u_i} \tag{5.46}$$

5.2.1 Choice of kernel functions

As discussed in Section 2.4.4, there are several available equations to compute break-up and coalescence frequencies. None of the cited have been used on the HIPS bulk polymerization to date. However, some have been used in other polymeric systems [205, 291], which helps to establish a decision criterion. As a general rule, those expressions that have been developed for bubbles in liquids are disregarded, leaving preferably those that are employed in liquid-liquid dispersions. It is also desired to use equations that take into account the majority of the discussed effects on both particle break-up and particle coalescence. That is, expressions that show a dependence on both phase densities, both phase viscosities and on the interfacial tension.

5.2.1.1 Break-up

The choice of the breakage frequency seems to be narrowed down to the work developed originally by Narsimhan et al. [283] and continued by Alopaeus et al. [293]:

$$\omega_{b(v)} = C_{1b} \varepsilon^{1/3} \mathrm{erfc} \left(\sqrt{C_{2b} \frac{\gamma}{\rho_c \varepsilon^{2/3}} \left(\frac{\pi}{6v} \right)^{5/9} + C_{3b} \frac{\eta_d}{\sqrt{\rho_c \rho_d} \varepsilon^{1/3}} \left(\frac{\pi}{6v} \right)^{4/9}} \right) \tag{5.47}$$

where erfc(v) is the complementary error function and ε is the energy dissipation rate. Subscripts c and d stand for the continuous and the dispersed phase respectively.

Despite not showing a dependence on the continuous phase viscosity, this equation has been used extensively in liquid-liquid dispersions [204, 207, 420] with population balance applications. It is therefore taken to be the most suitable for this system. Figure 5.3 shows the evolution of ω_b as a function of particle size for different values of the main physical properties compared to a base case with $n = 100$ rpm, $\rho_c = 800$ kg/m^3, $\rho_d = 850$ kg/m^3, $\eta_d = 50$ cP and $\gamma = 10$ mN/m.

Regarding the daughter particle size distribution, the Beta function suggested by Hsia and Tavlarides [303] in Eq. 5.48 is adopted in this work, due to its simplicity and good results with liquid-liquid dispersions [304].

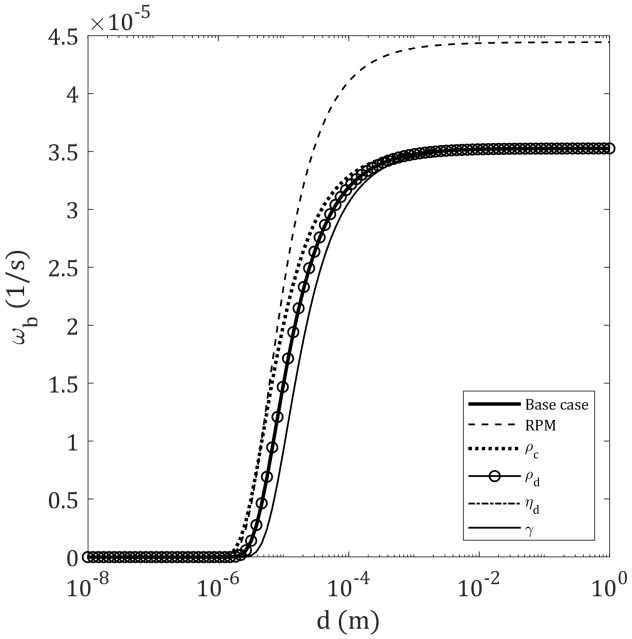

FIGURE 5.3: Predicted break-up frequency, ω_b for variations of the most important parameters. Each line represents a 100% increase on the corresponding variable compared to a base case.

$$\beta_{(v|v')} = 30\left(\frac{v}{v'}\right)^2\left(1-\frac{v}{v'}\right)^2 \tag{5.48}$$

5.2.1.2 Coalescence

As discussed in Section 2.4.4.1, the coalescence frequency is usually expressed as the product of a collision frequency and a coalescence efficiency, which serves to reflect the fact that not all particle collisions end in a coalescence event.

By far the most popular equation for the frequency of two colliding drops of volumes v and v' is the one by Coulaloglou and Tavlarides [228]:

$$\omega_{cd(v,v')} = C_{1c}\frac{\varepsilon^{1/3}}{1+\phi_d}\left(v+v'\right)^2\left(v^{2/9}+v'^{2/9}\right)^{1/2} \tag{5.49}$$

This equation was developed on the grounds of the kinetic gas theory, which may only apply to liquid-liquid dispersions if $\phi_d \to 0$ (that is, in dilute systems). A reasonable correction is needed if it is to be applied to a system like the one of this thesis, which rapidly becomes a dense dispersion. According to Hu et al. [79], this equation may still be the right choice but only if coupled with a radial distribution function. This accounts for the fact that

the probability of a particle of volume v "seeing" one of volume v' is not uniform. In this case, the distribution function developed by Song et al. [421] (based on the Carnhan-Starling equation of state) is used:

$$h_{(v,v')} = \frac{1}{1-\phi_d} + \frac{3}{2\left(1-\phi_d\right)^2}\xi_{(v,v')} + \frac{1}{2\left(1-\phi_d\right)^3}\xi^2_{(v,v')} \tag{5.50}$$

where

$$\xi_{(v,v')} = 2\left(\frac{vv'}{v+v'}\right)^{1/3}\sum_{i=1}^{N}\hat{N}_i v_i^{2/3} \tag{5.51}$$

where $\hat{N}_i$ is the number of particles of size v_i per unit volume of physical space and N is the total number of particles.

Then,

$$\omega_{cd(v,v')} = C_{1c}h_{(v,v')}\frac{\varepsilon^{1/3}}{1+\phi_d}\left(v+v'\right)^2\left(v^{2/9}+v'^{2/9}\right)^{1/2} \tag{5.52}$$

In turn, there are several possibilities for the coalescence efficiency (although not as many as the ones available for bubble-bubble collisions). In this case, four expressions will be considered and compared, namely those from Coulaloglou and Tavlarides [228] (**CT**), Hasseine et al. [255] (**H1** and **H2**) and Sovová [220] (**S**):

$$\lambda_{CT(v,v')} = \exp\left\{-C_{2c}\frac{\eta_c\rho_c\varepsilon}{\gamma^2\left(1+\phi_d\right)^3}\left(\frac{v^{1/3}v'^{1/3}}{v^{1/3}+v'^{1/3}}\right)^4\right\} \tag{5.53}$$

$$\lambda_{H1(v,v')} = \exp\left\{-C_{2c}\frac{\eta_d\rho_c^{1/2}\varepsilon^{2/3}d_{eq}^{11/6}(6/\pi)^{1/9}\left(v^{1/3}+v'^{1/3}\right)^{1/3}}{\gamma^{3/2}\left(1+C_{3c}\phi_d\right)^2 h_c}\right\} \tag{5.54}$$

$$\lambda_{H2(v,v')} = \exp\left\{-C_{2c}\frac{\eta_d}{\eta_c}\left[\frac{\eta_d\varepsilon^{1/2}d_{eq}}{\gamma}\left(\frac{\eta_c}{\rho_c}\right)^{-1/2}\right]^{3/2}\frac{d_{eq}}{h_c}\right\} \tag{5.55}$$

where

$$d_{eq} = 2\left(\frac{6}{\pi}\right)^{1/3} \frac{(vv')^{1/3}}{v^{1/3} + v'^{1/3}} \tag{5.56}$$

$$h_c = \left(\frac{d_{eq}}{16\pi\gamma}\right)^{1/3} \tag{5.57}$$

Finally,

$$\lambda_{S(v,v')} = \lambda_1 + \lambda_2 - \lambda_1\lambda_2 \tag{5.58}$$

where

$$\lambda_1 = \exp\left\{-C_{2c}\frac{\eta_c\rho_c\varepsilon}{\gamma^2}\left(\frac{v^{1/3}v'^{1/3}}{v^{1/3} + v'^{1/3}}\right)^4\right\} \tag{5.59}$$

$$\lambda_2 = \exp\left\{-C_{3c}\frac{\gamma}{\rho_d\varepsilon^{2/3}}\frac{(v+v')\left(v^{2/3} + v'^{2/3}\right)}{vv'\left(v^{2/9} + v'^{2/9}\right)}\right\} \tag{5.60}$$

It should be noted that the original expression for h_c in the models by Hasseine et al. include the use of a Hamaker constant, which is complex to evaluate in the system of this thesis. Therefore, it is assumed that, whichever its value, it will remain approximately constant throughout the reaction and may be lumped together with the C_{2c} parameter.

In order to compare and contrast each coalescence efficiency model, several simulations were performed, changing the value of the main physical properties that have an effect on these equations. The comparative results are shown in Figures 5.4-5.8, where the average value of λ is plotted as a function of drop diameter. The base case considers $n = 30$ rpm, $\rho_c = 800$ kg/m^3, $\rho_d = 850$ kg/m^3, $\eta_c = 100$ cP, $\eta_d = 50$ cP and $\gamma = 10$ mN/m.

As observed, all models predict that coalescence should be less efficient at high drop sizes, which is expected. However, an interesting feature is noticed in the expression by Sovová, where a local minimum can be found. This would seem to imply that there exists a range of particle sizes for which coalescence is not *as efficient*, and particles in that range may therefore "survive" more than others. This becomes particularly interesting for the case of HIPS, where a large number of small particles seem to never undergo coalescence and are consequently left as occlusions (as observed in the TEM images).

Besides, the expression by this author combines the two most popular approaches of the

coalescence efficiency theory: the film drainage and the energetic models. It seems to be a robust equation that may account for the observed phenomena of the HIPS polymerizing system, and is therefore adopted in this work.

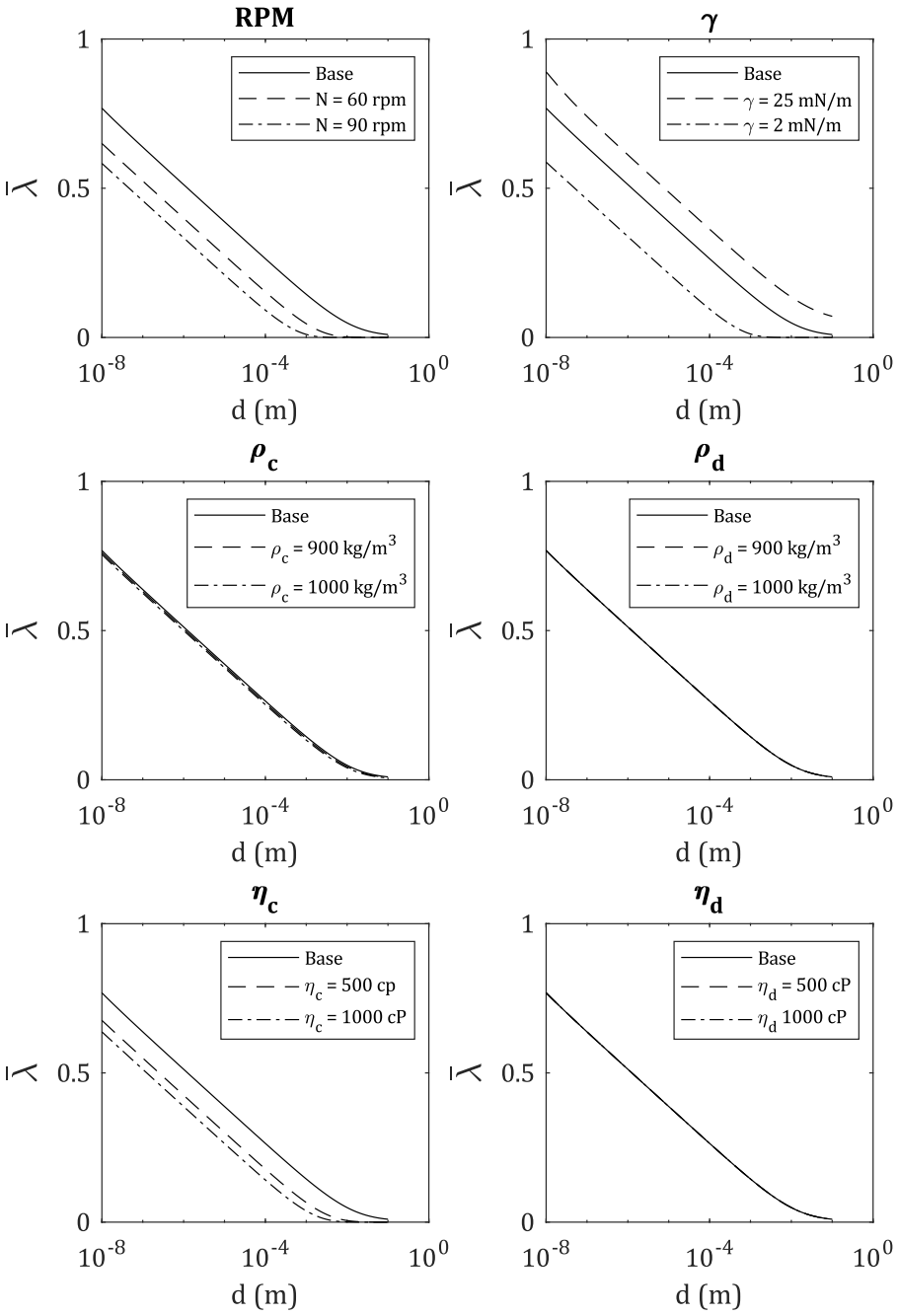

FIGURE 5.4: Coalescence efficiency model by Coulaloglou and Tavlarides [228], λ_{CT}.

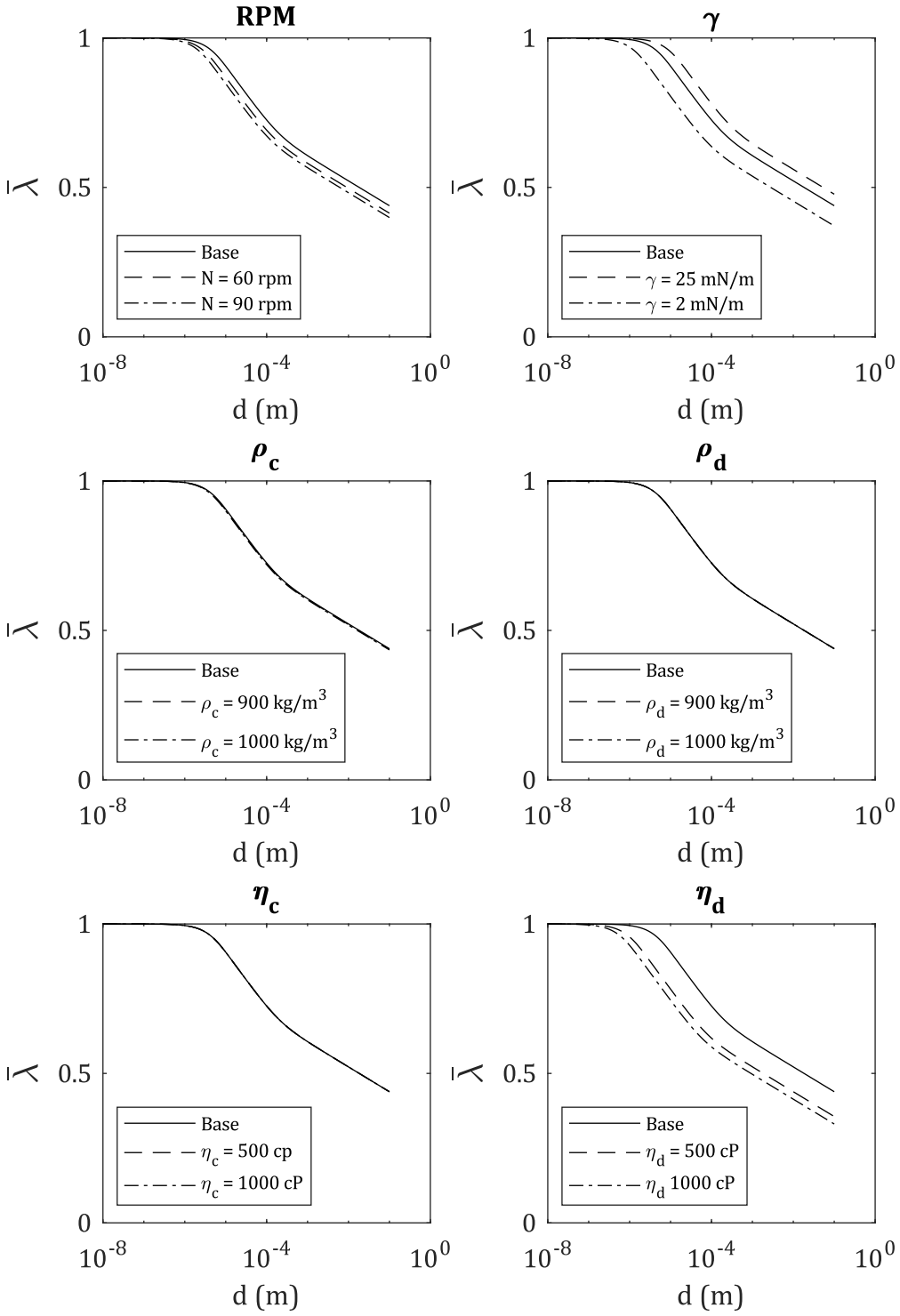

FIGURE 5.5: Coalescence efficiency model by Hasseine [255], λ_{H1}.

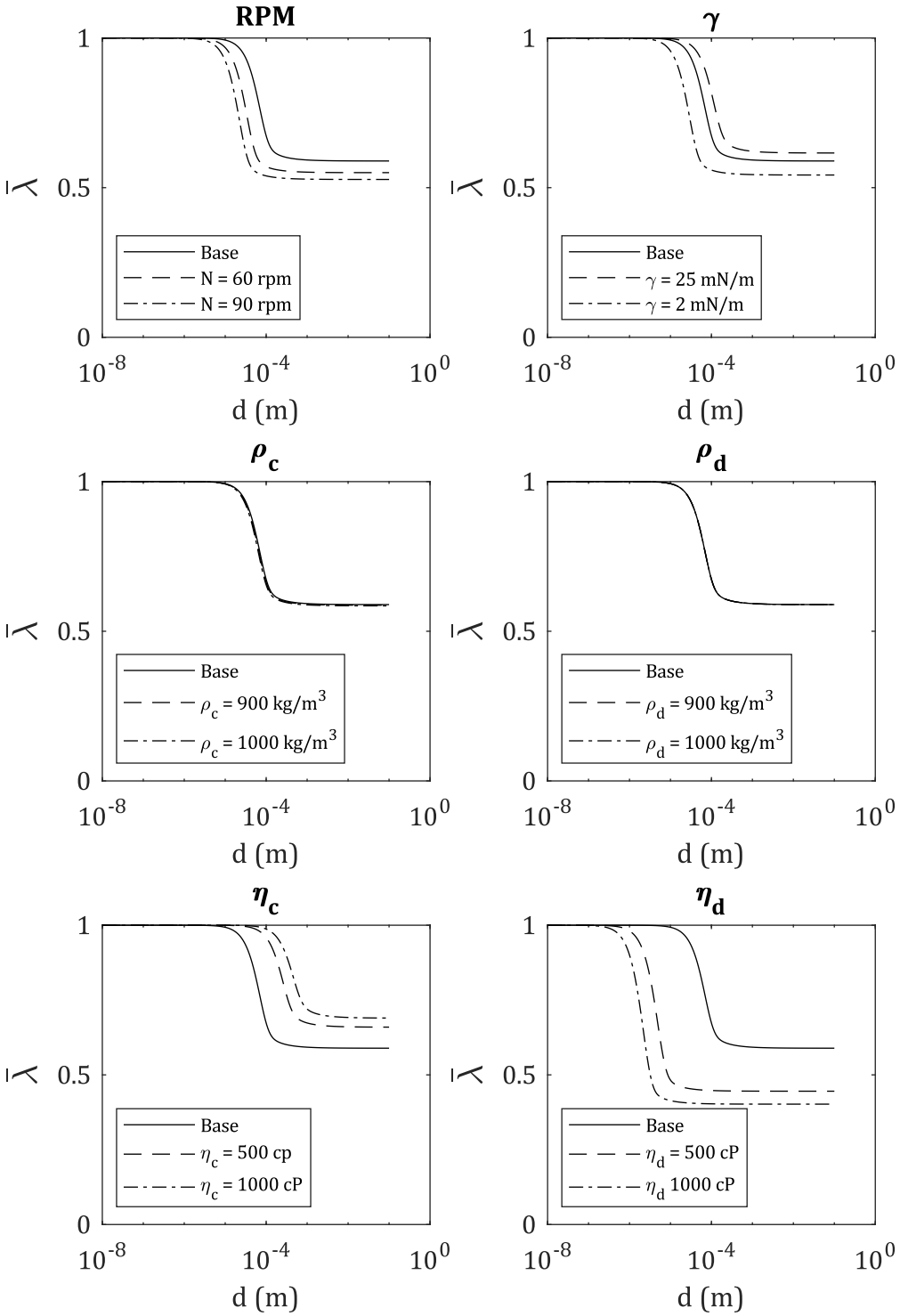

FIGURE 5.6: Coalescence efficiency model by Hasseine [255], λ_{H2}.

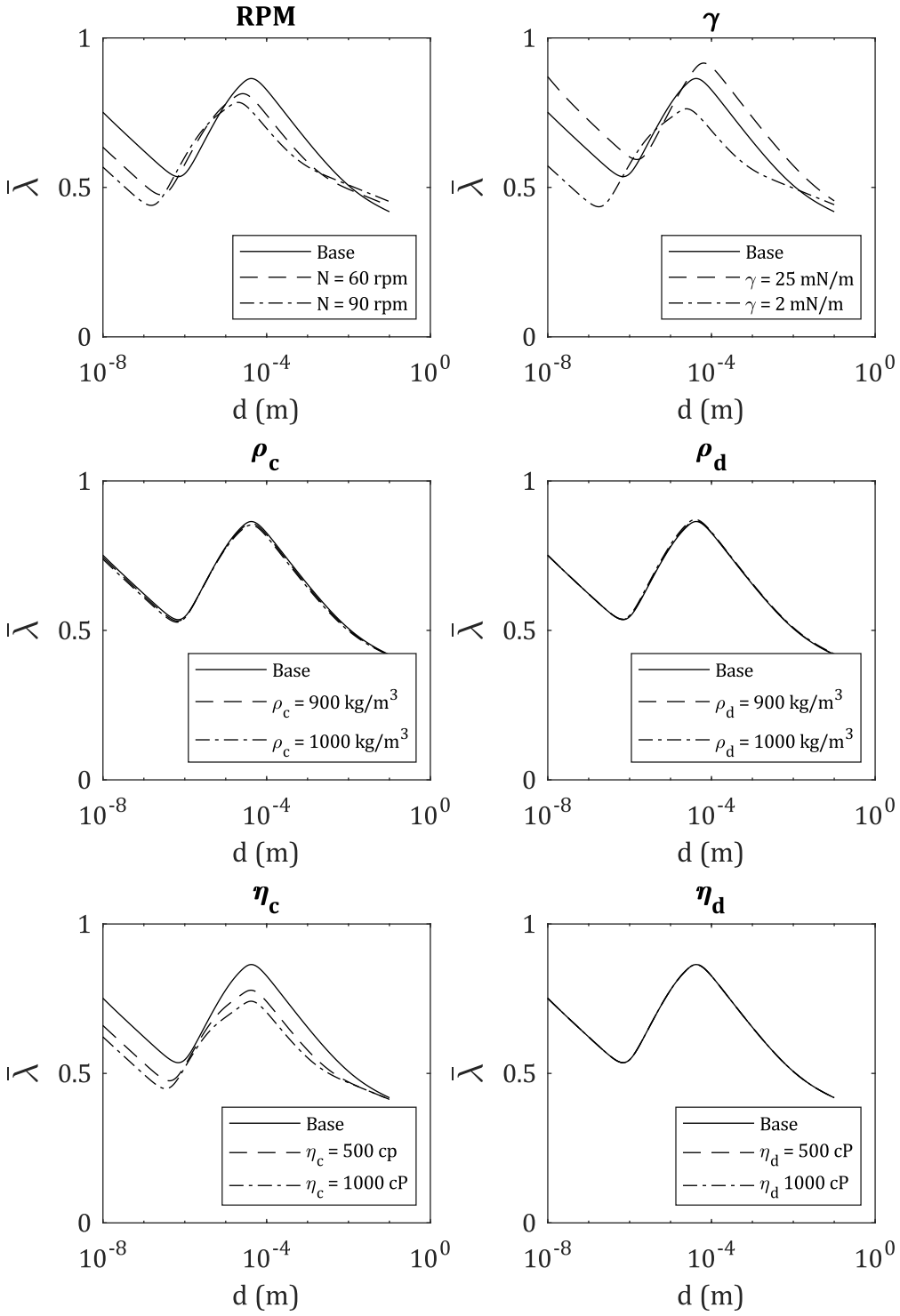

FIGURE 5.7: Coalescence efficiency model by Sovová [220], λ_S.

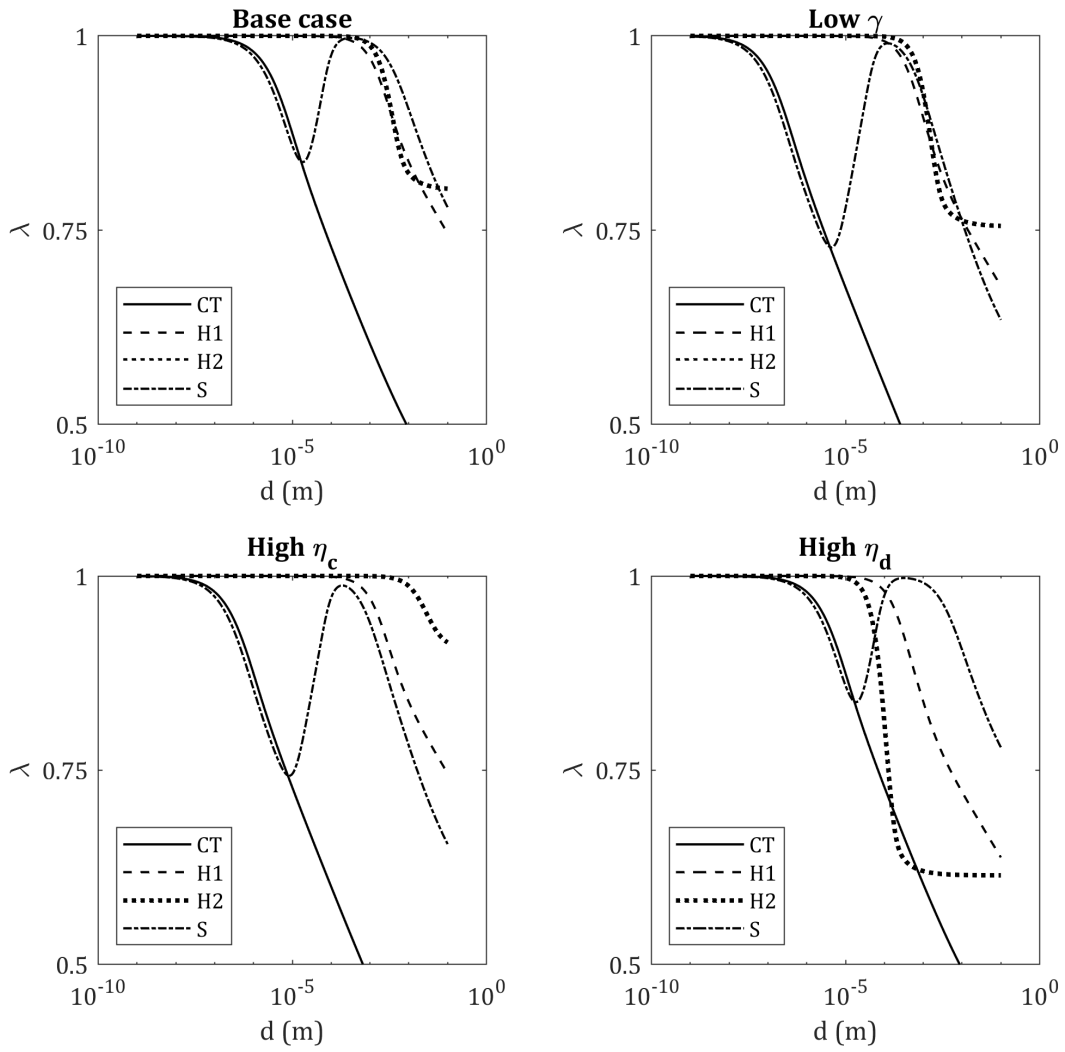

FIGURE 5.8: Comparison of coalescence efficiency models.

5.2.2 Phase properties

The densities of styrene, polystyrene and polybutadiene (in kg/m^3) vary with temperature (in °C) according to the expressions found in Table 5.1. The phase densities are computed from the values of each pure compound assuming additive volumes. Regarding the phase viscosities, the expressions used in this model are essentially the same as the ones used in Chapter 4, corrected by temperature and shear rate. They are summarized in Table 5.2.

Given that the polymeric mixture exhibits a non-Newtonian behaviour, it is necessary to compute the effective shear rate inside the reactor. For achor-type impellers, it may be computed with Eq. 5.61 [424].

Density	Reference
$\rho_{St} = 924 - 0.918T$	[404]
$\rho_{PS} = 1084.8 - 0.605T$	[404]
$\rho_{PB} = \left[1.097 \times 10^{-3} + 7.679 \times 10^{-7}T - 2.222 \times 10^{-10}T^2\right]^{-1}$	[422]

TABLE 5.1: Compound densities.

Viscosity	Reference
$\eta_r = \exp\left[a\left(\frac{1}{T} - \frac{1}{298}\right) + \ln(\eta_{r0})\right]$	
$a = 1052.192$	[423]
$\ln(\eta_{r0}) = 38.7\left[1 - \exp\left(-1.6974\dot{\gamma}\right)\right](1 - w_{St,r}) + \dfrac{2.4589}{\dot{\gamma} + 0.3472} + 2.3387$	Eqs. 4.20-4.22
$\eta_v = \dfrac{\eta_0}{\left(1 + \dfrac{\eta_0\dot{\gamma}^{1.2}}{35000}\right)^{0.6}}$	[403]
$\eta_0 = 1000\exp\left\{-11.091 + \dfrac{1109}{T} + M_{w,PS}^{0.1413}\left[12.032w_{PS,v} - 19.501w_{PS,v}^2 + 2.923w_{PS,v}^3 + \dfrac{1}{T}\left(-1327w_{PS,v} + 1359w_{PS,v}^2 + 3597w_{PS,v}^3\right)\right]\right\}$	

TABLE 5.2: Phase viscosities (in cP).

$$\dot{\gamma} = 25n\sqrt{\frac{D_I}{D_T}} \tag{5.61}$$

Regarding the interfacial tension, it is computed with a combination of the expression by Kwok and Neumann [425] for a copolymer-free system, γ_0, and that of Noolandi and Hong [426] to account for its reduction in the presence of the graft copolymer, $\Delta\gamma$:

$$\gamma_0 = \sigma_v + \sigma_r - 2\sqrt{\sigma_v\sigma_r}\exp\left[-\alpha\left(\sigma_v - \sigma_r\right)^2\right] \tag{5.62}$$

where $\alpha = 1.247 \times 10^{-3}$ m^2/mN^2 is a quasi-universal constant.

$$\Delta\gamma = W\phi_{cop}\left\{\frac{\chi}{2}\left(\phi_{PB}+\phi_{PS}\right)+\frac{1}{z_{St}+z_B}\left[1-\exp\left[\frac{\chi}{2}\left(z_{St}+z_B\right)\left(\phi_{PB}+\phi_{PS}\right)\right]\right]\right\} \quad (5.63)$$

where χ is the Flory-Huggins parameter for the PS-PB pair (here calculated with solubility parameters [427]), ϕ_{cop} is the volume fraction of the graft copolymer, while z_{St} and z_B are the polymerization degrees of the PS and PB chains in the copolymer molecule respectively. Furthermore, W is the width at half height of the copolymer profile, which is here approximated to [428]:

$$W = b\left(\frac{2\chi}{3(1-\phi_{St})}\right)^{0.5} \quad (5.64)$$

where b is the average Kuhn length (6.95 Å [429]).

Then, the interfacial tension is calculated as:

$$\gamma = \gamma_0 + \Delta\gamma \quad (5.65)$$

It should be noted that, even though the original equation by Noolandi and Hong was developed for block copolymers, the research by Asaletha et al. [430] suggests that it may be applied to graft copolymers as well, and it is therefore used in this system.

On Eq. 5.62, the surface tension of the vitreous phase, σ_v, is computed with the following correlation, which was obtained from the empirical data reported by Cerpa-Gallegos et al. [431]:

$$\sigma_v = S_0 + K\left(1-w_{St,v}\right)^a M_{w,PS}^b \quad (5.66)$$

where S_0 is the surface tension of pure styrene (31.627 mN/m) and $M_{w,PS}$ is expressed in kg/mol. $K = 2.75$ mN/m, $a = 1.07725$ and $b = 0.49657$ were found to accurately fit the experimental data.

Furthermore, the surface tension of the rubber-rich phase is computed through a mixing rule, following Prigogine and Marechal [432]:

$$\sigma_r = S_0\phi_{St,r} + \sigma_{PB}\left(1-\phi_{St,r}\right) \quad (5.67)$$

where σ_{PB} is the surface tension of polybutadiene, which is here computed using the Parachor method with the group contributions assigned by Sugden [433].

Finally, the temperature dependence on each surface tension is computed using the ratio of the phase densities [434]:

$$\sigma_{i(T)} = \sigma_{i(T_0)} \left(\frac{\rho_{i(T)}}{\rho_{i(T_0)}} \right)^4 \tag{5.68}$$

5.3 Results

5.3.1 Model adjustment

The set of equations that correspond to the kinetic heterogeneous model is solved in the first place. A traditional differential equation solution method, based on a 2nd order Rosenbrock formula (suitable for stiff systems) is used. Kinetic parameters are taken from literature [389, 405, 406].

Figure 5.9 shows the evolution of monomer conversion, PS weight-average molecular weight and grafting efficiency, both as measured experimentally and as predicted by the model. A very good agreement is observed between the theoretical curves and the corresponding measurements.

The evolutions of all the main reaction variables are then fed to the PBE model with an acceptable level of accuracy. Then, this model calculates the particle size distributions (PSDs) along the polymerization. In this case, the adjusting procedure consists of finding an acceptable order of magnitude for the values of C_{1c}, C_{2c}, C_{3c}, C_{1b}, C_{2b} and C_{3b} and fine-tuning with the values of μ and σ (the statistical parameters that provide the initial condition for the number density function) so that the calculated PSDs fit the ones observed from the available TEM images. It should be noted that, since the micrographs show "unswollen" morphologies (that is, without styrene), the theoretical PSDs are drawn as a function of a modified particle size - one that contains no monomer. This is easily achieved since each vitreous drop has the same composition, calculated with Eq. 4.3 at any timestep.

The need of varying the initial conditions obeys to an empirical obstacle: while it is expected that temperature, initiator concentration and stirring speed all have an effect on the initial PSD (as per phase separation theory [435, 436]), they are not known due to the lack of sufficient experimental evidence. Therefore, these are not computed and are rather introduced as adjustable parameters to serve a fitting purpose. This feature may be certainly

improved with additional empirical work.

An image analysis technique, similar to the one used to compute the PSD shown in Figure 4.5, is now performed on the available TEM images before the phase inversion point. These measured distributions are shown in Figure 5.10, and compared with the theoretical evolution as per the PBE model. As observed, an acceptable agreement is obtained. The values of the adjusted parameters are given in Tables 5.3.

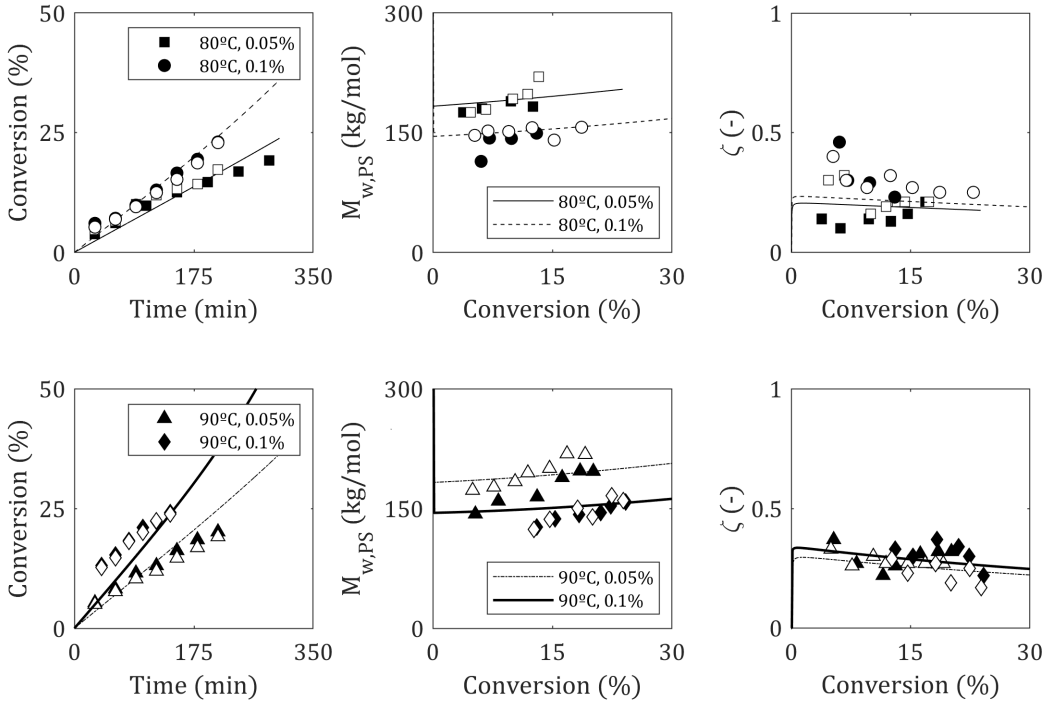

FIGURE 5.9: Main reaction variables predicted by the heterogeneous model. Black markers: reactions at 30 rpm; white markers: reactions at 60. Lines: theoretical evolutions.

Constant	Value
C_{1c}	5×10^{-4}
C_{2c}	1×10^{3}
C_{3c}	1×10^{-9}
C_{1b}	1×10^{-4}
C_{2b}	1×10^{-5}
C_{3b}	1×10^{-5}

TABLE 5.3: Values of the adjusted parameters in the coalescence and breakage frequencies.

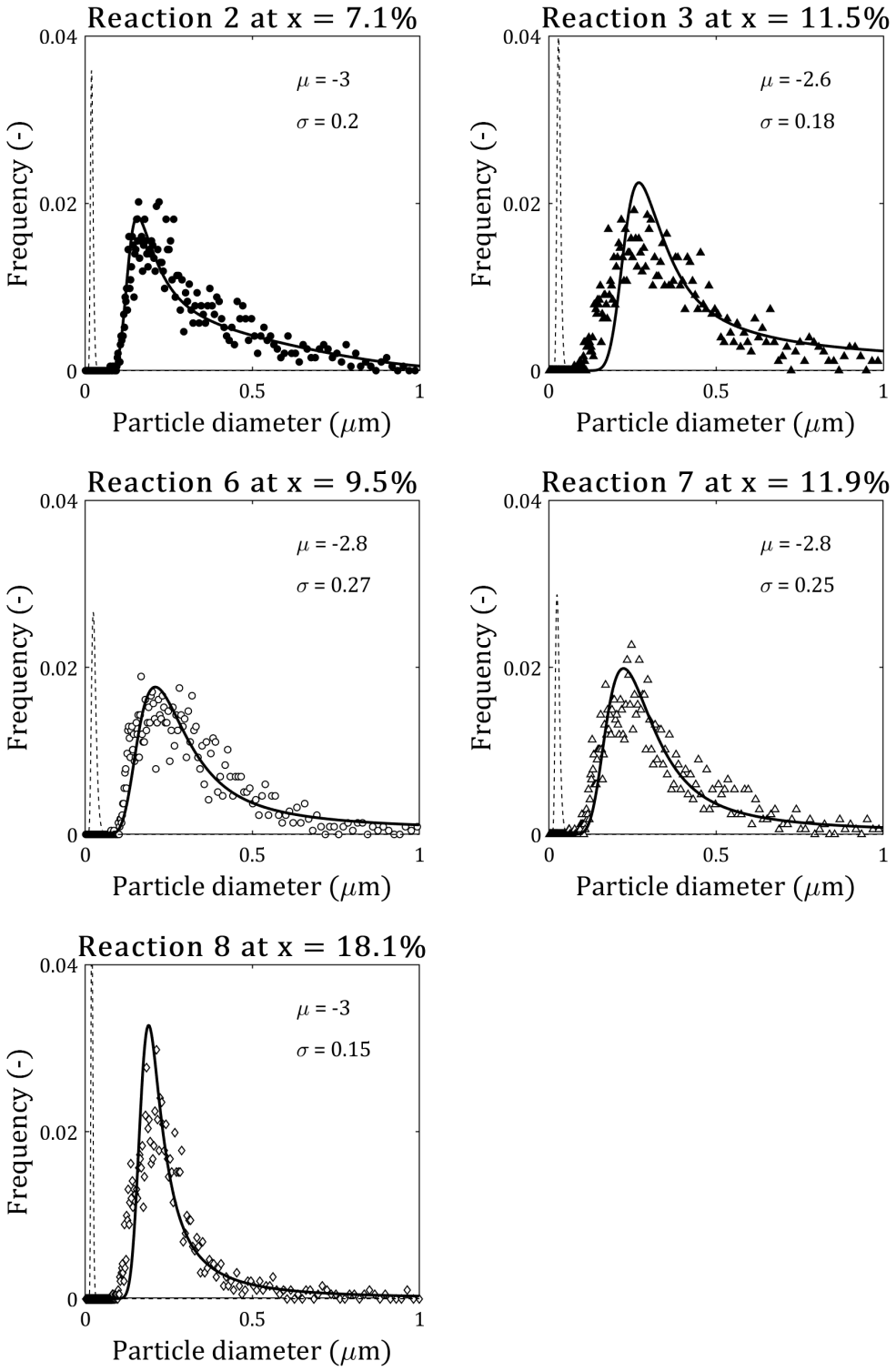

FIGURE 5.10: Particle size distributions for the set of reactions for which available TEM images could be analyzed. Dashed lines correspond to the initial conditions. Each subfigure shows the values of μ and σ set for the initial condition.

5.3.2 Phase inversion criterion

After adjusting the model parameters to correctly predict the monomer-free PSDs, the criterion for phase inversion is assessed. As discussed in Chapter 2, several authors claim that PI will occur when the coalescence frequency increases to an infinitely high value, or when it becomes infinitely higher than the breakage velocity [54, 79]. That is, either $\Omega_c \to \infty$ or $\Omega_c \gg \Omega_b$.

The PBE model is able to calculate these frequencies along the polymerization. For example, Figure 5.11 shows the evolution of the fractional coalescence frequency (fraction of particle pairs coalescing per unit time), where no exponential increase is observed. On the contrary, coalescence decreases along the reaction after having reached a local maximum. This means that, as the polymerization advances, less and less particles actually participate in the coalescence process.

Furthermore, Figure 5.12 shows the coalescence-to-brekage ratio for each reaction, with the respective PI zone highlighted in gray (as a visual aid). It is clear that the coalescence rate does not overwhelm the break-up rate at any point during any of the reactions. It does seem to be much higher than its counterpart (sometimes even three orders of magnitud), but never spikes to infinity. Moreover, even if it is thousands of times greater than the break-up rate, only few particles (less than 1% of them per second) actually undergo coalescence, according to Figure 5.11.

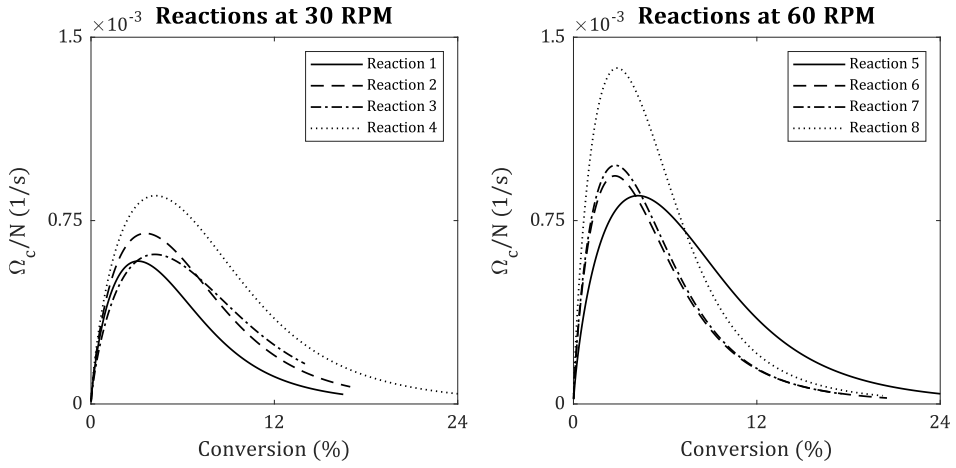

FIGURE 5.11: Fractional coalescence frequency for each reaction.

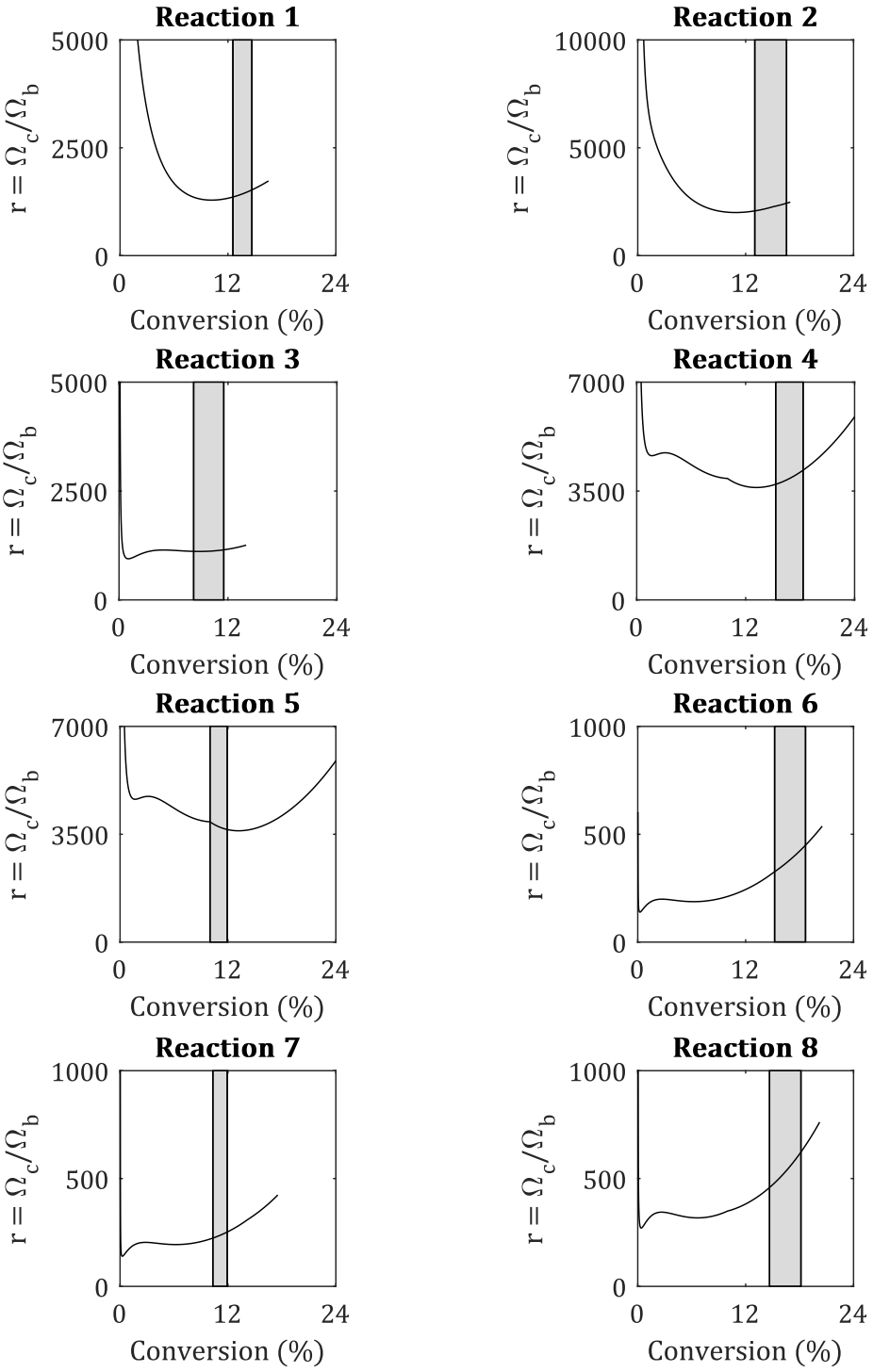

FIGURE 5.12: Coalescence-to-breakage velocity ratio for each reaction.

At first sight, this behaviour seems to imply that either PI does not occur at any point during the polymerizations, or that this model fails to predict the physics behind this phenomenon. However, after careful analysis, these theoretical evolutions may account for all

the physical evidence correctly.

To begin with, why would the coalescence rate increase during the reaction? As the polymerization proceeds, the following is observed:

- Phase viscosities increase considerably.
- Dispersed phase density increases.
- If $\Omega_c > \Omega_b$ (as is the case according to Figure 5.12), the net number of particles decreases along the reaction.
- Interfacial tension increases (due to monomer loss), but is dampened by the presence of the graft copolymer [437].

All these facts point towards a natural *decrease* in the collision frequency, and therefore in the coalescence rate, as the reaction proceeds. In consequence, the theoretical evolutions shown in Figure 5.11 seem to describe (at least qualitatively) a correct behaviour of the coalescence frequency. The local maximum is the result of an early increase in the collision rates, due to the presenence of a very large number of small particles, which gradually decelerates and becomes less and less frequent.

Secondly, even if the coalescence rate is infinitely high, it may not imply that the dispersed phase will consequently become the continuous one. Rather, the criterion that the coalescence frequency should be higher than the break-up one must be understood as a *necessary* condition (if the break-up rate is higher than the coalescence rate, PI is indeed impossible as more and more smaller particles would be formed), but not a *sufficient* one.

Phase inversion must be understood by its definition. For this purpose, consider the PI attempt shown illustratively in Figure 5.13a). In such a simplified system, the dispersed phase (line pattern) represents 54% of the system (in surface). As coalescence proceeds in the absence of breakage ($r_\Omega \to \infty$), all particles come together to form one large drop. Yet, no continuous phase is observed. For this particle to actually become the continuous phase, it **must** adhere to the system boundaries, as shown in subfigure b).

The need for the dispersed phase to stick to the solid surface of the vessel is perhaps taken for granted in most pieces of research, as there is little to no mention of it. The only work that seems to have considered this idea in its suggested model is the one by Brauner and Ullmann [200]. In their work, which was developed for O/W transport pipelines, the authors state - on an interesting combination of a thermodynamic and a fluid-dynamic approach - that Eq. 5.69 should hold at the PI point.

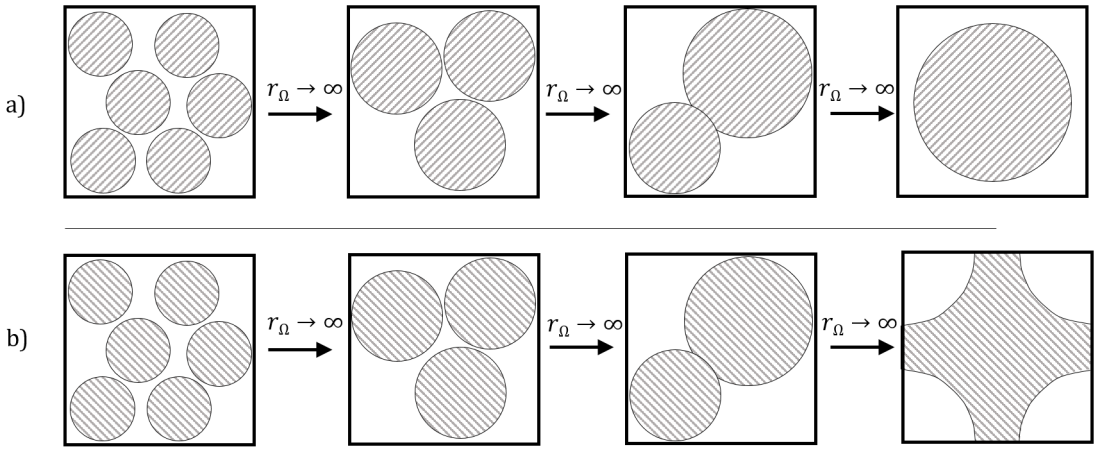

FIGURE 5.13: Phase inversion through particle coalescence: a) no phase inversion despite high coalescence rate, b) phase inversion occurs after the droplets correctly adhere to the system's boundaries. Each line-patterned phase represents 54% of the total area of the square.

$$\phi_o = \frac{1/d_{32,w/o} + \frac{s}{6}\cos(\theta)}{1/d_{32,w/o} + 1/d_{32,o/w}} \tag{5.69}$$

where $d_{32,o/w}$ and $d_{32,w/o}$ are the Sauter mean diameters of each dispersion, θ is the contact angle between the continuous phase and the vessel surface, and s is the solid surface area per unit volume.

The fact that the contact angle appears on this expression is an indication that surface adhesion should influence the PI point. This equation is of course difficult to verify in a predictive way, since the particle size distribution *right after* the PI point is not known. At most, a PBE model can calculate the PSD right up to the PI point, but does not actually detect that there has been a change in the identity of the dispersed phase.

In light of this discussion, how can the PBE model be used to predict the PI point during the HIPS prepolymerization reaction? In a strict sense, the model follows the evolution of the number density function along the reaction, considering that the dispersed phase is always the same. The $\Omega_c \to \infty$ criterion seems not apply in this case, since PI occurs gradually, without the need for the coalescence frequency to accelerate to an infinitely large value. PI can occur as long as $\Omega_c > \Omega_b$; this criterion alone is not enough to predict *when* it happens.

It would seem that, in a preliminary analysis, it is difficult for the PBE model to be used in a predictive way, without a clear criterion for inversion. Yet, it may still be used to verify any distinctive feature that *should* happen at the PI point.

For instance, judging by what is observed in the TEM images, it is clear that most part of

the dispersed particles do not actually participate in the inversion process. A large number of droplets are left behind as occlusions. Under the hypothesis that these occlusions do not migrate between the PI point and the time at which the first sample is taken (post PI), the occluded fraction observed by TEM may help to determine the fraction of vitreous phase that actually participates in the inversion process. This is done by separating the vitreous phase volume into the continous fraction and the occluded one:

$$\phi_v = \frac{V_{v,c} + V_{v,oc}}{V_T} = \frac{V_{v,c} + V_r \frac{\phi_{oc}}{1-\phi_{oc}}}{V_T} \tag{5.70}$$

which may be evaluated at $x = x_{PI}$ and rearranged to introduce $\Phi = \dfrac{V_{v,c}}{V_v}$, the fraction of vitreous phase that participates in the inversion process:

$$\phi_v\Big|_{x=x_{PI}} = \left[\phi_v \Phi + (1-\phi_v)\frac{\phi_{oc}}{1-\phi_{oc}}\right]\Bigg|_{x=x_{PI}} \tag{5.71}$$

from which:

$$\Phi = \left[1 - \frac{(1-\phi_v)}{\phi_v}\frac{\phi_{oc}}{(1-\phi_{oc})}\right]\Bigg|_{x=x_{PI}} \tag{5.72}$$

Furthermore, if the PBE balance is valid up to right before the PI point, the cumulative frequency distribution in particle **volume** (not in number) may be used to verify what would be expected at such a point. Consider the system of Figure 5.14, which represents a multiple dispersion and suppose that it has *just* inverted. Then, a differential timestep before PI, the total volume of the (soon-to-be) continuous phase may be represented by one large particle (regardless of its shape). At that point, the cumulative frequeny distribution would look like what is shown in the right box of the figure: if a fraction Φ participates in the inversion process, there would be a smooth growth up to $1 - \Phi$ and then it would increase sharply to 1.

In reality, the cumulative frequency distribution is expected to be a continuous function without increasing in a step-like manner when reaching the inversion fraction. However, its derivative should show a peak at that point, indicating the analogue version of the scheme shown in Figure 5.14.

With the information collected by the TEM micrographs, the average occluded phase fractions were determined as explained in Section 4.2.3. These values are summarized in Table 5.4 together with the corresponding values of Φ.

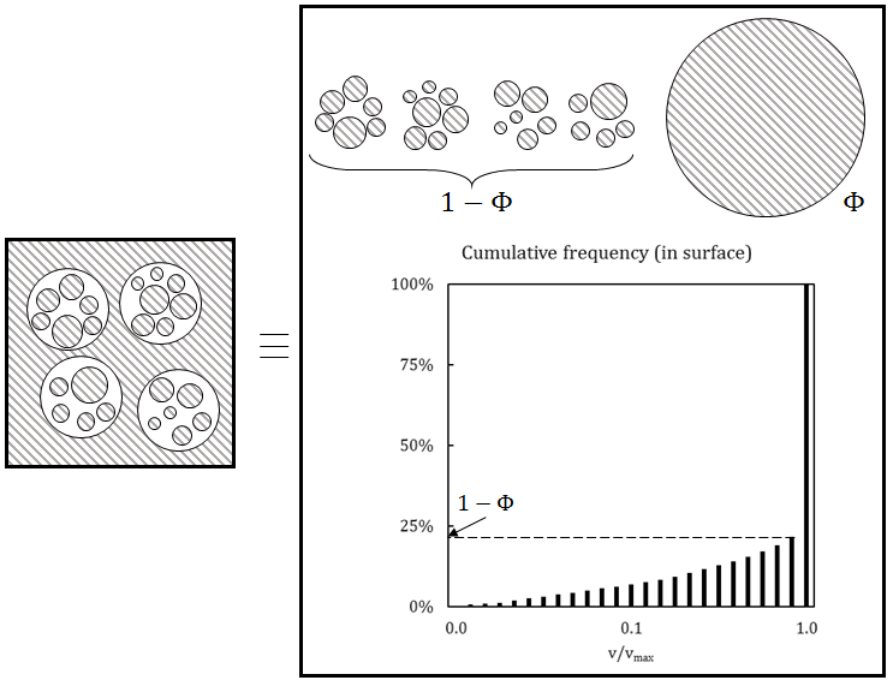

FIGURE 5.14: Visual representation of the volume cumulative frequency at the PI point.

The cumulative frequency distributions (φ) and its derivatives as calculated by the PBE model are shown in Figure 5.15 for each reaction (except for number 4, for there were no available TEM images) at the experimental inversion point. As observed, the peak in the derivatives occur around the calculated values of Φ, which is a good sign of consistency.

Reaction	$\overline{\phi_{\mathbf{oc,0}}}$	$\mathbf{\Phi}$ (Eq. 5.72)
1	0.5216	0.3692
2	0.5742	0.3059
3	0.4825	0.3196
4	–	–
5	0.4432	0.4368
6	0.5757	0.3782
7	0.4438	0.4186
8	0.5903	0.3215

TABLE 5.4: Average occluded fraction for each reaction at the PI point and the calculated inversion fraction.

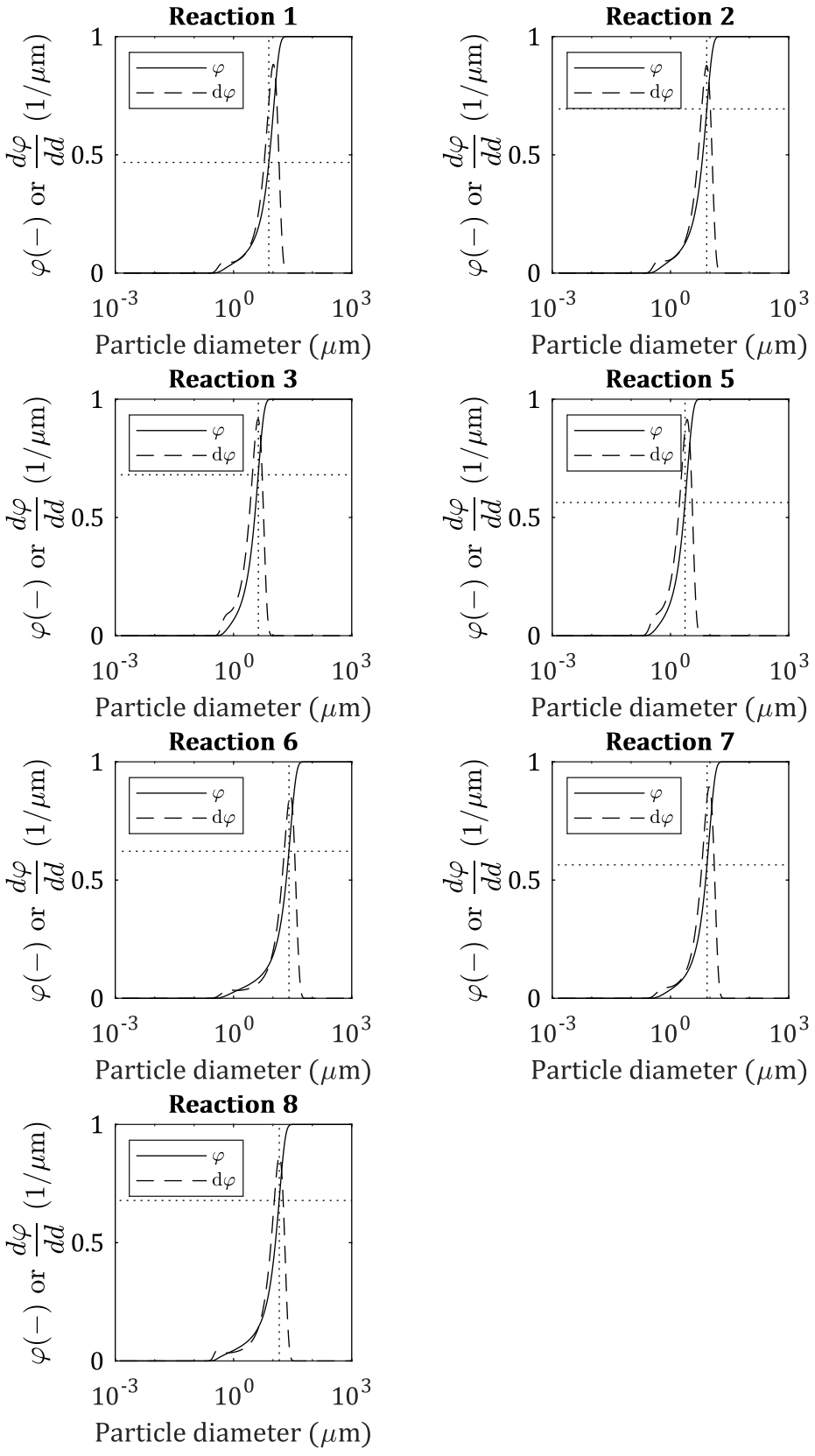

FIGURE 5.15: Volume cumulative frequency and its derivative for each reaction. The horizontal dotted line is drawn at Φ, and the vertical one is plotted as a visual aid to show the point at which $\varphi = \Phi$.

5.4 Summary and conclusions

An attempt to predict the phase inversion point during the batch polymerization of HIPS (under different initial conditions) was developed, in this case using a population balance approach. The evolution of the dispersed vitreous phase was modeled following a heterogeneous kinetic mechanism that accounts for the monomer partition at all times, thus enabling the discrete phase to incorporate styrene along the reaction as more polystyrene is produced. Such growth of the dispersed phase may be computed both algebraically or as the result of the differential kinetic model.

Alongside the growth process, the particle break-up and particle coalescence events were also computed. Expressions available in literature were used, after having analysed their suitability. Since it is not possible to actually measure the breakage and coalescence frequencies in this sytem (particles are initially too small to detect and the mixture becomes increasingly opaque as the polymerization proceeds), these expressions are not validated empirically but rather adjusted to fit the observed particle size distributions (obtained form TEM images) - which are *the result* of the breakage-coalescence balance. The physical properties on which these expressions depend are computed with equations available in literature and the ones developed in Chapter 4.

In the population balance model (a partial differential equation model) particle volume was chosen as the state variable, mainly for two reasons: i) most equations for particle break-up and coalescence frequencies are derived for a particle of a given volume, avoiding the need to assume a given geometry; and ii) particle growth rate is easily shown to be proportional to its volume. A log-scale grid is built to discretize the particle state continuum, as particles are expected to cover a wide range of sizes (from nm in the initial condition to cm in the final stages). An allocation function is further used to correctly compute the contribution to each bin of the grid after each coalescence of break-up event.

The fitting procedure included a fine tuning with the initial particle size distributions, for these are not known. Each initial and operating condition has an effect on the particle size distribution at the moment of phase separation. However, there are no available measurements to qualitatively describe this dependence. Had there been any, the initial PSDs would have been set without any adjustable parameters and the fitting process would have been done solely with the break-up and coalescence frequency models. This means that this feature may be improved with further experimental measurements.

Results show a very good agreement between the observed and the calculated PSDs. In consequence, the criterion for the occurence of phase inversion was assessed: interestingly, the coalescence frequency was not seen to have overwhelmed the breakage counterpart at any point in any reaction. After careful analysis, this was found not to necessarily mean

that PI does not occur in these reactions. Rather, it shows that - at least this system - PI probably occurs in a more gradual transition without the need for the coalescence rate to rise to infinity. Since a large fraction of the vitreous phase is left behind as occlusions (thus not participating in the inversion process), not all particles need to coalesce to form the continuous phase. This implies that the condition $\Omega_c \to \infty$ may not be a good criterion for this system.

Unfortunately, predicting the fraction of dispersed phase that will form the occluded phase at the inversion point is not currently possible with this model. This means that using the population balance model for the accurate prediction of the PI point is not feasible as it is. However, the model may correctly compute the cumulative frequency distributions, which show an acceptable shape, consistent with what would be expected at the PI point. This, at least, provides the model with a good level of consistency. Future research may include efforts to compute the occluded phase fraction *at the inversion point* so as to provide the model with a more predictive capability.

Chapter 6

Conclusions

"Endings, to be useful, must be inconclusive"

Samuel R. Delany

Throughout this thesis, the theoretical and empirical aspects of phase inversion (PI) processes were studied, in both traditional oil-water and polymeric dispersions. This phenomenon, by which the continuous phase becomes the dispersed phase and *vice versa*, holds a significant interest in several Chemical Engineering fields, from oil transport pipelines [438] to polymeric membranes [439]. In particular, this work focuses on the phase inversion that occurs during the manufacturing process of high impact polystyrene (HIPS), a reinforced engineering plastic. In this particular system, the PI process plays a major role, since it determines the final particle morphology of the material, which is tightly related to its advantageous physical properties.

The phenomenon of phase inversion - in general - is influenced by a number of physical and operating variables: densities, viscosities, interfacial tension, stirring speed, materials, etc., all of which were described in depth in Chapter 2. Being a nonlinear, multivariate, complex physical phenomenon, comprehensive models are still difficult to develop. Some empirical correlations can be found - especially in non-reactive systems - but no other advanced attempts have been researched. This is probably due to the wide variety of experimental evidence available, in which it is difficult to study the effect of one isolated variable on the PI point without overlapping the effect of another.

With the aim of understanding the underlying physics behind the PI mechanism in the presence of such an obstacle, artificial intelligence models were developed in Chapter 3. Insightful conclusions were drawn from such a study, the most important being:

- Geometrical aspects present a very strong and non-linear effect on the PI point. It is perhaps the most difficult effect to model accurately, since it is related to the turbulent dynamics of the breakage-coalescence imbalance.
- Interfacial tension and surface active components play a key role: surface deformability seems to be the entry point to an inversion path. It does not hold, however, a straightforward relationship with the inversion point, since a deformable interface is prone both to be ruptured and to be exposed to particle-particle collisions as its surface area increases.
- The known asymmetry between the O/W to W/O inversions and their counterparts is probably related to the ability of the organic phase to engulf stable water droplets, thus producing W/O/W double emulsions and changing the apparent dispersed phase fraction.
- The difference in phase densities seems to play a more important role than what has so far been reported. It is likely that this effect is masked by the effect of another variable when trying to study it experimentally (it is hard to produce two dispersions which differ *only* in one phase density).

After having harvested interesting information about the physics of this phenomenon, the PI process was studied for the HIPS system in Chapter 4. Particularly, the effect of reaction temperature, stirring speed and initiator concentration on the PI point were investigated, following the apparent viscosity of the mixture as an indicator of the inversion process. A rheological characterization determined that the mixture behaved as a non-Newtonian fluid whose apparent viscosity may be modeled at a chosen shear rate. Empirical expressions that depend on the reaction main variables (monomer conversion, molecular weights, grafting efficiency) were successfully developed, for mixtures before and after the PI point. These tools, however, cannot be used in a predictive way since the viscosity curves for already inverted mixtures depend on the monomer conversion *at* the PI point and on the occluded vitreous phase at that same moment. Notwithstanding, the theoretical/empirical work contributed to a better understanding on the weight of each variable on the inversion point, establishing a methodology for future research.

Finally, a second attempt on predicting the PI point during the polymerization of styrene in presence of polybutadiene was conducted. In Chapter 5, a population balance model (PBM) was developed which, coupled with a kinetic polymerization module, successfully predicted the particle size distributions of several reactions. The expressions for the break-up and coalescence frequencies for this model need to be chosen from a variety of options available in literature. The current lack of experimental evidence makes it impossible to assess them empirically, as is the case for the initial conditions. The suggested expressions used in this work can be modified or improved in future works, with more and better experimental

techniques. The most interesting conclusion drawn from the results of this model is the fact that the inversion point does not need to occur when the coalescence rate becomes infinitely larger than the break-up one; rather, only a fraction of the dispersed phase needs to adhere to the vessel walls for PI to occur. This accounts for the fact that a large portion of the vitreous phase never inverts and stays as particle occlusions once PI has befallen. Unfortunately, this also means that this model - at least as it is - cannot be used to predict the PI point either.

The work developed in this thesis may allow for future research to continue on this line or even to extend it to other similar systems. For example, the AI models developed in Chapter 3 may be implemented for emulsions, with the correct characterization of each surfactant. A more direct improvement would be the extension to the continuous manufacturing process of HIPS, both for continually stirred tank reactors (CSTR)s and non-agitated tubular reactors. A modified version of the population balance model could be implemented to predict the PI point and the morphology that is therein developed. A comprehensive model that can accurately predict the system properties at the inversion point may serve as an optimization opportunity for the HIPS industry and, for that matter, to any other composite materials in whose morphology lie the quality variables of interest.

Hybrid models, comprised of an artificial intelligence module and a polymerization-PBM module, could also be of interest. Together with Design of Experiment (DoE) techniques, which have already been implemented in other polymeric systems [440, 441], a route towards modelling taylor-made polymers seems to be possible.

Appendix A

Phase Inversion Data from Literature

In the following table, NB = number of baffles, TM = tank material (G = glass, SS = stainless steel) and IT = impeller type, with the following number code: 1: Rushton Turbine, 2: Propeller, 3: Saw-teeth, 4: Single-bladed.

Author	**Organic phase**	**Aqueous phase**	ρ_o	ρ_w	μ_o	μ_w	γ	**N**	**IT**	$\mathbf{D_I}$	$\mathbf{D_I/D_T}$	**NB**	**TM**	ϕ_o	ϕ_w
			kg/m^3	kg/m^3	cP	cP	mN/m	RPM		m					
Arashmid and Jeffreys (1980) [74]	CCl_4	Water	1595	1000	2.03	1	49.57	307	1	0.05	0.49	4	G	0.602	
			1595	1000	2.03	1	49.57	311	1	0.05	0.49	4	G		0.795
			1595	1000	2.03	1	49.57	435	1	0.05	0.49	4	G	0.537	
			1595	1000	2.03	1	49.57	411	1	0.05	0.49	4	G		0.835
			1595	1000	2.03	1	49.57	362	1	0.05	0.49	4	G	0.567	
			1595	1000	2.03	1	49.57	511	1	0.05	0.49	4	G	0.528	0.781
			1595	1000	2.03	1	49.57	580	1	0.05	0.49	4	G		0.76
			1595	1000	2.03	1	49.57	612	1	0.05	0.49	4	G	0.517	
			1595	1000	2.03	1	49.57	660	1	0.05	0.49	4	G	0.512	0.735
			1595	1000	2.03	1	49.57	753	1	0.05	0.49	4	G	0.501	0.709
			1595	1000	2.03	1	49.57	801	1	0.05	0.49	4	G	0.494	0.696
	Kerosene	Water	746	1000	1.31	1	10.6	160	1	0.05	0.49	4	G	0.559	0.961
			746	1000	1.31	1	10.6	270	1	0.05	0.49	4	G	0.522	0.96
			746	1000	1.31	1	10.6	383	1	0.05	0.49	4	G	0.509	0.959
			746	1000	1.31	1	10.6	493	1	0.05	0.49	4	G	0.493	0.955
			746	1000	1.31	1	10.6	601	1	0.05	0.49	4	G	0.489	0.954
			746	1000	1.31	1	10.6	302	1	0.05	0.49	4	G	0.96	
			746	1000	1.31	1	10.6	350	1	0.05	0.49	4	G	0.943	
			746	1000	1.31	1	10.6	400	1	0.05	0.49	4	G	0.923	
			746	1000	1.31	1	10.6	552	1	0.05	0.49	4	G	0.904	
Deshpande and Kumar (2003) [96]	Nitrobenzene	Water	1200	1000	1.86	1	51.24	547	1	0.045	0.44	4	G	0.949	0.369
			1200	1000	1.86	1	51.24	746	1	0.045	0.44	4	G	0.928	0.448
			1200	1000	1.86	1	51.24	948	1	0.045	0.44	4	G	0.898	0.49

		1200	1000	1.86	1	51.24	1147	1	0.045	0.44	4	G	0.892	0.49
		1200	1000	1.86	1	51.24	1349	1	0.045	0.44	4	G	0.849	0.51
		1200	1000	1.86	1	51.24	1450	1	0.045	0.44	4	G	0.839	
		1200	1000	1.86	1	51.24	1498	1	0.045	0.44	4	G	0.82	
		1200	1000	1.86	1	51.24	1548	1	0.045	0.44	4	G	0.79	0.507
		1200	1000	1.86	1	51.24	1649	1	0.045	0.44	4	G	0.749	
		1200	1000	1.86	1	51.24	1748	1	0.045	0.44	4	G	0.741	0.51
		1200	1000	1.86	1	51.24	1849	1	0.045	0.44	4	G	0.73	
		1200	1000	1.86	1	51.24	1950	1	0.045	0.44	4	G	0.724	
		1200	1000	1.86	1	51.24	598	1	0.045	0.44	4	G	0.67	
		1200	1000	1.86	1	51.24	799	1	0.045	0.44	4	G	0.647	0.755
		1200	1000	1.86	1	51.24	999	1	0.045	0.44	4	G	0.636	0.774
		1200	1000	1.86	1	51.24	1199	1	0.045	0.44	4	G	0.636	0.785
Benzene	Water	879	1000	0.65	1	25	549	1	0.045	0.44	4	G	0.76	0.408
		879	1000	0.65	1	25	752	1	0.045	0.44	4	G	0.76	0.469
		879	1000	0.65	1	25	952	1	0.045	0.44	4	G	0.688	0.517
		879	1000	0.65	1	25	1150	1	0.045	0.44	4	G	0.681	0.567
		879	1000	0.65	1	25	1350	1	0.045	0.44	4	G	0.651	0.58
		879	1000	0.65	1	25	1553	1	0.045	0.44	4	G	0.641	0.577
		879	1000	0.65	1	25	1751	1	0.045	0.44	4	G	0.615	0.586
		879	1000	0.65	1	25	1956	1	0.045	0.44	4	G	0.598	0.596
		879	1000	0.65	1	25	549	1	0.055	0.54	4	G	0.648	0.509
		879	1000	0.65	1	25	749	1	0.055	0.54	4	G	0.631	0.549
		879	1000	0.65	1	25	947	1	0.055	0.54	4	G	0.61	0.57
		879	1000	0.65	1	25	1150	1	0.055	0.54	4	G	0.612	0.584
		879	1000	0.65	1	25	1350	1	0.055	0.54	4	G	0.611	0.595
		879	1000	0.65	1	25	1550	1	0.055	0.54	4	G	0.598	

		879	1000	0.65	1	25	1753	1	0.055	0.54	4	G	0.598	
		879	1000	0.65	1	25	1951	1	0.055	0.54	4	G	0.6	
		879	1000	0.65	1	25	751	1	0.045	0.35	4	G		0.54
		879	1000	0.65	1	25	949	1	0.045	0.35	4	G		0.562
		879	1000	0.65	1	25	1152	1	0.045	0.35	4	G		0.602
		879	1000	0.65	1	25	1356	1	0.045	0.35	4	G		0.595
		879	1000	0.65	1	25	1746	1	0.045	0.35	4	G		0.613
		879	1000	0.65	1	25	949	1	0.045	0.35	4	G	0.718	
		879	1000	0.65	1	25	1152	1	0.045	0.35	4	G	0.677	
		879	1000	0.65	1	25	1356	1	0.045	0.35	4	G	0.65	
		879	1000	0.65	1	25	1551	1	0.045	0.35	4	G	0.616	
		879	1000	0.65	1	25	1754	1	0.045	0.35	4	G	0.618	
Heptane	Acetonitrile	684	786	0.38	0.33	8.9	550	1	0.045	0.44	4	G		0.317
		684	786	0.38	0.33	8.9	750	1	0.045	0.44	4	G		0.366
		684	786	0.38	0.33	8.9	1150	1	0.045	0.44	4	G		0.421
		684	786	0.38	0.33	8.9	1350	1	0.045	0.44	4	G		0.43
		684	786	0.38	0.33	8.9	550	2	0.068	0.66	4	G		0.368
		684	786	0.38	0.33	8.9	750	2	0.068	0.66	4	G		0.382
		684	786	0.38	0.33	8.9	950	2	0.068	0.66	4	G		0.391
		684	786	0.38	0.33	8.9	1150	2	0.068	0.66	4	G		0.433
		684	786	0.38	0.33	8.9	1350	2	0.068	0.66	4	G		0.426
		684	786	0.38	0.33	8.9	550	1	0.045	0.44	4	G	0.728	
		684	786	0.38	0.33	8.9	750	1	0.045	0.44	4	G	0.726	
		684	786	0.38	0.33	8.9	950	1	0.045	0.44	4	G	0.711	
		684	786	0.38	0.33	8.9	1150	1	0.045	0.44	4	G	0.709	
		684	786	0.38	0.33	8.9	1350	1	0.045	0.44	4	G	0.695	
		684	786	0.38	0.33	8.9	550	2	0.068	0.66	4	G	0.728	

			684	786	0.38	0.33	8.9	750	2	0.068	0.66	4	G	0.726	
			684	786	0.38	0.33	8.9	950	2	0.068	0.66	4	G	0.711	
			684	786	0.38	0.33	8.9	1150	2	0.068	0.66	4	G	0.709	
			684	786	0.38	0.33	8.9	1350	2	0.068	0.66	4	G	0.695	
			684	786	0.38	0.33	8.9	550	3	0.048	0.47	4	G	0.728	
			684	786	0.38	0.33	8.9	750	3	0.048	0.47	4	G	0.726	
			684	786	0.38	0.33	8.9	950	3	0.048	0.47	4	G	0.711	
			684	786	0.38	0.33	8.9	1150	3	0.048	0.47	4	G	0.709	
			684	786	0.38	0.33	8.9	1350	3	0.048	0.47	4	G	0.695	
Guilinger et al. (1988) [63]	Kerosene	Water	746	998	1.31	1.04	10.6	300	1	0.06	0.53	4	SS		0.618
			746	998	1.31	1.04	10.6	400	1	0.06	0.53	4	SS		0.703
			746	998	1.31	1.04	10.6	500	1	0.06	0.53	4	SS		0.777
			746	998	1.31	1.04	10.6	300	1	0.06	0.53	4	G		0.843
			746	998	1.31	1.04	10.6	400	1	0.06	0.53	4	G		0.877
			746	998	1.31	1.04	10.6	500	1	0.06	0.53	4	G		0.893
			746	998	1.31	1.04	10.6	300	1	0.12	0.35	4	SS	0.96	
			746	998	1.31	1.04	10.6	350	1	0.12	0.35	4	SS	0.944	
			746	998	1.31	1.04	10.6	400	1	0.12	0.35	4	SS	0.925	
			746	998	1.31	1.04	10.6	550	1	0.12	0.35	4	SS	0.905	
Kumar et al. (1991) [92]	2-methyl-propanol	Water	802	1000	3.95	1	49.9	600	1	0.105	0.5	4	G	0.859	
			802	1000	3.95	1	49.9	799	1	0.105	0.5	4	G	0.831	
			802	1000	3.95	1	49.9	1000	1	0.105	0.5	4	G	0.813	
			802	1000	3.95	1	49.9	1201	1	0.105	0.5	4	G	0.796	
			802	1000	3.95	1	49.9	600	1	0.105	0.5	4	G		0.576
			802	1000	3.95	1	49.9	799	1	0.105	0.5	4	G		0.593

			802	1000	3.95	1	49.9	1002	1	0.105	0.5	4	G		0.607
			802	1000	3.95	1	49.9	1197	1	0.105	0.5	4	G		0.611
			802	1000	3.95	1	49.9	597	1	0.105	0.5	4	G	0.857	0.748
			802	1000	3.95	1	49.9	802	1	0.105	0.5	4	G	0.83	0.687
			802	1000	3.95	1	49.9	999	1	0.105	0.5	4	G	0.813	0.68
			802	1000	3.95	1	49.9	1200	1	0.105	0.5	4	G	0.799	0.672
	Heptane	Acetonitrile	684	786	0.38	0.33	8.9	600	1	0.105	0.5	4	G	0.731	0.347
			684	786	0.38	0.33	8.9	800	1	0.105	0.5	4	G	0.708	0.364
			684	786	0.38	0.33	8.9	1000	1	0.105	0.5	4	G	0.685	0.388
			684	786	0.38	0.33	8.9	1200	1	0.105	0.5	4	G	0.674	0.404
	Heptane	DMF	684	944	0.38	0.92	6.79	600	1	0.105	0.5	4	G	0.817	0.372
			684	944	0.38	0.92	6.79	800	1	0.105	0.5	4	G	0.777	0.424
			684	944	0.38	0.92	6.79	1000	1	0.105	0.5	4	G	0.742	0.477
			684	944	0.38	0.92	6.79	1200	1	0.105	0.5	4	G	0.726	0.513
Norato et al. (1998) [76]	Toluene	Water	867	996	0.57	0.96	32.3	562	1	0.051	0.5	4	G	0.758	
			867	996	0.57	0.96	32.3	721	1	0.051	0.5	4	G	0.739	
			867	996	0.57	0.96	32.3	765	1	0.051	0.5	4	G	0.734	
			867	996	0.57	0.96	32.3	883	1	0.051	0.5	4	G	0.702	
			867	996	0.57	0.96	32.3	1040	1	0.051	0.5	4	G	0.681	
			867	996	0.57	0.96	32.3	1072	1	0.051	0.5	4	G	0.659	
			867	996	0.57	0.96	32.3	1227	1	0.051	0.5	4	G	0.647	
			867	996	0.57	0.96	32.3	511	1	0.051	0.5	4	G		0.513
			867	996	0.57	0.96	32.3	541	1	0.051	0.5	4	G		0.524
			867	996	0.57	0.96	32.3	732	1	0.051	0.5	4	G		0.558
			867	996	0.57	0.96	32.3	781	1	0.051	0.5	4	G		0.57
			867	996	0.57	0.96	32.3	821	1	0.051	0.5	4	G		0.575
			867	996	0.57	0.96	32.3	850	1	0.051	0.5	4	G		0.602

		867	996	0.57	0.96	32.3	870	1	0.051	0.5	4	G		0.594
		867	996	0.57	0.96	32.3	1046	1	0.051	0.5	4	G		0.599
		867	996	0.57	0.96	32.3	1218	1	0.051	0.5	4	G		0.628
Toluene	Water + Glycerol	867	996	0.57	2.97	27.8	1154	1	0.051	0.5	4	G	0.854	
		867	996	0.57	2.97	27.8	1708	1	0.051	0.5	4	G	0.787	
		867	996	0.57	2.97	27.8	1932	1	0.051	0.5	4	G	0.764	
		867	996	0.57	2.97	27.8	537	1	0.051	0.5	4	G		0.656
		867	996	0.57	2.97	27.8	555	1	0.051	0.5	4	G		0.651
		867	996	0.57	2.97	27.8	663	1	0.051	0.5	4	G		0.697
		867	996	0.57	2.97	27.8	702	1	0.051	0.5	4	G		0.644
		867	996	0.57	2.97	27.8	979	1	0.051	0.5	4	G		0.745
		867	996	0.57	2.97	27.8	1009	1	0.051	0.5	4	G		0.738
		867	996	0.57	3.78	27.5	1024	1	0.051	0.5	4	G	0.844	
		867	996	0.57	3.78	27.5	1232	1	0.051	0.5	4	G	0.823	
		867	996	0.57	3.78	27.5	1239	1	0.051	0.5	4	G	0.799	
		867	996	0.57	3.78	27.5	1311	1	0.051	0.5	4	G	0.83	
		867	996	0.57	3.78	27.5	557	1	0.051	0.5	4	G		0.727
		867	996	0.57	3.78	27.5	741	1	0.051	0.5	4	G		0.76
		867	996	0.57	3.78	27.5	1014	1	0.051	0.5	4	G		0.783
		867	996	0.57	3.78	27.5	1078	1	0.051	0.5	4	G		0.791
Toluene	Water	867	996	0.57	0.96	32.3	558	1	0.051	0.5	4	G	0.63	
		867	996	0.57	0.96	32.3	601	1	0.051	0.5	4	G	0.612	
		867	996	0.57	0.96	32.3	778	1	0.051	0.5	4	G	0.6	
		867	996	0.57	0.96	32.3	841	1	0.051	0.5	4	G	0.589	
		867	996	0.57	0.96	32.3	937	1	0.051	0.5	4	G	0.581	
		867	996	0.57	0.96	32.3	562	1	0.051	0.5	4	G		0.528

867	996	0.57	0.96	32.3	686	1	0.051	0.5	4	G		0.593
867	996	0.57	0.96	32.3	780	1	0.051	0.5	4	G		0.615
867	996	0.57	0.96	32.3	940	1	0.051	0.5	4	G		0.628
867	996	0.57	0.96	32.3	1172	1	0.051	0.5	4	G		0.654
867	996	0.57	0.96	32.3	497	1	0.042	0.42	4	G	0.759	
867	996	0.57	0.96	32.3	639	1	0.042	0.42	4	G	0.742	
867	996	0.57	0.96	32.3	676	1	0.042	0.42	4	G	0.736	
867	996	0.57	0.96	32.3	781	1	0.042	0.42	4	G	0.706	
867	996	0.57	0.96	32.3	923	1	0.042	0.42	4	G	0.683	
867	996	0.57	0.96	32.3	952	1	0.042	0.42	4	G	0.659	
867	996	0.57	0.96	32.3	1090	1	0.042	0.42	4	G	0.647	
867	996	0.57	0.96	32.3	453	1	0.042	0.42	4	G		0.513
867	996	0.57	0.96	32.3	479	1	0.042	0.42	4	G		0.525
867	996	0.57	0.96	32.3	646	1	0.042	0.42	4	G		0.558
867	996	0.57	0.96	32.3	690	1	0.042	0.42	4	G		0.568
867	996	0.57	0.96	32.3	726	1	0.042	0.42	4	G		0.575
867	996	0.57	0.96	32.3	751	1	0.042	0.42	4	G		0.601
867	996	0.57	0.96	32.3	765	1	0.042	0.42	4	G		0.594
867	996	0.57	0.96	32.3	930	1	0.042	0.42	4	G		0.599
867	996	0.57	0.96	32.3	1082	1	0.042	0.42	4	G		0.628
867	996	0.57	0.96	32.3	558	1	0.051	0.5	4	G	0.629	
867	996	0.57	0.96	32.3	598	1	0.051	0.5	4	G	0.614	
867	996	0.57	0.96	32.3	778	1	0.051	0.5	4	G	0.6	
867	996	0.57	0.96	32.3	842	1	0.051	0.5	4	G	0.588	
867	996	0.57	0.96	32.3	940	1	0.051	0.5	4	G	0.581	
867	996	0.57	0.96	32.3	559	1	0.051	0.5	4	G		0.527
867	996	0.57	0.96	32.3	686	1	0.051	0.5	4	G		0.592

867	996	0.57	0.96	32.3	775	1	0.051	0.5	4	G		0.614
867	996	0.57	0.96	32.3	939	1	0.051	0.5	4	G		0.63
867	996	0.57	0.96	32.3	1181	1	0.051	0.5	4	G		0.652
867	996	0.57	0.96	32.3	530	1	0.063	0.62	4	G	0.67	
867	996	0.57	0.96	32.3	578	1	0.063	0.62	4	G	0.684	
867	996	0.57	0.96	32.3	643	1	0.063	0.62	4	G	0.665	
867	996	0.57	0.96	32.3	667	1	0.063	0.62	4	G	0.658	
867	996	0.57	0.96	32.3	665	1	0.063	0.62	4	G	0.629	
867	996	0.57	0.96	32.3	684	1	0.063	0.62	4	G	0.639	
867	996	0.57	0.96	32.3	695	1	0.063	0.62	4	G	0.658	
867	996	0.57	0.96	32.3	831	1	0.063	0.62	4	G	0.591	
867	996	0.57	0.96	32.3	875	1	0.063	0.62	4	G	0.648	
867	996	0.57	0.96	32.3	1011	1	0.063	0.62	4	G	0.63	
867	996	0.57	0.96	32.3	1086	1	0.063	0.62	4	G	0.62	
867	996	0.57	0.96	32.3	1118	1	0.063	0.62	4	G	0.632	
867	996	0.57	0.96	32.3	599	1	0.063	0.62	4	G		0.573
867	996	0.57	0.96	32.3	616	1	0.063	0.62	4	G		0.61
867	996	0.57	0.96	32.3	624	1	0.063	0.62	4	G		0.604
867	996	0.57	0.96	32.3	692	1	0.063	0.62	4	G		0.651
867	996	0.57	0.96	32.3	810	1	0.063	0.62	4	G		0.592
867	996	0.57	0.96	32.3	805	1	0.063	0.62	4	G		0.618
867	996	0.57	0.96	32.3	873	1	0.063	0.62	4	G		0.63
867	996	0.57	0.96	32.3	1156	1	0.063	0.62	4	G		0.644
867	996	0.57	0.96	32.3	907	2	0.051	0.5	4	G	0.674	
867	996	0.57	0.96	32.3	1182	2	0.051	0.5	4	G	0.644	
867	996	0.57	0.96	32.3	1197	2	0.051	0.5	4	G	0.65	
867	996	0.57	0.96	32.3	1323	2	0.051	0.5	4	G	0.672	

		867	996	0.57	0.96	32.3	1350	2	0.051	0.5	4	G	0.662	
		867	996	0.57	0.96	32.3	1396	2	0.051	0.5	4	G	0.662	
		867	996	0.57	0.96	32.3	1407	2	0.051	0.5	4	G	0.635	
		867	996	0.57	0.96	32.3	1035	2	0.051	0.5	4	G		0.55
		867	996	0.57	0.96	32.3	1279	2	0.051	0.5	4	G		0.562
		867	996	0.57	0.96	32.3	1389	2	0.051	0.5	4	G		0.572
		867	996	0.57	0.96	32.3	1516	2	0.051	0.5	4	G		0.579
		867	996	0.57	0.96	32.3	1660	2	0.051	0.5	4	G		0.576
		867	996	0.57	0.96	32.3	1716	2	0.051	0.5	4	G		0.607
MIBK	Water	805	996	0.61	1	8.9	561	1	0.051	0.5	4	G	0.648	
		805	996	0.61	1	8.9	700	1	0.051	0.5	4	G	0.657	
		805	996	0.61	1	8.9	840	1	0.051	0.5	4	G	0.653	
		805	996	0.61	1	8.9	937	1	0.051	0.5	4	G	0.64	
		805	996	0.61	1	8.9	1102	1	0.051	0.5	4	G	0.635	
Toluene + CCl_4	Water	867	996	0.57	0.96	32.3	506	1	0.051	0.5	4	G		0.485
		867	996	0.57	0.96	32.3	556	1	0.051	0.5	4	G	0.758	
		867	996	0.57	0.96	32.3	535	1	0.051	0.5	4	G		0.476
		867	996	0.57	0.96	32.3	719	1	0.051	0.5	4	G	0.74	
		867	996	0.57	0.96	32.3	730	1	0.051	0.5	4	G		0.439
		867	996	0.57	0.96	32.3	759	1	0.051	0.5	4	G	0.737	
		867	996	0.57	0.96	32.3	776	1	0.051	0.5	4	G		0.433
		867	996	0.57	0.96	32.3	820	1	0.051	0.5	4	G		0.426
		867	996	0.57	0.96	32.3	866	1	0.051	0.5	4	G		0.408
		867	996	0.57	0.96	32.3	875	1	0.051	0.5	4	G	0.706	
		867	996	0.57	0.96	32.3	1035	1	0.051	0.5	4	G	0.685	
		867	996	0.57	0.96	32.3	1046	1	0.051	0.5	4	G		0.401

867	996	0.57	0.96	32.3	1067	1	0.051	0.5	4	G	0.662	
867	996	0.57	0.96	32.3	1214	1	0.051	0.5	4	G		0.371
867	996	0.57	0.96	32.3	1224	1	0.051	0.5	4	G	0.649	
900	996	0.59	0.96	29.9	382	1	0.051	0.5	4	G	0.706	
900	996	0.59	0.96	29.9	634	1	0.051	0.5	4	G		0.464
900	996	0.59	0.96	29.9	677	1	0.051	0.5	4	G		0.458
900	996	0.59	0.96	29.9	707	1	0.051	0.5	4	G	0.683	
900	996	0.59	0.96	29.9	747	1	0.051	0.5	4	G		0.403
900	996	0.59	0.96	29.9	843	1	0.051	0.5	4	G		0.387
900	996	0.59	0.96	29.9	884	1	0.051	0.5	4	G	0.66	
900	996	0.59	0.96	29.9	944	1	0.051	0.5	4	G		0.364
900	996	0.59	0.96	29.9	976	1	0.051	0.5	4	G		0.401
900	996	0.59	0.96	29.9	1035	1	0.051	0.5	4	G	0.635	
900	996	0.59	0.96	29.9	1073	1	0.051	0.5	4	G	0.606	
900	996	0.59	0.96	29.9	1290	1	0.051	0.5	4	G	0.366	
1040	996	0.65	0.96	22.7	446	1	0.051	0.5	4	G	0.738	
1040	996	0.65	0.96	22.7	657	1	0.051	0.5	4	G		0.401
1040	996	0.65	0.96	22.7	677	1	0.051	0.5	4	G		0.401
1040	996	0.65	0.96	22.7	695	1	0.051	0.5	4	G	0.724	
1040	996	0.65	0.96	22.7	739	1	0.051	0.5	4	G	0.701	
1040	996	0.65	0.96	22.7	767	1	0.051	0.5	4	G		0.387
1040	996	0.65	0.96	22.7	875	1	0.051	0.5	4	G	0.663	
1040	996	0.65	0.96	22.7	893	1	0.051	0.5	4	G	0.66	
1040	996	0.65	0.96	22.7	941	1	0.051	0.5	4	G		0.353
1040	996	0.65	0.96	22.7	994	1	0.051	0.5	4	G	0.687	0.349
1040	996	0.65	0.96	22.7	1627	1	0.051	0.5	4	G	0.623	
1180	996	0.73	0.96	26.3	539	1	0.051	0.5	4	G		0.388

			1180	996	0.73	0.96	26.3	600	1	0.051	0.5	4	G	0.403
			1180	996	0.73	0.96	26.3	763	1	0.051	0.5	4	G	0.351
			1180	996	0.73	0.96	26.3	802	1	0.051	0.5	4	G	0.688	
			1180	996	0.73	0.96	26.3	802	1	0.051	0.5	4	G	0.659	
			1180	996	0.73	0.96	26.3	997	1	0.051	0.5	4	G	0.352
			1180	996	0.73	0.96	26.3	1121	1	0.051	0.5	4	G	0.627	
			1180	996	0.73	0.96	26.3	1485	1	0.051	0.5	4	G	0.627	
Pacek and Nienow (1995) [323]	C_6H_5Cl	Water	1106	1000	0.75	1	33	400	1	0.075	0.5	4	G	0.68	0.545
	Benzene	Water	879	1000	0.65	1	25	500	1	0.075	0.5	4	G	0.717	0.541
	Toluene	Water	867	1000	0.59	1	28	500	1	0.075	0.5	4	G	0.705	0.528
	Cyclohexane	Water	779	1000	1.02	1	44	500	1	0.075	0.5	4	G	0.843	0.521
Quinn and Sigloh (1963) [64]	CCl4	Water	1590	996	0.84	0.8	45	217	4	0.079	0.56	4	SS	0.468	
			1590	996	0.84	0.8	45	233	4	0.079	0.56	4	SS	0.457	
			1590	996	0.84	0.8	45	251	4	0.079	0.56	4	SS	0.449	
			1590	996	0.84	0.8	45	252	4	0.079	0.56	4	SS	0.446	
			1590	996	0.84	0.8	45	263	4	0.079	0.56	4	SS	0.437	
			1590	996	0.84	0.8	45	281	4	0.079	0.56	4	SS	0.428	
			1590	996	0.84	0.8	45	289	4	0.079	0.56	4	SS	0.426	
			1590	996	0.84	0.8	45	346	4	0.079	0.56	4	SS	0.417	
			1590	996	0.84	0.8	45	349	4	0.079	0.56	4	SS	0.418	
			1590	996	0.84	0.8	45	356	4	0.079	0.56	4	SS	0.418	
			1590	996	0.84	0.8	45	368	4	0.079	0.56	4	SS	0.415	
	Mesityl oxide	Water	860	996	0.65	0.8	7.6	171	4	0.079	0.56	4	SS	0.555	
			860	996	0.65	0.8	7.6	178	4	0.079	0.56	4	SS	0.555	
			860	996	0.65	0.8	7.6	183	4	0.079	0.56	4	SS	0.544	

		860	996	0.65	0.8	7.6	190	4	0.079	0.56	4	SS	0.535
		860	996	0.65	0.8	7.6	194	4	0.079	0.56	4	SS	0.532
		860	996	0.65	0.8	7.6	207	4	0.079	0.56	4	SS	0.526
		860	996	0.65	0.8	7.6	214	4	0.079	0.56	4	SS	0.524
		860	996	0.65	0.8	7.6	231	4	0.079	0.56	4	SS	0.515
		860	996	0.65	0.8	7.6	239	4	0.079	0.56	4	SS	0.515
		860	996	0.65	0.8	7.6	266	4	0.079	0.56	4	SS	0.502
		860	996	0.65	0.8	7.6	270	4	0.079	0.56	4	SS	0.504
		860	996	0.65	0.8	7.6	303	4	0.079	0.56	4	SS	0.5
		860	996	0.65	0.8	7.6	310	4	0.079	0.56	4	SS	0.5
		860	996	0.65	0.8	7.6	342	4	0.079	0.56	4	SS	0.495
		860	996	0.65	0.8	7.6	350	4	0.079	0.56	4	SS	0.495
		860	996	0.65	0.8	7.6	409	4	0.079	0.56	4	SS	0.491
Toluene	Water	866	996	0.52	0.8	36.1	230	4	0.079	0.56	4	SS	0.593
		866	996	0.52	0.8	36.1	242	4	0.079	0.56	4	SS	0.579
		866	996	0.52	0.8	36.1	246	4	0.079	0.56	4	SS	0.572
		866	996	0.52	0.8	36.1	267	4	0.079	0.56	4	SS	0.553
		866	996	0.52	0.8	36.1	276	4	0.079	0.56	4	SS	0.545
		866	996	0.52	0.8	36.1	282	4	0.079	0.56	4	SS	0.543
		866	996	0.52	0.8	36.1	290	4	0.079	0.56	4	SS	0.54
		866	996	0.52	0.8	36.1	302	4	0.079	0.56	4	SS	0.533
		866	996	0.52	0.8	36.1	345	4	0.079	0.56	4	SS	0.521
		866	996	0.52	0.8	36.1	370	4	0.079	0.56	4	SS	0.514
		866	996	0.52	0.8	36.1	374	4	0.079	0.56	4	SS	0.514
		866	996	0.52	0.8	36.1	399	4	0.079	0.56	4	SS	0.511
		866	996	0.52	0.8	36.1	408	4	0.079	0.56	4	SS	0.513
		866	996	0.52	0.8	36.1	433	4	0.079	0.56	4	SS	0.51

		866	996	0.52	0.8	36.1	454	4	0.079	0.56	4	SS	0.506
		866	996	0.52	0.8	36.1	481	4	0.079	0.56	4	SS	0.503
		866	996	0.52	0.8	36.1	510	4	0.079	0.56	4	SS	0.503
		866	996	0.52	0.8	36.1	598	4	0.079	0.56	4	SS	0.499
Heptane	Water	684	996	0.37	0.8	50.3	306	4	0.079	0.56	4	SS	0.571
		684	996	0.37	0.8	50.3	314	4	0.079	0.56	4	SS	0.57
		684	996	0.37	0.8	50.3	337	4	0.079	0.56	4	SS	0.553
		684	996	0.37	0.8	50.3	344	4	0.079	0.56	4	SS	0.553
		684	996	0.37	0.8	50.3	390	4	0.079	0.56	4	SS	0.535
		684	996	0.37	0.8	50.3	396	4	0.079	0.56	4	SS	0.535
		684	996	0.37	0.8	50.3	495	4	0.079	0.56	4	SS	0.518
		684	996	0.37	0.8	50.3	636	4	0.079	0.56	4	SS	0.501
Isobutanol	Water	838	996	2.77	0.8	2.1	200	4	0.079	0.56	4	SS	0.627
		838	996	2.77	0.8	2.1	200	4	0.079	0.56	4	SS	0.622
		838	996	2.77	0.8	2.1	224	4	0.079	0.56	4	SS	0.62
		838	996	2.77	0.8	2.1	226	4	0.079	0.56	4	SS	0.616
		838	996	2.77	0.8	2.1	250	4	0.079	0.56	4	SS	0.618
		838	996	2.77	0.8	2.1	299	4	0.079	0.56	4	SS	0.619
		838	996	2.77	0.8	2.1	325	4	0.079	0.56	4	SS	0.615
		838	996	2.77	0.8	2.1	330	4	0.079	0.56	4	SS	0.616
		838	996	2.77	0.8	2.1	349	4	0.079	0.56	4	SS	0.615
		838	996	2.77	0.8	2.1	399	4	0.079	0.56	4	SS	0.617
		838	996	2.77	0.8	2.1	424	4	0.079	0.56	4	SS	0.614
		838	996	2.77	0.8	2.1	450	4	0.079	0.56	4	SS	0.616
		838	996	2.77	0.8	2.1	500	4	0.079	0.56	4	SS	0.618
		838	996	2.77	0.8	2.1	516	4	0.079	0.56	4	SS	0.617
Hexane	Water	659	996	0.29	0.8	51.1	293	4	0.079	0.56	4	SS	0.574

			659	996	0.29	0.8	51.1	327	4	0.079	0.56	4	SS	0.551
			659	996	0.29	0.8	51.1	346	4	0.079	0.56	4	SS	0.534
			659	996	0.29	0.8	51.1	361	4	0.079	0.56	4	SS	0.531
			659	996	0.29	0.8	51.1	401	4	0.079	0.56	4	SS	0.511
			659	996	0.29	0.8	51.1	445	4	0.079	0.56	4	SS	0.496
			659	996	0.29	0.8	51.1	464	4	0.079	0.56	4	SS	0.491
			659	996	0.29	0.8	51.1	474	4	0.079	0.56	4	SS	0.484
			659	996	0.29	0.8	51.1	510	4	0.079	0.56	4	SS	0.482
			659	996	0.29	0.8	51.1	520	4	0.079	0.56	4	SS	0.476
			659	996	0.29	0.8	51.1	570	4	0.079	0.56	4	SS	0.468
			659	996	0.29	0.8	51.1	591	4	0.079	0.56	4	SS	0.465
			659	996	0.29	0.8	51.1	651	4	0.079	0.56	4	SS	0.461
Reeve and	Cumene	Water +	868	1006	0.81	1.08	16.8	192	1	0.177	0.59	0	SS	0.735
Godfrey	+	Isobu-	868	1006	0.81	1.08	16.8	258	1	0.177	0.59	0	SS	0.762
(2002) [94]	Isobutyric	tyric	868	1006	0.81	1.08	16.8	299	1	0.177	0.59	0	SS	0.784
	acid	acid	868	1006	0.81	1.08	16.8	408	1	0.177	0.59	0	SS	0.8
			868	1006	0.81	1.08	16.8	500	1	0.177	0.59	0	SS	0.798
			868	1006	0.81	1.08	16.8	200	1	0.177	0.59	0	SS	0.798
			868	1006	0.81	1.08	16.8	252	1	0.177	0.59	0	SS	0.786
			868	1006	0.81	1.08	16.8	304	1	0.177	0.59	0	SS	0.758
			868	1006	0.81	1.08	16.8	394	1	0.177	0.59	0	SS	0.76
			868	1006	0.81	1.08	16.8	481	1	0.177	0.59	0	SS	0.758
	Cumene	Water	862.8	1006	0.77	1.04	36	197	1	0.177	0.59	0	SS	0.674
			862.8	1006	0.77	1.04	36	261	1	0.177	0.59	0	SS	0.7
			862.8	1006	0.77	1.04	36	296	1	0.177	0.59	0	SS	0.718
			862.8	1006	0.77	1.04	36	410	1	0.177	0.59	0	SS	0.736
			862.8	1006	0.77	1.04	36	502	1	0.177	0.59	0	SS	0.764

862.8	1006	0.77	1.04	36	200	1	0.177	0.59	0	SS	0.87
862.8	1006	0.77	1.04	36	259	1	0.177	0.59	0	SS	0.863
862.8	1006	0.77	1.04	36	300	1	0.177	0.59	0	SS	0.852
862.8	1006	0.77	1.04	36	398	1	0.177	0.59	0	SS	0.856
862.8	1006	0.77	1.04	36	498	1	0.177	0.59	0	SS	0.859

TABLE A.1: Experimental data on different ambivalent ranges gathered from literature

Appendix B

Mathematical Model for the Homogeneous Polymerization of Styrene in Presence of Polybutadiene

Following Estenoz et al. [389], the mass balances showed in this section correspond to the kinetic mechanism shown in Table 4.3 for the pseudo-homogeneous batch polymerization of high impact polystyrene.

Initiator

$$\frac{d}{dt}\left([I_2]\,V\right) = -k_d\,[I_2]\,V \tag{B.1}$$

Monomer

$$\frac{d}{dt}\left([St]\,V\right) = -R_pV = -k_p\,[St]\left([S^\bullet] + [P^\bullet]\right)V \tag{B.2}$$

Here, $[S^\bullet]$ and $[P^\bullet]$ are the sum of each styrene and copolymer radicals respectively, and R_p is the overall rate of St consumption. This expression assumes the "long chain approximation", by which propagation is the only monomer-consuming reaction.

Ungrafted butadiene units

$$\frac{d}{dt}\left([B]\,V\right) = -\{k_{i2}[I^\bullet] + k_{fG}\left([S^\bullet] + [P^\bullet]\right)\}[B]V + k_{fM}[St][P_0^\bullet]V \tag{B.3}$$

B stands for the unreacted butadiene units, generated by transfer of P_0 radicals and consumed by any attack to the rubber.

Radical species

$$\frac{d}{dt}\left([I^\bullet]V\right) = \{2fk_d[I_2] - \left(k_{i1}[St] + k_{i2}[B]\right)[I^\bullet]\}V \tag{B.4}$$

$$\frac{d}{dt}\left([S_1^\bullet]V\right) = \{k_{i1}[St][I^\bullet] + 3k_{i0}[St]^3 - k_p[St][S_1^\bullet] + k_{fM}[St][P_0^\bullet] + k_{fM}[St]\left([S^\bullet] + [P^\bullet]\right)\}V - \{k_{fG}[B] + k_{tc}\left([S^\bullet] + [P^\bullet] + [P_0^\bullet]\right) + k_{fM}[St]\}[S_1^\bullet]V \quad \text{(B.5)}$$

$$\frac{d}{dt}\left([S_n^\bullet]V\right) = k_p[St][S_{n-1}^\bullet]V - \{k_p[St] + k_{fM}[St] + k_{fG}[B] + k_{tc}\left([S^\bullet] + [P^\bullet] + [P_0^\bullet]\right)\}[S_n^\bullet]V \quad \text{(B.6)}$$

for $n > 1$

$$\frac{d}{dt}\left([P_0^\bullet]V\right) = k_{i2}[I^\bullet] + k_{fG}[S^\bullet] + [P^\bullet][B]V - \{k_{i3}[St] + k_{fM}[St] + k_{tc}[S^\bullet] + [P^\bullet] + [P_0^\bullet]\}[P_0^\bullet]V \quad \text{(B.7)}$$

$$\frac{d}{dt}\left([P_1^\bullet]V\right) = k_{i3}[St][P_0^\bullet]V - \{k_p[St] + k_{fM}[St] + k_{fG}[B] + k_{tc}[S^\bullet] + [P^\bullet] + [P_0^\bullet]\}[P_1^\bullet]V \quad \text{(B.8)}$$

$$\frac{d}{dt}\left([P_n^\bullet]V\right) = k_p[St][P_{n-1}^\bullet]V - \{k_p[St] + k_{fM}[St] + k_{fG}[B] + k_{tc}[S^\bullet] + [P^\bullet] + [P_0^\bullet]\}[P_n^\bullet]V \quad \text{(B.9)}$$

for $n > 1$

Equations B.5 and B.6 may be combined to obtain the global balance for St radicals, while adding equations B.7-B.9 gives the mass balance for all P radicals.

Chain length distributions of free PS

The number chain length distribution (NCLD) is calculated as the result of the mass balance for each PS species. First define the following auxiliary variables:

$$\beta = \frac{k_{tc}R_p}{\left(k_p\left[St\right]\right)^2} \quad \text{(B.10)}$$

$$\gamma = \frac{[P_0^\bullet]}{[S^\bullet] + [P^\bullet]} \quad \text{(B.11)}$$

$$\psi = \frac{[S^{\bullet}]}{[S^{\bullet}] + [P^{\bullet}]} \tag{B.12}$$

$$\tau = \frac{k_{fM}}{k_p} + \frac{k_{fG}\,[B]}{k_p\,[St]} + \gamma\beta \tag{B.13}$$

$$\alpha = \tau + \beta \tag{B.14}$$

Using the above variables in Eq. B.5 yields:

$$[S_1{}^{\bullet}] = \frac{\psi R_p \alpha}{k_p[St]\,(1+\alpha)} \tag{B.15}$$

Similarly, in Eq. B.6 for $n > 1$:

$$[S_n{}^{\bullet}] = \frac{\psi R_p \alpha}{k_p[St]\,(1+\alpha)^n} \tag{B.16}$$

Thus, for all the possible values of chain length, n, the balance gives:

$$\frac{d}{dt}\left([S_n]\,V\right) = \psi R_p \alpha \left(\tau - \gamma\beta + \frac{\beta\psi\alpha n}{2}\right)(1+\alpha)^{-n}\,V \tag{B.17}$$

If n is large enough ($\approx 1 \times 10^4$), the term $(1+\alpha)^{-n}$ may be approximated to $e^{-\alpha n}$ and the NCLD of free PS can be obtained by the numerical integration of:

$$\frac{d}{dt}\left([S_n]\,V\right) = \psi R_p \alpha \left(\tau - \gamma\beta + \frac{\beta\psi\alpha n}{2}\right)e^{-\alpha n}V \tag{B.18}$$

The weight CLD can be readily calculated by multiplying Eq. B.18 by the molecular weight of each chain, which is nM_{St}, and integrating numerically:

$$\frac{d}{dt}\left([S_n]\,VnM_{St}\right) = \psi R_p \alpha \left(\tau - \gamma\beta + \frac{\beta\psi\alpha n}{2}\right)e^{-\alpha n}nM_{St}V \tag{B.19}$$

Appendix C

Mathematical Model for the Heterogeneous Polymerization of Styrene in Presence of Polybutadiene

The mass balances showed in this section correspond to the kinetic mechanism shown in Table 4.3, but under the following considerations:

1. Initially, the reacting mixture consists of a polybutadiene in styrene solution. The monofunctional initiator is dissolved in the corresponding concentration.
2. Once the polymerization begins, the vitreous phase is immediately separated from the rubber-rich phase. Styrene is transferred from the continuous to the dispersed phase so as to guarantee an equilibrium partition coefficient of 1. The transferred flux of styrene also carries initiator, initiator radicals, and styrene propagating radicals, all in their corresponding concentration at each time step.
3. Polybutadiene, copolymer propagating radicals and dead copolymer chains do not get transferred across the interface. It is assumed that the presence of the graft copolymer does not substantially modify the density of the ungrafted polybutadiene.
4. The long chain approximation is assumed, by which monomer is mostly consumed in the propagation reactions.
5. The termination by combination rate constant includes the *gel effect* from the work by Hui and Hamielec [404], computing it for each phase separately, since it depends on the polymer concentration present.
6. All other kinetic constants are assumed equal in each phase.

Rubber-rich phase

Initiator

$$\frac{d}{dt}\left([I_2]_r\, V_r\right) = -k_d\,[I_2]_r\, V_r \tag{C.1}$$

Monomer

$$\frac{d}{dt}\left(M_{St}\,[St]_r\, V_r\right) = -k_p\,[St]_r\left([S^\bullet]_r + [P^\bullet]\right) V_r M_{St} - \dot{F} \tag{C.2}$$

Here, $[S^\bullet]_r$ and $[P^\bullet]$ are the total styrene and copolymer radicals in the rubbery phase respectively.

Ungrafted butadiene units

$$\frac{d}{dt}\left([B]\, V_r\right) = -\{k_{i2}[I^\bullet]_r + k_{fG}\left([S^\bullet]_r + [P^\bullet]\right)\}[B]V_r + k_{fM}[St]_r[P_0{}^\bullet]V_r \tag{C.3}$$

B stands for the unreacted butadiene units, generated by transfer of P_0 radicals and consumed by any attack to the rubber.

Radical species

$$\frac{d}{dt}\left([I^\bullet]_r\, V_r\right) = 2fk_d\,[I_2]_r\, V_r - k_{i1}[St]_r\,[I^\bullet]_r\, V_r - \frac{\dot{F}}{\rho_{St}}\,[I^\bullet]_r \tag{C.4}$$

$$\frac{d}{dt}\left([S_1{}^\bullet]_r V_r\right) = \{k_{i1}[St]_r[I^\bullet]_r + 3k_{i0}[St]_r^3 - k_p[St]_r[S_1{}^\bullet]_r + k_{fM}[St]_r[P_0{}^\bullet] + k_{fM}[St]_r\left([S^\bullet]_r + [P^\bullet]\right)\}V_r -$$
$$\{k_{fG}[B] + k_{tcr}\left([S^\bullet]_r + [P^\bullet] + [P_0{}^\bullet]\right) + k_{fM}[St]_r\}[S_1{}^\bullet]_r V_r - \frac{\dot{F}}{\rho_{St}}[S_1{}^\bullet]_r \tag{C.5}$$

$$\frac{d}{dt}\left([S_n{}^\bullet]_r V_r\right) = k_p[St]_r[S_{n-1}{}^\bullet]_r V_r - \{k_p[St]_r + k_{fM}[St]_r + k_{fG}[B] +$$
$$k_{tcr}\left([S^\bullet]_r + [P^\bullet] + [P_0{}^\bullet]\right)\}\,[S_n{}^\bullet]_r V_r - \frac{\dot{F}}{\rho_{St}}[S_n{}^\bullet]_r \tag{C.6}$$

for $n > 1$

$$\frac{d}{dt}\left([P_0^{\bullet}]V_r\right) = k_{i2}[I^{\bullet}]_r + k_{fG}[S^{\bullet}]_r + [P^{\bullet}][B]V_r - \{k_{i3}[St]_r + k_{fM}[St]_r + k_{tcr}[S^{\bullet}]_r + [P^{\bullet}] + [P_0^{\bullet}]\}\,[P_0^{\bullet}]V_r \quad \text{(C.7)}$$

$$\frac{d}{dt}\left([P_1^{\bullet}]V_r\right) = k_{i3}[St]_r[P_0^{\bullet}]V_r - \{k_p[St]_r + k_{fM}[St]_r + k_{fG}[B] + k_{tcr}[S^{\bullet}]_r + [P^{\bullet}] + [P_0^{\bullet}]\}[P_1^{\bullet}]V_r \quad \text{(C.8)}$$

$$\frac{d}{dt}\left([P_n^{\bullet}]V_r\right) = k_p[St]_r[P_{n-1}^{\bullet}]V_r - \{k_p[St]_r + k_{fM}[St]_r + k_{fG}[B] + k_{tcr}[S^{\bullet}]_r + [P^{\bullet}] + [P_0^{\bullet}]\}[P_n^{\bullet}]V_r \quad \text{(C.9)}$$

for $n > 1$

Equations C.5 and C.6 may be combined to obtain the global balance for St radicals in the rubber-rich phase, while adding equations C.7-C.9 gives the mass balance for all P radicals.

Phase volume

$$\frac{dV_r}{dt} = \frac{-k_p\,[St]_r\left([S^{\bullet}]_r + [P^{\bullet}]\right)V_r M_{St} - \dot{F}}{\rho_{St}} \quad \text{(C.10)}$$

Vitreous phase

Initiator

$$\frac{d}{dt}\left([I_2]_v\,V_v\right) = -k_d\,[I_2]_v\,V_v \quad \text{(C.11)}$$

Monomer

$$\frac{d}{dt}\left(M_{St}\,[St]_v\,V_v\right) = -k_p[St]_v\,[S^{\bullet}]_v\,V_v M_{St} + \dot{F} \quad \text{(C.12)}$$

Here, $[S^{\bullet}]_r$ represents the total styrene radicals in the vitreous phase.

Radical species

$$\frac{d}{dt}\left([I^{\bullet}]_v\,V_v\right) = 2fk_d\,[I_2]_v\,V_v - k_{i1}[St]_v\,[I^{\bullet}]\,V_v + \frac{\dot{F}}{\rho_{St}}\,[I^{\bullet}]_r \quad \text{(C.13)}$$

$$\frac{d}{dt}\left([S_1^\bullet]_v V_v\right) = \{k_{i1}[St]_v[I^\bullet]_v + 3k_{i0}[St]_r^3 - k_p[St]_v[S_1^\bullet]_+ k_{fM}[St]_v[S^\bullet]_v\}V_v - \\ + k_{tcv}\left([S^\bullet]_v\right) + k_{fM}[St]_v\}[S_1^\bullet]_v V_v + \frac{\dot{F}}{\rho_{St}}[S_1^\bullet]_r \quad \text{(C.14)}$$

$$\frac{d}{dt}\left([S_n^\bullet]_v V_v\right) = k_p[St]_v[S_{n-1}^\bullet]_v V_v - \{k_p[St]_v + k_{fM}[St]_v + \\ k_{tcv}\left([S^\bullet]_r\right)\}\left[S_n^\bullet\right]_v V_v + \frac{\dot{F}}{\rho_{St}}[S_n^\bullet]_r \quad \text{(C.15)}$$

for $n > 1$

Equations C.14 and C.15 may be combined to obtain the global balance for St radicals in the vitreous phase.

Phase volume

$$\frac{dV_v}{dt} = \frac{-k_p[St]_v\left[S^\bullet\right]_v V_v M_{St} + \dot{F}}{\rho_{St}} + \frac{k_p[St]_v\left[S^\bullet\right]_v V_v M_{St}}{\rho_{PS}} \quad \text{(C.16)}$$

Transferred styrene from the rubber-rich to the vitreous phase

$$\dot{F} = \frac{\left[\left(m_{St_r} + m_{PB}\frac{\rho_{PS}}{\rho_{PB}}\right)k_p[St]_v\left[S^\bullet\right]_v V_v + \left(m_{St_r} - m_{PS}\right)k_p\left[St\right]_r\left(\left[S^\bullet\right]_r + \left[P^\bullet\right]\right)V_r\right]}{m_{PB}\frac{\rho_{PS}}{\rho_{PB}} + m_{PS}} M_{St} \quad \text{(C.17)}$$

Chain length distributions of free PS

The number chain length distribution (NCLD) is calculated as the result of the mass balance for each PS species as shown in Appendix B, only that in this case the calculation is performed for each separate phase and then added term-by-term, following Casis et al. [376].

Bibliography

[1] TECH Report 2018-6: Styrene/Ethylbenzene. Technical report, Nexant, 2018.

[2] Global Styrene/Market Outlook on Size, Trends and 2020 Key Player Analysis Report. Technical report, The Business Research Company, London, 2020.

[3] R. E. Kirk and D. F. Othmer. Styrene. In *Kirk-Othmer Encyclopedia of Chemical Technology*, pages 476–492. Wiley and Sons, 4th edition, 2001.

[4] E. Ali and M. Hadj-Kali. Energy efficiency analysis of styrene production by adiabatic ethylbenzene dehydrogenation using exergy analysis and heat integration. *Polish Journal of Chemical Technology*, 20(1):35–46, 2018.

[5] C. Hermann, P. Quicker, and R. Dittmeyer. Mathematical simulation of catalytic dehydrogenation of ethylbenzene to styrene in a composite palladium membrane reactor. *Journal of Membrane Science*, 136(1-2):161–172, 1997.

[6] B. K. Abdalla and S. S. E. H. Elnashaie. A membrane reactor for the production of sytrene from ethylbenzene. *Journal of Membrane Science*, 85(3):229–239, 1993.

[7] Y. Tamsilian, A. N. Ebrahimi, S. A. A. Ramazani, and H. Abdollahzadeh. Modeling and sensitivity analysis of styrene monomer production process and investigation of catalyst behavior. *Computers and Chemical Engineering*, 40:1–11, 2012.

[8] T. Spyra. China's styrene monomer market and its push for higher self-sufficiency. Technical report, IHS Markit, 2020.

[9] Polystyrene Global Market Report 2020. Technical report, The Business Research Company, 2020.

[10] Polystyrene (PS): Production, Market, Price and its Properties, 2019.

[11] J. Maul, B. G. Fushour, J. R. Kontoff, H. Eichenauer, K. H. Ott, and C. Schade. Polystyrene and Styrene Copolymers, 2007.

[12] N. Niessner and H. Gausepohl. Polystyrene and Styrene Copolymers - An Overview. In J. Scheirs and D. B. Priddy, editors, *Modern Styrenic Polymers*, chapter 2. Wiley and Sons, London, 2003.

[13] A. Lakatos and F. Kalmár. Investigation of thickness and density dependence of thermal conductivity of expanded polystyrene insulation materials. *Materials and Structures/Materiaux et Constructions*, 46(7):1101–1105, 2013.

[14] A. Kaya and F. Kar. Properties of concrete containing waste expanded polystyrene and natural resin. *Construction and Building Materials*, 105:572–578, 2016.

[15] A. A. Sayadi, J. V. Tapia, T. R. Neitzert, and G. C. Clifton. Effects of expanded polystyrene (EPS) particles on fire resistance, thermal conductivity and compressive strength of foamed concrete. *Construction and Building Materials*, 112:716–724, 2016.

[16] Styrene Monomer (SM) Market Global Review and Outlook (2019). Technical report, HDIN Research, Beijing, 2019.

[17] Styrene Acrylonitrile (SAN) Market Size, Industry Analysis Report, Regional Outlook, Growth Potential, Competitive Market Share & Forecast, 2020 - 2026. Technical report, Global Market Insights, Selbyville, 2019.

[18] Styrene-Acrylonitrile (SAN) Resins Market - Global Industry Analysis, Size, Share, Growth, Trends and Forecast, 2014 - 2020. Technical report, Transparency Market Research, Albany, 2013.

[19] B. G. Frushour and J. R. Kontoff. Polystyrene and Styrene Copolymers, 2007.

[20] M. R. El-Aassar, H. S. Hassan, M. F. Elkady, M. S. Masoud, and A. A. Elzain. Isothermal, kinetic, and thermodynamic studies on copper adsorption on modified styrene acrylonitrile copolymer. *International Journal of Environmental Science and Technology*, 16:7037–7048, 2019.

[21] H. Eichenauer and K. H. Ott. Polystyrene and Styrene Copolymers, 2007.

[22] C. B. Bucknall and R. R. Smith. Stress-whitening in high-impact polystyrenes. *Polymer*, 6(8):437–446, 1965.

[23] L Bohn. Effect of acrylonitrile content on the toughness of abs materials. *Angew. Makromol. Chem.*, 20:129–133, 1971.

[24] Acrylonitrile Butadiene Styrene (ABS) Market Size, Share & Trends Analysis Report By Application (Appliances, Automotive, Consumer Goods, Construction), And Segment Forecasts To 2022. Technical report, Grand View Research, San Francisco, 2018.

[25] A. Augustyn, P. Bauer, B. Duignan, A. Eldridge, E. Gregersen, A. McKenna, M. Petruzzello, J. P. Rafferty, M. Ray, K. Rogers, A. Tikkanen, J. Wallenfeldt, A. Zeidan, and A. Zelazko. Styrene-butadiene rubber, 2018.

[26] J. A. Brydson. Styrene-Butadiene Rubber. In A. Whelan and K. S. Lee, editors, *Developments in Rubber Technology*, chapter 2, pages 21–49. Springer, Dordrecht, 1981.

[27] Styrene-butadiene rubber (SBR) uses and outlook. Technical report, Independent Commodity Intelligence Services, New York, 2010.

[28] Global Styrene-Butadiene Rubber (SBR) Market: Information by Type (Emulsion SBR (E-SBR) and Solution SBR (S-SBR)), Application (Tires, Industrial, Footwear, Polymer Modification and Adhesives) and Region (North America, Europe, Asia-Pacific, Latin America. Technical report, Market Research Future, Maharashtra, 2019.

[29] Polypropylene & High-Impact Polystyrene Market for Injection Molding by Material and Application: Global Opportunity Analysis and Industry Forecast, 2017-2023. Technical report, Allied Market Research, Portland, 2017.

[30] A. M. Donald and E. J. Kramer. Internal structure of rubber particles and craze breakdown in high-impact polystyrene (HIPS). *Journal of Materials Science*, 17(8):2351–2358, 1982.

[31] G. Dagli, A. S. Argont, and R. E. Cohen. Particle-size effect in craze plasticity of high-impact polystyrene. *Polymer*, 36(11):2173–2180, 1995.

[32] D. A. Estenoz, G. R. Meira, N. Gómez, and H. M. Oliva. Mathematical model of a continuous industrial high-impact polystyrene process. *AIChE Journal*, 44(2):427–441, 1998.

[33] C. C. Chen. Simulation of a continuous bulk styrene polymerization process with catalytic initiation for crystal-clear polystyrene and rubber-modified polystyrene. *Polymer Reaction Engineering*, 6(3-4):145–192, 1998.

[34] E. Berkenwald. *Mathematical modeling of discontinuous bulk syrene polymerization process using multifunctional initiators.* PhD thesis, Instituto Tecnológico de Buenos Aires, 2016.

[35] J. L. Amos. The SPE international award address—1973 the development of impact polystyrene–a review. *Polymer Engineering and Science*, 14(1):1–11, 1974.

[36] M. L. Laganá, E. Berkenwald, P. Acuña, J. Enríquez Medrano, G. Morales, and D. Estenoz. New advances in the mathematical modeling of the continuous bulk process for the production of high-impact polystyrene using multifunctional initiators. *Polymer Engineering and Science*, 59(s2):E231–E246, 2019.

[37] B. Bilé, J. M. Gloaguen, J. M. Lefebvre, and J. P. Tancrez. Fracture behaviour of high impact polystyrene Influence of particle morphology. *Plastics, Rubber and Composites Processing and Applications*, 30(2):77–81, 2001.

[38] E. T. C. Mui, V. B. Boateng, J. F. Fellers, and J. L. White. Interaction of Polymerization Conditions, Structural Variables, and Mechanical Properties of Rubber-Modified Plastics Produced From Bulk Polymerized Styrene/Poly(Butadiene-Co-Styrene). *Journal of Applied Polymer Science*, 27(4):1395–1407, 1982.

[39] Y. Okamoto, H. Miyagi, M. Kakugo, and K. Takahashi. Impact Improvement Mechanism. *Macromolecules*, 24(1):5639–5644, 1991.

[40] S. Anzaldi, L. Bonifaci, E. Malaguti, M. Vighi, and G. P. Ravanetti. Some considerations on the second phase structure in high impact polystyrene and on the related measurement methods. *Journal of Materials Science Letters*, 13(21):1555–1557, 1994.

[41] I. Katime, J. R. R. Quintana, and C. Price. Influence of the microstructural morphology on the mechanical properties of high-impact polystyrene. *Materials Letters*, 22(5-6):297–301, 1995.

[42] E. P. Chang and A. Takahashi. Factors Influencing the Impact Strength of High Impact Polystyrene. *Polymer Engineering and Science*, 18(5):350–354, 1978.

[43] X. R. Li, X. L. Wang, and H. Koseki. Study on thermal decomposition characteristics of AIBN. *Journal of Hazardous Materials*, 159(1):13–18, 2008.

[44] G. P. Leal and J. M. Asua. Evolution of the morphology of HIPS particles. *Polymer*, 50(1):68–76, 2009.

[45] G. Riess, M. Schlienger, and S. Marti. New Morphologies in Rubber-Modified Polymers. *Journal of Macromolecular Science, Part B*, 17(2):355–374, 1980.

[46] R. Díaz De León, G. Morales, P. Acuña, J. Olivo, and L. F. Ramos-DeValle. Mechanical behavior of high impact polystyrene based on SBR copolymers: Part I. *Polymer Engineering and Science*, 45(9):1288–1296, 2005.

[47] G. Soto, E. Nava, M. Rosas, M. Fuenmayor, I. M. González, G. R. Meira, and H. M. Oliva. Bulk Polymerization of Styrene in the Presence of Polybutadiene: Effect of Initiator Type and Prepolymerization Conditions on Particle Morphology. *Journal of Applied Polymer Science*, 92:1397–1412, 2004.

[48] S. J. Lee, H. G. Jeoung, and K. H. Ahn. Influence of solvent contents on the rubber-phase particle size distribution of high-impact polystyrene. *Journal of Applied Polymer Science*, 89(13):3672–3679, 2003.

[49] F. Soriano-Corral, G. Morales, P. Acuña, E. Diaz Barriga, B. Arellano, C. Vargas, and O. De La Paz. Synthesis and Characterization of High Impact Polystyrene from a Heterogeneous Styrene-Rubber-Polystyrene Solution : Influence of PS Concentration on the Phase Inversion , Morphology and Impact Strength. *Macromolecular Symposia*, 325-326:177–183, 2013.

[50] Z. Song, H. Yuan, and Z. Pen. Studies on the rheological behavior of high-impact polystyrene prepolymerizing systems. *Journal of Applied Polymer Science*, 32(2):3349–3369, 1986.

[51] K. Sardelis, H. J. Michels, and G. Allen. Toughened polystyrene containing high cis-1,4-polybutadiene rubber. *Journal of Applied Polymer Science*, 28(10):3255–3268, 1983.

[52] B. Hu, O. K. Matar, G. F. Hewitt, and P. Angeli. Population balance modelling of phase inversion in liquid-liquid pipeline flows. *Chemical Engineering Science*, 61(15):4994–4997, 2006.

[53] C. Solans and I. Solé. Nano-emulsions: Formation by low-energy methods. *Current Opinion in Colloid and Interface Science*, 17(5):246–254, 2012.

[54] A. Perazzo, V. Preziosi, and S. Guido. Phase inversion emulsification: Current understanding and applications. *Advances in Colloid and Interface Science*, 222:581–599, 2015.

[55] K. Dedecker and G. Groeninckx. Reactive compatibilisation of A /(B/C) polymer blends part 2 Analysis of the phase inversion region and the co-continuous phase morphology. *Polymer*, 39(21):4993–5000, 1998.

[56] E. B. Nauman and D. Q. He. Morphology predictions for ternary polymer blends undergoing spinodal decomposition. *Polymer*, 35(11):2243–2255, 1994.

[57] M. Vonka, L. Šeda, and J. Kosek. Modelling of the High-Impact Polystyrene Morphogenesis. *Macromolecular Symposia*, 302(1):151–160, 2011.

[58] A. A. Alfarraj and E. B. Nauman. Reactive phase separation : Prediction of an occlusion morphology. *Polymer*, 49:339–344, 2008.

[59] M. Vonka and J. Kosek. Modelling the morphology evolution of polymer materials undergoing phase separation. *Chemical Engineering Journal*, 207-208:895–905, 2012.

[60] C. Luciani, D. A. Estenoz, G. Morales, and G. R. Meira. High impact polystyrene (HIPS). Predicting its molecular, morphological and mechanical properties. In *Proceedings of the CONAMET/SAM Congress*, La Serena, Chile, 2004.

[61] M. Fischer and G. P. Hellmann. On the Evolution of Phase Patterns during the High-Impact-Modified Polystyrene Process. *Macromolecules*, 29(7):2498–2509, 1996.

[62] G. M. Jordhamo, J. a. Manson, and L. H. Sperling. Phase Continuity and Inversion in Polymer Blends and Simultaneous Interpenetrating Networks. *Polymer Engineering and Science*, 26(8):517–524, 1986.

[63] T. R. Guilinger, A. K. Grislingas, and O. Erga. Phase inversion behavior of water-kerosene dispersions. *Industrial & Engineering Chemistry Research*, 27:978–982, 1988.

[64] J. A. Quinn and D. B. Sigloh. Phase Inversion in the Mixing of Immiscible Liquids. *The Canadian Journal of Chemical Engineering*, pages 15–18, 1963.

[65] A. H. Selker and C. A. Sleicher. Factors Affecting which Phase will Disperse when Immiscible Liquids are Stirred Together. *The Canadian Journal of Chemical Engineering*, 43(6):298–301, 1965.

[66] S. Kumar. On phase inversion characteristics of stirred dispersions. *Chemical Engineering Science*, 51(5):831–834, 1996.

[67] E. Dickinson. Interpretation of emulsion phase inversion as a cusp catastrophe. *Journal of Colloid and Interface Science*, 84(1):1–4, 1981.

[68] F. Bouchama, G. A. Van Aken, A. J.E. E Autin, and G. J.M. M Koper. On the mechanism of catastrophic phase inversion in emulsions. *Colloids and Surfaces A: Physicochemical and Engineering Aspects*, 231(1-3):11–17, 2003.

[69] P. Becher. *Encyclopedia of Emulsion Technology Vol. 3.* Marcel Dekker, New York, 1 edition, 1987.

[70] P. Hietaoja, R. Holsti-Miettinen, J. Seppala, and O. Ikkala. The Effect of Viscosity Ratio on the Phase Inversion of Polyamide 66 / Polypropylene Blends. *Journal of Applied Polymer Science*, 54:1613–1623, 1994.

[71] G. E. Molau. Heterogeneous Polymer Systems. I. Polymeric Oil-in-Oil Emulsions. *Journal of Polymer Science: Part A*, 3(4):1267–1278, 1965.

[72] C. Shih. Fundamentals of Polymer Compounding: The Phase-Inversion Mechanism During Mixing of Polymer Blends. *Advances in Polymer Technology*, 11(3):223–226, 1992.

[73] J. M. Maffi, G. R. Meira, and D. A. Estenoz. Mechanisms and conditions that affect phase inversion processes: A review. *The Canadian Journal of Chemical Engineering*, 99(1):178–208, 2020.

[74] M. Arashmid and V. Jeffreys. Analysis of the Phase Inversion Characteristics of Liquid-Liquid Dispersions. *AIChE Journal*, 26(1):51–55, 1980.

[75] M. J. McClarey and G. A. Mansoori. Factors affecting the phase inversion of dispersed immiscible liquid–liquid mixtures. *AIChE Symposium Series*, 74:134–139, 1978.

[76] M. Norato, C. Tsouris, and L. Tavlarides. Phase Inversion Studies in Liquid-Liquid Dispersions. *The Canadian Journal of Chemical Engineering*, 76:486–494, 1998.

[77] G. C. Yeh, F. H. Haynie, and R. E. X. A. Moses. Phase-Volume Relationship at the Point of Phase Inversion in Liquid Dispersions. *AIChE Journal*, 10(2):260–265, 1964.

[78] L. Y. Yeo, O. K. Matar, E. S. Perez de Ortiz, and G. F. Hewitt. Simulation studies of phase inversion in agitated vessels using a Monte Carlo technique. *Journal of Colloid and Interface Science*, 248(2):443–454, 2002.

[79] B. Hu, P. Angeli, O. K. Matar, and G. F. Hewitt. Prediction of phase inversion in agitated vessels using a two-region model. *Chemical Engineering Science*, 60(13):3487–3495, 2005.

[80] A. R. Almeida Colmanetti, M. S. de Castro, M. C. Barbosa, and O. M. Hernandez Rodriguez. Phase inversion phenomena in vertical three-phase flow: Experimental study on the influence of fluids viscosity, duct geometry and gas flow rate. *Chemical Engineering Science*, 189:245–259, 2018.

[81] A. K. Chesters. The modelling of coalescence processes in fluid-liquid dispersions : a review of current understianding. *Chemical Engineering Research and Design*, 69(4):259–227, 1991.

[82] I. S. Miles and A. Zurek. Preparation, Structure, and Properties of Two-Phase Co-Continuous Polymer Blends. *Polymer Engineering and Science*, 28(12):796–805, 1988.

[83] R. M. Ho, C. H. Wu, and A. C. Su. Morphology of plastic/rubber blends. *Polymer Engineering & Science*, 30(9):511–518, 1990.

[84] T. H. Chen and A. C. Su. Morphology of poly(p-phenylene sulfide)polyethylene blends. *Polymer*, 34(23):4826–4831, 1993.

[85] N. Kitayama, H. Keskkula, and D. R. Paul. Reactive compatibilization of nylon 6/styrene–acrylonitrile copolymer blends Part 3. Tensile stress-strain behavior. *Polymer*, 42(8):3751–3759, 2001.

[86] V. Everaert, L. Aerts, and G. Groeninckx. Phase morphology development in immiscible PP /(PS / PPE) blends influence of the melt-viscosity ratio and blend composition. *Polymer*, 40:6627–6644, 1999.

[87] S. Arirachakaran, K. D. Oglesby, M. S. Malinowsky, O. Shoham, and J. P. Brill. An Analysis of Oil/Water Flow Phenomena in Horizontal Pipes. *SPE Production Operations Symposium*, 18836:155, 1989.

[88] V. I. Metelkin and V. S. Blekht. Formation of a continuous phase in heterogeneous polymer mixtures. *Colloid Journal of the USSR*, 46(3):425–429, 1984.

[89] L. A. Utracki. On the viscosity-concentration dependence of immiscible polymer blends. *Journal of Rheology*, 35(8):1615–1637, 1991.

[90] S. Steinmann, W. Gronski, and C. Friedrich. Cocontinuous polymer blends: Influence of viscosity and elasticity ratios of the constituent polymers on phase inversion. *Polymer*, 42(15):6619–6629, 2001.

[91] A. W. Pacek, A. W. Nienow, and I. P. T. Moore. On the structure of turbulent liquid-liquid dispersed flows in an agitated vessel. *Chemical Engineering Science*, 49(20):3485–3498, 1994.

[92] S. Kumar, R. Kumar, and K. S. Gandhi. Influence of the wetting characteristics of the impeller on phase inversion. *Chemical Engineering Science*, 46(9):2365–2367, 1991.

[93] L. Liu, O. K. Matar, E. S. Perez de Ortiz, and G. F. Hewitt. Experimental investigation of phase inversion in a stirred vessel using LIF. *Chemical Engineering Science*, 60(1):85–94, 2005.

[94] R. N. Reeve and J. C. Godfrey. Phase Inversion During Liquid – Liquid Mixing in Continuous Flow, Pump – Mix, Agitated Tanks. *Chemical Engineering Research and Design*, 80(8):864–871, 2002.

[95] M. Tidhar, J. C. Merchuk, A. N. Sembira, and D. Wolf. Characteristics of a motionless mixer for dispersion of immiscible fluids- II. Phase inversion of liquid-liquid systems. *Chemical Engineering Science*, 41(3):457–462, 1986.

[96] K. B. Deshpande and S. Kumar. A new characteristic of liquid – liquid systems — inversion holdup of intensely agitated dispersions. *Chemical Engineering Science*, 58(16):3829–3835, 2003.

[97] W. A. Rodger, V. G. Trice, and J. H. Rushton. Effect of fluid motion on interfacial area of dispersions. *Chemical Engineering Progress*, 52, 1956.

[98] L. Y. Yeo, O. K. Matar, E. S. de Perez Ortiz, and Hewitt G. F. Phase inversion and associated phenomena, 2000.

[99] J. L. Cayias, R. S Schechter, and W. H Wade. Modeling Crude Oils for Low Interfacial Tension. *Society of Petroleum Engineers Journal*, 16(6):351–357, 1976.

[100] J. C. Morgan, R. S. Schechter, and W. H. Wade. Improved Oil Recovery by Surfactant and Polymer Flooding. In D. O. Shah and R. S. Shechter, editors, *Improved Oil Recovery by Surfactant and Polymer Flooding*, page 103. Academic Press, Inc., New York, 1977.

[101] J. L. Salager, J. C. Morgan, R. S. Schechter, W. H. Wade, and E. Vasquez. Optimum Formulation of Surfactant/Water/Oil Systems for Minimum Interfacial Tension or Phase Behavior. *Society of Petroleum Engineers Journal*, 19(02):107–115, 1979.

[102] J. L. Salager, A. M. Forgiarini, and J. Bullón. How to Attain Ultralow Interfacial Tension and Three-Phase Behavior with Surfactant Formulation for Enhanced Oil Recovery : A Review . Part 1 . Optimum Formulation for Simple Surfactant – Oil – Water Ternary Systems. *Journal of Surfactants and Detergents*, 16:449–472, 2013.

[103] T. Sottmann and R. Strey. Ultralow interfacial tensions in water-n-alkane-surfactant systems. *Journal of Chemical Physics*, 106(20):8606–8615, 1997.

[104] H. Leitão, A. M. Somoza, M. M. Telo Da Gama, T. Sottmann, and R. Strey. Scaling of the interfacial tension of microemulsions: A phenomenological description. *Journal of Chemical Physics*, 105(7):2875–2883, 1996.

[105] R. Strey. Microemulsion microstructure and interfacial curvature. *Colloid & Polymer Science*, 272(8):1005–1019, 1994.

[106] S. Sajjadi, M. Zerfa, and B. W. Brooks. Dynamic behaviour of drops in oil/water/oil dispersions. *Chemical Engineering Science*, 57(4):663–675, 2002.

[107] S. Clarke and H. Sawistowski. Phase inversion of stirred liquid/liquid dispersions under mass transfer conditions. *Chemical Engineering Research Design*, 56:50–55, 1978.

[108] R. W. Luhning and H. Sawistowski. Phase inversion in stirred liquid-liquid systems. In *Proceedings International Solvent Extraction Conference*, pages 873–887, 1971.

[109] S. Kato, E. Nakayama, and J. Kawasaki. Types of dispersion in agitated liquid-liquid systems. *The Canadian Journal of Chemical Engineering*, 69(1):222–227, 1991.

[110] G. F. Freeguard and M. Karmarkar. The Production of Rubber-Modified Polystyrene. Some Criteria Influencing the Selection and Design of the Agitator System. *Journal of Applied Polymer Science*, 16:69–82, 1972.

[111] M. Homs, G. Calderó, M. Monge, D. Morales, and C. Solans. Influence of polymer concentration on the properties of nano-emulsions and nanoparticles obtained by a low-energy method. *Colloids and Surfaces A: Physicochemical and Engineering Aspects*, 536:204–212, 2018.

[112] F. Wang, Y. Ouyang, H. Zou, Z. Yang, and H. Liu. Self-assembling behavior and stimuli-responsive emulsifying performance of coumarin-containing amphiphilic terpolymer. *Colloids and Surfaces A: Physicochemical and Engineering Aspects*, 535:274–282, 2017.

[113] L. Besnard, F. Marchal, J. F. Paredes, J. Daillant, N. Pantoustier, P. Perrin, and P. Guenoun. Multiple emulsions controlled by stimuli-responsive polymers. *Advanced Materials*, 25(20):2844–2848, 2013.

[114] X. Huang, R. Fang, D. Wang, J. Wang, H. Xu, Y. Wang, and X. Zhang. Tuning Polymeric Amphiphilicity via Se-N Interactions: Towards One-Step Double Emulsion for Highly Selective Enzyme Mimics. *Small*, 11(13):1537–1541, 2015.

[115] X. Huang, Y. Yang, J. Shi, H. T. Ngo, C. Shen, W. Du, and Wang Y. High-Internal-Phase Emulsion Tailoring Polymer Amphiphilicity towards an Efficient NIR-Sensitive Bacteria Filter. *Small*, 11(37):4876–4883, 2015.

[116] G. Duan, A. Kumar, S. Li, C. M. Cheng, and D. Lee. Effect of triblock copolymer surfactant composition on flow-induced phase inversion emulsification in a tapered channel. *Journal of Colloid and Interface Science*, 537:579–587, 2019.

[117] B. W. Brooks and H. N. Richmond. Phase inversion in non-ionic surfactant-oil-water systems II. Drop size studies in catastrophic inversion with turbulent mixing. *Chemical Engineering Science*, 49(7):1065–1075, 1994.

[118] A. T. Florence and J. A. Rogers. Emulsion stabilization by non-ionic sufractants: experiment and theory. *Journal of Pharmacy and Pharmacology*, 23:233–251, 1971.

[119] P. Becher. The effect of the nature of the emulsifying agent on emulsion inversion. *Journal of the Society of Cosmetic Chemists*, 9:141–145, 1958.

[120] W H Wade, James C Morgan, R S Schechter, J K Jacobson, and Jean-louis Salager. Interfacial tension and phase behavior of surfactant systems. *SPE Journal*, pages 242–252, 1978.

[121] J. L. Salager, N. Marquez, A. Graciaa, and J. Lachaise. Partitioning of ethoxylated octylphenol surfactants in microemulsion-oil-water systems: influence of temperature and relation between partitioning coefficient and physicochemical formulation. *Langmuir*, 16:5534–5539, 2000.

[122] P. A. Winsor. Hydrotropy, solubilisation and related emulsification processes. *Transactions of the Faraday Society*, 44:376–398, 1948.

[123] B. W. Brooks and H. N. Richmond. Dynamics of liquid-liquid phase inversion using non-ionic surfactants. *Colloids and Surfaces*, 58(1-2):131–148, 1991.

[124] J. L. Salager, A. Forgiarini, L. Márquez, A. Peña, A. Pizzino, M. P. Rodriguez, and M. Rondón-González. Using emulsion inversion in industrial processes. *Advances in Colloid and Interface Science*, 108-109:259–272, 2004.

[125] S. Queste, J. L. Salager, R. Strey, and J. M. Aubry. The EACN scale for oil classification revisited thanks to fish diagrams. *Journal of Colloid and Interface Science*, 312(1):98–107, 2007.

[126] E. J. Acosta. The HLD-NAC equation of state for microemulsions formulated with non-ionic alcohol ethoxylate and alkylphenol ethoxylate surfactants. *Colloids and Surfaces A: Physicochemical and Engineering Aspects*, 320(1-3):193–204, 2008.

[127] L. Jin, A. Jamili, Z. Li, J. Lu, H. Luo, B. J. Shiau, M. Delshad, and J. H. Harwell. Physics based HLD-NAC phase behavior model for surfactant/crude oil/brine systems. *Journal of Petroleum Science and Engineering*, 136:68–77, 2015.

[128] A. Maestro, I. Solè, C. González, C. Solans, and J. M. Gutiérrez. Influence of the phase behavior on the properties of ionic nanoemulsions prepared by the phase inversion composition method. *Journal of Colloid and Interface Science*, 327(2):433–439, 2008.

[129] K. Shinoda and H. Arai. The correlation between phase inversion temperature in emulsion and cloud point in solution of nonionic emulsifier. *The journal of Phisical Chemistry*, 68(12):3485–3490, 1964.

[130] K. Shinoda and H. Saito. The Effect of Temperature on the Phase Equilibria and the Types of Dispersions of the Ternary System Composed of Water ,. *Journal of Colloid And Interface Science*, 26(1):70–74, 1968.

[131] K. Shinoda and H. Saito. The Stability of O/W type emulsions as functions of temperature and the HLB of emulsifiers: The emulsification by PIT-method. *Journal of Colloid And Interface Science*, 30(2):258–263, 1969.

[132] K. Shinoda and H. Takeda. The effect of added salts in water on the hydrophile-lipophile balance of nonionic surfactants: The effect of added salts on the phase inversion temperature of emulsions. *Journal of Colloid And Interface Science*, 32(4):642–646, 1970.

[133] C. Parkinson and P. Sherman. Phase inversion temperature as an accelerated method for evaluating emulsion stability. *Journal of Colloid And Interface Science*, 41(2):328–330, 1972.

[134] P. Dokic and P. Sherman. Study on thremal induced phase inversion of concentrted O/W emulsions stabilized by various tween emulsifiers. *Colloid and Polymer Science*, 258:1159–1163, 1980.

[135] J. Rao and D. J. McClements. Stabilization of phase inversion temperature nanoemulsions by surfactant displacement. *Journal of Agricultural and Food Chemistry*, 58(11):7059–7066, 2010.

[136] A. Kabalnov and H. Wennerström. Macroemulsion Stability: The Oriented Wedge Theory Revisited. *Langmuir*, 12:276–292, 1996.

[137] H. Kunieda and K. Shinoda. Correlation between Critical Solution Phenomena and Ultralow Interfacial Tensions in a Surfactant/Water/Oil System. *Bulletin of the Chemical Society of Japan*, 55(6):1777–1781, 1982.

[138] F. Boscán, M. J. Barandiaran, and . Paulis. From miniemulsion to nanoemulsion polymerization of superhydrophobic monomers through low energy phase inversion temperature. *Journal of Industrial and Engineering Chemistry*, 58:1–8, 2018.

[139] E. Dickinson. Thermodynamic aspects of emulsion phase inversion. *Journal of Colloid And Interface Science*, 87(2):416–423, 1982.

[140] P. Poesio and G. P. Beretta. Minimal dissipation rate approach to correlate phase inversion data. *International Journal of Multiphase Flow*, 34(7):684–689, 2008.

[141] T. Al-Sahhaf, A. Elkamel, A. S. Ahmed, and A. R. Khan. The influence of temperature, pressure, salinity, and surfactant concentration on the interfacial tension of the n-octane-water system. *Chemical Engineering Communications*, 192(4-6):667–684, 2005.

[142] L. H. Chen and Y. L. Lee. Adsorption behavior of surfactants and mass transfer in single-drop extraction. *AIChE J.*, 46(1):160–168, 2000.

[143] A. Bąk and W. Podgórska. Interfacial and surface tensions of toluene/water and air/water systems with nonionic surfactants Tween 20 and Tween 80. *Colloids and Surfaces A: Physicochemical and Engineering Aspects*, 504:414–425, 2016.

[144] A. Domínguez, A. Fernández, N. González, E. Iglesias, and L. Montenegro. Determination of Critical Micelle Concentration of Some Surfactants by Three Techniques. *Journal of Chemical Education*, 74(10):1227–1231, 1997.

[145] J. Saien and S. Akbari. Interfacial Tension of Toluene + Water + Sodium Dodecyl Sulfate from (20 to 50) C and pH between 4 and 9. *Journal of Chemical & Engineering Data*, 51(5):1832–1835, 2006.

[146] F. Groeneweg, W.G.M. Agterof, P. Jaeger, J.J.M. Janssen, J.A. Wieringa, and J.K. Klahn. On the Mechanism of the Inversion of Emulsions. *Chemical Engineering Research and Design*, 76(1):55–63, 1998.

[147] I. Solè, A. Maestro, C. González, C. Solans, and M. Gutie. Optimization of nano-emulsion preparation by low-energy methods in an ionic surfactant sytem. *Langmui*, 22:8326–8332, 2006.

[148] E. Assadpour, Y. Maghsoudlou, S. M. Jafari, M. Ghorbani, and M. Aalami. Optimization of folic acid nano-emulsification and encapsulation by maltodextrin-whey protein double emulsions. *International Journal of Biological Macromolecules*, 86:197–207, 2016.

[149] C. V. Sternling and L. E. Scriven. Interfacial turbulence: Hydrodynamic instability and the marangoni effect. *AIChE Journal*, 5(4):514–523, 1959.

[150] A. Kumar, S. Li, C. M. Cheng, and D. Lee. Recent Developments in Phase Inversion Emulsification. *Industrial and Engineering Chemistry Research*, 54(34):8375–8396, 2015.

[151] Y. Deng and N. L. Thomas. Blending poly(butylene succinate) with poly(lactic acid): Ductility and phase inversion effects. *European Polymer Journal*, 71:534–546, 2015.

[152] A. Adedeji, A. M. Jamieson, and S. D. Hudson. Phase Inversion in Compatibilized Immiscible Polymer Blends with Exothermic Interfacial Mixing. *Macromolecules*, 28(15):5255–5261, 1995.

[153] P. Charoensirisomboon, T. Chiba, T. Inoue, and M. Weber. In situ formed copolymers as emulsifier and phase-inversion-aid in reactive polysulfone/polyamide blends. *Polymer*, 41(15):5977–5984, 2000.

[154] X. Zhang, Z. Yin, and J. Yin. The phase inversion and morphology of nylon 1010/polypropylene blends. *Journal of Applied Polymer Science*, 62:893–901, 1996.

[155] C. Épinat, L. Trouillet-Fonti, and P. Sotta. Predicting phase inversion based on the rheological behavior in Polyamide 6/Polyethylene blends. *Polymer*, 137:132–144, 2018.

[156] D. Bourry and B. D. Favis. Cocontinuity and phase inversion in HDPE/PS blends: Influence of interfacial modification and elasticity. *Journal of Polymer Science, Part B: Polymer Physics*, 36(11):1889–1899, 1998.

[157] R. Díaz de León, G. Morales, P. Acuña, and F. Soriano. Phenomenon of Phase Inversion in High Impact Polystyrene: Physico-Chemical, Rheological and Morphological Study in the Presence of Chain Transfer Agent and Using Different Tapered Block Copolymers as the Precursor Rubber. *Polymer Engineering and Science*, 50(2):373–383, 2010.

[158] P. Becher. *Emulsions: theory and practice*. Reinhold Publishing Corporation, New York, 2 edition, 1965.

[159] D. B. Genovese. Shear rheology of hard-sphere, dispersed, and aggregated suspensions, and filler-matrix composites. *Advances in Colloid and Interface Science*, 171-172:1–16, 2012.

[160] C. Liu, M. Li, R. Han, J. Li, and C. Liu. Rheology of Water-In-Oil Emulsions with Different Drop Sizes. *Journal of Dispersion Science and Technology*, 37(3):333–344, 2016.

[161] R. Pal. Effect of Droplet Size on the Rheology of Emulsions. *AIChE Journal*, 42(11):3181–3190, 1996.

[162] J. Bałdyga, M. Jasińska, and A. J. Kowalski. Effect of rheology of dense emulsions on the flow structure in agitated systems. *Chemical Engineering Research and Design*, 108:3–12, 2016.

[163] P. Sherman. Studies in water-in-oil emulsions. IV. The influence of the emulsifying agent on the viscosity of water-in-oil emulsions of high water content. *Journal of Colloid Science*, 10(1):63–70, 1955.

[164] P. Snabre and P. Mills. Rheology of concentrated suspensions of viscoelastic particles. *Colloids and Surfaces A: Physicochemical and Engineering Aspects*, 152(1-2):79–88, 1999.

[165] P. Kundu, V. Kumar, and I. M. Mishra. Study the electro-viscous effect on stability and rheological behavior of surfactant-stabilized emulsions. *Journal of Dispersion Science and Technology*, 39(3):384–394, 2018.

[166] J. M. Maffi, N. Casis, P. Acuña, G. Morales, and D. A. Estenoz. Mechanisms and Conditions that Affect Phase Inversion Processes. The Case of High-Impact Polystyrene. *Polymer Engineering and Science*, 60(3):491–502, 2020.

[167] G. F. Freeguard and M. Karmarkar. The production of rubber-modified polystyrene. I. Rheological behavior of the polymerizing system. *Journal of Applied Polymer Science*, 15(7):1649–1655, 1971.

[168] A. Einstein. Effect of suspended rigid spheres on viscosity. *Annals of Physics*, 19:289–306, 1906.

[169] F. Eirich, M. Bunzl, and H. Margaretha. Untersuchungen über die Viskosität von Suspensionen und Lösungen. 4. Über die Viskosität von Kugelsuspensionen. *Kolloid-Zeitschrift*, 74(3):266–275, 1936.

[170] D. R. Oliver and S. G. Ward. Relationship between relative viscosity and volume concentration of stable suspensions of spherical particles. *Nature*, 171:396–397, 1953.

[171] I. M Krieger and T. J. Dougherty. A Mechanism for Non-Newtonian Flow in Suspensions of Rigid Spheres. *Transactions of the Society of Rheology*, 3(1):137–152, 1959.

[172] D. Quemada. Rheology of concentrated disperse systems II. A model for non-newtonian shear viscosity in steady flows. *Rheologica Acta*, 17(6):632–642, 1978.

[173] R. Roscoe. The viscosity of suspensions of rigid spheres. *British Journal of Applied Physics*, 3(8):267–269, 1952.

[174] R. Lapasin, M. Grassi, and S. Pricl. Rheological modeling of fractal and dense suspensions. *Chemical Engineering Journal and the Biochemical Engineering Journal*, 64(1):99–106, 1996.

[175] G. Broughton and L. Squires. The viscosity of oil-water emulsions. *The Journal of Physical Chemistry*, 42(2):253–263, 1938.

[176] E. G. Richardson. Über die viskosität von Emulsionen. *Kolloid-Zeitschrift*, 65(1):32–37, 1933.

[177] M. Mooney. The viscosity of a concentrated suspension of spherical particles. *Journal of Colloid Science*, 6(2):162–170, 1951.

[178] S. Matsumoto and M. Kohda. The Viscosity of W/O/W Emulsions: An Attempt to Estimate the Water Permeation Coefficient of the Oil Layer from the Viscosity Changes in Diluted Systems on Aging under Osmotic Pressure Gradients. *Journal of Colloid And Interface Science*, 73(1):13–20, 1980.

[179] E. Hatschek. Viscosity of dispersions. *Kolloid-Zeitschrift*, 8:34, 1911.

[180] J. O. Sibree. The Viscosity of Emulsions. Part II. *Transactions of the Faraday Society*, 27:161–176, 1931.

[181] H. L. Bredée and J. de Booys. Die Konzentrationsabhäingigkeit der Viskosität und die Einteilung der Kolloide nach ihrer Teilchengestalt. II. *Kolloid-Zeitschrift*, 79(1):43–49, 1937.

[182] H. Eilers. The viscosity of the emulsion of highly viscous substances as function of concentration. *Kolloid-Zeitschrift*, 97(3):313–321, 1941.

[183] S. H. Maron and B. P. Madow. Rheology of synthetic latex. III. Concentration dependence of flow in type III Gr-S latex. *Journal of Colloid Science*, 8(1):130–136, 1953.

[184] G. I. Taylor. The Viscosity of a Fluid Containing Small Drops of Another Fluid. *Proceedings of the Royal Society of London A.*, 138(834):41–48, 1932.

[185] S. J. Choi and W. R. Schowalter. Rheological properties of nondilute suspensions of deformable particles. *Physics of Fluids*, 18(4):420, 1975.

[186] A. Leviton and A. Leighton. Viscosity relationships in emulsions containing milk fat. *The Journal of Physical Chemistry*, 40(1):71–80, 1936.

[187] P. Sherman. The influence of emulsifying agent concentration on emulsion viscosity. *Kolloid-Zeitschrift*, 165(2):156–161, 1959.

[188] P. Sherman. The influence of globule size on emulsion viscosity. In *Proceedings of the International Congress of Surface Activity*, page 596, 1960.

[189] M. von Smoluchowski. Theoretische Bemerkungen uber die Viskositat der Kolloide. *Kolloid-Zeitschrift*, 18(5):190–195, 1916.

[190] T. S. Omonov, C. Harrats, P. Moldenaers, and G. Groeninckx. Phase continuity detection and phase inversion phenomena in immiscible polypropylene / polystyrene blends with different viscosity ratios. *Polymer*, 48:5917–5927, 2007.

[191] N. Bremond, H. Doméjean, and J. Bibette. Propagation of drop coalescence in a two-dimensional emulsion: A route towards phase inversion. *Physical Review Letters*, 106(21):1–4, 2011.

[192] A. Kumar, S. Li, C. M. Cheng, and D. Lee. Flow-induced phase inversion of emulsions in tapered microchannels. *Lab on a Chip*, 16(21):4173–4180, 2016.

[193] A. Deblais, R. Harich, D. Bonn, A. Colin, and H. Kellay. Spreading of an Oil-in-Water Emulsion on a Glass Plate: Phase Inversion and Pattern Formation. *Langmuir*, 31(22):5971–5981, 2015.

[194] C. K. Shih. Mixing and morphological transformations in the compounding process for polymer blends: The phase inversion mechanism. *Polymer Engineering & Science*, 35(21):1688–1694, 1995.

[195] N. Mekhilef and H. Verhoogt. Phase inversion and dual-phase continuity in polymer blends: Theoretical predictions and experimental results. *Polymer*, 37(18):4069–4077, 1996.

[196] U. Sundararaj, C. W. Macosko, and C. K. Shih. Evidence for inversion of phase continuity during morphology development in polymer blending. *Polymer Engineering and Science*, 36(13):1769–1781, 1996.

[197] M. Zerfa, S. Sajjadi, and B. W. Brooks. Phase behaviour of polymer emulsions during the phase inversion process in the presence of non-ionic surfactants. *Colloids and Surfaces A: Physicochemical and Engineering Aspects*, 178(1-3):41–48, 2001.

[198] S. M. Fakhr-Din. *Phase inversion and droplet size measurements in agitated liquid-liquid systems*. Phd, University of Manchester, 1973.

[199] L. Y. Yeo, O. K. Matar, E. S. Perez de Ortiz, and G. F. Hewitt. The drainage and rupture of the film between colliding drops in the presence of surfactant. In *Proceeding of the International Solvent Extraction Conference*, pages 70–76, 2002.

[200] N. Brauner and A. Ullmann. Modeling of phase inversion phenomenon in two-phase pipe flows. *International Journal of Multiphase Flow*, 28(7):1177–1204, 2002.

[201] A. Kabalnov and J. Weers. Macroemulsion stability within the Winsor III region: theory versus experiment. *Langmuir*, 12(8):1931–1935, 1996.

[202] L. M. Oshinowo, C. G. Quintero, and R. D. Vilagines. CFD and Population Balance Modeling of Crude Oil Emulsions in Batch Gravity Separation—Comparison to Ultrasound Experiments. *Journal of Dispersion Science and Technology*, 37(5):665–675, 2016.

[203] Z. Gao, D. Li, A. Buffo, W. Podgórska, and D. L. Marchisio. Simulation of droplet breakage in turbulent liquid-liquid dispersions with CFD-PBM: Comparison of breakage kernels. *Chemical Engineering Science*, 142:277–288, 2016.

[204] D. Li, A. Buffo, W. Podgórska, D. L. Marchisio, and Z. Gao. Investigation of droplet breakup in liquid–liquid dispersions by CFD–PBM simulations: The influence of the surfactant type. *Chinese Journal of Chemical Engineering*, 25(10):1369–1380, 2017.

[205] S. Aryafar, N. Sheibat-Othman, and T. F. L. McKenna. Coupling of CFD Simulations and Population Balance Modeling to Predict Brownian Coagulation in an Emulsion Polymerization Reactor. *Macromolecular Reaction Engineering*, 11(5):1–17, 2017.

[206] G. Yang, H. Zhang, J. Luo, and T. Wang. Drag force of bubble swarms and numerical simulations of a bubble column with a CFD-PBM coupled model. *Chemical Engineering Science*, 192:714–724, 2018.

[207] C. Qin, C. Chen, Q. Xiao, N. Yang, C. Yuan, C. Kunkelmann, M. Cetinkaya, and K. Mülheims. CFD-PBM simulation of droplets size distribution in rotor-stator mixing devices. *Chemical Engineering Science*, 155:16–26, 2016.

[208] Le Xie, Qi Liu, and Zheng Hong Luo. A multiscale CFD-PBM coupled model for the kinetics and liquid–liquid dispersion behavior in a suspension polymerization stirred tank. *Chemical Engineering Research and Design*, 130:1–17, 2018.

[209] S. Castellano, N. Sheibat-Othman, D. Marchisio, A. Buffo, and S. Charton. Description of droplet coalescence and breakup in emulsions through a homogeneous population balance model. *Chemical Engineering Journal*, 354(May):1197–1207, 2018.

[210] A. S. C. Lawrence and O. S. Mills. Kinetics of the coagulation of emulsions. *Discussions of the Faraday Society*, 18:98–104, 1954.

[211] W.J. J Howarth. Coalescence of drops in a turbulent flow field. *Chemical Engineering Science*, 19(1):33–38, 1964.

[212] T. Gillespie. The distribution of particles in a dilute stirred suspension. *Journal of Colloid Science*, 17(3):290–291, 1962.

[213] R. Shinnar. On the behaviour of liquid dispersions in mixing vessels. *Journal of Fluid Mechanics*, 10(2):259–275, 1961.

[214] R. S. Allan and S. G. Mason. Particle motions in sheared suspensions. XIV. Coalescence of liquid drops in electric and shear fields. *Journal of Colloid Science*, 17(4):383–408, 1962.

[215] G. D. M. Mackay and S. G. Mason. The gravity approach and coalescence of fluid drops at liquid interfaces. *The Canadian Journal of Chemical Engineering*, 41(5):203–212, 1963.

[216] J. C. Lee and T. D. Hodgson. Film flow and coalescence-I Basic relations, film shape and criteria for interface mobility. *Chemical Engineering Science*, 23(11):1375–1397, 1968.

[217] S. L. Ross. *Measurements and models of the dispersed phase mixing process (PhD Thesis)*. Phd, The University of Michigan, Ann Arbor, 1971.

[218] B. Liu, R. Manica, Q. Liu, E. Klaseboer, Z. Xu, and G. Xie. Coalescence of bubbles with mobile interfaces in water. *Physical Review Letters*, 122(19):194501, 2019.

[219] G. Besagni and F. Inzoli. The effect of electrolyte concentration on counter-current gas–liquid bubble column fluid dynamics: Gas holdup, flow regime transition and bubble size distributions. *Chemical Engineering Research and Design*, 118:170–193, 2017.

[220] H. Sovová. Breakage and coalescence of drops in a batch stirred vessel II - Comparison of model and experiments. *Chemical Engineering Science*, 36(9):1567–1573, 1981.

[221] E. G. Chatzi, A. D. Gavrielides, and C. Kiparissides. Generalized Model for Prediction of the Steady-State Drop Size Distributions in Batch Stirred Vessels. *Industrial & Engineering Chemistry Research*, 28(11):1704–1711, 1989.

[222] M. Simon. *Koaleszenz von Tropfen und Tropfenschwärmen*. Phd, Teschinschen Universität Kaiserslautern, 2004.

[223] P. M. Bapat, L. L. Tavlarides, and G. W Smith. Monte carlo simulation of mass transfer in liquid-liquid dispersions. *Chemical Engineering Science*, 38(12):2003–2013, 1983.

[224] M. J. Prince and H. W. Blanch. Bubble Coalescence and Breakup in Air Sparged Bubble Columns. *AIChE Journal*, 36(10):1485–1499, 1990.

[225] M. A. Delichatsios and R. F. Probstein. Coagulation in Turbulent Flow: Theory and Experiment. *Journal of Colloid And Interface Science*, 51(3):394–405, 1975.

[226] G. Kocamustafaogullari and M. Ishii. Foundation of the interfacial area transport equation and its closure relations. *International Journal of Heat and Mass Transfer*, 38(3):481–493, 1995.

[227] T. Wang, J. Wang, and Y. Jin. Population balance model for gas - Liquid flows: Influence of bubble coalescence and breakup models. *Industrial and Engineering Chemistry Research*, 44(19):7540–7549, 2005.

[228] C. A. Coulaloglou and L. L. Tavlarides. Description of interaction processes in agitated liquid-liquid dispersions. *Chemical Engineering Science*, 32(11):1289–1297, 1977.

[229] A. W. Nienow. Break-up, coalescence and catastrophic phase inversion in turbulent contactors. *Advances in Colloid and Interface Science*, 108-109:95–103, 2004.

[230] H. Sovová and J. Prochazka. Breakage and coalescence of drops in a batch stirred vessel I - Comparison of continuous and discrete models. *Chemical Engineering Science*, 36:163–171, 1981.

[231] J. M. H. Janssen and H. E. Meijer. Dynamics of liquid-liquid mixing: a 2-zone model. *Polymer Engineering and Science*, 35(22):1766–1780, 1995.

[232] S. P. Lyu, F. S. Bates, and C. W. Macosko. Coalescence in polymer blends during shearing. *AIChE Journal*, 46(2):229–238, 2000.

[233] J. Kamp, J. Villwock, and M. Kraume. Drop coalescence in technical liquid/liquid applications: A review on experimental techniques and modeling approaches. *Reviews in Chemical Engineering*, 33(1):1–47, 2017.

[234] T. Hibiki and M. Ishii. One-group interfacial area transport of bubbly flows in vertical round tubes. *International Journal of Heat and Mass Transfer*, 43(15):2711–2726, 2000.

[235] F. Lehr, M. Millies, and D Mewes. Bubble size distributions and flow fields in bubble columns. *AIChE Journal*, 42(11):1225–1233, 2002.

[236] T. Wang, J. Wang, and Y. Jin. Theoretical prediction of flow regime transition in bubble columns by the population balance model. *Chemical Engineering Science*, 60(22):6199–6209, 2005.

[237] I. U. Vakarelski, R. Manica, E. Q. Li, E. S. Basheva, D. Y. C. Chan, and S. T. Thoroddsen. Coalescence Dynamics of Mobile and Immobile Fluid Interfaces. *Langmuir*, 34(5):2096–2108, 2018.

[238] D. Y . C. Chan, E. Klaseboer, and R. Manica. Film drainage and coalescence between deformable drops and bubbles. *Soft Matter*, 7(6):2235–2264, 2011.

[239] E. Klaseboer, J. Ph. Chevaillier, C. Gourdon, and O. Masbernat. Film drainage between colliding drops at constant approach velocity: Experiments and modeling. *Journal of Colloid and Interface Science*, 229(1):274–285, 2000.

[240] K. Guo, T. Wang, Y. Liu, and J. Wang. CFD-PBM simulations of a bubble column with different liquid properties. *Chemical Engineering Journal*, 329:116–127, 2017.

[241] S. G. Yiantsios and R. H. Davis. On the buoyancy-driven motion of a drop towards a rigid surface or a deformable interface. *Journal of Fluid Mechanics*, 217(91):547–573, 1990.

[242] C. Tsouris and L. L. Tavlarides. Breakage and coalescence models for drops in turbulent dispersions. *AIChE Journal*, 40(3):395–406, 1994.

[243] A. Vrij. Possible mechanism for the spontaneous rupture of thin, free liquid films. *Discussions Faraday Society*, 42:23–33, 1966.

[244] S. Abid and A. K. Chesters. The drainage and rupture of partially-mobile films between colliding drops at constant approach velocity. *International Journal of Multiphase Flow*, 20(3):613–629, 1994.

[245] T. G. M. van de Ven and S. G. Mason. The microrheology of colloidal dispersions IV. Pairs of interacting spheres in shear flow. *Journal of Colloid And Interface Science*, 57(3):505–516, 1976.

[246] G. R. Zeichner and W. R. Schowalter. Use of trajectory analysis to study stability of colloidal dispersions in flow fields. *AIChE Journal*, 23(3):243–254, 1977.

[247] M. Manga and H. A. Stone. Buoyancy-Driven Interactions Between Two Deformable Viscous Drops. *Journal of Fluid Mechanics*, 256:647–683, 1993.

[248] X. Zhang and R. H. Davis. The rate of collisions due to Brownian or gravitational motion of small drops. *Journal of Fluid Mechanics*, 230:479–504, 1991.

[249] H. Wang, A. Z. Zinchenko, and R. H. Davis. The Collision Rate of Small Drops in Linear Flow Fields. *Journal of Fluid Mechanics*, 265(1994):161–188, 1994.

[250] M. A. Rother, A. Z. Zinchenko, and R. H. Davis. Buoyancy-driven coalescence of slightly deformable drops. *Journal of Fluid Mechanics*, 346:117–148, 1997.

[251] M. A. Rother and R. H. Davis. The effect of slight deformation on droplet coalescence in linear flows. *Physics of Fluids*, 13(5):1178–1190, 2001.

[252] Y. Liao and D. Lucas. A literature review on mechanisms and models for the coalescence process of fluid particles. *Chemical Engineering Science*, 65(10):2851–2864, 2010.

[253] Y. Y. Li, Z. Q. Chen, Y. Huang, and J. Sheng. Morphology development in polypropylene/polystyrene blends during coalescence under shear. *Journal of Applied Polymer Science*, 104:666–671, 2007.

[254] V. Alopaeus, J. Koskinen, and K. I. Keskinen. Simulation of the population balances for liquid-liquid systems in a nonideal stirred tank . Part 1 Description and qualitative validation of the model. *Chemical Engineering and Science*, 54:5887–5899, 1999.

[255] A. Hasseine, A. H. Meniai, M. Bencheikh Lehocine, and H. J. Bart. Assessment of drop coalescence and breakup for stirred extraction columns. *Chemical Engineering and Technology*, 28(5):552–560, 2005.

[256] A. M. Kamp, A. K. Chesters, C. Colin, and J. Fabre. Bubble coalesce in turbulent flows: A mechanistic model for turbulence-induced coalescence applied to microgravity bubbly pipe flow. *International Journal of Multiphase Flow*, 27:1363–1396, 2001.

[257] L. A. Utracki and Z. H. Shi. Devlopment of polymer blend morphology during compounding in a twin-screw extruder. Part I: droplet dispersion and coalescence - A review. *Polymer Engineering and Science*, 32(24):1824–1833, 1992.

[258] S. Lyu, F. S. Bates, and C. W. Macosko. Modeling of Coalescence in Polymer Blends. *AIChE Journal*, 48(1):7–14, 2002.

[259] A. K. Chesters and I. B. Bazhlekov. Effect of insoluble surfactants on drainage and rupture of a film between drops interacting under a constant force. *Journal of Colloid and Interface Science*, 230(2):229–243, 2000.

[260] J. Boyd, C. Parkinson, and P. Sherman. Factors affecting emulsion stability, and the HLB concept. *Journal of Colloid And Interface Science*, 41(2):359–370, 1972.

[261] A. J. Ramic, J. C. Stehlin, S. D. Hudson, A. M. Jamieson, and I. Manas-Zloczower. Influence of Block Copolymer on Droplet Breakup and Coalescence in Model Immiscible Polymer Blends. *Macromolecules*, 33(2):371–374, 2000.

[262] L. Leibler. Emulsifying effects of block copolymers in incompatible polymer blends. *Makromolekulare Chemie. Macromolecular Symposia*, 16(1):1–17, 1988.

[263] M. Mathew and S. Thomas. Compatibilisation of heterogeneous acrylonitrile – butadiene rubber / polystyrene blends by the addition of styrene – acrylonitrile copolymer: effect on morphology and mechanical properties. *Polymer*, 44:1295–1307, 2003.

[264] D. Heikens and W. Barentsen. Particle dimensions in polystyrene/polyethylene blends as a function of their melt viscosity and of the concentration of added graft copolymer. *Polymer*, 18:69–72, 1977.

[265] S. Jouenne, J. A. González-Léon, A. V. Ruzette, P. Lodéfier, and L. Leibler. Styrene-butadiene gradient block copolymers for transparent impact polystyrene. *Macromolecules*, 41(24):9823–9830, 2008.

[266] C. Pagnoulle and R. Jérôme. Particle-in-particle morphology for the dispersed phase formed in reactive compatibilization of SAN/EPDM blends. *Polymer*, 42(5):1893–1906, 2001.

[267] D. A. Thomas and L. H. Sperling. Polymer Blends. In D. R. Paul and S. Newman, editors, *Polymer Blends*, volume 2. Academic Press, Inc., New York, 1978.

[268] H. R. Brown, K. Char, and V. R. Deline. Block Copolymers and Adhesion Between Immiscible Polymers. In P J Lemstra and L A Kleintjens, editors, *Integration of Fundamental Polymer Science and Technology*. Elsevier Applied Science, London, New York, 5th edition, 1990.

[269] J. C. Lepers, B. D. Favis, and C. Lacroix. The Influence of Partial Emulsification on Coalescence Suppression and Interfacial Tension Reduction in PP / PET Blends. *Journal of Polymer Science: Prat B: Polymer Physics*, 37(9):939–951, 1999.

[270] S. P. Lyu, T. D. Jones, F. S. Bates, and C. W. Macosko. Role of block copolymers on suppression of droplet coalescence. *Macromolecules*, 35(20):7845–7855, 2002.

[271] N. C. Beck Tan, S. K. Tai, and R. M. Briber. Morphology control and interfacial reinforcement in reactive polystyrene/ amorphous polyamide blends. *Polymer*, 37(16):3509–3519, 1996.

[272] S. T. Milner and H. Xi. How copolymers promote mixing of immiscible homopolymers. *Journal of Rheology*, 40(4):663–687, 1996.

[273] U. Sundararaj and C. W. Macosko. Drop Breakup and Coalescence in Polymer Blends : The Effects of Concentration and Compatibilization. *Macromolecules*, 28(8):2647–2657, 1995.

[274] X. Luo, X. Huang, H. Yan, D. Yang, P. Zhang, and L. He. An experimental study on the coalescence behavior of oil droplet in ASP solution. *Separation and Purification Technology*, 203:152–158, 2018.

[275] Y. Liao and D. Lucas. A literature review of theoretical models for drop and bubble breakup in turbulent dispersions. *Chemical Engineering Science*, 64(15):3389–3406, 2009.

[276] E. H. Herø, N. La Forgia, J. Solsvik, and H. A. Jakobsen. Determination of Breakage Parameters in Turbulent Fluid-Fluid Breakage. *Chemical Engineering and Technology*, 42(4):903–909, 2019.

[277] M. Kostoglou and A. J. Karabelas. Toward a unified framework for the derivation of breakage functions based on the statistical theory of turbulence. *Chemical Engineering Science*, 60(23):6584–6595, 2005.

[278] J. C. Lasheras, C. Eastwood, C. Martinez-Bazan, and J. L. Montanes. A review of statistical models for the break-up an immiscible fluid immersed into a fully developed turbulent flow. *International Journal of Multiphase Flow*, 28(2):247–278, 2002.

[279] J. Baldyga and W. Podgórska. Drop break-up in intermittent turbulence: maximum stable and transient sizes of drops. *Canadian Journal of Chemical Engineering*, 76(3):456–470, 1998.

[280] G. M. Evans, G. J. Jameson, and B. W. Atkinson. Prediction of the bubble size generated by a plunging liquid jet bubble column. *Chemical Engineering Science*, 47(13-14):3265–3272, 1992.

[281] A. K. Biń. Gas entrainment by plunging liquid jets. *Chemical Engineering Science*, 48(21):3585–3630, 1993.

[282] X. Y. Fu and M. Ishii. Two-group interfacial area transport in vertical air-water flow I. Mechanistic model. *Nuclear Engineering and Design*, 219:143–168, 2002.

[283] G. Narsimhan, J. P. Gupta, and D. Ramkrishna. A model for transitional breakage probability of droplets in agitated lean liquid-liquid dispersions. *Chemical Engineering Science*, 34(2):257–265, 1979.

[284] L. Hagesaether, H. A. Jakobsen, and H. F. Svendsen. A model for turbulent binary breakup of dispersed fluid particles. *Chemical Engineering Science*, 57(16):3251–3267, 2002.

[285] F. Lehr and D. Mewes. A transport equation for the interfacial area density applied to bubble columns. *Chemical Engineering Science*, 56:1159–1166, 2001.

[286] C. Y. Wang and R. V. Calabrese. Drop breakup in turbulent stirred-tank contactors. *AIChE Journal*, 32(4):667–676, 1986.

[287] T. Wang, J. Wang, and Y. Jin. A novel theoretical breakup kernel function for bubbles/droplets in a turbulent flow. *Chemical Engineering Science*, 58(20):4629–4637, 2003.

[288] P. H. M. Elemans, .J M. H. Janssen, and H. E. H. Meijer. The measurement of interfacial tension in polymer/polymer systems: The breaking thread method. *Journal of Rheology*, 34(8):1311–1325, 1990.

[289] R. Andersson and B. Andersson. On the breakup of fluid particles in turbulent flows. *AIChE Journal*, 52(6):2020–2030, 2006.

[290] R. P Hesketh, A. W. Etchells, and T. W. F. Russell. Experimental Observations of Bubble Breakage in Turbulent Flow. *Industrial and Engineering Chemistry Research*, 30(5):835–841, 1991.

[291] J. Alvarez, J. Alvarez, and M. Hernández. A population balance approach for the description of particle size distribution in suspension polymerization reactors. *Chemical Engineering Science*, 49(1):99–113, 1994.

[292] P. Chu, J. Finch, G. Bournival, S. Ata, C. Hamlett, and R. J. Pugh. A review of bubble break-up. *Advances in Colloid and Interface Science*, 270:108–122, 2019.

[293] V. Alopaeus, J. Koskinen, K. I. Keskinen, and J. Majander. Simulation of the population balances for liquid-liquid systems in a nonideal stirred tank. Part 2-parameter fitting and the use of the multiblock model for dense dispersions. *Chemical Engineering Science*, 57(10):1815–1825, 2002.

[294] C. H. Lee, L. E. Erickson, and L. A. Glasgow. Bubble breakup and coalescence in turbulent gas-Liquid dispersions. *Chemical Engineering Communications*, 59(1-6):65–84, 1987.

[295] C. Martinez-Bazan, J. L. Montanes, and J. C. Lasheras. On the breakup of an air bubble injected into a fully developed turbulent flow. Part 1. Breakup frequency. *Journal of Fluid Mechanics*, 401:S0022112099006680, 1999.

[296] J. Placek and L. L. Tavlarides. Turbulent flow in stirred tanks. Part I: Turbulent flow in the turbine impeller region. *AIChE Journal*, 31(7):1113–1120, 1985.

[297] H. Luo and H. F. Svendsen. Theoretical Model for Drop and Bubble Breakup. *AIChE Journal*, 42(5):1225–1233, 1996.

[298] G. K. Batchelor. *The Theory of Homogeneous Turbulence*. Cambridge University Press, Cambridge, 1982.

[299] P. H. M. Elemans, H. L. Bos, J. M. H. Janssen, and H. E. H. Meijer. Transient phenomena in dispersive mixing. *Chemical Engineering Science*, 48(2):267–276, 1993.

[300] S. Tomotika. On the Instability of a Cylindrical Thread of a Viscous Liquid Surrounded by Another Viscous Fluid. *Proceedings of the Royal Society A: Mathematical, Physical and Engineering Sciences*, 150(870):322–337, 1935.

[301] P. Carrica and A. Clausse. A mathematical description of the critical heat flux as a non-linear dynamic instability. *Instabilities in Multiphase Flows*, pages 101–111, 1993.

[302] K. J. Valentas, O. Bilous, and N. Amundson. Analysis of breakage in dispersed phase systems. *Industrial and Engineering Chemistry Fundamentals*, 5(2):271–279, 1966.

[303] M. A. Hsia and L. L. Tavlarides. Simulation analysis of drop breakage, coalescence and micromixing in liquid-liquid stirred tanks. *The Chemical Engineering Journal*, 26(3):189–199, 1983.

[304] S. L. Ross, F. H. Verhoff, and R. L Curl. Droplet Breakage and Coalescence Processes in an Agitated Dispersion. 2. Measurement and Interpretation of Mixing Experiments. *Industrial and Engineering Chemistry Fundamentals*, 17(2):101–108, 1978.

[305] C. H. Lee, L. E. Erickson, and L. A. Glasgow. Dynamics of Bubble Size Distribution in Turbulent Gas-Liquid Dispersions. *Chemical Engineering Communications*, 61(1-6):181–195, 1987.

[306] M. Konno, M. Aoki, and S. Saito. Scale effect on breakup process in liquid-liquid agitated tanks. *Journal of Chemical Engineering of Japan*, 16(4):312–319, 1983.

[307] H. P. Grace. Dispersion phenomena in high viscosity immiscible fluid systems and application of static mixer as dispersion device in such systems. *Chem. Eng. Commun.*, 277(March 2013):225–277, 1982.

[308] B. J. Bentley and L. G. Leal. An experimental investigation of drop deformation and breakup in steady, two-dimensional linear flows. *Journal of Fluid Mechanics*, 167:241–283, 1986.

[309] K. Arai, M. Konno, Y. Matunaga, and S. Saito. Effect of dispersed-phase viscosity on the maximum stable drop size for breakup in turbulent flow. *Journal of Chemical Engineering of Japan*, 10(4):325–330, 1977.

[310] S. Wu. Formation of dispersed phase in incompatible polymer blends: interfacial and rheological effects. *Polymer Engineering and Science*, 27(5):335–343, 1987.

[311] J. J. Elmendorp. A study on polymer blending microrheology. *Polymer Engineering & Science*, 26(6):418–426, 1986.

[312] R. A. de Bruijn. Tipstreaming of drops in simple shear flows. *Chemical Engineering Science*, 48(2):277–284, 1993.

[313] J. O. Hinze. Fundamentals of the hydrodynamic mechanism of splitting in dispersion processes. *AIChE Journal*, 1(3):289–295, 1955.

[314] J. S. Lagisetty, P. K. Das, R. Kumar, and K. S. Gandhi. Breakage of viscous and non-Newtonian drops in stirred dispersions. *Chemical Engineering Science*, 41(1):65–72, 1986.

[315] C. A. Coulaloglou and L. L. Tavlarides. Drop Size Distributions and Coalescence Frequencies of Liquid-Liquid Dispersions in Flow Vessels. *AIChE Journal*, 22(2):289–297, 1976.

[316] A. Koshy, R. Kumar, and K. S. Gandhi. Effect of drag-reducing agents on drop breakage in stirred dispersions. *Chemical Engineering Science*, 44(10):2113–2120, 1989.

[317] H. A. Stone and L. G. Leal. The effects of surfactants on drop deformation and breakup. *Journal of Fluid Mechanics*, 220:161–186, 1990.

[318] C. D. Eggleton, T. M. Tsai, and K. J. Stebe. Tip streaming from a drop in the presence of surfactants. *Physical Review Letters*, 87(4):48302–48304, 2001.

[319] N. Ashgriz and J. Y. Poo. Coalescence and separation in binary collisions of liquid drops. *Journal of Fluid Mechanics*, 221:183–204, 1990.

[320] F. Jahanzad, Gordon Crombie, Robert Innes, and Shahriar Sajjadi. Catastrophic phase inversion via formation of multiple emulsions: A prerequisite for formation of fine emulsions. *Chemical Engineering Research and Design*, 87(4):492–498, 2009.

[321] W. Seifriz. Studies in Emulsions. III. *The Journal of Physical Chemistry*, 29(6):738–749, 1924.

[322] A. Gilchrist, K. N. Dyster, I. P. T. Moore, A. W. Nienow, and K. J. Carpenter. Delayed phase inversion in stirred liquid-liquid dispersions. *Chemical Engineering Science*, 44(10):2381–2384, 1989.

[323] A. W. Pacek and A. W. Nienow. A problem for the description of turbulent dispersed liquid-liquid systems. *International Journal of Multiphase Flow*, 21(2):323–328, 1995.

[324] E. Sheppard and N. Tcheurekdjian. Comments on multiple-phase emulsions. *Journal of Colloid And Interface Science*, 62(3):564–565, 1977.

[325] T. J. Lin, H. Kurihara, and T. Ohta. Effects of phase inversion and surfactant location on the formation of o/w emulsions. *Journal of the Society of Cosmetic Chemists*, 57:353–361, 1975.

[326] D. P. Kessler and J. L. York. Characteristics of inclusions in the dispersed phase of liquid-liquid suspensions. *AIChE Journal*, 16(3):369–374, 1970.

[327] S. Matsumoto, Y. Kita, and D. Yonezawa. An attempt at preparing water-in-oil-in-water multiple-phase emulsions. *Journal of Colloid And Interface Science*, 57(2):353–361, 1976.

[328] S. Matsumoto and W. W. Kang. Formation and Applications of Multiple Emulsions. *Journal of Dispersion Science and Technology*, 10(5):455–482, 1989.

[329] M. Frenkel, R. Shwartz, and N. Garti. Multiple emulsions. I. Stability: Inversion, apparent and weighted HLB. *Journal of Colloid And Interface Science*, 94(1):174–178, 1983.

[330] M. Ficheux, L. Bonakdar, and J. Bibette. Some Stability Criteria for Double Emulsions. *Langmuir*, 14(11):2702–2706, 1998.

[331] L. Y. Chu, A. S. Utada, R. K. Shah, J. W. Kim, and D. A. Weitz. Controllable monodisperse multiple emulsions. *Angewandte Chemie - International Edition*, 46(47):8970–8974, 2007.

[332] A. T. Florence and D. Whitehill. Some features of breakdown in water-in-oil-in-water multiple emulsions. *Journal of Colloid And Interface Science*, 79(1):243–256, 1981.

[333] J. M. Morais, O. D. H Santos, C. F. Nunes, J. R L .and Zanatta, and P. A. Rocha-Filho. W/O/W multiple emulsions obtained by one-step emulsification method and evaluation of the involved variables. *Journal of Dispersion Science and Technology*, 29(1):63–69, 2008.

[334] J. M. Morais, P. A. Rocha-Filho, and D. J. Burgess. Influence of phase inversion on the formation and stability of one-step multiple emulsions. *Langmuir*, 25(14):7954–7961, 2009.

[335] R. Pal. Pipeline flow of unstable and surfactant-stabilized emulsions. *AIChE Journal*, 39(11):1754–1764, 1993.

[336] A. W. Pacek, I. P.T. Moore, A. W. Nienow, and R. V. Calabrese. Video technique for measuring dynamics of liquid-liquid dispersion during phase inversion. *AIChE Journal*, 40(12):1940–1949, 1994.

[337] S. Sajjadi, F. Jahanzad, M. Yianneskis, and B. W Brooks. Phase Inversion in Abnormal O/W/O Emulsions. 2. Effect of Surfactant Hydrophilic - Lipophilic Balance. *Industrial & Engineering Chemistry Research*, 42(15):3571–3577, 2003.

[338] J. Yan and R. Pal. Effects of aqueous-phase acidity and salinity on isotonic swelling of W/O/W emulsion liquid membranes under agitation conditions. *Journal of Membrane Science*, 244(1-2):193–203, 2004.

[339] G. A. Davies, G. V. Jeffreys, D. V. Smith, and F. A. Ali. The formation of secondary droplets in a dispersion at a phase boundary. *The Canadian Journal of Chemical Engineering*, 48(3):328–329, 1970.

[340] H. Bararnia, S. M. Seyyedi, D. D. Ganji, and B. Khorshidi. Numerical investigation of the coalescence and breakup of falling multi-droplets. *Colloids and Surfaces A: Physicochemical and Engineering Aspects*, 424:40–51, 2013.

[341] J. M. Lee, K. H. Lim, and D. H. Smith. Formation of two-phase multiple emulsions by inclusion of continuous phase into dispersed phase. *Langmuir*, 18(20):7334–7340, 2002.

[342] A. T. Florence and D. Whitehill. The formulation and stability of multiple emulsions. *International Journal of Pharmaceutics*, 11(4):277–308, 1982.

[343] L. Hong, G. Sun, J. Cai, and T. Ngai. One-step formation of W/O/W multiple emulsions stabilized by single amphiphilic block copolymers. *Langmuir*, 28(5):2332–2336, 2012.

[344] A. S. Utada, E. Lorenceau, D. R. Link, P. D. Kaplan, H. A. Stone, and D. A. Weitz. Monodisperse double emulsions generated from a microcapillary device. *Science*, 308(5721):537–541, 2005.

[345] C. H. Choi, D. A. Weitz, and C. S. Lee. One step formation of controllable complex emulsions: From functional particles to simultaneous encapsulation of hydrophilic and hydrophobic agents into desired position. *Advanced Materials*, 25(18):2536–2541, 2013.

[346] S. Okushima, T. Nisisako, T. Torii, and T. Higuchi. Controlled production of monodisperse double emulstion by two step droplet breakup in microfluidic devices. *Langmuir*, 20(23):905–9908, 2004.

[347] S. Sajjadi, F. Jahanzad, M. Yianneskis, and B. W. Brooks. Phase Inversion in Abnormal O/W/O Emulsions. I . Effect of Surfactant Concentration. *Industrial and Engineering Chemistry Research*, 41(24):6033–6041, 2002.

[348] Y. Liu, E. L. Carter, G. V. Gordon, Q. J. Feng, and S. E. Friberg. An investigation into the relationship between catastrophic inversion and emulsion phase behaviors. *Colloids and Surfaces A: Physicochemical and Engineering Aspects*, 399:25–34, 2012.

[349] E. Tyrode, I. Mira, N. Zambrano, L. Márquez, M. Rondón-Gonzalez, and J. L. Salager. Emulsion catastrophic inversion from abnormal to normal morphology. 3. Conditions for triggering the dynamic inversion and application to industrial processes. *Industrial and Engineering Chemistry Research*, 42(19):4311–4318, 2003.

[350] S. Sajjadi, F. Jahanzad, and M. Yianneskis. Catastrophic phase inversion of abnormal emulsions in the vicinity of the locus of transitional inversion. *Colloids and Surfaces A: Physicochemical and Engineering Aspects*, 240(1-3):149–155, 2004.

[351] L. K. Saw, B. W. Brooks, K. J. Carpenter, and D. V. Keight. Different dispersion regions during the phase inversion of an ionomeric polymer-water system. *Journal of Colloid and Interface Science*, 257(1):163–172, 2003.

[352] L. Nielsen and R. Landel. *Mechanical properties of polymers and composites*. CRC Press, 2 edition, 1993.

[353] G. K. Raju and C. L. Cooney. Active learning from process data. *AIChE Journal*, 44(10):2199–2211, 1998.

[354] J. H. Lee, J. Shin, and M. J. Realff. Machine learning: Overview of the recent progresses and implications for the process systems engineering field. *Computers and Chemical Engineering*, 114:111–121, 2018.

[355] J. M. Maffi and D. A. Estenoz. Predicting phase inversion in agitated dispersions with machine learning algorithms. *Chemical Engineering Communications*, pages 1–18, 2020.

[356] L. Girifalco and R. J. Good. A theory for estimation of surface and interfacial energies. *Journal of Physical Chemistry*, 61(7):904–909, 1957.

[357] R. Afshar Ghotli, A. A. A. Raman, S. Ibrahim, and S. Baroutian. Liquid-Liquid Mixing in Stirred Vessels: A Review. *Chemical Engineering Communications*, 200(5):595–627, 2013.

[358] C. Olaru and L. Wehenkel. A complete fuzzy decision tree technique. *Fuzzy Sets and Systems*, 138(2):221–254, 2003.

[359] L. Breiman. Bagging predictors. *Machine Learning*, 24(2):123–140, 1996.

[360] Md Ridwan Al Iqbal. Rule extraction from ensemble methods using aggregated decision trees. *Lecture Notes in Computer Science (including subseries Lecture Notes in Artificial Intelligence and Lecture Notes in Bioinformatics)*, 7664 LNCS(PART 2):599–607, 2012.

[361] H. Deng. Interpreting tree ensembles with inTrees. *International Journal of Data Science and Analytics*, 7(4):277–287, 2019.

[362] S. Abe. *Support Vector Machines for Pattern Classification*, volume 53. Springer-Verlag, London, 2005.

[363] A. Prieto, B. Prieto, E. Martinez Ortigosa, E. Ros, F. Pelayo, J. Ortega, and I. Rojas. Neural networks: An overview of early research, current frameworks and new challenges. *Neurocomputing*, 214:242–268, 2016.

[364] J. Schmidhuber. Deep Learning in neural networks: An overview. *Neural Networks*, 61:85–117, 2015.

[365] A. Shichkin, A. Buevich, Al. Sergeev, E. Baglaeva, I. Subbotina, J. Vasilev, and M. Kehayova-Stoycheva. Training algorithms for artificial neural network in predicting of the content of chemical elements in the upper soil layer. In *AIP Conference Proceedings*, volume 2048, 2018.

[366] L. Behera, S. Kumar, and A. Patnaik. On adaptive learning rate that guarantees convergence in feedforward networks. *IEEE Transactions on Neural Networks*, 17(5):1116–1125, 2006.

[367] C. C. Yu and B. D. Liu. a Backpropagation Algorithm With Adaptive Learning Rate. In *Proceedings of the 2002 International Joint Conference on Neural Networks. IJCNN'02*, pages 1218–1223, 2002.

[368] E. G. Birgin and J. M. Martinez. A spectral conjugate gradient method for solving large-scale unconstrained optimization. *Applied Mathematics and Optimization*, 43:117–128, 2001.

[369] N. Andrei. Scaled conjugate gradient algorithms for unconstrained optimization. *Computational Optimization and Applications*, 38(3):401–416, 2007.

[370] T. Therneau and Atkinson B. rpart: Recursive Partitioning and Regression Trees. R package version 4.1-13., 2018.

[371] C. Lv, Y. Xing, J. Zhang, X. Na, Y. Li, T. Liu, D. Cao, and F. Y. Wang. Levenberg-Marquardt backpropagation training of multilayer neural networks for state estimation of a safety-critical cyber-physical system. *IEEE Transactions on Industrial Informatics*, 14(8):3436–3446, 2018.

[372] T. Nakama. Systematic comparisons of single- and multiple-hidden-layer neural networks. In *International Symposium on Neural Networks*, pages 270–279, Berlin, Heidelberg, 2011. Springer.

[373] P. Chuesiang, U. Siripatrawan, R. Sanguandeekul, L. McLandsborough, and D. J. McClements. Optimization of cinnamon oil nanoemulsions using phase inversion temperature method: Impact of oil phase composition and surfactant concentration. *Journal of Colloid and Interface Science*, 514:208–216, 2018.

[374] C. V. Luciani, D. A. Estenoz, G. R. Meira, N. L. García, and H. M. Oliva. Bulk High-Impact Polystyrene Process, 1. Partitions of tert-Butyl Peroctoate and Styrene in Blends Containing Polystyrene and Rubber. *Macromolecular Theory and Simulations*, 16:703–710, 2007.

[375] R. L. Kruse. Styrene-polymer interaction parameters in high impact polystyrene. In *Copolymers, Polyblends and Composites: A Symposium*, chapter 13, pages 141–147. American Chemical Society, Washington D. C., 1975.

[376] N. Casis, D. Estenoz, L. Gugliotta, H. Oliva, and G. Meira. Heterogeneous Bulk Polymerization of Styrene in the Presence of Polybutadiene: Calculation of the macromolecular structure. *Journal of Applied Polymer Science*, 99:3023–3039, 2006.

[377] W. A. Ludwico and S. L. Rosen. The Kinetics of Two-Phase Bulk Polymerization. I. Monomer and Initiator Distribution. *Journal of Applied Polymer Science*, 19:757–768, 1975.

[378] G. E. Molau and H. Keskkula. Heterogeneous Polymer Systems . IV . Mechanism of Rubber Particle Formation in Rubber-Modified Vinyl Polymers. *Journal of Polymer Science: Part A-1*, 4:1595–1607, 1966.

[379] J. L. White and R. D. Patel. Phase separation conditions in polystyrene–styrene–(butadiene–styrene) copolymer solutions. *Journal of Applied Polymer Science*, 19(6):1775–1778, 1975.

[380] R. J. J. Williams, B. A. Rozenberg, and J. P. Pascault. Reaction-Induced Phase Separation in Modified Thermosetting Polymers. In K. Dusek, editor, *Polymer Analysis Polymer Physics. Advances in Polymer Science.*, pages 95–156. Springer, Berlin, Heidelberg, 1997.

[381] G. F. Freeguard and M. Karmarkar. The production of rubber-modified polystyrene. II. The significance of shear in the phase inversion. *Journal of Applied Polymer Science*, 15(7):1657–1663, 1971.

[382] M. R. Rivera, R. Herrera, and L. Ríos. Structure and properties of model polybutadienes and HIPS: effect of rubber microstructure on HIPS dynamic mechanical properties. *Journal of Elastomers and Plastics*, 38:133–146, 2006.

[383] M. E. Shivokhin, L. Urbanczyk, J. Michel, and C. Bailly. The influence of molecular weight distribution of industrial polystyrene on its melt extensional and ultimate properties. *Polymer Engineering and Science*, 56(9):1012–1020, 2016.

[384] S. H. Anastasiadis, I. Gancarz, and J. T. Koberstein. Interfacial tension of immiscible polymer blends: temperature and molecular weight dependence. *Macromolecules*, 21(10):2980–2987, oct 1988.

[385] P. Gaillard, M. Ossenbach-Sauter, and G. Riess. Tensions interfaciales de systèmes polymères biphaseiques en présence de copolymères séquencés. *Makromolekulare Chemie. Rapid Communications.*, 1:771–774, 1980.

[386] S. H. Anastasiadis, I. Gancarz, and J. T. Koberstein. Compatibilizing Effect of Block Copolymers Added to the Polymer/Polymer Interface. *Macromolecules*, 22(3):1449–1453, 1989.

[387] R. C. Willemse, A. Posthuma De Boer, J. Van Dam, and A. D. Gotsis. Co-continuous morphologies in polymer blends: The influence of the interfacial tension. *Polymer*, 40(4):827–834, 1999.

[388] J. Silberberg and C. D. Han. The Effect of Rubber Particle Size on the Mechanical Properties of High-Impact Polystyrene. *Journal of Applied Polymer Science*, 22:599–609, 1978.

[389] D. A. Estenoz, E. Valdez, H. Oliva, and G. R. Meira. Bulk polymerization of styrene in presence of polybutadiene: Calculation of molecular macrostructure. *Journal of Applied Polymer Science*, 59:861–885, 1996.

[390] J. D. Moore. An electron microscope study of the microstructure of some rubber-reinforced polystyrenes. *Polymer*, 12:478–486, 1971.

[391] G. R. Meira and C. Kiparissides. Free Radical Polymerization: Heterogeneous Systems. In J. M. Asua, editor, *Polymer Reaction Engineering*, chapter 4, pages 179–208. Blackwell Publishing, Oxford, 1 edition, 2007.

[392] S. Joseph and S. Thomas. Morphology, morphology development and mechanical properties of polystyrene/polybutadiene blends. *European Polymer Journal*, 39:115–125, 2003.

[393] D. A. Estenoz, G. P. Leal, Y. R. Lopez, H. M. Oliva, and G. R. Meira. Bulk polymerization of styrene in the presence of polybutadiene. The use of bifunctional initiators. *Journal of Applied Polymer Science*, 62:917–939, 1996.

[394] L. I. Tolosa, A. Forgiarini, P. Moreno, and J. L. Salager. Combined effects of formulation and stirring on emulsion drop size in the vicinity of three-phase behavior of surfactant-oil-water systems. *Industrial and Engineering Chemistry Research*, 45:3810–3814, 2006.

[395] W. Wang, W. Cheng, J. Duan, J. Gong, B. Hu, and P. Angeli. Effect of dispersed holdup on drop size distribution in oil-water dispersions: Experimental observations and population balance modeling. *Chemical Engineering Science*, 105:22–31, 2014.

[396] P. Cigana, B. D. Favis, and R. Jerome. Diblock copolymers as emulsifying agents in polymer blends: Influence of molecular weight, architecture, and chemical composition. *Journal of Polymer Science, Part B: Polymer Physics*, 34(9):1691–1700, 1996.

[397] T. A. Vilgis and J. Noolandi. On the compatibilization of polymer blends. *Makromol. Chem., Macromol. Symp.*, 16:225–234, 1988.

[398] I. T. Norton, F. Spyropoulos, and P. W. Cox. Effect of emulsifiers and fat crystals on shear induced droplet break-up, coalescence and phase inversion. *Food Hydrocolloids*, 23(6):1521–1526, 2009.

[399] B. W. Bender. Dispersion of microgel in impact polystyrene. *Journal of Applied Polymer Science*, 9(8):2887–2894, 1965.

[400] D. J. Miller, T. Henning, W. Grunbein, and W. Grünbein. Phase inversion of W / O emulsions by adding hydrophilic surfactant — a technique for making cosmetics products. *Colloids and Surfaces A: Physicochemical and Engineering Aspects*, 183-185:681–688, 2001.

[401] G. Riess, J. Nervo, and D. Rogez. Emulsifying Properties of Block Copolymers. Oil-Water Emulsions and Microemulsions. *Polymer Engineering and Science*, 17(8):6–10, 1977.

[402] E. V. Menezes and W. W. Graessley. Nonlinear Rheological Behavior of Polymer Systems for Several Shear-Flow Histories. *Journal of Polymer Science: Polymer Physics Edition*, 20:1817–1833, 1982.

[403] D. Kim and E. B. Nauman. Solution viscosity of polystyrene at conditions applicable to commercial manufacturing processes. *Journal of Chemical Engineering Data*, 37:427–432, 1992.

[404] A. W. Hui and A. E. Hamielec. Thermal polymerization of styrene at high conversions and temperatures. An experimental study. *Journal of Applied Polymer Science*, 16:749–769, 1972.

[405] N. Friis and A. E. Hamielec. Gel-effect in emulsion polymerization of vinyl monomers. *ACS Symp. Ser.*, 24:82–91, 1976.

[406] F. R. Mayo. The Dimerization of Styrene. *Journal of the American Chemical Society*, 90(5):1289–1295, 1968.

[407] S. Fadda, A. Cincotti, and G. Cao. A novel population balance model to investigate the kinetics of in vitro cell proliferation: Part I model development. *Biotechnology and Bioengineering*, 109(3):772–781, 2012.

[408] J. Serrin. Mathematical Principles of Classical Fluid Mechanics. In C. Truesdell, editor, *Encyclopedia of Physics, vol 3/8/1*, pages 125–263. Springer, Berlin, Heidelberg, 1959.

[409] D. Ramkrishna. *Population Balances. Theory and Applications to Particulate Systems in Engineering.* Academic Press, Inc., London, 2000.

[410] D. L. Marchisio, J. T. Pikturna, R. O. Fox, R. D. Vigil, and A. A. Barresi. Quadrature method of moments for population-balance equations. *AIChE Journal*, 49(5):1266–1276, 2003.

[411] D. L. Marchisio and R. O. Fox. Solution of population balance equations using the direct quadrature method of moments. *Journal of Aerosol Science*, 36(1):43–73, 2005.

[412] T. T. Nguyen, F. Laurent, R. O. Fox, and M. Massot. Solution of population balance equations in applications with fine particles: Mathematical modeling and numerical schemes. *Journal of Computational Physics*, 325:129–156, 2016.

[413] M. Attarakih and H. J. Bart. *Solution of the Population Balance Equation by the Meshless Moving Particle Method (MMPM)*, volume 43. Elsevier Masson SAS, 2018.

[414] S. Kumar and D. Ramkrishna. On the solution of population balance equations by discretization - II. A moving pivot technique. *Chemical Engineering Science*, 51(8):1333–1342, 1996.

[415] S. Kumar and D. Ramkrishna. On the solution of population balance equations by discretization - III. Nucleation, growth and aggregation of particles. *Chemical Engineering Science*, 52(24):4659–4679, 1997.

[416] S. Kumar and D. Ramkrishna. On the solution of population balance equation by discretization - I. A fixed pivot technique. *Chemical Engineering Science*, 51(8):1131–1332, 1996.

[417] C. Chinwanitcharoen, S. Kanoh, T. Yamada, S. Hayashi, and S. Sugano. Preparation of aqueous dispersible polyurethane: Effect of acetone on the particle size and storage stability of polyurethane emulsion. *Journal of Applied Polymer Science*, 91(6):3455–3461, 2004.

[418] E. Jurado, V. Bravo, F. Camacho, J. M. Vicaria, and A. Fernández-Arteaga. Estimation of the distribution of droplet size, interfacial area and volume in emulsions. *Colloids and Surfaces A: Physicochemical and Engineering Aspects*, 295(1-3):91–98, 2007.

[419] N. Nizamidin, U. P. Weerasooriya, and G. A. Pope. Systematic Study of Heavy Oil Emulsion Properties Optimized with a New Chemical Formulation Approach: Particle Size Distribution. *Energy and Fuels*, 29(11):7065–7079, 2015.

[420] J. Solsvik, P. J. Becker, N. Sheibat-Othman, and H. A. Jakobsen. Population balance model: Breakage kernel parameter estimation to emulsification data. *Canadian Journal of Chemical Engineering*, 92(6):1082–1099, 2014.

[421] Y. Song, S. M. Lambert, and J. M. Prausnitz. Equation of state for mixtures of hard-sphere chains including copolymers. *Macromolecules*, 27(2):441–448, 1994.

[422] R. P. Danner and M. S. High. *Handbook of Polymer Solution Thermodynamics*. American Institute of Chemical Engineers, New York, 1993.

[423] J. Ansorena, J. J. Iruin, and G. M. Guzmán. Solvent influence on the viscosity-temperature relationship for dilute polybutadiene solutions. *European Polymer Journal*, 16:165–167, 1980.

[424] A. Bakker and L. Gates. Properly Choose Mechanical Agitators for Viscous Liquids. *Chemical Engineering Progress*, 91(12):25–34, 1995.

[425] D. Y. Kwok and A. W. Neumann. Contact angle measurement and contact angle interpretation. *Advances in Colloid and Interface Science*, 81(3):167–249, 1999.

[426] J. Noolandi and K. M. Hong. Effect of Block Copolymers at a Demixed Homopolymer Interface. *Macromolecules*, 17:1531–1537, 1984.

[427] P. C. Painter and M. M. Coleman. *Fundamentals of Polymer Science*. Technomic Publishing Co., Lancaster, 1 edition, 1997.

[428] J. Noolandi and K. M. Hong. Theory of block copolymer micelles in solution. *Macromolecules*, 16:1443–1448, 1983.

[429] J. Noolandi and K. M. Hong. Interfacial Properties of Immiscible Homopolymer Blends in the Presence of Block Copolymers. *Macromolecules*, 1(2):482–492, 1982.

[430] R. Asaletha, S. Thomas, and M. G. Kumaran. The Technological Compatibilization of Natural Rubber/Polystyrene Blends by the Addition of Natural Rubber-graft-Polystyrene. *Rubber Chemistry and Technology*, 68(4):671–687, 1995.

[431] M. A. Cerpa-Gallegos, C. F. Jasso-Gastinel, V. A. Lara-Valencia, and L. J. González-Ortiz. Improved methodology to measure surface tension and its application to polystyrene or poly(methyl methacrylate) in styrene solutions. *Langmuir*, 21(17):7726–7732, 2005.

[432] I. Prigogine and J. Marechal. The influence of differences in molecular size on the surface tension of solutions. IV. *Journal of Colloid Science*, 7(2):122–127, 1952.

[433] G. M. Kontogeorgis and S. Kiil. *Introduction to Applied Colloid and Surface Chemistry*. John Wiley & Sons, 2016.

[434] D. W. W. van Krevelen and K. te Nijenhuis. *Properties of Polymers*. Elsevier B.V., 4th edition, 2009.

[435] J. L. Ou, J. K. Yang, and H. Chen. Styrene/potassium persulfate/water systems: Effects of hydrophilic comonomers and solvent additives on the nucleation mechanism and the particle size. *European Polymer Journal*, 37(4):789–799, 2001.

[436] E. R. Soulé, G. E. Eliçabe, J. Borrajo, and R. J. J. Williams. Analysis of the phase separation induced by a free-radical polymerization in solutions of polyisobutylene in isobornyl methacrylate. *Industrial and Engineering Chemistry Research*, 46(23):7535–7542, 2007.

[437] K. M. Hong and J. Noolandi. The theory of interfacial tension in ternary homopolymer-solvent systems. *Macromolecules*, 14:736–742, 1981.

[438] L. Prieto, A. Pinilla, D. Becerra, P. Pico, J. P. Valdés, E. Pereyra, and N. Ratkovich. Phase inversion correlations analysis for oil-water flow in horizontal pipes. *Industrial and Engineering Chemistry Research*, 58(31):14436–14445, 2019.

[439] M. V. Brami, Y. Oren, C. Linder, and R. Bernstein. Nanofiltration properties of asymmetric membranes prepared by phase inversion of sulfonated nitro-polyphenylsulfone. *Polymer*, 111:137–147, 2017.

[440] T. Gruendling, M. Guilhaus, and C. Barner-Kowollik. Design of experiment (DoE) as a tool for the optimization of source conditions in SEC-ESI-MS of functional synthetic polymers synthesized via ATRP. *Macromolecular Rapid Communications*, 30(8):589–597, 2009.

[441] A. J. Scott, A. Nabifar, C. M. R. Madhuranthakam, and A. Penlidis. Bayesian design of experiments applied to a complex polymerization system: Nitrile butadiene rubber production in a train of CSTRs. *Macromolecular Theory and Simulations*, 24(1):13–27, 2015.